UNIVERSITÀ DEGLI STUDI DELLA TUSCIA

Dipertimento di Economia, Ingegneria, Società e Impresa

Corso di Dottorato di Ricerca in
Engineering for Energy and Environment
Curriculum Energy and Engineering Systems
XXXIII Ciclo

Tesi di Dottorato

Modeling, Design, and Optimization of Hydrogen Based Energy Conversion Systems

Settore scientifico disciplinare Ing-Ind/08

Tesi di dottorato di
Gabriele Loreti

Coordinatore del corso
Prof. Danilo Monarca

Tutore
Prof. Andrea L. Facci
Co-tutore
Prof. Stefano Ubertini

A.A. 2019/2020

Ai miei genitori.

Contents

Abstract

High-efficiency and low emissions hydrogen-based stationary multi-energy generation has an increasing important role. However, the full potential of hydrogen technologies can unfold only by accurate design and optimization of operation. In this regard, steady state modeling can quantify the performance and drive the design of innovative hydrogen-based energy systems. Moreover, the results of the modeling represent the input for realistic energy management scenario analysis. In such analysis, through an optimization algorithm is possible to quantify the overall economic and environmental advantages of the innovative energy systems with respect to state of the art systems for long time spans (i.e. one year operation). Specifically, this thesis studies three different fuel cell technologies: (i) polymer electrolyte membrane fuel cells, (ii) high temperature polymer electrolyte membrane fuel cells, and (iii) solid oxide fuel cells. All these systems have different peculiarities and critical issues to analyze.

Polymer electrolyte membrane fuel cells are the reference technology for automotive applications given the good dynamic characteristics. The high productive volume of automotive sector can be a crucial aspect to lower the cost also for stationary systems. However, automotive derivative polymer electrolyte membrane fuel cells require high purity hydrogen to be produced in advanced and high efficiency fuel processors. Therefore, chapter 1 studies the performance of combined heating and power systems based on automotive derivative fuel cell whose fuel processors integrate selective membranes. Moreover, chapter 2 studies the design of a membrane-integrated natural gas reforming system. The thermal power recovered in polymer electrolyte membrane fuel cells based combined heating and power systems can not be exploited in warm seasons and climates. Therefore, chapter 3 studies the integration of low temperature thermally driven cooling technologies in an automotive derivative combined heating and power system.

Solid oxide fuel cells are a promising technology for biogas energy conversion having high efficiency and high fuel flexibility. Moreover, solid oxide fuel cells combined heating and power systems can unlock the energy potential of several distributed and small scale biogas sources. However, the biogas fuel processor has to be carefully designed to increase the efficiency and the durability of the overall system. Therefore, chapter 4 compares integrated fuel processing options for biogas-fed solid oxide fuel cell combined heating and power systems.

High temperature polymer electrolyte membrane fuel cells inherit good dynamic characteristics from polymer electrolyte membrane fuel cells and fuel flexibility from solid oxide fuel cells. However, fuel processors designs originally conceived for both polymer electrolyte membrane fuel cells and solid oxide fuel cells are not optimal for high temperature polymer electrolyte membrane fuel cells systems. In fact, the intermediate temperature of such devices makes the steam reforming energetically inconvenient to sustain, given the fuel flexibility. Therefore, chapter 5 studies an innovative hybrid high temperature polymer electrolyte membrane fuel cell - gas turbine combined heating and power system whose fuel processor produces hydrogen from natural gas through the partial oxidation reaction.

Introduction

Innovative and high efficiency energy conversion systems has to be developed to reduce the anthropic emissions of greenhouse gases and pollutants. In fact, the CO_2 concentration in the atmosphere is now close to 410 ppm and constantly increases [1]. In the past 420k years the atmospheric CO_2 concentration has never been higher than 300 ppm before 20th century, clearly indicating the impact of recent human activities [2]. If the CO_2 atmospheric concentration reaches 450 ppm there is a 50 % chance of stabilizing the average global temperature rise below 2 °C according to the Intergovernmental Panel on Climate Change (IPCC) predictions [3]. Moreover, if the global temperature increase over 2 °C the human life will be directly affected by issues such as the sea level rise and the increase in the frequency of extreme weather events [4].

Hydrogen technologies play an increasingly important role for mobility, stationary energy generation and storage, and industrial applications [5–9]. Fuel Cells (FCs) produce electricity by highly efficiently (electrical efficiency up to more than 60 % [10, 11]) oxi-reducing hydrogen. Therefore, stationary and mobility applications implementing FCs can reduce the operational costs and the emissions of carbon dioxide and other pollutants compared to traditional energy conversion systems. In the stationary energy generation field, FCs are particularly emerging for distributed Combined Heating and Power (CHP) plants in residential and commercial applications [12–17]. The most promising aspects of FCs for this application are: (i) the high efficiency [18], which is independent from the size and increases at part load [19–22], (ii) the low level of pollutant emission [23], (iii) the absence of moving parts that results in no noise and no vibrations [24]. For these reasons, more than the 60.0 % of the micro-cogeneration [25] units sold in 2012 are based on fuel cells [14, 26, 27]. Also, electrolysers and FCs together enable the long term storage and reuse of the surplus renewable electricity [28–30] with competitive overall performance when

compared to batteries [21, 31–33].

Among the different kinds of fuel cells, low temperature ($< 100\,^{\circ}C$) Polymer Electrolyte Membrane Fuel Cells (PEMFCs) are technologically mature and provide several advantages [20–22]: (i) fast start-up and regulability, and (ii) high power density. Such characteristics make PEMFCs one of the most mature technology in the market. In fact, 75 % of new-installed FC units in 2017 were PEMFCs [7]. Moreover, PEMFCs market share is growing because in 2016 it accounted for the 65 % of new FC units. Such a success is mainly due to technological readiness and to the favorable performance at part load [20–22]. Despite 90 % of the polymer electrolyte membrane fuel cells newly-installed megawatts are used for transportation [7], the importance of such devices in the stationary field is still relevant. A great part of stationary FC-based units are installed within the Japanese ENE-FARM project, that mainly focuses on PEMFCs [7, 34]. However, the low operating temeprature implies that PEMFC can only operate with externally produced and purified hydrogen implying additional balance of plant costs and complexity.

Intermediate temperature (i.e. between $160\,^{\circ}C$ and $200\,^{\circ}C$) FCs, such as High Temperature Polymer Electrolyte Membrane Fuel Cells (HT-PEMFCs), maintain similar dynamic characteristics of PEMFCs while being tolerant to high impurities content in the feeding fuel (i.e. CO content up to 5%) without significantly losing efficiency [13, 35–39], and having a simplified water management. Even for HT-PEMFCs systems, the hydrogen production has to be handled externally.

Solide Oxide Fuel Cells (SOFCs) have high electrical efficiency and fuel flexibility thanks to the high operating temperature [40]. However, SOFCs have poor dynamic performance (i.e. start-ups, shutdowns, and regulations). Moreover, SOFCs fed with hydrocarbons based fuels can handle a large part of the reforming process directly in the anode.

The cost and environmental impact of hydrogen based systems depend heavily on the way the hydrogen is produced [41–44]. The current global hydrogen production is approximately 50 Mton per year. It is mainly produced from reforming reactions of steam with fossil feedstocks [31, 42, 43, 45–47], with close-to 50% from Natural Gas (NG). Other feedstocks include different hydrocarbons such as refinery off-gases, LPG, naphtha, petcoke, asphalts, vacuum tars, and others. Approximately 5% of the hydrogen produced worldwide is obtained through water electrolysis [31, 42, 43, 45–47]. Hydrogen production via water electrolysis is a carbon

dioxide and pollution free process. However, such a solution is only thoroughly emission free and economically viable if electricity from Renewable Energy Sources (RES) is available [42, 43]. Reforming of biogas and of power to gas products (synthetic NG or upgraded biogas) are also carbon neutral hydrogen production techniques [48]. The source of biomass and the biogas transformation process determine the emissions and the cost of the produced hydrogen [43]. Such emissions and costs are comparable to those associated to reforming of power to gas products [40, 43, 44].

Since low temperature PEMFCs are the most spread FC type for stationary power applications [7–9], complete external reforming systems featuring hydrogen purification are expected to have a major impact. Also, the same technology applies for the production of hydrogen to be used in industrial and mobility applications. The hydrogen purity required from low temperature FCs (i.e. 99.999%, according to SAE J2719 [49]) can be reached with a purification system such as [50, 51]: (i) Pressure Swing Adsorption (PSA), (ii) cryogenic distillation, or (iii) H_2 selective membranes. For syngas streams, PSA systems are the most common purification technology [52–55] because it can achieve a H_2 purity of 99.999 %, while being scalable in H_2 production from 10 Nm^3/h to 1000 Nm^3/h [50, 56]. However, PSA systems achieve limited H_2 recovery (i.e. in the range between 65% and 90%) [50, 52, 55, 57–61]. Moreover, the capital cost of PSA systems does not scale down for small-scale applications. Cryogenic distillation systems can only achieve limited H_2 purity (i.e. $\cong$ 99%) while being highly energy demanding and technically and economically not scalable for small-scale applications [50].

Hydrogen selective membranes are an emerging technology and incorporate all the advantages of PSA, without its drawbacks [50, 51, 62, 63]. Membranes can be applied in a separator module, but can as well be directly incorporated in steam reforming or water gas shift reactors [46] boosting the efficiency of the fuel processor because the H_2 separation shifts the reactions equilibrium towards products [46, 64]. An accurate selection of the operating parameters of membrane-integrated fuel processors is crucial to utilise the full potential of membranes. Moreover, the optimal operating parameters determine the most appropriate type of membranes [51].

Residential and commercial buildings are responsible for 38.0 % of the final energy consumed worldwide [65]. Moreover, about 30.0 % of CO_2 emissions related to energy conversion [66] are caused by the building

sector. The increase of households, the population rise, and the fragmentation of households will generate in the next years an increment in heating and cooling energy needs, and of electricity consumption, despite efficiency improvements in the final use [65–67]. In this scenario, CHP systems could bring relevant economical and environmental advantages [68], such as: (i) higher total efficiency, thanks to thermal recovery [19, 69], (ii) less greenhouse gases and pollutants emissions [69, 70], (iii) deferring investment on large centralized power plants and distribution lines [69, 70], (iv) lower distribution losses [70], (v) ancillary service to the main electric energy distribution grid [70], (vi) optimal integration of new and alternative technologies, such as renewable enery sources [28, 69, 71–73]. In particular [25] μ-CHP ($10^{-3}\,\mathrm{kW} < P_{\mathrm{el}} < 5\,\mathrm{kW}$) and small-CHP ($5\,\mathrm{kW} < P_{\mathrm{el}} < 5 \times 10^{3}\,\mathrm{kW}$) systems are suitable for residential and commercial building applications and have a great innovation potential, given the large market size. In particular, only in the US, more than 1 Million new residential units are built every year [74] and the trend is positive again.

Moreover, it is possible to incorporate a thermally activated cooling machine in a CHP plant in order to make thermal integration more effective in warm months and climates. Accordingly, a Combined Heat, Cooling, and Power (CHCP) plant is established [75]. Several thermally activated cooling technologies exist: absorption chillers [76, 77], adsorption chillers [76, 78] and desiccant cooling systems [76, 79]. Absorption chillers are the most established technology with variety of plant schemes as a function of the specific application [76, 77]. Double-effect absorption chillers are the most efficient and can be used if high quality heat is available (i.e. for temperatures between 120 °C and 220 °C). Single effect absorption chillers can be used with an heat source temperature in the range [80 °C; 120 °C], and have a Coefficient Of Performance (COP) between 0.5 and 0.7. Finally, the half-effect scheme can work with heat at a temperature below 80 °C, that could not be used in other kinds of absorption chillers. Such a feature is fundamental when a PEM fuel cell is the prime mover of the CHP plant.

The investment cost is the main obstacle to fuel cells diffusion. A survey on the market of FC CHP systems is reported in Table 1. These data show that commercial CHP systems costs [80–89] are far higher than the Fuel Cells and Hydrogen Joint Undertaking (FCH-JU) goals, that are between 3500 €/kW and 6500 €/kW for energy systems with a nominal

power in the range [5 kW - 400 kW] [90]. Moreover, a detailed techno-economic analysis [91] evidences that the cost of FCs for CHP applications should be lower than 3000 €/kW to be competitive with internal combustion engines.

Model	CHP	Cost [k€]	Power [kW]	Electrical Efficiency
Ballard ClearGEN [81]	Yes	NA	500	40%
Ballard ElectraGen [82]	No	$17 - 50$	$1.7 - 5$	40%
Baxi Gamma Premio [83]	Yes	NA	1	34%
Doosan FC Purocell 5 [84]	Yes	NA	440	43%
Elcore 2400 [83, 85]	Yes	9	0.3	33%
Panasonic [83, 86]	Yes	$20 - 30$	0.75	$37\% - 40\%$
Inhouse 5000+ [87]	Yes	NA	$1.5 - 5$	34%
Toshiba [83]	Yes	$20 - 30$	0.7	35%
Tropical NG-5 [88]	NO	NA	5	NA
Viessmann [83, 89]	Yes	36	0.75	39%
Eneos [86]	Yes	$24.5 - 28.5$	0.7	NA

Table 1: *Examples of PEM Fuel cell energy systems available in the market or in a pre-commercial stage in the power range 0-500 kW.*

The mobility market volume is much bigger than the stationary sector one. In fact, about 68 % of the power of the FC energy systems developed in 2017 is attributable to transport applications [7]. Moreover, it is widely acknowledged that the cost of energy systems decreases as the production volume increases [86, 92–94]. For these reasons, the usage of automotive derivative PEMFCs for stationary systems could be useful to reduce the investment costs of this technology [95, 96]. As a consequence, it is possible to build a constructive collaboration between two non-competitive industrial sectors, that could be crucial for FC CHP power plants development. This is the goal of the AutoRE project [95, 96], that aims at the establishment of the basis for the commercialization of an automotive derivative PEMFC based CHP system with a capital cost of 2000 €/kW and in the power range between 50 kW and 100 kW.

SOFCs are well suited for biogas energy conversion due to their high fuel flexibility. Moreover, SOFC CHPs can unlock the energy potential of several biogas sources. In fact, the biogas that can be produced from agricultural waste and Organic Fraction of Municipal Solid Wastes

(OFMSW) of small cities cannot be upgraded to be injected in the distibution grid because of the limited flowrate ($\ll 100\,m^3/h$) that would make the CH_4/CO_2 separation too expensive and because of the distance of the production site from the gas distribution grid. Moreover, the biogas produced in landfill sites is heavily N_2 diluted making the CO_2/N_2 separation too expensive. Valorizing the energy content of such biogas sources can result in more than 1 million 50 kWe SOFC CHP units [97]. For such applications, SOFC CHP systems are technologically superior than state-of-the-art systems such as Internal Combustion Engines (ICEs) because of the: (i) high electrical efficiency, even at small scale (i.e. 1 kWe), (ii) low pollutant emissions, and (iii) the possibility to higly efficiently convert gas mixtures with CH_4 strongly diluted with CO_2, and N_2. In such context, the project WASTE2WATTS (W2W) aims to design and engineer an integrated biogas-Solid Oxide Fuel Cell combined heat and power system with minimal gas pre-processing, focusing on low-cost biogas pollutant removal and optimal thermal system integration [97].

Chapters 1, 2, and 3 study PEMFCs based CHP and CHCP systems in the scope of the AutoRE project. Moreover, chapter 4 compares integrated fuel processing options for biogas-fed solid oxide fuel cell CHP systems in the scope of the W2W project. Finally, chapter 5 studies an innovative hybrid HT-PEMFC - GT CHP system.

Chapter 1

Numerical Modeling of an Automotive Derivative Polymer Electrolyte Membrane Fuel Cell Cogeneration System with Selective Membranes

Cogeneration power plants based on fuel cells are a promising technology to produce electric and thermal energy with reduced costs and environmental impact. One of the most mature fuel cell technology for this kind of applications are polymer electrolyte membrane fuel cells, which require high-purity hydrogen.

The most common and least expensive way to produce hydrogen within today's energy infrastructure is through steam reforming of natural gas. Such a process produces a syngas rich in hydrogen that has to be purified to be properly used in low temperature fuel cells. However, the hydrogen production and purification processes strongly affect the performance, the cost, and the complexity of the whole energy system.

Purification is usually performed through pressure swing adsorption, which is a semi-batch process that increases the plant complexity and incorporates a substantial efficiency penalty. A promising alternative option

for hydrogen purification is the use of selective metal membranes that can be integrated in the reactors of the fuel processing plant. Such a membrane separation may improve the thermo-chemical performance of the energy system, while reducing the power plant complexity, and potentially its cost.

Several studies have been performed in order to evaluate the integration of selective membranes in different parts of Natural Gas (NG) steam reforming based hydrogen production systems [64, 98–101]. In this work we focus on the fuel processor of a $50\,kW_{el}$ CHP power plant based on low temperature automotive derivative PEMFCs. Such an application and such a power range are almost untapped. Moreover, we retrieve part load performance, in order to lay the foundation of a study considering the CHP system in a real energy management scenario.

Therefore, in this chapter we perform a technical analysis, through thermo-chemical models, to evaluate the integration of Pd-based H_2-selective membranes in different sections of the fuel processing plant: (i) steam reforming reactor, (ii) water gas shift reactor, (iii) at the outlet of the fuel processor as a separator device. The results show that a drastic fuel processing plant simplification is achievable by integrating the Pd-membranes in the water gas shift and reforming reactors. Moreover, the natural gas reforming membrane reactor yields significant efficiency improvements.

The chapter is organized as follows. In section 1.1 the CHP system in study is presented. The numerical modeling methodology is accurately described in section 1.2. In section 1.3 the different fuel processing layouts analyzed are presented and characterized. Some in depth comparisons between the several case studies are presented in section 1.4. Finally, in section 1.5 we draw the conclusions of the work.

1.1 Problem Statement

The aim of this chapter is to assess the impact of H_2 selective membranes [64, 102] on the performance, cost, and system complexity reduction of the $50\,kW_{el}$ PEMFC based CHP plant, represented in Figure 1.1. Such a plant is connected to the NG line through a fuel processor based on SR, WGS, and syngas purification, that significantly impacts its performance.

1.1.1 Fuel Cell Based CHP Plant

We consider the 50 kW_{el} CHP power plant represented in Figure 1.1. The prime mover is an automotive derivative low temperature PEMFC that converts hydrogen into electrical energy [96].

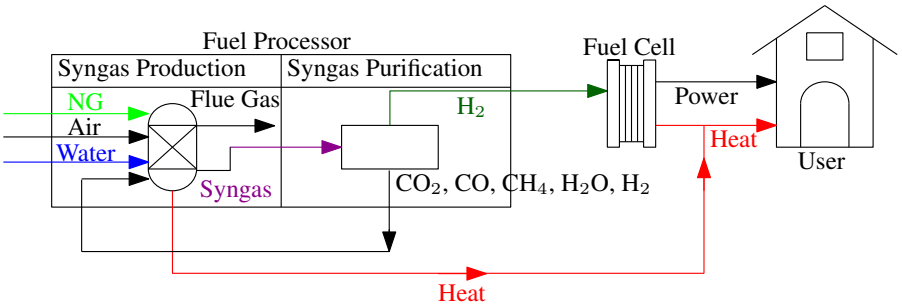

Figure 1.1: *Schematic of the cogenerative PEM fuel cell system.*

The fuel cell has been designed and produced by NuCellSys for the application in a small series of the Mercedes-Benz B-Class F-Cell produced from 2009. The FC based powertrain reliability has been demonstrated within a test of more than 300.000 km of harsh driving conditions on a single car. The automotive derivative PEMFC system is made of the fuel cell and a control system that regulates hydrogen and oxygen flows according to the operating conditions [95, 96].

The low temperature PEMFC requires very high purity H_2 (i.e. 99.999%, according to SAE J2719 [49]) that, in the near future, must be locally produced through a fuel processor (see Figure 1.1) because a diffused distribution grid for hydrogen is not present yet. A hydrogen rich syngas is obtained through NG steam reforming and WGS [102, 103]. Different technologies, including pressure swing adsorption separators and selective membranes [102], can be utilized to purify the syngas.

Fuel processing and purification strongly affect the overall performance of the considered energy system [104]. In fact, with a prime mover electrical efficiency in the range $[45\%, 55\%]$ [20–22, 104], the resulting overall plant efficiency is between 32% and 38% [104] when utilizing a PSA. Such an efficiency is below the 42% target set by the FCH-JU [90].

We focus on the fuel processor technology. Specifically, we analyze the option of utilizing Pd-based selective membranes to separate pure H_2 from reformate gas. We compare three configurations obtained by placing the membranes as separator device or integrating them in the WGS or SR

reactors. The global efficiency is the principal performance parameter and is evaluated through the following equation:

$$\eta_{\text{glob}} = \frac{P_{\text{el}} - W_{\text{aux}}^{\text{ref}}}{\dot{m}_{\text{NG}} \text{LHV}_{\text{NG}}}, \tag{1.1}$$

where P_{el} is the FC net electrical power, $W_{\text{aux}}^{\text{ref}}$ is the power required by the auxiliaries of the fuel processing section, $\dot{m}_{\text{NG}}$ is the total natural gas mass flow entering in the energy system and $\text{LHV}_{\text{NG}} = 46.5\,\text{MJ/kg}$ is the lower heating value of the natural gas. Note that in the evaluation of the global efficiency (eq. (1.1)) the electric power output P_{el} is a net value, as evidenced in a previous work [104], already reduced of the power required by the auxiliaries of the FC plant (feeding air compressor and refrigerant circulation pumps). The fuel processor efficiency (eq. (1.2)) is also defined as:

$$\eta_{\text{fp}} = \frac{\dot{m}_{\text{H}_2} \text{LHV}_{\text{H}_2}}{\dot{m}_{\text{NG}} \text{LHV}_{\text{NG}}}. \tag{1.2}$$

where $\dot{m}_{\text{H}_2}$ is the mass flow of H_2 and $\text{LHV}_{\text{H}_2} = 120\,\text{MJ/kg}$ is its lower heating value. Moreover, the effect of auxiliaries can be considered also for the fuel processor efficiency leading to the expression reported in eq. (1.3).

$$\eta_{\text{fp}}^{\text{tot}} = \frac{\dot{m}_{\text{H}_2} \text{LHV}_{\text{H}_2} - W_{\text{aux}}^{\text{ref}}}{\dot{m}_{\text{NG}} \text{LHV}_{\text{NG}}}. \tag{1.3}$$

Finally, we evaluate the thermal efficiency as follows:

$$\eta_{\text{th}} = \frac{Q_{\text{cog}}}{\dot{m}_{\text{NG}} \text{LHV}_{\text{NG}}}, \tag{1.4}$$

where Q_{cog} is the thermal power available via co-generation from the CHP plant.

The efficiencies are functions of the plant set-point, defined as:

$$\Phi = \frac{P_{\text{el}}}{P_{\text{el}}^{\text{nom}}}, \tag{1.5}$$

where $P_{\text{el}}^{\text{nom}} = 50\,\text{kW}_{\text{el}}$ is the maximum net electric power, and P_{el} is the net power output obtained by regulating the power plant.

1.1.2 H_2 selective membrane technology

Different types of membranes have been used to separate H_2 from syngas. Given the required temperature of operation for direct integration

of the membranes with the steam reforming reaction, high-temperature hydrogen-selective membranes such as Pd-alloy and inorganic proton-conducting membranes may be considered as leading candidates [105, 106]. These membrane types combine a high selectivity with an appropriate stability. The technology readiness level (TRL) of Pd-based membranes for example is currently around 5-6 and several commercialization initiatives are on-going [107, 108]. Microporous silica or zeolite membranes, or carbon membranes are also being explored, but typically have a limited selectivity, and potentially a lack of chemical stability under the operating conditions typically encountered [109].

State-of-the-art supported Pd-alloy membranes operate at elevated temperatures and are capable of separating H_2 from gaseous mixtures at typically 300 to 500 °C, at pressures up to 60 bar, in the presence of CO, H_2O, and other gases. These membranes represent thus an excellent match with the conditions applied in the H_2 production processes outlined above, even though an extension to even higher temperature may be desired in certain cases. CO inhibition is normally regarded as an issue for Pd-based membranes, however, at temperatures equal to or higher than 500 °C, it is revealed that the CO inhibition effect on hydrogen flux is extremely small even for state-of-the-art thin membranes [110]. Operation of Pd-based membranes over pro-longed times at such higher temperature, however, leads to slow degradation issues ascribed to pinhole formation [102, 111]. An increased Pd membrane thickness has been suggested as a solution, however, this unavoidably leads to a decrease in H_2 flux and increased cost. At higher temperature, i.e. > 600 °C, it seems thus more relevant to apply ceramic mixed conducting membrane technology [105]. Even though such membranes potentially show a lower absolute hydrogen flux per area, their temperature stability allows direct integration in the reforming stage of the steam reforming reaction process. For example, a protonic membrane reformer (PMR) that produces high-purity hydrogen from steam methane reforming in a single-stage reforming process with near-zero energy loss was reported recently by Coorstek Membrane Sciences [112]. The PMR comprises a $BaZrO_3$-based proton-conducting electrolyte deposited as a dense film on a porous Ni composite electrode with dual function as a reforming catalyst. The $BaZrO_3$-based electrolyte shows a good stability against bulk dissolution of carbonate species, i.e. in the presence of high concentrations of CO_2 [113]. The PMR is typically operated at 650 - 850 °C at 10-30 bar, and full methane conversion

is already obtained at 800 °C and 10 bar by removing 99 % of the formed hydrogen.

1.2 Methodology

We perform the steady state modeling of the power plants introduced in section 1.1 using a lumped parameter approach. The simulation software is Aspen Plus® [114], integrated with proprietary Fortran codes. The modeling strategy is consistent with other studies found in literature [64, 104, 115, 116].

The main components of the analyzed power plants are: (i) Membrane Separator; (ii) Heat Integrated Wall Reactor (HIWAR); (iii) Membrane Integrated Reforming Reactor; (iv) Water Gas Shift Reactor; (v) Membrane Integrated Water Gas Shift Reactor; (vi) Heat Exchangers; (vii) Auxiliaries; (viii) Automotive Derivative Fuel Cell; (ix) PSA Separator.

In the modeling environment we use the Peng Robinson equation [114] of state to compute the thermodynamic properties of working fluids. In addition, for pure water streams, the steamNBS tables are used [117].

1.2.1 Membrane Separator

The conceptual scheme for a membrane separator is shown in Figure 1.2. H_2 permeation through a selective membrane is described by the well-known Sieverts' law [118], which is expressed by eq. (1.6), in the case that H_2 diffusion through the bulk of Pd membrane is rate-limiting, i.e. the H_2 flux is proportional to the square root of the H_2 partial pressure difference ($n = 0.5$).

$$j_{H_2} = K_{H_2} \left(p^n_{H_2,\mathrm{ret}} - p^n_{H_2,\mathrm{perm}} \right), \tag{1.6}$$

where K_{H_2} is the hydrogen permeance of the membrane, $p_{H_2,\mathrm{ret}}$ and $p_{H_2,\mathrm{perm}}$ are the H_2 partial pressure on the retentate and permeate sides of the membrane, respectively. Deviations from Sieverts' law behavior (i.e. $n > 0.5$) have been attributed to various factors including surface and gas diffusion limitations, and have been used in literature to investigate the rate-controlling step of the permeation of H_2 through a selective membrane. The main factors determining the hydrogen permeance are the thickness of the membrane selective layer and the temperature [119]. In this study we consider state of the art Pd-alloy membranes. Such membranes

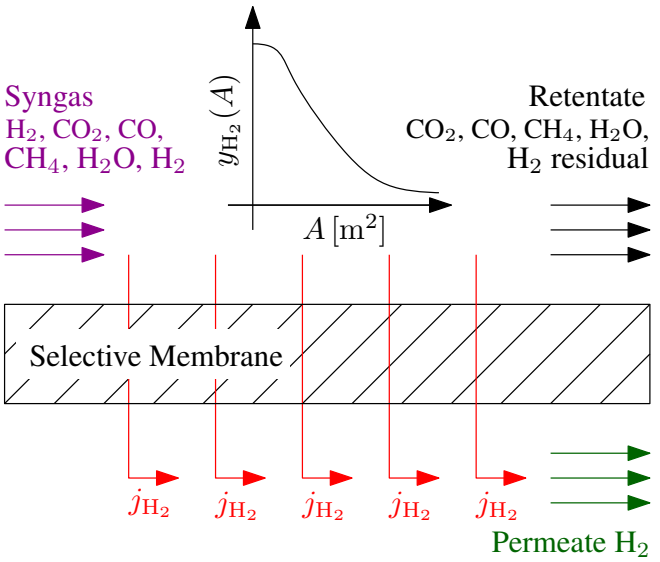

Figure 1.2: *Membrane separator scheme and nomenclature.*

can reach permeance values around $10^{-2}\text{mol}/\left(\text{m}^2\text{sPa}^{0.5}\right)$ at $350-400\,^{\circ}\text{C}$, thereby reaching values higher than the 2015 target set by the U.S. DoE ($8.5\times10^{-3}\text{mol}/\left(\text{m}^2\text{sPa}^{0.5}\right)$) [120]. However, these values are obtained in pure H_2 as feed gas where there are no surface and gas diffusion limitations for transport. Measurements obtained under real operating conditions have shown that the permeance can be decreased by roughly a factor of 5 compared to a situation where pure H_2 is applied as feed. In the current modelling study, we have therefore investigated the membrane performance assuming a permeance value of $8.5\times10^{-3}\text{mol}/\left(\text{m}^2\text{sPa}^{0.5}\right)$, which is the DoE target, and a permeance value one order of magnitude lower ($8.5\times10^{-4}\text{mol}/\left(\text{m}^2\text{sPa}^{0.5}\right)$). We underline that all the obtained results, except for the required membrane surface, would be the same also considering ceramic mixed conducting membrane technology.

Referring to eq. (1.6), the driving force vanishes when $p_{\text{H}_2,\text{ret}}=p_{\text{H}_2,\text{perm}}$. Note that we assume the absence of a sweep flow in the permeate side to have a better performing FC [100]. Thereafter, the minimum hydrogen concentration possible in the retentate is $y_{\text{H}_2}^{\text{min}}=p_{\text{perm}}/p_{\text{ret}}$ and can be reached only by using an infinite surface membrane.

The following equation evaluates the H_2 concentration in the retentate

as a function of the membrane area A ($y_{\mathrm{H_2}}(A)$):

$$y_{\mathrm{H_2}}(A) = \frac{n_{\mathrm{H_2,syn}} - \int_0^A j_{\mathrm{H_2}}(A)\, dA}{n_{\mathrm{tot}}(A)}, \tag{1.7}$$

where $n_{\mathrm{H_2,syn}}$ is the initial number of $\mathrm{H_2}$ moles in the syngas and $n_{\mathrm{tot}}(A)$ is the total number of moles in the retentate. Equation (1.7) is numerically integrated using the Euler method to obtain $y_{\mathrm{H_2}}(A)$ shown in Figure 1.3. Therein, we consider the following retentate and the permeate total pressures, $p_{\mathrm{ret}} = 11.5\,\mathrm{bar}$ and $p_{\mathrm{perm}} = 1.20\,\mathrm{bar}$, respectively. The initial syngas mole flow is $\dot{f}^{\mathrm{syn}} = 0.944\,\mathrm{mol/s}$, carrying a hydrogen mole flow $\dot{f}^{\mathrm{syn}}_{\mathrm{H_2}} = 0.482\,\mathrm{mol/s}$. The selectivity of the membrane is assumed to be infinite, and hydrogen is separated. For the integration of eq.(1.7), we assume $dA = 10^{-3}\mathrm{m}^2$ after a convergence analysis on the total pure hydrogen flux $J_{\mathrm{H_2}}$. Figure 1.3 evidences that $K_{\mathrm{H_2}}$ influences the area required for the separation, but not $y^{\mathrm{min}}_{\mathrm{H_2}}$, or in other words the separation efficiency.

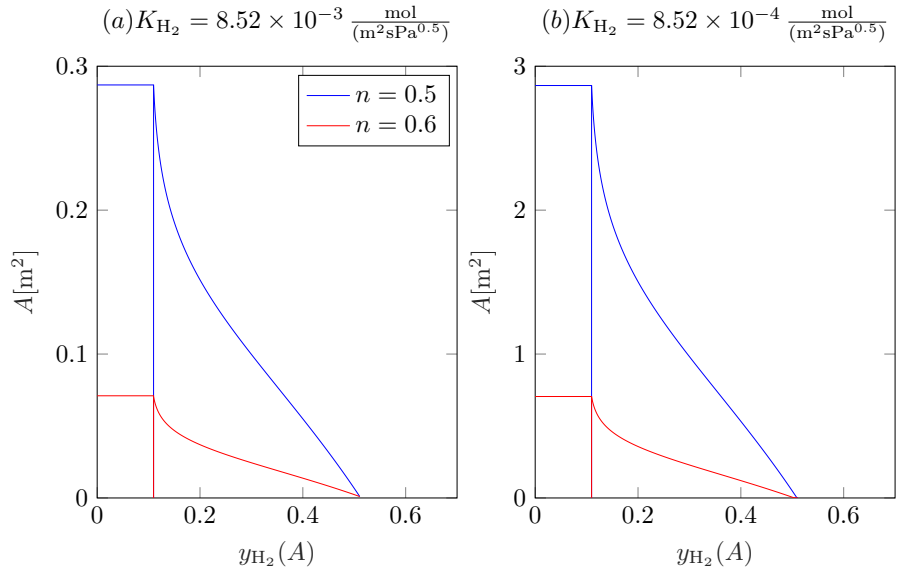

Figure 1.3: *Variation of the surface of the membrane separator with respect to the hydrogen concentration in the retentate, as a function of the driving force exponent in two different cases: a)* $K_{H_2} = 8.52 \times 10^{-3}\, mol/\left(m^2 sPa^{0.5}\right)$*; b)* $K_{H_2} = 8.52 \times 10^{-4}\, mol/\left(m^2 sPa^{0.5}\right)$.

For $y_{\mathrm{H_2}} \geq 0.2$ (i.e. $y_{\mathrm{H_2}} \geq 1.92 y^{\mathrm{min}}_{\mathrm{H_2}}$) the membrane area increases linearly by reducing the $\mathrm{H_2}$ concentration (see Figure 1.3). Conversely,

a further reduction of y_{H_2} causes a sharp increment of the required surface. Thus, in the followings, we assume that the H_2 concentration at the exit of the membrane separator is $y_{H_2} = 1.05 y_{H_2}^{\min}$and we denote $J_{H_2} = \int_0^A j_{H_2}(A)\, dA$. The separation efficiency (also known as hydrogen recovery factor) is defined as:

$$\eta^{\text{SEP}} = \frac{J_{H_2}}{\dot{f}_{H_2}^{\text{syn}}}. \tag{1.8}$$

The retentate pressure largely determines η^{SEP} through its influence on $y_{H_2}^{\min}$, as evidenced in Figure 1.4. Specifically, η^{SEP} increases from 2.65 % to 89.3 % varying p_{ret} from 2.50 bar to 12.5 bar. On the contrary it further increments just to 94.3 % increasing p_{ret} to 22.5 bar.

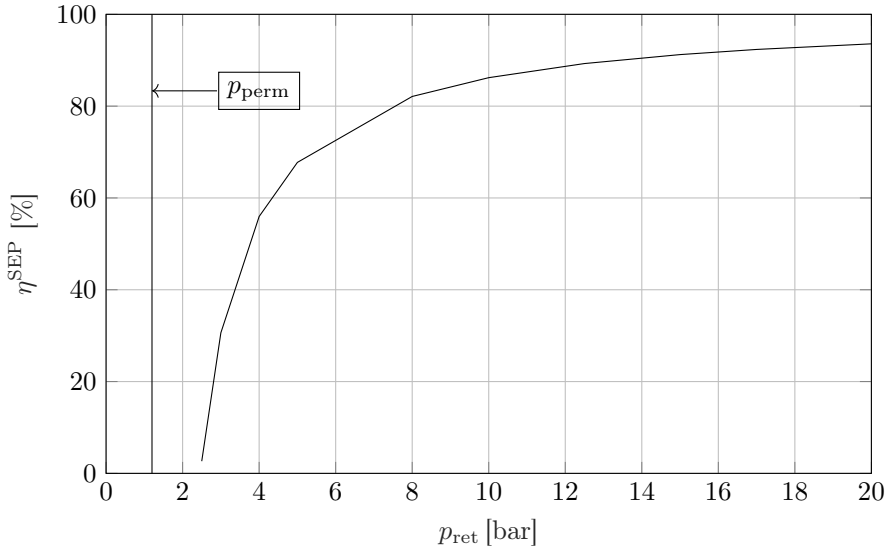

Figure 1.4: *Maximum attainable separation efficiency of Pd-based selective membranes as a function of the feed pressure, for* $p_{perm} = 1.20\,bar$, $\dot{f}^{ret} = 0.944\,mol/s$, $\dot{f}_{H_2}^{ret} = 0.482\,mol/s$, *and* $y_{H_2} = 1.05 y_{H_2}^{min}$.

1.2.2 HIWAR

Steam reforming is performed in the HIWAR [121, 122], where the catalytic oxidation of natural gas and the steam reforming reactions take place in a single element. Such a device is a ceramic tube coated with a metal catalyst film, specific for the oxydation, in its inner side and with

another catalytic substance, specific for the reforming, in the outer. The heat flux between the two sides of the reactor is allowed by the conductive wall.

In our model such a component is simulated through two separate reactors. The coupling of the elements, i.e. the heat integration, is then implemented through an heat flux from the burner to the reformer (Figure 1.5).

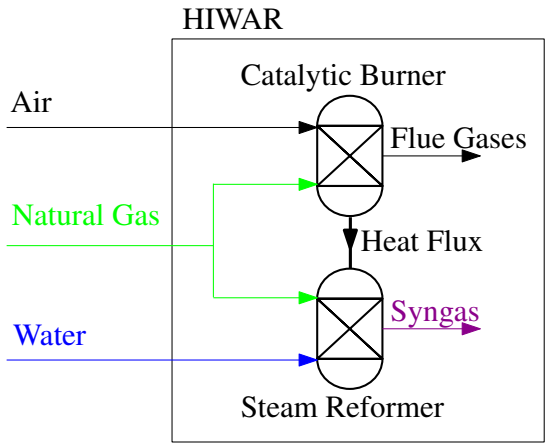

Figure 1.5: *Schematic overview of the HIWAR reactor model.*

The temperature of the catalytic burner is 845 °C. Thus a common equilibrium reactor would be not effective. Therefore, we use the stoichiometric reactor (RStoic in Aspen Plus®) and specify the chemical reactions that take place and the associated fractional conversion. The following equation reports the reactions implemented for the catalytic burner reactor:

$$\begin{cases} 2H_2 + O_2 \rightarrow 2H_2O \\ C_xH_z + \left(\frac{z}{4} + x\right) O_2 \rightarrow \frac{z}{2}H_2O + xCO_2. \end{cases} \tag{1.9}$$

The fractional conversion of each oxidized element is set to 100%.

The steam reforming is modeled as an equilibrium reactor (called RGibbs in the modeling environment). Aspen Plus® calculates the equilibrium composition of the resulting flows minimizing the Gibbs free energy [114]. The temperature and pressure of the reactor will determine the prevailing reactions through the equilibrium constants. The reforming side of the HIWAR reactor is operated at a temperature of 770 °C. The

following equation, reports the dominant reactions at such a temperature:

$$\begin{cases} C_xH_z + xH_2O \rightleftharpoons \left(x + \frac{z}{2}\right) H_2 + xCO, \\ CO + H_2O \rightleftharpoons CO_2 + H_2. \end{cases} \tag{1.10}$$

Note that at 770°C, the chemical reaction equilibrium constants for methane (the main component of NG) steam reforming and water gas shift are $K_{\mathrm{REF}} = 84.4$ and $K_{\mathrm{WGS}} = 1.21$ [123] respectively. The NG steam reforming is the largely predominant reaction, being $K_{\mathrm{REF}} \cong 70 \times K_{\mathrm{WGS}}$.

1.2.3 Water Gas Shift Reactor

The water gas shift reaction is conventionally applied in fuel processing plants, to produce further hydrogen from carbon monoxide and water, as follows:

$$CO + H_2O \rightleftharpoons CO_2 + H_2. \tag{1.11}$$

We utilize the stoichiometric equilibrium reactor that allows the user to specify the stoichiometry of the reactions that has to be simulated (in this case the reaction reported in eq. (1.11)). Such a modeling choice is required to exclude the steam reforming reaction from chemical equilibrium computations. The reforming reaction besides having a lower equilibrium constant compared to reaction (1.11) is also kinetically hindered: at 320°C, the chemical reaction equilibrium constants for water gas shift and methane steam reforming are $K_{\mathrm{WGS}} = 24.9$ and $K_{\mathrm{REF}} = 2.32 \times 10^{-7}$ [123] respectively, and this reactor utilizes specific catalysts to promote reaction (1.11) rather than steam reforming. For these reasons, the water gas shift is largely predominant.

1.2.4 Membrane Reforming and Water Gas Shift Reactors

Pd-based selective membranes resist to relatively high temperatures and pressures and thus can be integrated directly in reactors (Figure 1.6). In this way the hydrogen produced is separated from the reactants, shifting the reaction towards products. The integration can be performed both in the water gas shift and in the reforming reactors.

For these processes we have developed a 1-D reactor model in Aspen Plus®, that is an inherently 0-D simulation environment. To this aim,

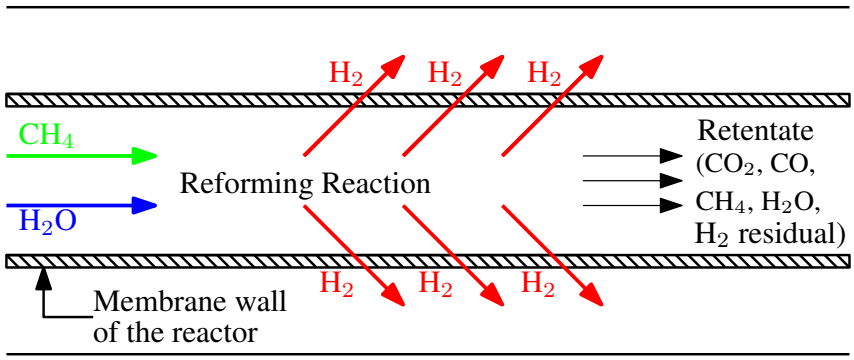

Figure 1.6: *Schematic overview of membrane reactors.*

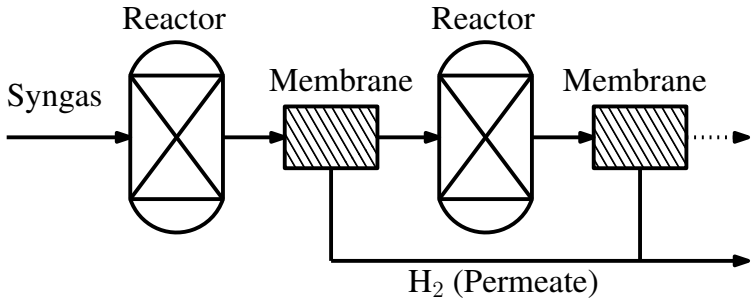

Figure 1.7: *Modeling approach used for the membrane reactors.*

we discretize the membrane reforming and membrane WGS as a sequence of reactors and separators, as shown in Figure 1.7.

To determine the most appropriate number of discretization steps a convergence analysis is performed. Specifically, the mass flow of the pure hydrogen produced by the fuel processing plant is considered as the convergence parameter. We verified that the H_2 flow varies less then a 1% by incrementing the number of discretization steps from five to six, for both reforming and water gas shift reactor. Therefore, 6 steps are used for the discretization of all membrane reactors.

1.2.5 Heat Exchangers

All heat exchangers are studied through the logarithmic mean temperature difference model. An accurate modeling of the off-design perfor-

mance is considered, since the thermal resistance varies as a function of the hydrogen mass flow rate. In design conditions the product between the heat exchange coefficient and the area of the heat exchanger is calculated as [124]:

$$\Gamma^* = \frac{Q}{\Delta \mathrm{T}_{\mathrm{ml}}}, \tag{1.12}$$

where Q is the thermal power and $\Delta \mathrm{T}_{\mathrm{ml}}$ the logarithmic mean temperature difference.

When mass flows change, the product UA is calculated as:

$$\Gamma = \Gamma^* \left(\frac{\dot{m}}{\dot{m}^*} \right)^{0.8}, \tag{1.13}$$

where $\dot{m}$ and $\dot{m}^*$ are the mass flows in off-design and design conditions respectively.

When $\dot{m} \neq \dot{m}^*$ for both the hot and the cold side of the heat exchanger, the mass flow with the lower heat transfer coefficient is considered in eq. (3.3).

We underline that Aspen Plus® is a thermodynamic modeling software based on a lumped parameter approach. Thus, heat exchangers are characterized using a logarithmic mean temperature difference modeling that takes into account only input and output conditions. However, the heat capacity can vary during the heat exchange process, as a consequence of phase changes of one or more species. In these situations, the constant heat capacity assumption underlying the logarithmic mean temperature difference approach is not longer valid and the thermal resistance calculated by the software can be incorrect. Such a wrong evaluation of the thermal resistance cause a wrong estimation of the heat exchanged in off-design conditions. To overcome this problem, we divide each heat exchanger in several fictitious elements, as evidenced in Figure 1.8. The heat exchange process is thus discretized in small sub-processes, in which the heat capacity can be considered constant. The number of discretization steps is determined through a convergence analysis based on the output enthalpy of hot and cold streams. As the most critical case converges in 10 discretization steps, all the heat exchangers are split in 10 elements.

1.2.6 Auxiliaries

Several fluid machineries provide the required pressure to the fluids in each plant section. Specifically, there are: (i) a natural gas compressor,

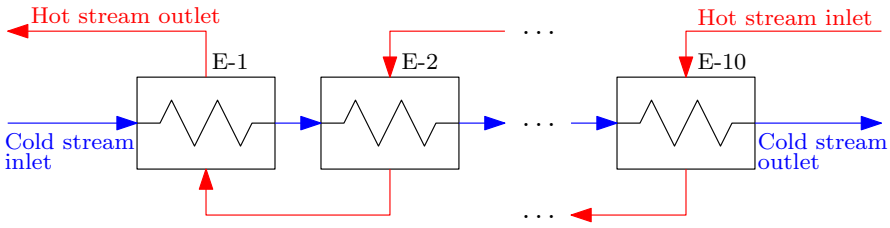

Figure 1.8: *Discretization process for heat exchangers.*

(ii) a water pump for the high pressure steam generation, (iii) an air compressors for circulation, (iv) an air compressor for the fuel cell, (v) two water pumps for circulation in the fuel cell balance of plant and, in some cases, (vi) an hydrogen compressor.

The power required from the auxiliaries, is evaluated as:

$$W_{\text{aux}} = \eta^{\text{is}} \left(h^{\text{out}} - h^{\text{in}} \right), \tag{1.14}$$

where h is the enthalpy of the fluid calculated from the Peng Robinson equation [114] of state and η^{is} is the isoentropic efficiency of the pump/compressor. Values for the efficiency of the devices are retrieved from an Aspen Plus library of real machines.

1.2.7 Automotive Derivative Fuel Cell

The main components of the fuel cell model are (Figure 1.9): (i) the PEMFC stack, (ii) the air compressor, (iii) two cooling circuit with different temperature levels, (iv) two pumps for water circulation, (v) two heat exchanger for co-generation. In the model a control system is also simulated, in order to maintain the proper ratio between air and hydrogen mass flows.

The cathodic exhaust and the high temperature cooling circuit stream of the fuel cell are exploited for co-generation purposes.

The model of the PEMFC stack relies on experimental data of the automotive FC provided by NuCellSys and reported in Figure 1.10. Specifically the black-box model calculates the electric power as a function of the input hydrogen mass flow rate. It also returns the thermo-physical properties, compositions, and mass flow rates of air, purge, exhaust, and coolants mass flows.

Note that in Figure 1.10(d) each temperature profile is normalized with respect to its nominal value. As a consequence, despite normalized

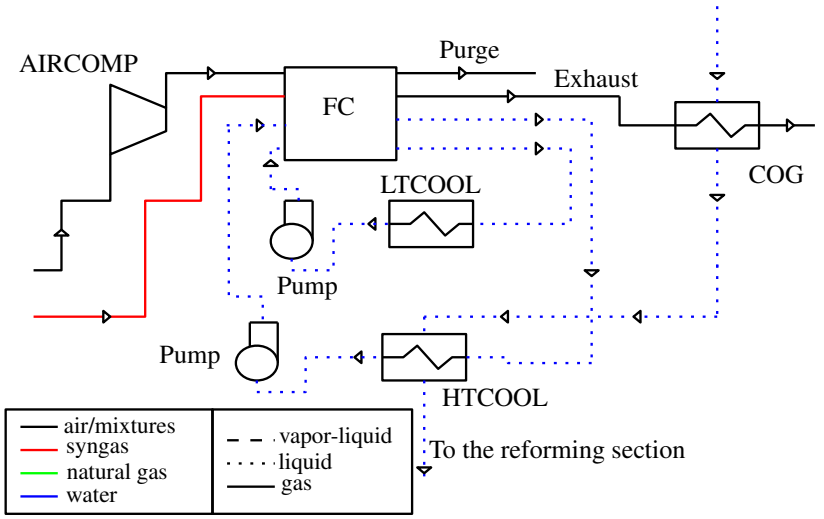

Figure 1.9: *Schematic representation of the model implemented for the fuel cell.*

inlet temperature is lower than normalized outlet, the physical values are coherent (i.e. outlet lower than inlet).

1.2.8 Pressure Swing Adsorption Separator

The PSA is modeled with a black box phenomenological approach. The utilized experimental data are reported in Figure 1.11. The separation efficiency varies between 76% and 85%, respectively at 8 bar and 20 bar syngas feed pressure, p_{ret}.

The black-box model calculates composition, mass flow rate and pressure of the pure hydrogen and retentate flows, taking as input such characteristics of the syngas.

1.3 Case Studies

Table 1.1 summarizes the considered power plant configurations. Note that each plant has a different natural gas mass flow rate to obtain the same H_2 mass flow rate entering the FC. In this way, the comparison is not biased by the FC efficiency, which is a function of its H_2 input mass flow rate, or equivalently of the set-point, as evidenced in Figure 1.10.

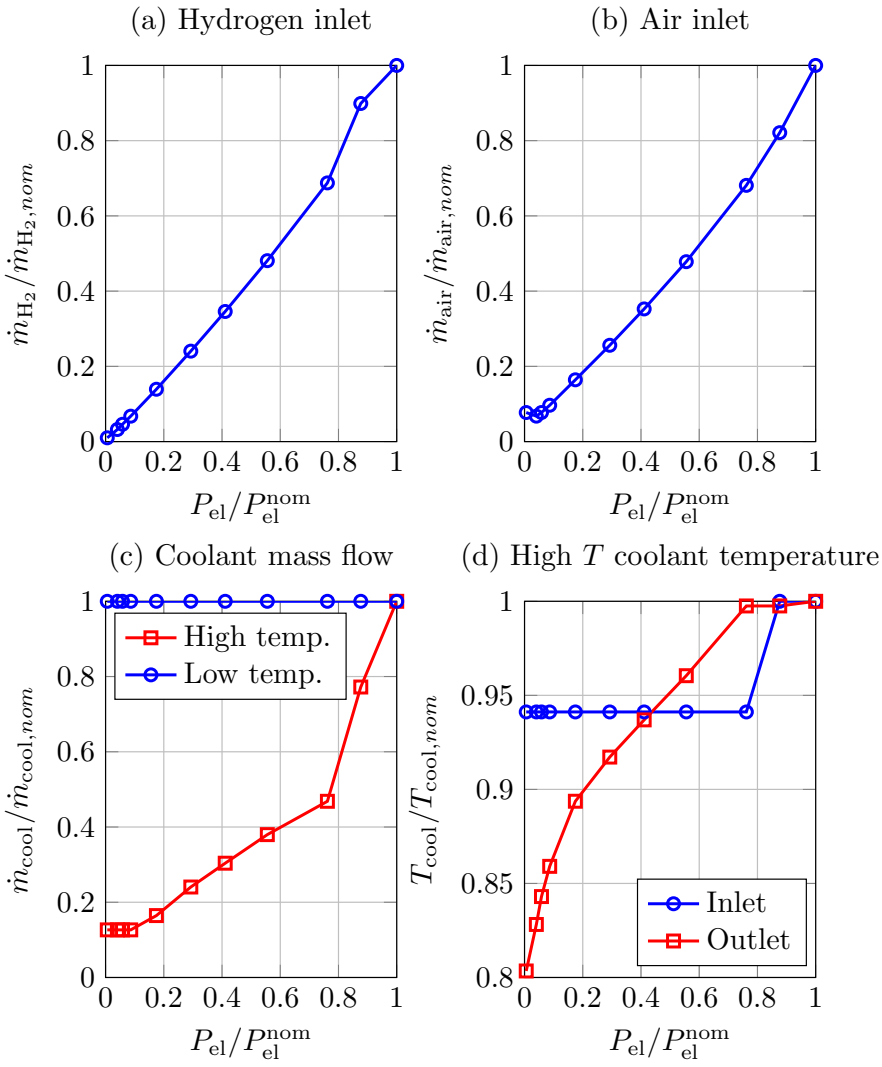

Figure 1.10: *Experimental performance of the automotive derivative PEMFC system. Data are reported in a non-dimensional form.*

1.3.1 Plant A: Baseline Plant

Plant A, schematically reported in Figure 1.12, is the baseline configuration.

At $\Phi = 1$, 10.4 kg/h of NG are compressed to 12 bar and mixed with 38.7 kg/h of super-heated steam at a temperature of 457 °C. The ratio between the mass flow rates of the NG and of the steam entering the

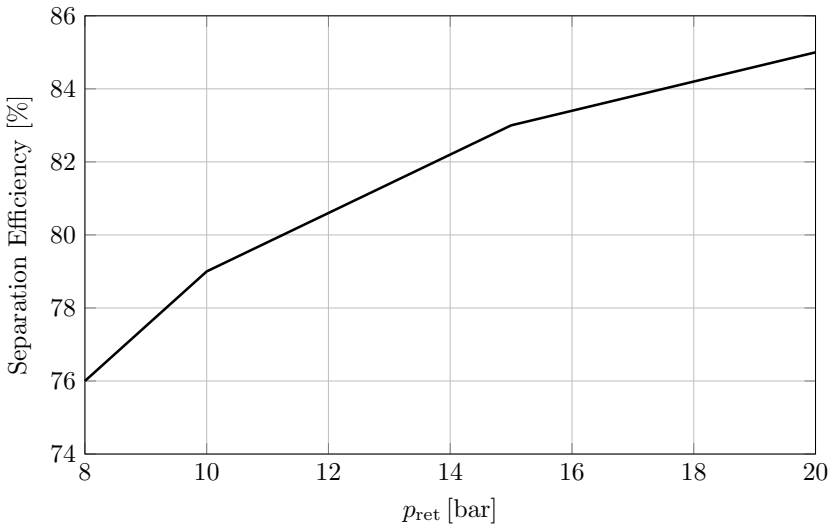

Figure 1.11: *Experimental data for the pressure swing adsorption separator: separation efficiency is expressed as a function of the feed pressure.*

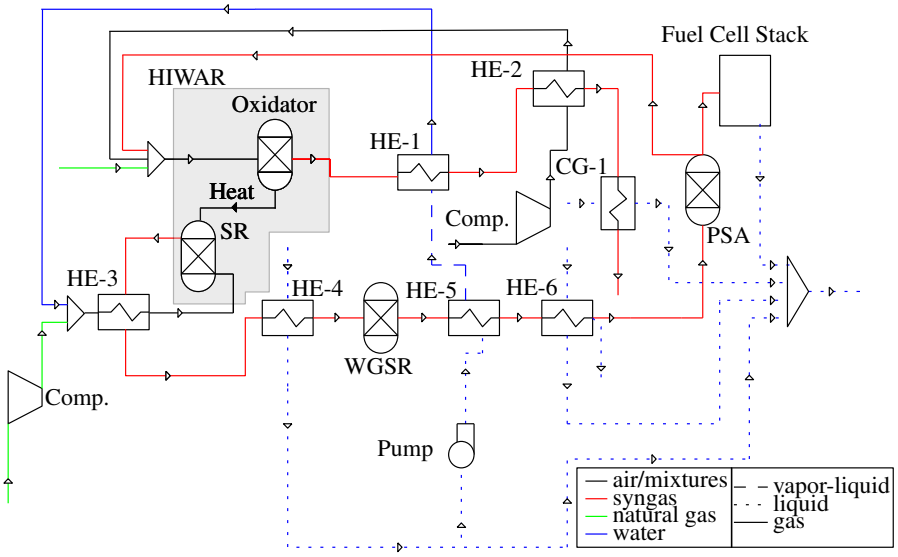

Figure 1.12: *Schematic overview of the baseline energy conversion plant.*

reformer is fixed to $\psi = 3.73$. The resulting mixture, at a temperature of 399 °C, is further heated in HE-3 to 760 °C. Such a temperature is the minimum possible to avoid an efficiency drop of the reaction [22, 125]. In the same heat exchanger the syngas temperature is reduced from 770 °C

Table 1.1: *Summary of the considered fule processor configurations.*

Case	Description	$\dot{m}_{NG}^{REF} + \dot{m}_{NG}^{BURN}$ [kg/h]
Plant A	Steam reforming, water gas shift, purification via PSA	10.4+0.204
Plant B	Steam reforming, water gas shift, purification via selective membranes	9.45+0.886
Plant C	Steam reforming, membrane integrated water gas shift	9.21+0.868
Plant D	Membrane integrated steam reforming	6.90+2.62

to 436 °C . The working pressure is imposed as a trade-off between the reaction performance [98, 103] and the PSA efficiency (see Figure 1.11).

In HE-4 the syngas is further cooled to 320 °C, in order to have a favorable water gas shift reaction kinetics. The thermal power extracted from the hydrogen rich gas in HE-4 is used for co-generation. The syngas exits the WGSR at 381 °C, being the CO shift an exothermic reaction. The thermal energy still present in the H_2 rich gas is used both to preheat the water necessary for the reforming reaction and for co-generation purposes. Specifically, in HE-5 the water is heated from 15.0 °C to 188 °C with a vapour fration of 0.25, while the syngas is cooled to 128 °C.

The hydrogen rich gas is further cooled to 50 °C for co-generation purposes in HE-6. The gas mixture is then purified in the PSA section and a flux of pure hydrogen is separated to be used in the fuel cell. The rest of the syngas is used in the burner side of the HIWAR reactor (see section 1.2.2) together with air and natural gas.

The combustion reaction occurs at 845 °C and at ambient pressure and 0.204 kg/h of NG are burned in the oxidator to guarantee the thermal equilibrium of the HIWAR. The total NG mass flow rate is 10.6 kg/h (see Table 1.1) yielding 3.09 kg/h of pure H_2, that generates 50 kW_{el} of net electrical power in the FC. In HE-1 the mixture of water and steam exiting HE-5 is heated at 457 °C and the flue gases are cooled down from 845 °C to 198 °C. Subsequently in HE-2 the combustion products are further cooled to 101 °C. As a consequence, the air temperature rises to 188 °C. Finally flue gases are left to the environment at 75 °C after a co-generative heat recovery.

The mass flow rate of the hot water produced in CG-1, HE-6 and HE-4 is determined such that its temperature $T_{COG} = 99\,°C$. The resulting overall hot water mass flow rate is 246 kg/h. Thereof, the cogenerated power is 82.5 kW_{th}, including 68.3 kW_{th} from the fuel cell.

Concentrated pressure drops are considered in several elements of the fuel processing plant. Specifically, the pressure drop is reduced by: (i) 0.100 bar in the reformer, (ii) 0.050 bar in both hot and cold side of HE-3, (iii) 0.010 bar in HE-4, (iv) 0.250 bar in the water gas shift reactor, (v) 0.030 bar in HE-1, HE-5 and HE-6, (vi) 0.020 bar in HE-2.

We underline that such a CHP power plant has been already studied in a previous work of the authors [104], however in this case we refine the thermal integration of the components and we implement the accurate modeling approach for heat exchangers described in section 1.2.5.

We determine the part load efficiency of plant A by reducing $\dot{m}_{NG}^{ref}$ to 5.19 kg/h. A further reduction is hindered by the PSA. Figure 3.7 reports η_{glob} and η_{th} as function of Φ.

The overall electrical efficiency varies between 35.0% and 40.0%, as a function of Φ, being higher at part load. This is a typical feature of CHP plants based on fuel cells [20–22, 104]. Such a behavior is dominated by the efficiency curve of the FC [20–22, 104].

The shadowed region in the plot (Figure 3.7(a)) is obtained considering two limit cases. For the upper curve, NG comes from the distribution grid already at the working pressure of 12 bar. For the lower curve, the natural gas is distributed at 1 bar and has to be compressed to 12 bar within the power plant. In real cases NG will be delivered with a pressure between 1 bar and 12 bar, and the real efficiency will be somewhere in the shadowed area. The efficiency difference between the upper and the lower curve is always 1.19 %.

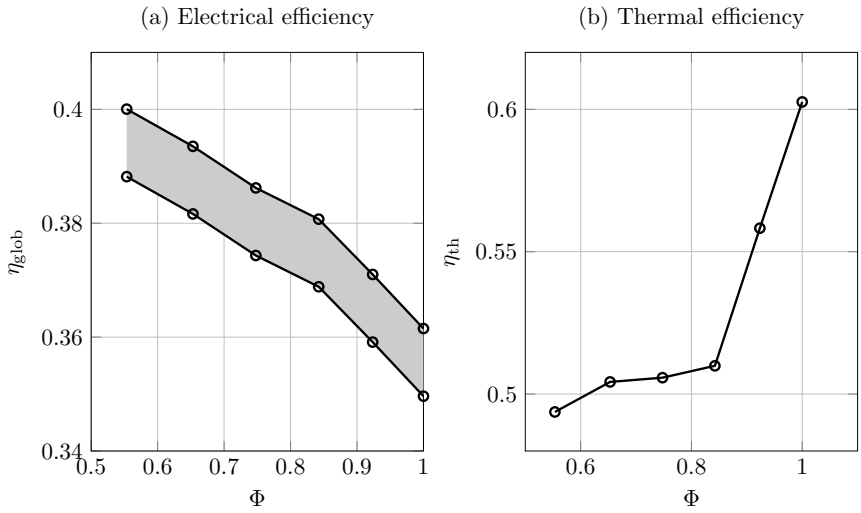

Figure 1.13: *Efficiency of the baseline power plant (Plant A) as a function of Φ: (a) overall electrical efficiency; (b) thermal efficiency. The shaded band between the two lines in graph (a) identifies the performance with and without including the work needed to compress the natural gas at the fuel processor inlet.*

The presence of auxiliary elements has a huge impact on the CHP efficiency. Specifically, in design conditions, the energy consumption of the natural gas compressor and of the other auxiliaries of the fuel processing plant are respectively 3.24 % and 1.43 % of the nominal fuel cell electric power.

Thermal efficiency (see Figure 3.7 (b)) varies between 49.4% and 60.2%. The higher Φ, the higher is η_{th}, as a consequence of the fuel cell performance variation from part to full load operations. The rapid change in slope of the thermal efficiency curve at $\Phi = 84.2\,\%$ is probably due to the increasing relevance of the gas transport losses [20–22]. Such a statement is validated also looking at the sudden increment in the coolant mass flow rate for $\Phi > 80.0\,\%$ shown in Figure 1.10.

1.3.2 Plant B: Membrane Separator

Plant B is schematically depicted in Figure 1.14.

The fuel processing plant is similar to Plant A (see section 1.3.1). The main difference is that the PSA is replaced by a selective membrane.

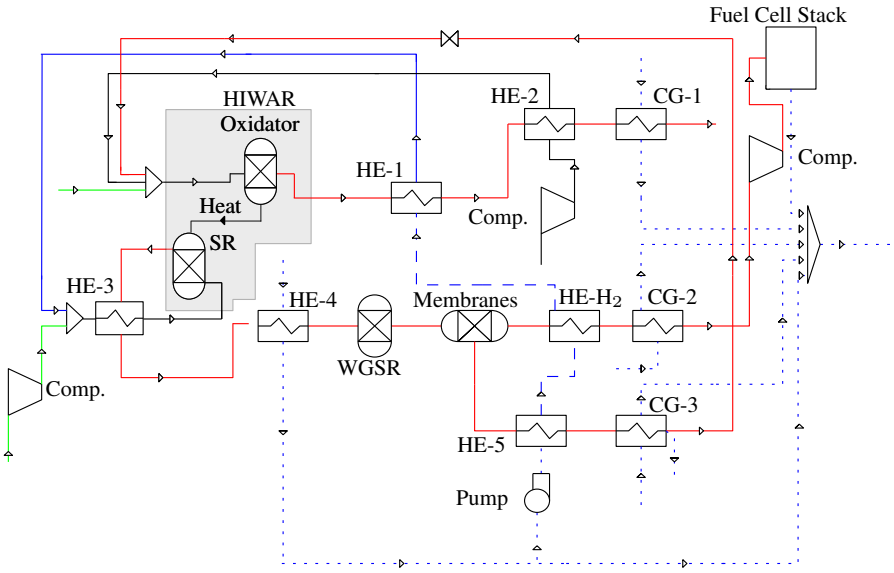

Figure 1.14: *Schematic overview of the energy conversion plant with a membrane separator.*

The membrane unit in Figure 1.14 is modeled according to the approach described in section 1.2.1. Pure H_2 is released at 1.20 bar and compressed to 2.00 bar to be utilized in the fuel cell. The required membrane area to obtain $y_{H_2} = 1.05 y_{H_2}^{\min}$ in nominal conditions and considering $K_{H_2} = 8.5 \times 10^{-3} \text{mol}/\left(\text{m}^2\text{sPa}^{0.5}\right)$ is $A_{\text{memb}}^{\text{SEP}} = 0.286\,\text{m}^2$. The resulting separation efficiency of the membrane is 80.3 %.

The working pressure of the reformer is kept to 12 bar. Thus, the reaction performance is not significantly varied [98, 103], while the membrane efficiency (maintaining permeate conditions at 1.20 bar) is similar to the PSA ones (see section 1.3.2, specifically Figure 1.4).

In this plant configuration, the hydrogen production system is more efficient than in Plant A. In fact, in Plant B it is possible to produce the same mass flow of hydrogen, using 9.13 % less natural gas in the reformer. However in the last case the NG mass flow rate required in the burner is 4.34 times the amount registered in Plant A case. This is due to the lower amount of hydrogen in the retentate, that requires to integrate the overall thermal balance with additional chemical energy.

The overall electrical efficiency varies between 35.5 % and 40.5 %, while $49.3\,\% < \eta_{\text{th}} < 59.8\,\%$, as evidence in Figure 1.15.

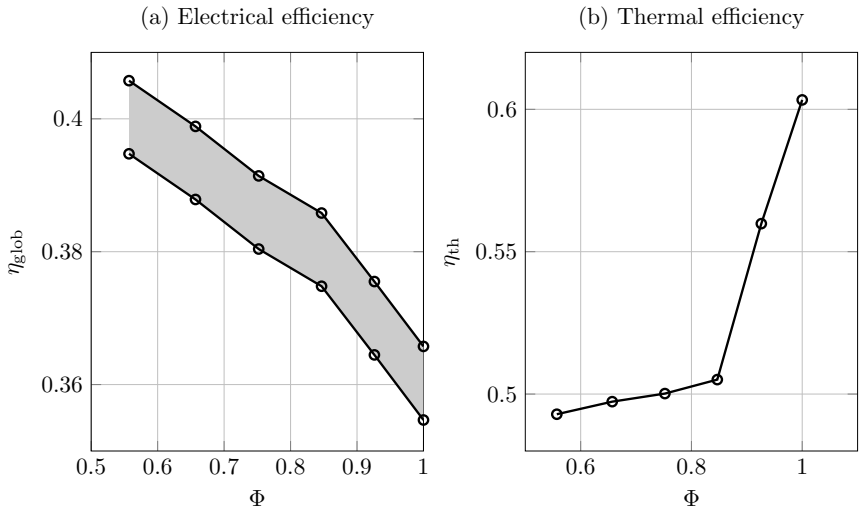

Figure 1.15: *Efficiency of the membrane separator power plant (Plant B) as a function of Φ: (a) overall electrical efficiency; (b) thermal efficiency. The shaded band between the two lines in graph (a) identifies the performance with and without including the work needed to compress the natural gas at the fuel processor inlet.*

The impact of the auxiliaries is pivotal also in this case. In fact, the energy consumption of the natural gas compressor and of the other auxiliaries of the fuel processing plant are 2.95 % and 1.30 % of P_{el}^{nom}, respectively. Note that also the H_2 compressor has a relevant impact on η_{glob}. In fact, its power consumption is 1.38 % of P_{el}^{nom}.

1.3.3 Plant C: Water Gas Shift Membrane Reactor

The water gas shift membrane reactor power plant is reported (Figure 1.16).

In this configuration hydrogen purification takes place directly in the water gas shift reactor. Thus, the purification section downstream is not necessary anymore, leading to a significant plant simplification. The membrane separator integration in the WGS reactor is performed following the approach illustrated in section 1.2.4.

The water required by the steam reforming is first preheated in HE-5, reducing the retentate gas temperature, and then in HE-H_2 reducing the temperature of the pure H_2. Similarly, the water of the co-generation

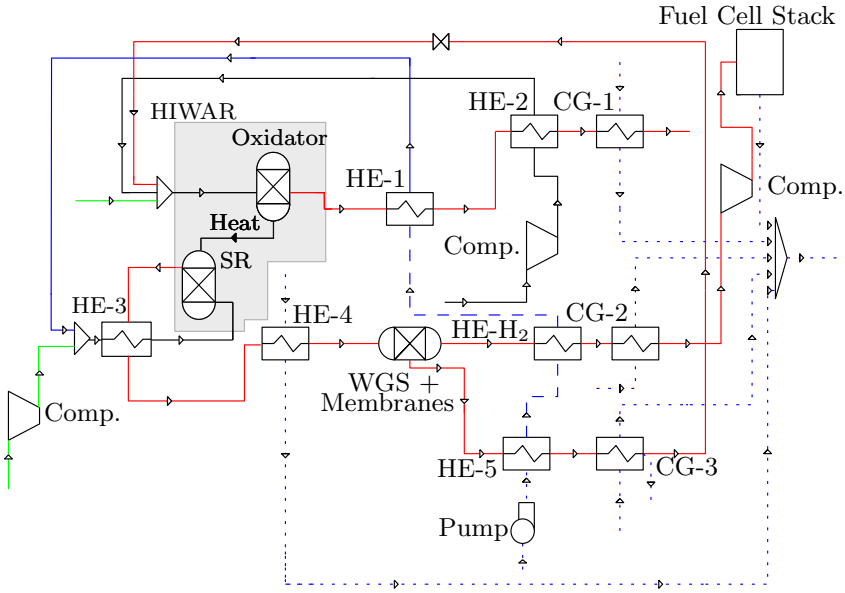

Figure 1.16: *Schematic overview of the energy conversion plant with a water gas shift membrane reactor.*

circuit first exchanges heat with retentate gases (CG-2) and then with pure H_2 (CG-3).

The WGS reactor is operated at 12 bar, wich is the optimal trade off between hydrogen separation and auxiliaries work [98].

The membrane surface necessary to achieve $y_{H_2} = 1.05 y_{H_2}^{min}$ is $A_{memb}^{WGS} = 0.260\,m^2$, considering $K_{H_2} = 8.5 \times 10^{-3} mol/\left(m^2 sPa^{0.5}\right)$. The resulting $\dot{m}_{H_2}$ is 99.0 % of the one obtainable with an infinite surface reactor, given the initial syngas conditions.

In this case 10.1 kg/h of NG are required to obtain 50 kW_{el} of nominal net electrical power from the FC, or, equivalently, 3.09 kg/h of pure H_2. Membranes shift the equiliblium of reaction (1.10) towards H_2. Thereafter, the CO concentration in the tail gases is 0.498 %. Such a value is considerably lower compared to Case A (3.20 %) and B (2.90 %).

The global electrical efficiency varies between a minimum of 36.3% and a maximum of 41.6%, as evidenced in Figure 1.17.

The thermal efficiency (see Figure 1.17 (b)) is comprised between 50.6% and 61.8%.

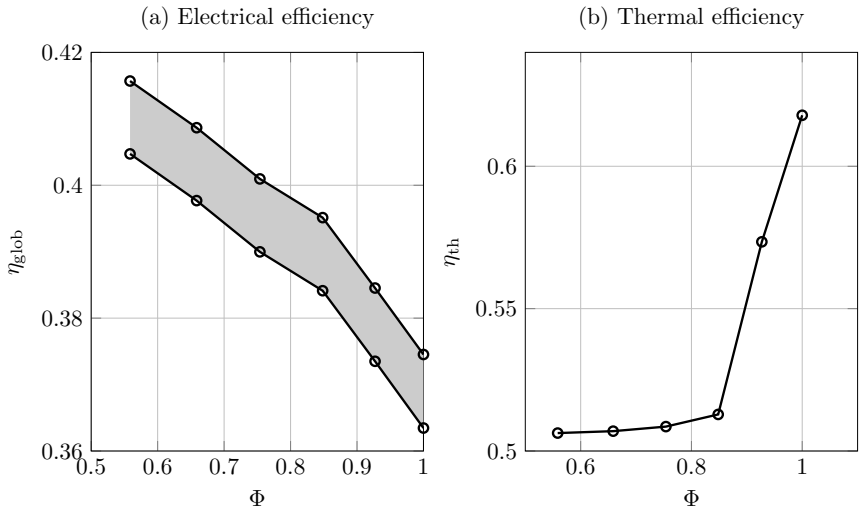

Figure 1.17: *Efficiency of the water gas shift membrane reactor power plant (Plant C) as a function of Φ: (a) overall electrical efficiency; (b) thermal efficiency. The shaded band between the two lines in graph (a) identifies the performance with and without including the work needed to compress the natural gas at the fuel processor inlet.*

1.3.4 Plant D: Reforming Membrane Reactor

Figure 2.1 represents configuration D. In this case, the membranes are integrated directly in the steam reforming side of the HIWAR reactor, making the water gas shift reactor unnecessary. Note that only H_2 is drained by the membrane shifting the equilibrium of reaction (1.10)(b) towards the products. As a consequence the CO mass flow rate in the retentate is just 1.68 % of the total pure hydrogen produced, much lower than 3.20 % and 2.94 % observed for plants A and B, respectively. On the contrary, the CO concentration in the retentate is higher than that observed for plant C due to the lower temperature of the shift reactor, compared to the reformer.

Note that the membrane separator integration in the steam reforming reactor is performed according to the approach illustrated in section 1.2.4.

The working pressure of the reformer is set to 35 bar. Such an assumption is justified by the sensitivity analysis reported in section 1.4.1.

The surface of the selective membrane required to obtain $y_{H_2} = 1.05 y_{H_2}^{min}$ is $A_{memb}^{REF} = 0.250\,m^2$, considering $K_{H_2} = 8.5 \times 10^{-3} mol/\left(m^2 sPa^{0.5}\right)$. We

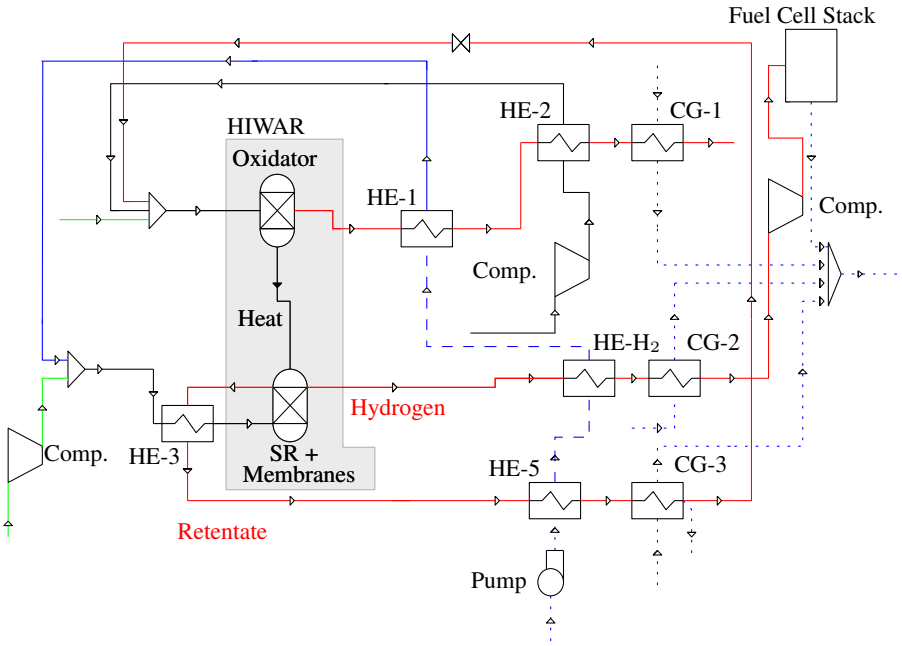

Figure 1.18: *Schematic overview of the energy conversion plant with a reforming membrane reactor.*

use here the same permeance value of the other plant configurations. However, the relatively high temperature of the reformer reactor (i.e. 770 °C) would result in a higher K_{H_2} and, as a consequence, a lower membrane surface for the same performance. Such aspect would lower the cost of the energy system, that here is not investigated in detail.

The range of the possible set-points in cases A, B, C is limited around 60.0% by PSA and reformer constraints of the real fuel processing plant under construction within the European project [96]. However, in this case the fuel converter is completely different in the construction, so we cannot determine a priori the minimum possible set-point. For this reason the sensitivity analysis is performed for a wider operating range (see Figure 1.19). The value of the natural gas mass flow rate entering the power plant, in design conditions, is, in this case, $\dot{m}_{NG}^{REF} + \dot{m}_{NG}^{BURN} = 9.52\,kg/h$.

The global electric efficiency of the power plant varies between 38.4% and 47.8%, being the highest of all analyzed configurations, as represented in Figure 1.19(a).

The thermal efficiency increases by increasing Φ as evidenced in Fig-

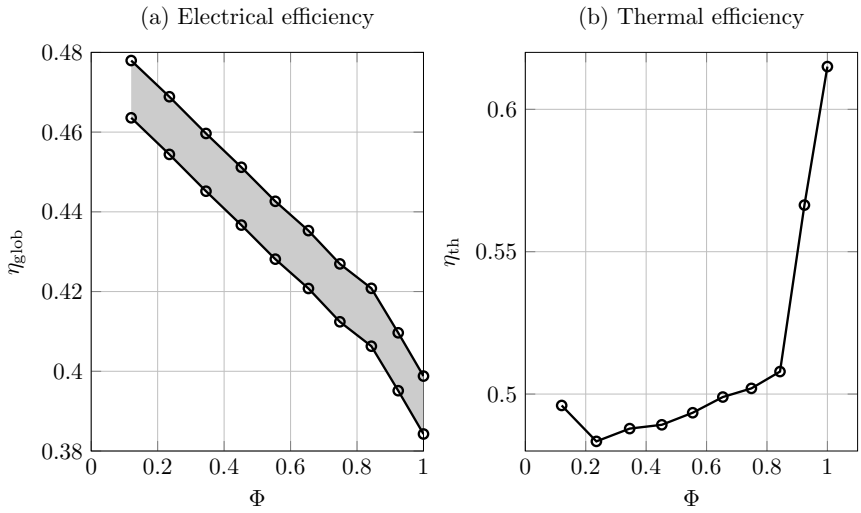

Figure 1.19: *Efficiency of the reforming membrane reactor power plant (Plant D) as a function of* Φ*: (a) overall electrical efficiency; (b) thermal efficiency. The shaded band between the two lines in graph (a) identifies the performance with and without including the work needed to compress the natural gas at the fuel processor inlet.*

ure 1.19(b), mainly because the FC operation is less efficient (degradating more chemical energy into heat). In particular, η_{th} varies in the range [49.6%, 61.5%]. The sharp change of slope for set-points $\Phi < 12.0\%$ is probably due to the fuel processor efficiency drop in such a region (see Figure 1.20(a)).

1.4 Discussion

A comparison between the results obtained in all the configurations previously presented is now performed. The efficiency values for each power plant, for $\Phi = 1$, are reported in table 1.2.

Figure 1.20 reports the relevant performance of the power plant as functions of the set-point.

The fuel processor efficiency has almost a flat response to the load condition. The average values are $\eta_{\text{fp}} = 75.1\,\%$, $\eta_{\text{fp}} = 77.0\,\%$, $\eta_{\text{fp}} = 78.8\,\%$, $\eta_{\text{fp}} = 83.7\,\%$, respectively for Plant A, B, C and D. Rearranging eqs. (1.1),

Table 1.2: *Efficiency values in nominal conditions for each power plant analyzed.*

Case	η_{fp} [%]	η_{glob} [%]	η_{th} [%]
Plant A	75.1	35.0	60.3
Plant B	77.0	35.5	60.3
Plant C	78.7	36.3	61.8
Plant D	83.8	38.4	61.5

and (1.2) and defining the fuel cell efficiency as:

$$\eta_{\mathrm{FC}} = \frac{P_{\mathrm{el}}}{\dot{m}_{\mathrm{H_2}} \mathrm{LHV}_{\mathrm{H_2}}} \,, \tag{1.15}$$

we can write the following equation for the fuel processor efficiency:

$$\eta_{\mathrm{fp}} = \frac{\eta_{\mathrm{glob}}}{\eta_{\mathrm{FC}}} + \frac{W_{\mathrm{aux}}^{\mathrm{ref}}}{\dot{m}_{\mathrm{NG}} \mathrm{LHV}_{\mathrm{NG}} \eta_{\mathrm{FC}}} \,. \tag{1.16}$$

Considering the target $\eta_{\mathrm{glob}} = 0.420$, and a mean $\eta_{\mathrm{FC}} = 0.500$ and $W_{\mathrm{aux}}^{\mathrm{ref}} / \dot{m}_{\mathrm{NG}} \mathrm{LHV}_{\mathrm{NG}} = 0.0191$ we get $\eta_{\mathrm{fp}} = 0.878$. Such an efficiency of the fuel processor should be reached in nominal conditions to attend the FCH-JU [90] goal.

The most relevant parameter is η_{glob} that, at nominal conditions, increases by 9.71 % (i.e. from 35.0 % to 38.4 %) switching from Plant A to Plant D. This is possible mainly for two reasons: (i) shift of the reforming reaction towards products; (ii) better thermal integration for heat recovery in the reacting fluxes. The target for the overall plant electric efficiency set by the FCH-JU [90] is 42.0%, Plant D configuration meets such a prescription for $\Phi < 65\,\%$. However, in a real energy management scenario, the plant set-point will rarely be 1, making the effective electrical efficiency supposedly higher than the target. Moreover, configurations aiming at increasing the energy converter efficiency can be adopted, like for example the usage of two fuel cells of nominal power $50\,\mathrm{kW_{el}}$ in parallel downstream the fuel processor to improve the FC electrical efficiency [104].

We note that configurations B and C significantly reduce the fuel processor complexity with respect to the baseline configuration A by eliminating the semi-batch PSA process. However, their impact on the system efficiency is minor compared to configuration D.

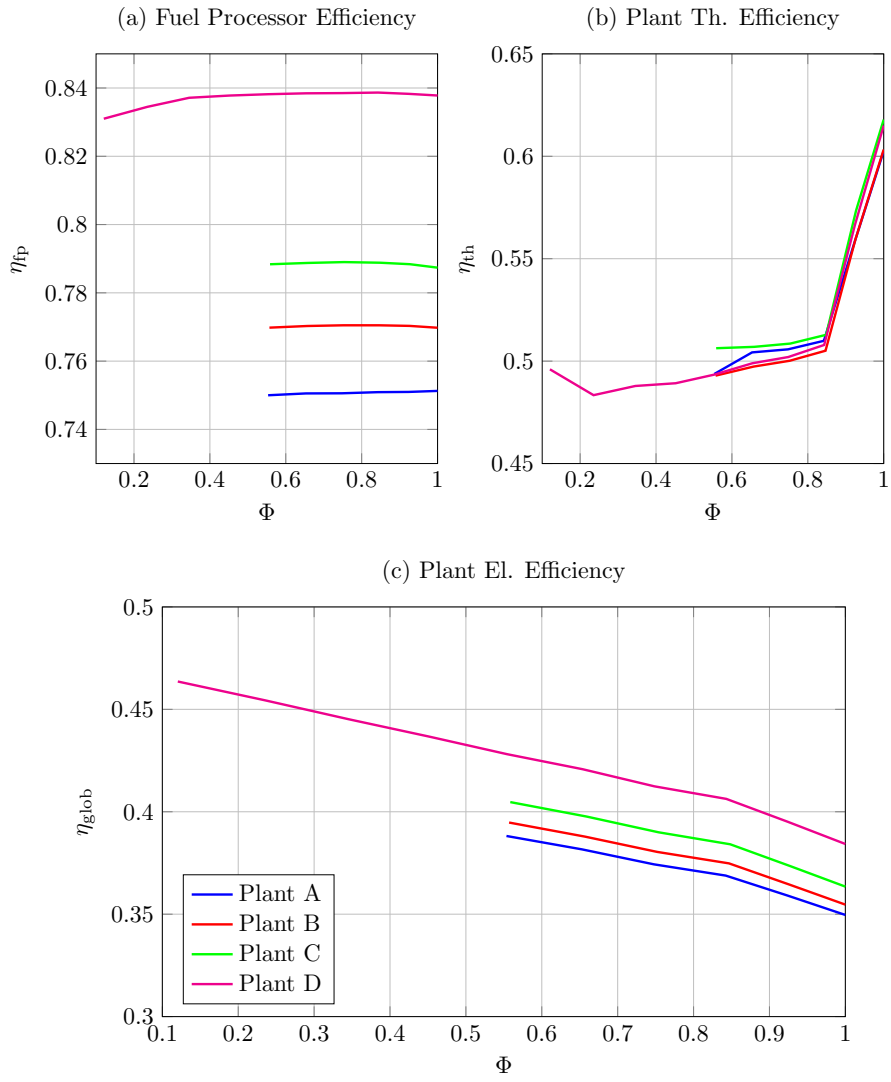

Figure 1.20: *Performance of the considered power plants as functions of* Φ*: (a) fuel processor efficiency; (b) plant thermal efficiency; (c) plant minimun electric efficiency (natural gas from the grid at 1 bar).*

In fact, only the integration of the membrane within the HIWAR promotes an effective shift of the equilibrium reactions towards H_2 production. Moreover, it significantly improves the thermal integration of the fuel processor components by avoiding the cooling process to 320° C, necessary for water gas shift reaction, before thermal recovery.

Thereafter, in the following sections we further dissect the power plant

D by systematically varying the important operating parameters (i.e. pressure, applied membrane surface, reformer temperature and pinch point of the heat exchangers). The aim is to establish the most convenient working parameters, considering thermodynamic performance as well as technological and economic aspects.

1.4.1 Effects of the Reformer Pressure and of the Membrane Surface

We study the effect of the reformer pressure, in order to establish the optimal operating conditions for configuration D. In fact, literature data are available for the simple reforming reaction [98, 103]. The presence of hydrogen separation through selective membranes, that is a function of the pressure gradient, might change the optimal operating conditions. In addition a sensitivity analysis to the applied membrane surface area is performed. Results for $\dot{m}_{\mathrm{NG}}^{\mathrm{REF}} = 6.90\,\mathrm{kg/h}$, and considering $K_{\mathrm{H_2}} = 8.5 \times 10^{-3}\mathrm{mol}/\left(\mathrm{m^2 sPa^{0.5}}\right)$, are reported in Figure 1.21. The power required from the auxiliaries is evaluated assuming the natural gas coming from the grid at 1 bar

We note, from Figure 1.21, that $\eta_{\mathrm{fp}}^{\mathrm{tot}}$ varies in the range [63.0 %-81.5 %], as a function of the reformer pressure and of the applied membrane surface area. In fact, the fuel processor total efficiency increases augmenting such parameters. However, we also note a saturation in the performance increase. We consider in this analysis the fuel processor total efficiency $\eta_{\mathrm{fp}}^{\mathrm{tot}}$, defined in eq (1.3), in order to take into account the effects of the pressure rise in the work required by the auxiliaries. Summarizing, $A_{\mathrm{memb}}^{\mathrm{REF}} = 0.250\,\mathrm{m^2}$ and $p^{\mathrm{REF}} = 35.0\,\mathrm{bar}$ shoud be considered as a techno-economic compromise. In fact, decreasing these two values results in a decrement of the performance. On the other hand, further increasing them is unnecessary because the efficiency improvement would be marginal and would not compensate the higher cost of the overall energy plant.

For $p^{\mathrm{REF}} > 30\,\mathrm{bar}$ and $A_{\mathrm{memb}}^{\mathrm{REF}} \geq 0.200\,\mathrm{m^2}$ the efficiency curves collapse. Nevertheless, Figure 1.21 evidences that, when the membrane surface is too small (e.g. $0.100\,\mathrm{m^2}$) $\eta_{\mathrm{fp}}^{\mathrm{tot}}$ is significantly lower compared to the other cases, even for $p^{\mathrm{REF}} = 50.0\,\mathrm{bar}$.

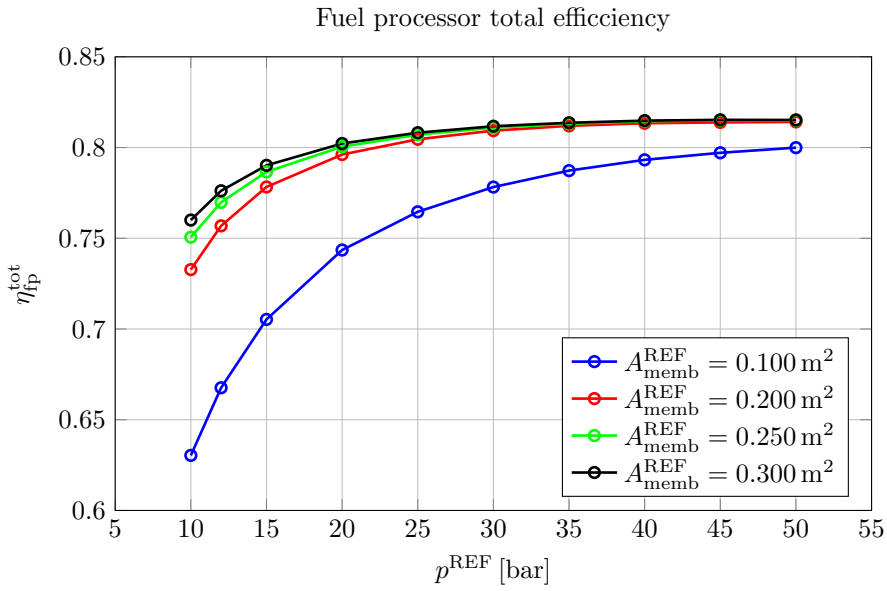

Figure 1.21: *Fuel processor efficiency as a function of the pressure p^{REF}, and of the applied membrane surface area A_{memb}^{REF}. The power required from the auxiliaries is evaluated considering the natural gas coming from the grid a 1 bar.*

1.4.2 Reforming Temperature Analysis

The temperature of the membrane reforming reactor strongly affects the membrane stability [102] and the plant performance [22, 125]. For stability purposes it should be relatively low, while higher T^{REF} might improve the reformer performance. For this reason, η_{fp} is estimated varying T^{REF} in the range [590 °C, 850 °C]. The results reported in Figure 1.22 are retrieved for $\dot{m}_{\mathrm{NG}}^{\mathrm{REF}} = 6.90\,\mathrm{kg/h}$.

We comment that, for a reforming temperature $T^{\mathrm{REF}} = 600\,^{\circ}\mathrm{C}$, the chemical energy present in the retentate (in the form of un-reacted natural gas and non separated hydrogen) is enough to provide the thermal power necessary for the reforming, without providing additional NG to the burner. As a consequence the system in study cannot be operated at $T^{\mathrm{REF}} < 600\,^{\circ}\mathrm{C}$, otherwise some chemical energy in the retentate should be wasted, leading to a dramatical decrease in the efficiency of the fuel processor.

For $\dot{m}_{\mathrm{NG}}^{\mathrm{REF}} = 6.90\,\mathrm{kg/h}$, the pure hydrogen mass flow rate produced

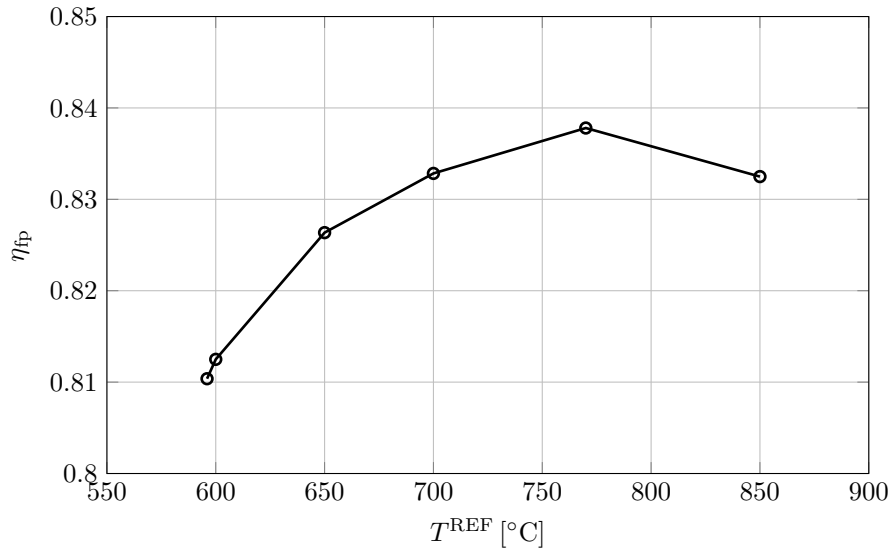

Figure 1.22: *Fuel processor efficiency as a function of the reformer temperature (T^{REF}).*

varies between $\dot{m}_{\mathrm{H_2}} = 3.09\,\mathrm{kg/h}$ for a reformer temperature of 770 °C, and $\dot{m}_{\mathrm{H_2}} = 2.22\,\mathrm{kg/h}$ for a reformer temperature of 600 °C. Thereafter, lowering the temperature reduces the system power density. Moreover, η_{fp} decreases from 83.8 % to 81.2 % by reducing T^{REF} from 770 °C to 600 °C. Such a performance derating might be acceptable if necessary to use selective membranes integrated in the steam reforming reactor.

A drop in the fuel processor efficiency is observed, from Figure 1.22, for $T^{\mathrm{REF}} = 850\,^{\circ}\mathrm{C}$. In fact, while the yield of reaction (1.10) is almost constant for temperatures higher than 770 °C, the thermal power necessary to sustain the process increases. As a consequence the natural gas send to the burner increases, while the pure hydrogen produced remains almost constant.

1.4.3 Pinch Point Analysis

The thermal integration in an endothermic process, such as the production of hydrogen via natural gas steam reforming, is a key aspect to obtain a good efficiency of the fuel conversion. For this reason, the heat exchangers for thermal energy recovery in the fuel processor are crucial elements. In fact, decreasing the pinch point temperature difference would

result in a better exploitation of the thermal power available in the hot fluxes. However, such a process entails increasing the cost of the heat exchanger. For this reason, it is interesting to assess the impact of the pinch point temperature difference, of all heat exchangers in the plant, on the efficiency of the fuel processor. The results of such analysis are reported in Figure 1.23.

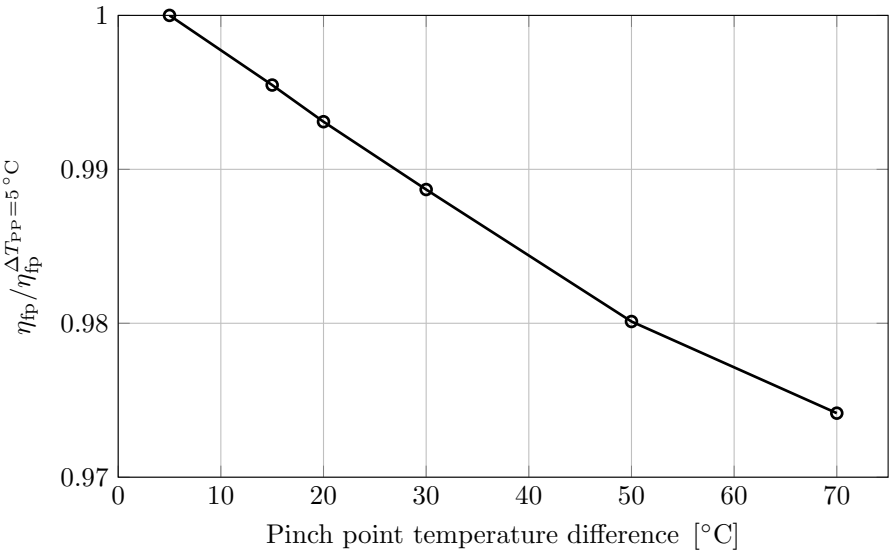

Figure 1.23: *Ratio between the fuel processor efficiency and η_{fp} calculated for a pinch point temperature difference of $5\,^{\circ}C$, as a function of the pinch point temperature difference of all heat exchangers in the fuel processor.*

Figure 1.23 shows that a significant correlation between the pinch point temperature difference and the fuel processor efficiency is not present. In fact, η_{fp} decreases only by 3 % by increasing ΔT_{PP} from 5 °C to 70 °C.

1.5 Summary

In this chapter we assess the effects of the integration of Pd-based selective membranes in the fuel processor of a $50\,\mathrm{kW_{el}}$ PEMFC based CHP system, fed by natural gas. Specifically, we evaluate the following performance indicators: (i) the overall electric efficiency, (ii) the fuel processor efficiency, (iii) and the thermal efficiency. Both design and off-design operating conditions are considered. We use a quasi-lumped parameter approach, integrating Aspen Plus® with physical and phenomenological

models. We systematically study the integration of selective membranes in the fuel processor, through four case studies. First, we evaluate the performance of a baseline plant, that accounts for steam reforming, water gas shift and syngas purification via pressure swing adsorption unit. Such a system represents the state of the art of PEMFC CHP systems fueled with natural gas. Then, we assess the integration of Pd-based selective membranes as purification unit and integrated both in the water gas shift reactor and in the steam reforming unit. Moreover, detailed analyses are performed on the working parameters, such as the reactors pressure and temperature together with selective membranes surface, of the most innovative fuel processing plant configuration.

The results show that the usage of selective membranes can boost the power plant efficiency. Specifically, the fuel processor nominal efficiency increases from 75.1 %, for the baseline configuration, to 83.8 %, for the fuel processing plant with selective membranes integrated in the steam reformer. As a consequence, the overall electrical efficiency rises from 35.0 % to 38.4 %. This is mainly due the shift of the reforming reaction towards products and to the better thermal integration for heat recovery in reacting fluxes. However, when selective membranes are used as separator or integrated in the water gas shift reactor, the performance boost is minor. In addition, the necessary membrane surface, that largely determine the power plant cost, decreases if the separator is integrated in the reactors. The minimum value of selective membrane area is reached for Plant D configuration, which integrates the membranes into the steam reformer reactor. The real convenience of the improved energy systems studied should be assessed in a real energy management scenario, to thoroughly evaluate the economical and environmental benefits associated to the improved efficiency.

The integration of Pd-based selective membranes leads also to an important fuel processing plant simplification, in particular when the reforming membrane reactor configuration is considered.

At part load, similar conclusions can be made. In fact, the fuel processor efficiency is insensitive to the set-point, while the overall electrical efficiency increases at part load, due to the FC efficiency curve. The thermal efficiency has the opposite behavior. Such trends could be favorable in a real energy management scenario, where the power plant can be often used in off-design conditions (thus at higher electrical efficiency) to meet the user requirements.

In addition, when using Pd-selective membranes integrated in the steam reforming reactor, we found that the optimal working pressure for the system is 35 bar, as a compromise between chemical equilibrium, auxiliary power, and membrane separation efficiency.

The membrane surface is also recognized as a limiting factor to performance, if not properly sized. However, an overestimation could lead to unnecessary additional costs. For these reasons an accurate 2-D or 3-D modeling of the Pd-based selective membranes, also when integrated in reactors could be useful. In fact, phenomena such as the boundary layer formation (i.e. concentration polarisation), or the spatial distribution of the selective membranes in a specific geometry should be investigated. Moreover, several effects such as the how the hydrogen permeance of the membrane varies with temperature could be studied.

To facilitate the integration of selective membranes, the steam reforming reactor can be operated at 600 °C instead of 770 °C, with a fuel processor efficiency decrease of 3.20 %. We also comment that for Plant D at $650-700$°C, which is well in the range proposed in [106], η_{fp} is still higher compared to the baseline plant. Thus, significant enhancement of fuel processor performance can be obtained also with the current membrane technology through Plant D. We cannot reduce the reformer temperature below 600 °C, as the chemical energy present in the retentate would be enough to sustain the thermal requirements from the endothermic reactions.

It is also important to note that, according to the state of the art technology, selective membranes made by Pd-Ag alloys can operate in a temperature range of (300°C-700°C) [106]. For this reason the technological implementation of Plant D configuration is still questionable. However, from a performance point of view the just cited case is the most relevant, accounting for highest electrical efficiency values. As a consequence, this work focuses on showing the possible advantages related to the selective membranes usage in a CHP energy system, just from the energy performance point of view. Relying on our results we can conclude that the technological development of selective membranes should be directed towards the extension of the range of possible operating temperatures.

Finally, we underline that the absolute value of the hydrogen permeance of the membrane does not influence the efficiency. On the other hand, the permeance value obviously affects the required membrane area for a certain separation, and thus the economics of the concept, which is not

investigated in this chapter.

Chapter 2

Design and Optimisation of a Membrane-Integrated Fuel Processor for High Purity Hydrogen Generation

Efficient and high purity hydrogen production from reforming of natural or synthetic gaseous hydrocarbons is an enabling technology for the competitiveness of hydrogen-based systems. The efficiency and sustainability of such a process strongly depends on the employed hydrogen purification technology. Membrane-integrated fuel processors are potentially more efficient than state-of-the-art systems featuring separate reforming and water gas shift reactors, and a pressure swing adsorption purification unit.

The efficiency of a membrane-integrated fuel processor strongly depends on the operating parameters. Therefore, herein we analyse the effects on the efficiency of the pressure and temperature of the steam reforming reactor and the steam to fuel and air to fuel ratios, being such analysis a relatively untapped topic. The results show that the fuel processor efficiency based on lower heating value varies between 75 % and 84 %. Notably, it always exceeds 75 % that can be considered a reference value for a state-of-the-art fuel processor based on pressure swing adsorption purification. Moreover, the fuel processor efficiency appears to be most sensitive to the temperature and the ratio between reactants of the steam reforming reactor. Finally, we note that the retentate composition has a

relevant impact on the fuel processor performance.

The chapter is organized as follows. Section 2.1 states the scope of the work and section 2.2 describes the calculation methodology. Section 2.3 presents and analyses the results, while section 2.4 draws the conclusions of the work.

2.1 Problem statement

This chapter dissects the operation and the performance of a fuel processor that converts hydrocarbon fuel into high purity hydrogen utilizing membranes to purify the syngas.

The hydrocarbon Steam Reforming Reaction (SRR) reported in eq. (2.1) is the leading mechanism that takes place in the fuel processor schematically depicted in Figure 2.1.

$$C_xH_z + xH_2O \rightleftharpoons \left(x + \frac{z}{2}\right) H_2 + xCO\,. \tag{2.1}$$

The Water Gas Shift Reaction (WGSR), reported in eq (2.2), might also occur in the reactor, depending on its temperature.

$$CO + H_2O \rightleftharpoons CO_2 + H_2\,. \tag{2.2}$$

However, in the temperature range typical of SRR based fuel processors (i.e. $600^\circ\,C - 900^\circ\,C$), reaction (2.1) is prevailing. For instance at $770^\circ\,C$ $K_{REF} \cong 70 \times K_{WGS}$ [123], being K_{REF} and K_{WGS} the SRR and WGSR equilibrium constants respectively. Also considering one or more additional WGS stages, the resulting syngas would contain about $80\%H_2$, $18\%CO_2$, $2\%CO$, and traces of CH_4, other hydrocarbons, and impurities [21, 51, 126]. As a consequence, contaminants such as CO_2 and in particular CO, must be separated from H_2 to obtain the desired purity.

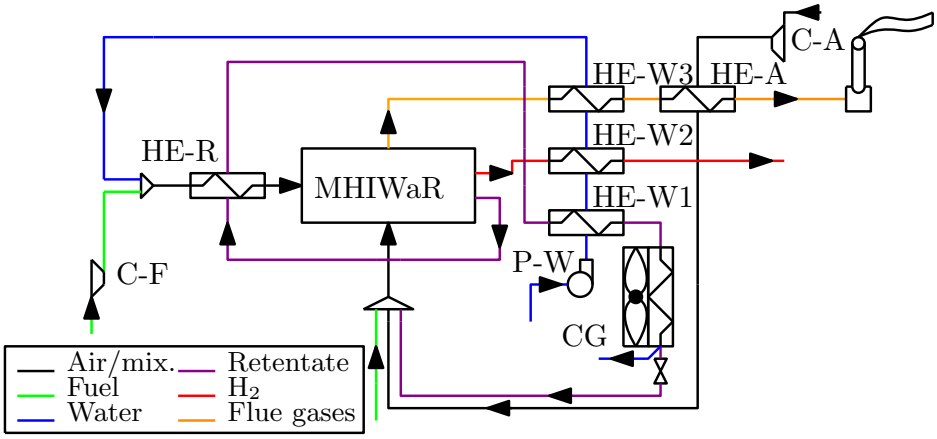

Figure 2.1: *Schematic overview of the membrane-integrated fuel processor for high purity hydrogen generation.*

Hydrogen purification is a complex task that significantly impacts the system efficiency [64, 104], and can represent up to 50% of the plant cost [104] in state-of-the-art PSA based systems. Syngas purification through membranes has proven to be an efficient alternative to PSA that also simplifies the plant layout [64, 99, 127–132] (see also chapter 1). Integrating the membranes directly into the SRR reactor is the most efficient configuration [64], as a consequence of the shift of chemical equilibrium of reactions (2.1) and (2.2) towards the products.

The effects of the operating parameters on the performance of the membrane-integrated fuel processor are relevant and a systematic analysis of such effects seems to be a relatively untapped topic. In fact, only few demonstrations on actual membrane-integrated reformers exist, such as a unit from Tokyo Gas [133]. In this case, the reactor operates at 550 °C and 10 bar with a Lower Heating Value (LHV) based efficiency of 77 %. However, the results of several simulation studies on membrane-integrated fuel processors show that the LHV based efficiency that potentially can be achieved ranges from 77 % to 84 % [64, 98], (see also chapter 1).

Leveraging from the results reported in chapter 1, this chapter seeks for the optimal operating parameters for a membrane-integrated steam reformer, schematized in Figure 2.1, and described in section 2.1.1, through a systematic sensitivity analysis. Specifically, the considered variables are (see section 2.2.2): (i) the excess steam to fuel ratio Φ, (ii) the excess air to fuel ratio Ψ, (iii) the dimensionless reformer pressure Π, and (iv) the

dimensionless reformer temperature τ.

2.1.1 Description of the fuel processor

The core of the fuel processor, envisioned in the current work and schematically depicted in Figure 2.1, is the Membrane and Heat Integrated Wall Reactor (MHIWaR) (Figure 2.2). The MHIWaR concept builds up on the Heat Integrated Wall Reactor (HIWAR) concept [121, 122] (see also chapter 1), originally developed and marketed by Helbio S.A. [134]. Specifically, the MHIWaR is the fuel processor of the plant presented in section 1.3.4.

The SRR is highly endothermic [21] (enthalpy of reaction $\Delta h_{\mathrm{SRR}} = 206.4\,\mathrm{kJ/mol}$ for methane at standard state $T = 20\,^{\circ}\mathrm{C}$, $p = 1\,\mathrm{atm}$) and the WGSR is slightly exothermic ($\Delta h_{\mathrm{WGS}} = -41.2\,\mathrm{kJ/mol}$) [21]. Thus, the overall reaction of SRR + WGSR is endothermic, even considering the complete shift of CO ($\Delta h_{\mathrm{SW}} = 165.2\,\mathrm{kJ/mol}$ for methane). The heat source for such reaction is the Catalytic Oxidation Reaction (COR), reported in eq. (2.3), that takes place at a temperature of 845 °C to mitigate the formation of high temperature developing pollutants (i.e. NO_x). The COR reactants can also include H_2, resulting from purification by-products.

$$\begin{cases} C_xH_z + \left(\frac{z}{4} + x\right) O_2 \rightarrow \frac{z}{2}H_2O + xCO_2. \\ H_2 + \frac{1}{2}O_2 \rightarrow H_2O \end{cases} \tag{2.3}$$

In the MHIWaR, the COR, the NG SRR, the WGSR, and the hydrogen purification take place in a single element (Figure 2.2). The MHIWaR is a shell and tube reactor where a metal catalyst coating is applied on both sides of the tubes. The COR takes place in the outer side of the tubes, and the SRR and WGSR in the inner side. Possible catalysts are the Group VIII metals such as Ni, Rh, Ru, Pt, Ir and Pd for both sides of the reactor [121, 135]. The heat flows through the conductive wall. Moreover, the MHIWaR has a membrane tube inside every SRR tube to separate the hydrogen. We refer to the syngas after hydrogen separation as retentate. The retentate can be rich in hydrocarbons and hydrogen content, depending on the operating conditions. Therefore, it is used as part of the fuel of the COR. In fact, the mix of NG and water (in change of phase) enters the tube side, while the mix of NG, air and retentate enters

the shell side. The purified hydrogen is at 1 bar and we do not consider a sweep flow as it would affect the FC performance [100].

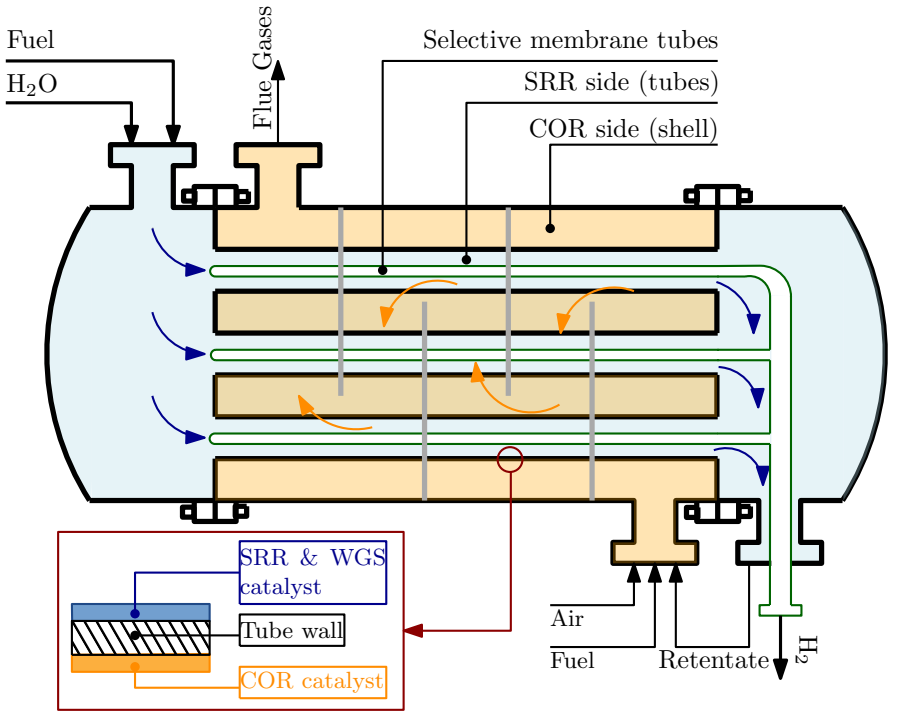

Figure 2.2: *Schematic overview of the MHIWaR reactor concept.*

2.2 Methodology

2.2.1 Modeling and performance parameters

To study the fuel processor introduced in section 2.1.1 we use the steady state model with a hybrid lumped-distributed parameter approach already presented in chapter 1.

The fuel processor efficiency is the key performance parameter of the analysis and in this chapter we follow the definition given in chapter 1. In this chapter, we consider as fuel a NG with an average european composition (Table 5.1) [136], which results in a $\mathrm{LHV}_{\mathrm{fuel}} = 46.5\,\mathrm{MJ/kg}$.

Table 2.1: *Average european natural gas molar fraction composition [136].*

Component	Molar fraction [%]
CH_4	90.21
C_2H_6	4.77
C_3H_8	1.16
Normal butane (C_4H_{10})	0.19
Isobutane (C_4H_{10})	0.19
Normal pentane (C_5H_{12})	0.04
Isopentane (C_5H_{12})	0.05
Normal hexane (C_6H_{14})	0.08
CO_2	1.17
N_2	2.14

2.2.2 Sensitivity analysis

We present a sensitivity analysis on four parameters of the fuel processor: (i) excess steam to fuel ratio Φ, (ii) excess air to fuel ratio Ψ, (iii) dimensionless MHIWaR SRR side pressure Π, and (iv) dimensionless MHIWaR SRR side temperature τ.

The excess steam to fuel ratio is:

$$\Phi = \frac{\phi - \phi_{\mathrm{STO}}}{\phi_{\mathrm{STO}}}. \tag{2.4}$$

In Equation (2.4) the steam to fuel ratio ϕ is:

$$\phi = \frac{\dot{m}_{\mathrm{H_2O}}}{\dot{m}_{\mathrm{fuel,SRR}}}, \tag{2.5}$$

where $\dot{m}_{\mathrm{H_2O}}$ is the water mass flow rate for the SRR and $\dot{m}_{\mathrm{fuel,SRR}}$ is the fuel mass flow rate for the SRR. The stoichiometric steam to fuel ratio ϕ_{STO} is:

$$\phi_{\mathrm{STO}} = \frac{\dot{m}_{\mathrm{H_2O,STO}}}{\dot{m}_{\mathrm{fuel,SRR}}}, \tag{2.6}$$

where $\dot{m}_{\mathrm{H_2O,STO}}$ is the stoichiometric water mass flow rate.

The excess air to fuel ratio is:

$$\Psi = \frac{\psi - \psi_{\mathrm{STO}}}{\psi_{\mathrm{STO}}}. \tag{2.7}$$

In Equation (2.7), the air to fuel ratio ψ is:

$$\psi = \frac{\dot{m}_{\text{air}}}{\dot{m}_{\text{fuel,COR}}}, \tag{2.8}$$

where $\dot{m}_{\text{air}}$ is the air mass flow rate and $\dot{m}_{\text{fuel,COR}}$ is the fuel mass flow rate, both entering the MHIWaR COR side. $\dot{m}_{\text{fuel,COR}}$ does not consider the fuel content in the retentate. The stoichiometric air to fuel ratio ψ_{STO} is:

$$\psi_{\text{STO}} = \frac{\dot{m}_{\text{air,STO}}}{\dot{m}_{\text{fuel,COR}}}, \tag{2.9}$$

where $\dot{m}_{\text{air,STO}}$ is the stoichiometric air mass flow rate necessary to oxidize $\dot{m}_{\text{fuel,COR}}$.

Note that, Ψ is a control parameter based on physical quantities measurable externally from the fuel processor. Therefore, the definition of Ψ given in equation (2.7) does not consider the flow rate of the fuel conveyed through the recirculated retentate flow. Hence, to better analyze the results we consider also the internal excess air to fuel ratio:

$$\Psi^* = \frac{\psi^* - \psi^*_{\text{STO}}}{\psi^*_{\text{STO}}}, \tag{2.10}$$

where ψ^* and ψ^*_{STO} consider also the fuel mass flow rate entering the MHIWaR COR side though the retentate flow.

Both Φ and Ψ affect the sensible, latent, and reaction heat required or produced in the two MHIWaR sides.

Note that Φ and Ψ have the same value if calculated with mass flow rates or mole flow rates.

The definitions of Φ and Ψ include all the flow rate-related physical variables that affect the fuel processor efficiency. Moreover, the definitions in terms of excess from the stoichiometric value of the ratio make the results valid for any fuel, such as a NG with different composition.

We define the dimensionless MHIWaR SRR side pressure as:

$$\Pi = \frac{p_{\text{SRR}}}{p_{\text{perm}}}, \tag{2.11}$$

where p_{SRR} is the MHIWaR SRR side pressure and $p_{\text{perm}} = 1\,\text{bar}$ is the pressure of the purified hydrogen. Π affects the fuel processor efficiency through the following phenomena: (i) H_2 recovery factor and permeation rate through the membrane, and (ii) syngas equilibrium compositions variation with pressure, according to Le Chateliers' principle [21, 137]. In this

chapter $p_{\text{perm}} = 1\,\text{bar}$, is also the reference condition (standard state) for the equilibrium compositions of the syngas produced from the SRR.

We define the dimensionless MHIWaR SRR side temperature as:

$$\tau = \frac{T_{\text{SRR}}}{\Delta G_{\text{SW}}/\Re}, \tag{2.12}$$

where T_{SRR} is the SRR temperature, $\Delta G_{\text{SW}} = 1.19 \times 10^5\,\text{J/mol}$ is the standard state ($T = 20\,^{\circ}\text{C}$, $p = 1\,\text{bar}$) Gibbs free energy variation for the complete NG SRR+WGSR reaction [138], $\Re = 8.314\,\text{J/(mol K)}$ is the universal gas constant. The value of τ represents: (i) the SRR and WGSR equilibrium constants variation with temperature, according to Le Chateliers' principle [21, 137], (ii) the variation of sensible and latent heat necessary to preheat the reactants, (iii) the type of reactions (SRR and WGSR in this case), and (iv) the reference condition (standard state) for the equilibrium constants.

The selected parameters affect the fuel processor efficiency both by influencing the hydrogen production, and by influencing the thermal balance of the power plant. Table 2.2 reports the domain of variation for the investigated parameters.

Table 2.2: *Domain of variation for the four free parameters of the sensitivity analysis.*

Parameter	Domain
Φ	[0.17, 1.35]
Ψ	[0.3, 11.6]
Π	[20, 40]
$\tau \times 10^2$	[6.11, 7.85]

The excess steam to fuel ratio has to be higher than 0 to avoid water starvation for SRR + WGSR, and to avoid carbon deposition for $600\,^{\circ}\text{C} < T_{\text{SRR}} < 850\,^{\circ}\text{C}$ [21, 139]. Some degree of steam excess increases the hydrogen yield of the NG SRR [21], and we expect this factor to be relevant also for membrane-integrated reactors. Therefore we start the sensitivity analysis from $\Phi = 0.17$. However, we expect that Φ greater than 1.35, being much higher than the stoichiometric value, causes an in-

crease of thermal power required to produce steam without an increase in hydrogen yield.

The excess air to fuel ratio has to be higher than 0 to avoid air starvation in the COR. The retentate conveys unreacted hydrocarbons and unseparated hydrogen, that are not considered in the Ψ definition, to the COR. Therefore, we start the sensitivity analysis from $\Psi = 0.3$. Moreover, a growth of Ψ increases the amount of thermal power necessary to keep the reactants at the reaction temperature. Therefore, we expect to obtain the maximum efficiency with $\Psi < 11.6$. We also note that for every analyzed case Ψ^* has to be lower than Ψ. For most of the operating conditions $\Psi - \Psi^* < 1$ because the content of fuel in the retentate is almost negligible. However, $\Psi - \Psi^*$ increases for few operating conditions where the retentate is rich in fuel content.

A growth of p_{SRR} decreases the yield of the SRR [98, 103], according to Le Chateliers' principle [21, 137]. At the same time, it increases the H_2 partial pressure difference over the membrane and thus maximum attainable hydrogen recovery factor (that in turn influences the equilibrium syngas composition) (see chapter 1). We select p_{SRR} in the range 20-40 bar, according to the results of previous publications [64, 127] and of chapter 1. Within such a pressure range the fuel processor concept is feasible for any system size from low (i.e. $1\,\mathrm{m^3/s}$) to high (i.e. $10^4\,\mathrm{m^3/s}$) SRR NG flow rate [140].

With an increase in T_{SRR} the higher is the yield of the endothermic SRR and the lower is the yield of the exothermic WGSR [21, 137]. We expect that the yield of SRR+WGSR increases by increasing T_{SRR}. At the same time, the thermal power to heat the reactants is proportional to T_{SRR}. As a consequence, we expect to find the optimum trade-off value of T_{SRR} between 600 °C and 850 °C [64]. Additionally, we underline that $T_{\mathrm{SRR}} = 600\,^{\circ}\mathrm{C}$ is a significant point to investigate being the watershed between the applicability domains of dense metallic membranes and dense ceramic membranes. Consequently, we decide to investigate the range of T_{SRR} [°C]: [600, 650, 770, 850]. Thus, τ varies in the range [6.11, 6.46, 7.3, 7.85]$\times 10^{-2}$.

All the analyzed cases are verified to be carbon deposition risk free in both sides of the MHIWaR, according to [139].

The results in section 2.3 show that the globally optimal combination of parameters is $\Phi = 0.64$, $\Psi = 0.3$, $\Pi = 35$, and $\tau = 7.3\times 10^{-2}$. Therefore, the investigated domain for every parameter contains the most relevant

values. Moreover, the results show that the proposed fuel processor concept can operate with $\tau \leq 6.11 \times 10^{-2}$ only if the other parameters are significantly distant from the optimal values.

2.3 Results and discussion

2.3.1 Results

A five dimensional space represents the analyzed cases in the sensitivity analysis (Figure 2.3), where each sphere represents the outcome of each analyzed case in the four dimensional sub-space of the four free parameters. The color of the sphere is proportional to the fuel processor efficiency.

The fuel processor efficiency varies between 75 % and 84 % as a function of the sensitivity parameters. A state-of-the-art NG fuel processor that includes a PSA unit to purify the hydrogen produced through SRR and WGSR operates in optimal conditions with a fuel processor efficiency of 75 % [64] (see also chapter 1), due to the limited H_2 recovery [50, 52, 55, 57–61]. Notably, a membrane-integrated fuel processor even operated in a non-optimised manner equals the performance of a state-of-the-art system, with the additional benefit of simplifying the plant layout.

Sections 2.3.1.1 to 2.3.1.6 report the detail of six dissections of the five dimensional space of Figure 2.3. In each dissection the fuel processor efficiency varies as a function of two parameters, while the other two are kept constant. The six dissections investigate all the interactions between the free parameters, by analyzing all the non-repeating possible couples of varying free parameters. When kept constant the parameters are set to: (i) $\Phi = 0.75$, (ii) $\Psi = 11.6$, (iii) $\Pi = 35$, and (iv) $\tau = 7.3 \times 10^{-2}$.

2.3.1.1 Excess steam to fuel ratio and excess air to fuel ratio

The fuel processor efficiency varies between 77 % and 84 % as a function of Ψ and Φ, for $\Pi = 35$ and $\tau = 7.3 \times 10^{-2}$ (Figure 2.4a). In this dissection, η_{fp} peaks at $\Psi = 0.3$ and $\Phi = 0.64$.

For all the considered values of Φ, the fuel processor efficiency peaks at $\Psi = 0.3$ (Figure 2.4b), that is on the extreme lower boundary of the domain. In fact, any increment of the excess of air in the COR reduces the fuel processor efficiency because it only increases the thermal power to maintain the reaction temperature. Moreover, the sensitivity of η_{fp} to Ψ

increases by increasing Φ because the effect of the self-consumed thermal power in the COR (that is proportional to Ψ) is more relevant when the thermal power required from the SRR side is high (i.e. high Ψ). Indeed, for $\Phi = 0.17$ the maximum η_{fp} is 3.25% higher than the minimum η_{fp}, whereas, such a difference is 5.74% for $\Phi = 1.35$.

The fuel processor efficiency reaches the maximum for [0.41< Φ <0.75] as a function of Ψ, consequently to the trade-off between hydrogen yield and thermal energy consumption (Figure 2.4c). In fact, for Φ lower than the optimal value the increase in hydrogen yield from the excess water in the SRR dominates compared to the increase of the thermal power necessary to produce the steam. On the contrary, after the optimal value, the process is dominated by the steam production and η_{fp} decreases by further increasing Φ. The optimal Φ increases from 0.41 to 0.64 by decreasing Ψ from 11.6 to 0.3. Indeed, the lower is Φ the lower is the heat required by the COR, promoting higher H_2 yield parameters combinations. For the same reason, the sensitivity of fuel processor efficiency to Φ decreases by decreasing Ψ.

2.3.1.2 MHIWaR SSR side dimensionless pressure and temperature

The fuel processor efficiency varies between 78 % and 81 % as a function of Π and τ, for $\Phi = 0.75$ and $\Psi = 11.6$ (Figure 2.5a) and peaks in the lower right corner of the domain, for $\Pi = 35$ and $\tau = 6.11 \times 10^{-2}$. Efficiency values reported in Figure 2.5(a) are generally lower compared to Figure 2.4(a), due to the value of Ψ. In fact, the high excess of air ($\Psi = 11.6$) is very far from the global optimum.

The white region in the lower right corner of the plot in Figure 2.5(a) represents physically unfeasible cases. Indeed, when $\Phi = 0.75$, $\Psi = 11.6$, $\Pi = 40$, and $\tau = 6.11 \times 10^{-2}$ the chemical energy of the fuel in the retentate is greater than the thermal power required by the SRR, making the MHIWaR exothermic. In fact, the low $\tau = 6.11 \times 10^{-2}$ reduces the heat required from the SRR side and disadvantages the SRR implying: (i) low reaction thermal power required from the SRR side, (ii) high content of unreacted natural gas in the retentate, and (iii) high content of unseparated hydrogen due to poor membranes separation performance due to the low H_2 partial pressure. Meanwhile, the high $\Pi = 40$ penalizes the SRR, but improves the membrane separation performance. The negative

effect of the combination of high Π and low τ on the SRR H_2 production prevails on the positive effect on membranes H_2 separation. Therefore, the retentate is rich in fuel content (16 % NG and 6 % H_2 molar fractions after dehydration) and the MHIWAR is exothermic. The hydrogen content in the retentate is relevant because the H_2 partial pressure is low due to the low yield of the SRR at low τ despite a high $\Pi = 40$. Moreover, η_{fp} peaks in this dissection at the border of the unfeasible (i.e. $\tau = 6.11 \times 10^{-2}$ and $\Pi = 35$), given that the fuel processor efficiency monotonically increases as the effective air excess decreases. Indeed, for such a combination of τ and Π the effective $\Psi^* = 0.41 \ll \Psi = 11.6$.

The effect of the increase of $\Psi - \Psi^*$ on η_{fp} is also shown in Figure 2.5 (b). In this plot all the η_{fp} curves monotonically increase by increasing Π. However, for $\tau = 6.11 \times 10^{-2}$ the fuel processor efficiency marginal gain increases by increasing Π because in this case η_{fp} is dominated by the reduction of the effective air excess. Conversely, for $\tau > 6.11 \times 10^{-2}$ $\Psi - \Psi^* < 1$ and the fuel processor efficiency marginal gain decreases by increasing Π. In fact, in this case η_{fp} is dominated by the the improvement of the H_2 separation rate. However, for larger Π the shift of the equilibrium composition towards the reactants becomes relatively more important.

For $\tau > 6.11 \times 10^{-2}$, where the reduction of the effective air excess is not relevant, we observe that the increase in the hydrogen recovery factor and the shift of equilibrium composition towards SRR products with Π are relevant at high τ, where the hydrogen yield of the SRR is high (Figure 2.5b). Indeed, for $\tau = 6.46 \times 10^{-2}$ the maximum η_{fp} is 1.1 % higher than the minimum η_{fp}. Whereas, such a percentage difference for $\tau = 7.85 \times 10^{-2}$ is 2.3 %.

Constraining $\tau > 6.11 \times 10^{-2}$, the optimal MHIWaR SSR dimensionless temperature is $\tau = 7.3 \times 10^{-2}$ (Figures 2.5a and c). Such a value is the best trade-off considering that increasing τ causes both an increment in hydrogen yield due to the SRR equilibrium constant variation, and an increment of the thermal power required (sensible, latent, and of reaction) from the SRR. Such a trend is valid for all the Π values analyzed (Figure 2.5c). However, the curves in Figure 2.5(c) diverge by increasing τ, showing again that the increase of hydrogen recovery factor with Π has more impact on η_{fp} when the hydrogen yield is higher (i.e. at high τ).

2.3.1.3 Excess air to fuel ratio and MHIWaR SSR side dimensionless pressure

The fuel processor efficiency varies between 79 % and 84 % as a function of Ψ and Π, for $\Phi = 0.75$ and $\tau = 7.3 \times 10^{-2}$ (Figure 2.6a). In this dissection, $\Pi = 40$ and $\Psi = 0.3$ yield the maximum η_{fp}, as already noted from Figures 2.4 and 2.5 (see sections 2.3.1.1 and 2.3.1.2) .

The optimal efficiency parameters combination is located on the upper left corner of the domain (Figure 2.6a). Figures 2.6(b) and(c) support the analyses of sections 2.3.1.1 and 2.3.1.2 with respect to the Ψ and τ effects on η_{fp}.

Ψ has a weaker influence than τ on the fuel processor efficiency correlation with Π. In fact, in Figure 2.6(c) all the curves maintain a similar slope for different Ψ values. Conversely, Figure 2.5(b) shows that the sensitivity of fuel processor efficiency to Π increases by increasing τ.

2.3.1.4 Excess air to fuel ratio and MHIWaR SSR side dimensionless temperature

The fuel processor efficiency varies between 79 % and 84 % as a function of Ψ and τ, for $\Phi = 0.75$ and $\Pi = 35$ (Figure 2.7a). In this dissection, η_{fp} peaks at $\Psi = 0.3$, as already observed in Figures 2.4 and 2.6. Moreover, the optimal trade-off value for τ is 7.3×10^{-2}, as noted in Figure 2.5, excluding $\tau = 6.11 \times 10^{-2}$.

The white region in the lower left corner of Figure 2.7(a) represents physically unfeasible cases, that are: (i) one case at $\Phi = 0.75$, $\Pi = 35$, $\Psi = 0.3$, and $\tau = 6.46 \times 10^{-2}$, and (ii) four cases at $\Phi = 0.75$, $\Pi = 35$, $\tau = 6.11 \times 10^{-2}$ and $\Psi = [0.3, 1.5, 4, 6.9]$. Indeed, the low τ enriches the content of unreacted natural gas and hydrogen in the retentate making $\Psi - \Psi^* > 1$, as already evidenced in section 2.3.1.2. However, in this dissection, the unconverged region is larger because when Ψ is low ($\Psi \leq 0.3$ for $\tau = 6.46 \times 10^{-2}$, and $\Psi \leq 6.9$ for $\tau = 6.11 \times 10^{-2}$) the oxygen in the COR is insufficient to oxidize the fuel. Also, in this case, the high $\Psi - \Psi^*$ increases the fuel processor efficiency in the proximity of the unfeasible region. In fact, for $\Psi = 9.7$ and $\Psi = 11.6$ the fuel processor efficiency peaks at $\tau = 6.11 \times 10^{-2}$ (Figure 2.7c).

The effect of Ψ on the fuel processor efficiency does not mutually interact with Φ, Π, or τ. Indeed, all the fuel processor efficiency curves monotonically decrease as Ψ increases (Figure 2.7b), as already observed

from Figures 2.4(b) and 2.6(b).

For $\tau > 6.11 \times 10^{-2}$, the fuel processor efficiency increases with τ until the optimal trade-off value $\tau = 7.3 \times 10^{-2}$, and then decrease (Figure 2.7c), as already observed from Figure 2.5(c). Such a result proves that the effect of τ on the fuel processor efficiency does not mutually interact with Π or Ψ.

2.3.1.5 Excess steam to fuel ratio and MHIWaR SSR side dimensionless pressure

The fuel processor efficiency varies between 76 % and 81 % as a function of Φ and Π, for $\Psi = 11.6$ and $\tau = 7.3 \times 10^{-2}$ (Figure 2.8a). The optimal $\Phi = 0.41$ is the same observed for $\Psi = 11.6$ in Figure 2.4(c). Moreover, the optimal $\Pi = 40$ is the same for Figures 2.5 and 2.6 (for $\tau > 6.11 \times 10^{-2}$). The efficiency values reported in Figure 2.8(a) are generally lower compared to Figures 2.4(a), 2.6(a), and 2.7(a) due to the air excess value ($\Psi = 11.6$) that is far higher than the optimal value.

Increasing Φ, the fuel processor efficiency reaches a maximum for $\Phi = 0.41$, for every Π (Figure 2.8b). Comparing Figure 2.4(c), for $\Psi = 11.6$ and Figure 2.8(b) we note that the effect of Φ on the fuel processor efficiency does not mutually interact with neither Ψ nor Π.

The fuel processor efficiency curves for $\Phi > 0.17$ have the same increasing trend with Π and peak at $\Pi = 40$, as already observed in Figures 2.6(c) and 2.5(b) (for $\tau > 6.11 \times 10^{-2}$) irrespective of Ψ. Such a result proves that the effect of Π on the fuel processor efficiency does not mutually interact with τ, Ψ, or Φ provided that there is no steam starvation in the SRR (i.e. $\Phi > 0.17$). Moreover, an increase in the hydrogen recovery factor driven by high Π is relevant only if the yield of the SRR is not the limiting factor (i.e. for high Φ). In fact, the sensitivity of the fuel processor efficiency to Π increases by increasing Φ: $\frac{\max(\eta_{\mathrm{fp}}) - \min(\eta_{\mathrm{fp}})}{\min(\eta_{\mathrm{fp}})}$ is 1.2 % for $\Phi = 0.41$ and is 3 % for $\Phi = 1.35$.

2.3.1.6 Excess steam to fuel ratio and MHIWaR SSR side dimensionless temperature

The fuel processor efficiency varies between 75 % and 81 % as a function of Φ and τ, for $\Psi = 11.6$ and $\Pi = 35$ (Figure 2.8a). The high air excess ($\Psi = 11.6$) makes the obtained efficiency in Figure 2.9(a) generally lower compared to Figures 2.4(a), 2.6(a), and 2.7(a)

As already evidenced in sections 2.3.1.2 and 2.3.1.5, the white region in left down corner in Figure 2.9(a) represents some exothermic regime cases due to low τ and low Φ. Such cases are: (i) one case at $\Pi = 35$, $\Psi = 11.6$, $\tau = 6.46 \times 10^{-2}$, and $\Phi = 0.17$, and (ii) three cases at $\Pi = 35$, $\Psi = 11.6$, $\tau = 6.11 \times 10^{-2}$, and $\Phi = [0.17, 0.41, 0.64]$.

The coordinates of the optimal case in this dissection are $\Psi = 11.6$, $\Pi = 35$, $\Phi = 0.75$ and $\tau = 6.11 \times 10^{-2}$. Such an operating point lies at the boundary of the exothermic region. Indeed, the resulting maximum efficiency is biased from the high $\Psi - \Psi^*$ due to the low τ. Specifically, looking at Figure 2.9(b) the efficiency for $\tau = 6.11 \times 10^{-2}$ exponentially increases by decreasing Φ, with a trend completely different from the curves for other τ values. The effect on efficiency of the high $\Psi - \Psi^*$ (due to low τ) is also evident in Figure 2.9(c). In this figure, the efficiency value in the curves for $\Phi = 0.75$ abruptly increases lowering τ from 6.46×10^{-2} to 6.11×10^{-2}. Such a trend is not visible for $\Phi \leq 0.64$ because the MHIWaR turns to an exothermic regime for $\tau = 6.11 \times 10^{-2}$. Moreover, the trend is less evident for $\Phi \geq 0.88$ due to the increasing water excess.

In the following we consider only $\tau > 6.11 \times 10^{-2}$ to avoid nearly exothermic regime. In such a scenario, the optimal $\Phi = 0.41$ is the same observed commenting the results in Figure 2.8 and the results for $\Psi = 11.6$ in Figure 2.4. Moreover, the optimal trade-off value of the MHIWaR SSR side dimensionless temperature is $\tau = 7.3 \times 10^{-2}$, as already observed from Figures 2.5 and 2.7.

Still considering $\tau > 6.11 \times 10^{-2}$ the trend of the fuel processor efficiency as a function of Φ is analogous to that reported in Figures 2.8(b) and 2.4(c). Such a result proves that the effect of Φ on the fuel processor efficiency does not mutually interact with Ψ, Π, or τ, if τ is high enough to not increase $\Psi - \Psi^*$.

The fuel processor efficiency curves for the considered Φ values as a function of τ (Figure 2.9c) follow the trend already evidenced in Figure 2.7(c) and 2.5(c) if $\tau > 6.11 \times 10^{-2}$ is considered. The results prove that when τ is high enough to not increase $\Psi - \Psi^*$, the effect of τ on η_{fp} does not mutually interact with Π, Ψ, or Φ.

2.3.2 Discussion

The results of the sensitivity analysis reported in Figures 2.4 to 2.9 evidence that the shape of the function correlating the fuel processor effi-

ciency to any of the four free parameters is insensitive to the other three, when $\Psi - \Psi^* < 1$. We conclude that the effects of Φ, Ψ, Π, and τ on the fuel processor efficiency do not mutually interact, at least in the region where the fuel processor should be reasonably operated.

The efficiency η_{fp} increases by increasing Π (see Figures 2.5, 2.6, and 2.8) due to the improved performance of the membrane at higher pressure, when there is not steam starvation in the SRR. However, the marginal increment is a decreasing function of Π and the maximum efficiency at $\Pi = 35$ is only 0.28 % lower than the global, while the peak efficiency values at $\Pi = 30$ and $\Pi = 20$ are respectively 0.54 % and 1.7 % lower than the global optimum. Therefore, in the following we will consider $\Pi = 35$ as the optimal value from an engineering perspective and considering the analyzed domain. In fact, decreasing Π under 35 causes a significant efficiency drop while increasing of Π over 35 would result in an irrelevant efficiency gain with an increase of the capital cost of the fuel processor. Therefore, the globally optimal combination of parameters is $\Phi = 0.64$, $\Psi = 0.3$, $\Pi = 35$, and $\tau = 7.3 \times 10^{-2}$, considering the investigated domain. While Φ and τ optimal results from a trade-off, the optimal Ψ value is the lowest physically possible.

Figure 2.10 shows the impact on η_{fp} of a relative variation from the optimal value of $\pm 10\%$ for Φ and Π, of $[-8\%; +10\%]$ for τ, and of $+10\%$ for Ψ. While varying each parameter the others are kept at optimal value. The parameters that dominate the behavior of η_{fp} in the proximity of the optimum are Φ and τ (Figure 2.10). Indeed, the increase of Π from the optimal value increases η_{fp} of 0.11 %, whereas the decrease of Π decreases η_{fp} of 0.2 %. In addition, η_{fp} drops of 0.75 % and of 0.07 % respectively as a consequence of the increase and of the decrease of Φ. Moreover, the increase of Ψ decreases η_{fp} of 0.14 %. Finally, the increase of τ gives a η_{fp} drop of 0.5 %. The maximum possible τ decrease from the optimal value is 8 % with a η_{fp} drop of 0.6 %. Lower τ would result in physically unfeasible cases.

Considering the NG composition reported in Table 5.1 and the operating conditions described in section 2.1, the optimal set of non-dimensional parameters corresponds to the following physical values: $p_{\text{SRR}} = 35\,\text{bar}$, $T_{\text{SRR}} = 770\,^{\circ}\text{C}$, $\phi = 3.5$, that in terms of mole flows is $\phi_{\text{n}} = \frac{\dot{n}_{\text{H}_2\text{O}}}{\dot{n}_{\text{fuel,SRR}}} = 3.47$, and $\psi = 20$, that in terms of mole flows is $\psi_{\text{n}} = \frac{\dot{n}_{\text{air}}}{\dot{n}_{\text{fuel,COR}}} = 12.4$. Therefore, the operating pressure is the main difference in the optimal operating parameters with respect to a state-of-the-art PSA-based fuel

processor, that are usually operated between 10 bar and 25 bar [64] (see also chapter 1).

Dense metallic and dense ceramic membranes ensure the hydrogen purity reguired for low temperature FC applications [51]. However, the relevant impact of τ on performance and operation of the fuel processor proves that dense metallic membranes are not suited for this kind of application. In fact, such membrane can stably operate at temperatures lower than 600 °C [51] (i.e. $\tau < 6.11 \times 10^{-2}$), mainly because of the limited stability of thin state-of-the-art Pd-based membranes at temperatures above 600 °C as evidenced by pore formation. Conversely, dense ceramic membranes are compatible with optimal operation of a fuel processor for high purity hydrogen production, being able to be operated between 600 °C and 900 °C [51]. Moreover, such membranes can be integrated in a SRR reactor without drastically changing its design. Indeed, considering the optimal operating conditions, the product of the membrane hydrogen permeance and surface is $\Gamma = K_{H_2} A = 2.56 \times 10^{-3}$ mol/ $\left(\text{sPa}^{0.5}\right)$. The permeance of dense ceramic membranes ranges from 1.9×10^{-5} mol/ $\left(\text{m}^2\text{sPa}^{0.5}\right)$ to 2.5×10^{-4} mol/ $\left(\text{m}^2\text{sPa}^{0.5}\right)$ [51]. With such permeance values the required flow specific surface for the optimal operating conditions ranges from 2.71×10^{-2} $\left(\text{m}^2\text{s}\right)$ /mol to 3.61×10^{-1} $\left(\text{m}^2\text{s}\right)$ /mol. Such a value is lower than the flow specific surface required by commercial SRR catalysts that ranges from 7.6×10^{-1} $\left(\text{m}^2\text{s}\right)$ /mol to 2.32 $\left(\text{m}^2\text{s}\right)$ /mol [141–143].

The retentate composition has a relevant impact on the fuel processor performance. Therefore, we consider the internal air to fuel ratio:

$$\psi^* = \frac{\dot{m}_{\text{air}}}{\dot{m}_{\text{HC,COR}} + \dot{m}_{\text{H2,COR}}}, \tag{2.13}$$

where $\dot{m}_{\text{air}}$ is the oxygen mass flow rate, $\dot{m}_{\text{HC,COR}}$ is the sum of the mass flow rates of all the hydrocarbons entering the COR side (from the inlet NG and retentate), and $\dot{m}_{\text{H2,COR}}$ is the hydrogen mass flow rate entering the COR side from the retentate. The investigated ψ^* domain [24, 238] translates in the Ψ domain [0.3, 83.9] given the high external air excess necessary to maintain a constant internal air excess. Ψ is a control parameter, while ψ^* is not because contains physical quantities not easily measurable for control purposes. However, ψ^* accurately represents the composition of the reactant flow entering the COR. Figures 2.5, 2.7, and 2.9 show that the content of hydrocarbons and H_2 of the retentate recirculated to the COR affects Ψ^*, and in turn the fuel processor efficiency.

Therefore, Figure 2.11 represents η_{fp} as a function of ψ^*, ϕ, and p_{SRR} for several T_{SRR} values.

The fuel processor efficiency monotonically increases with a decreasing marginal gain by increasing p_{SRR} (Figure 2.11a). Such a trend is valid for all the values of T_{SRR}, differently from what observed in Figure 2.5 (b), where the curve for $\tau = 6.11 \times 10^{-2}$ diverges from the curves for higher τ. Moreover, the definition of ψ^* eliminates the physically unfeasible domain. In fact, controlling ψ^* instead of Ψ avoids oxygen starvation in the COR even if the the fuel flow rate entering the COR from outside the fuel processor is low due to the rich retentate. Finally, the sensitivity to p_{SRR} increases by increasing T_{SRR}, as already observed in Figure 2.5 (b).

The fuel processor efficiency monotonically increases by decreasing ψ^* (Figure 2.11b), as already observed in Figure 2.7 (b). However, η_{fp} is minimized for $T_{\text{SRR}} = 600\,^{\circ}\text{C}$ for every ψ^* value, differently from what observed in Figure 2.7 (b) by varying Ψ. In such plot, η_{fp} is maximized for $\tau = 6.11 \times 10^{-2}$ in the Ψ range [9.7-11.6] as a result of the increase of $\Psi - \Psi^*$.

The fuel processor efficiency reaches the maximum for [2.5< ϕ <3.5] as a function of T_{SRR} (Figure 2.11c), as already observed in Figure 2.9 (b). However, in Figure 2.11 (c) η_{fp} is minimum at $T_{\text{SRR}} = 600\,^{\circ}\text{C}$ irrespective of ϕ. On the contrary, in Figure 2.9 (b) for $\Phi = 1.35$ the fuel processor efficiency is minimum at $\tau = 6.11 \times 10^{-2}$, while for $\Phi = 0.75$ the fuel processor efficiency is maximum at such τ. Indeed, at low τ the combustible content in the retentate is relevant and the effect of the increase of $\Psi - \Psi^*$ is evident, especially at a low Φ that hinders hydrocarbons reforming. Moreover, controlling ψ^* instead of Ψ reduces the extent of the exothermic domain. In fact, the increase of $\Psi - \Psi^*$ resulting from the Ψ-based control results in less air per fuel unit, reducing the self-consumed thermal power in the COR and hence increasing the exothermic domain.

2.4 Summary

This chapter systematically analyzes the effect of the operating parameters on the performance of a membrane-integrated fuel processor that produces high purity hydrogen for low temperature fuel cell applications. We study the fuel processor performance behaviour through a steady state model with a hybrid lumped-distributed parameter approach based on Aspen Plus®. The operating parameters that affect the fuel

processor efficiency are the pressure and temperature of the SRR reactor and the ratio of the reactants entering the COR and the SRR. We analyze the operating parameters in dimensionless form to generalize the results for different reactants and reference conditions.

The results show that the fuel processor efficiency varies between 75 % and 84 % as a function of the operating parameters. Moreover, there is not a mutual interaction of the effects of Φ, Ψ, Π, and τ on the fuel processor efficiency, when the retentate composition does not increase $\Psi - \Psi^*$. The engineering relevant optimal combination of operating parameters is $\Phi = 0.64$, $\Psi = 0.3$, $\Pi = 35$, and $\tau = 7.3 \times 10^{-2}$, considering the investigated domain. Indeed, η_{fp} always increases by increasing Π, however the marginal increment is not substantial for $\Pi > 35$. Moreover the optimal Φ and τ values result from a trade-off, while the optimal Ψ value is the lowest physically possible. The non-dimensional optimal operating parameters converted in dimensional form are $p_{\text{SRR}} = 35\,\text{bar}$, $T_{\text{SRR}} = 770\,^{\circ}\text{C}$, $\phi = 3.47$, that is equivalent to $\phi = 3.5$, and $\psi = 12.4$, that is equivalent to $\psi = 20$. Such results show that the high operating pressure is the optimal parameter that mainly differentiates PSA-based and membrane-integrated fuel processors, as also evidenced in chapter 1. The fuel processor efficiency is mostly sensitive to a variation of Φ and τ near the global optimum. Moreover, decreasing τ for more than 8 % from the optimal value results in oxygen starvation in the COR. The analysis shows that only dense ceramic membranes can withstand the optimal operation of the fuel processor. Moreover, such membranes appear to be compatible for the integration in a SRR reactor without drastically changing its design. The retentate composition has a significant impact on the results. In fact, for low τ, Ψ and Φ the fuel processor experiences oxygen starvation or exothermic regime due to the rich retentate. Moreover, near the unfeasible domain the high content of combustible in the retentate increases $\Psi - \Psi^*$, resulting in mutual interactions of the effects of the operating parameters on the fuel processor efficiency. Therefore, by representing the results in terms of ψ^* the effects of the content of fuel in the retentate disappear. Indeed, ψ^* accurately represents the composition of the reactant flow entering the COR. Therefore, by controlling ψ^* the unfesible domain is drastically reduced and there is not mutual interaction of the effects of the operating parameters on the fuel processor efficiency.

The sensitivity analysis presented in this chapter demonstrate that the appropriate selection of the operating parameters is crucial to efficiently

produce hydrogen with a membrane-integrated fuel processor. Moreover, the efficiency and economic competitiveness of an optimum membrane-integrated fuel processor relies on the implementation of ceramic dense membranes. The detail design of a membrane-integrated fuel processor has to be investigated taking into account the membranes surface, the catalyst surface, and the heat exchange surface.

Figure 2.3: *Space plot representing the analyzed dominion of the free parameters. Each sphere represent a combination of the free parameters. The color of the sphere is proportional to the fuel processor efficiency.*

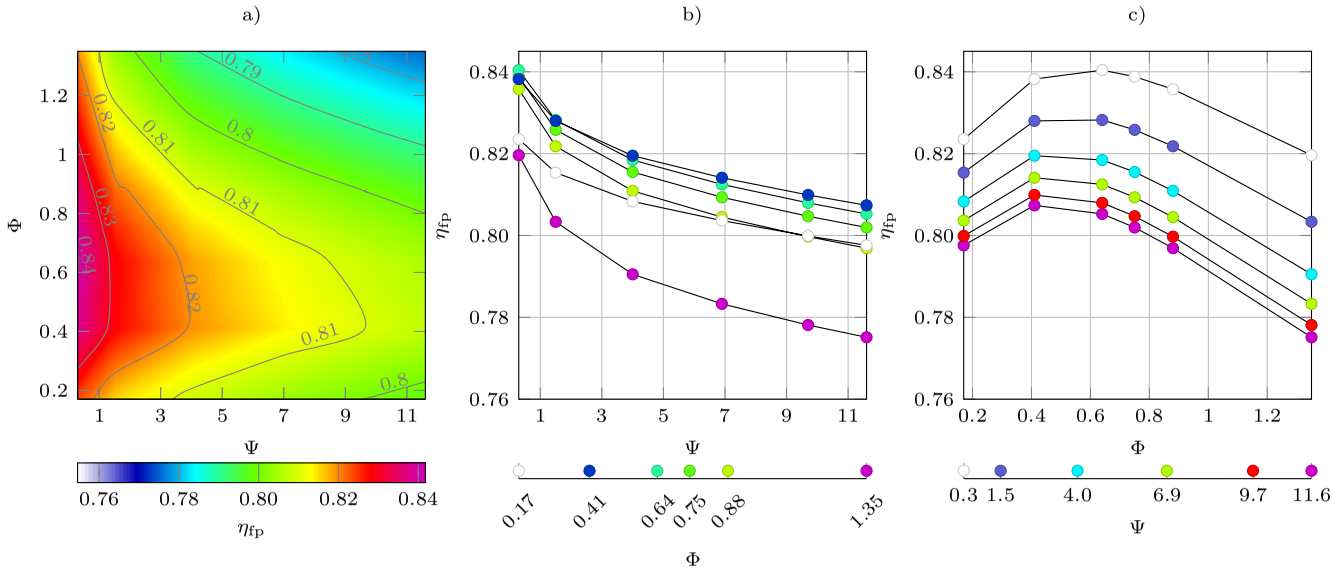

Figure 2.4: *Fuel processor efficiency as a function of the excess steam to fuel ratio and of the excess air to fuel ratio: a) contour plot, b) fuel processor efficiency as a function of excess air to fuel ratio for several excess steam to fuel ratios, and c) fuel processor efficiency as a function of excess steam to fuel ratio for several excess air to fuel ratios. In this analysis the constant parameters are* $\Pi = 35$ *and* $\tau = 7.3 \times 10^{-2}$.

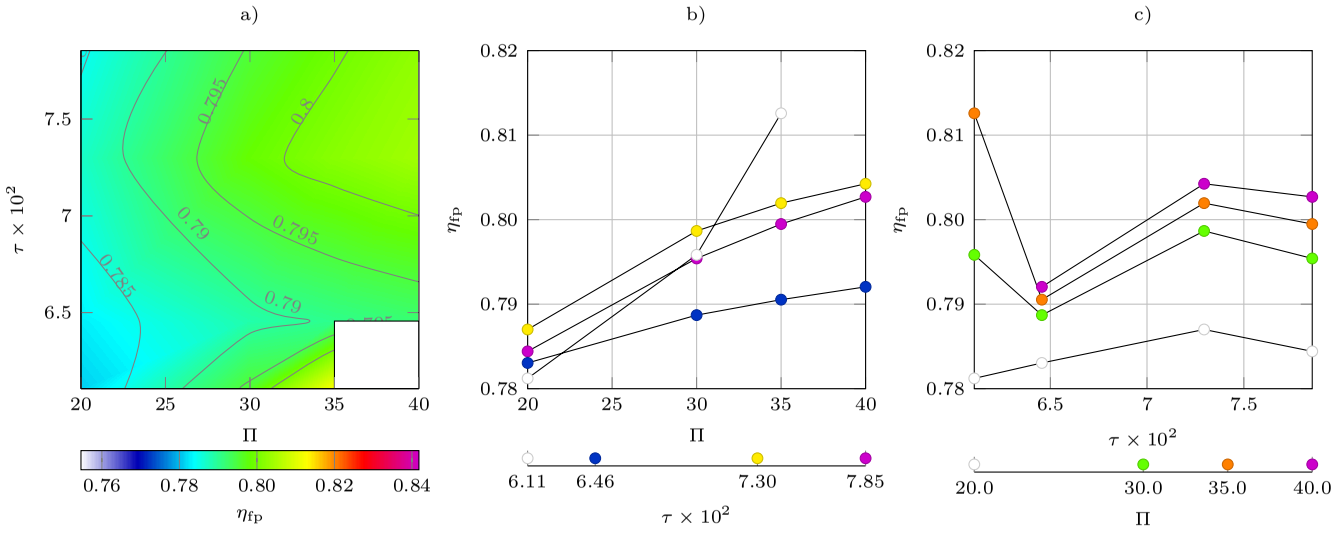

Figure 2.5: *Fuel processor efficiency as a function of the MHIWaR SSR side dimensionless pressure and temperature: a) contour plot, b) fuel processor efficiency as a function of the MHIWaR SSR side dimensionless pressure for several MHIWaR SSR side dimensionless temperatures, and c) fuel processor efficiency as a function of the MHIWaR SSR side dimensionless temperature for several MHIWaR SSR side dimensionless pressures. In this analysis the constant parameters are* $\Phi = 0.75$ *and* $\Psi = 11.6$.

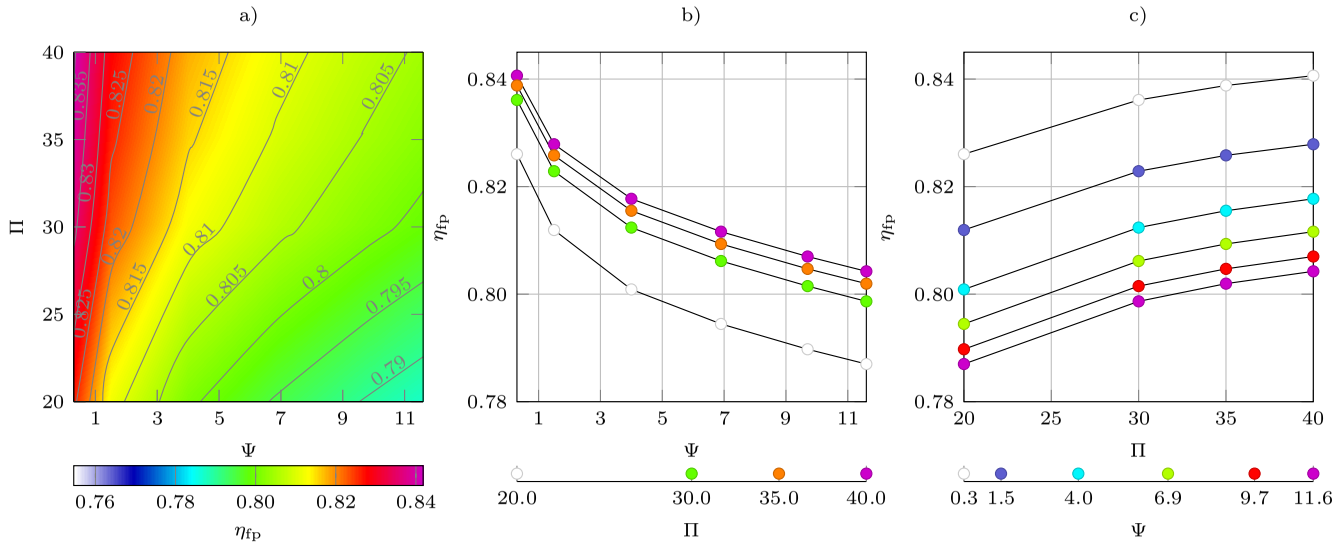

Figure 2.6: *Fuel processor efficiency as a function of the excess air to fuel ratio and of the MHIWaR SSR side dimensionless pressure: a) contour plot, b) fuel processor efficiency as a function of the excess air to fuel ratio for several MHIWaR SSR side dimensionless pressures, and c) fuel processor efficiency as a function of the MHIWaR SSR side dimensionless pressure for several excess air to fuel ratios. In this analysis the constant parameters are* $\Phi = 0.75$ *and* $\tau = 7.3 \times 10^{-2}$.

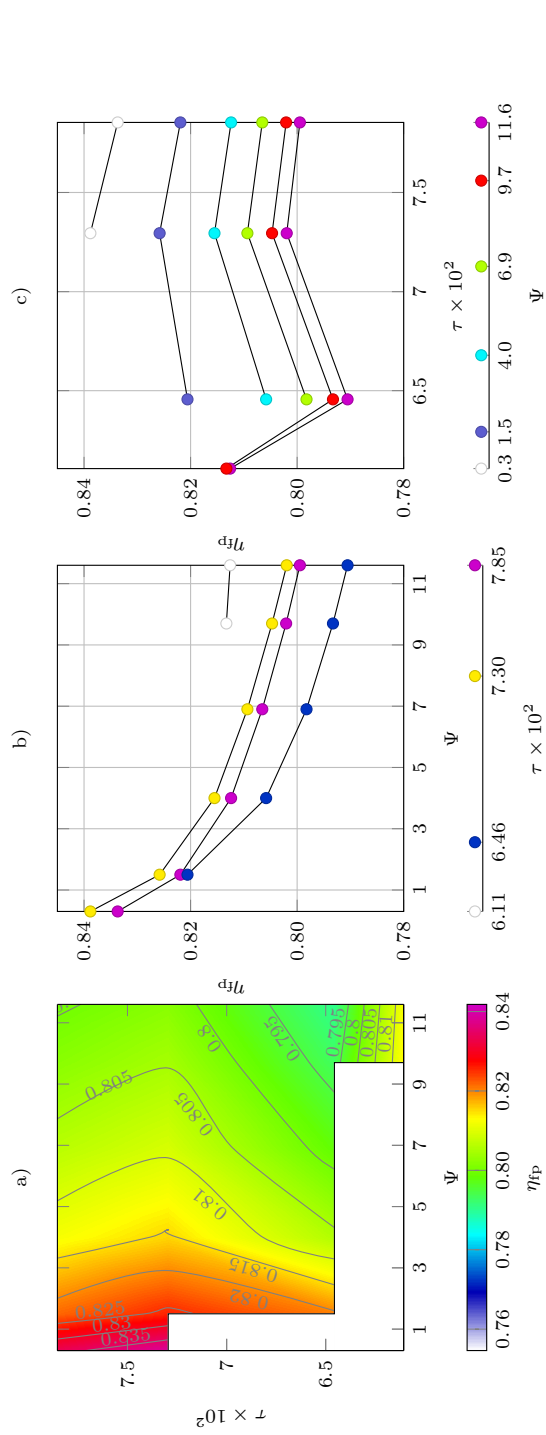

Figure 2.7: *Fuel processor efficiency as a function of the excess air to fuel ratio and of the MHIWaR SSR side dimensionless temperature: a) contour plot, b) fuel processor efficiency as a function of the excess air to fuel ratio for several MHIWaR SSR side dimensionless temperatures, and c) fuel processor efficiency as a function of the MHIWaR SSR side dimensionless temperature for several excess air to fuel ratios. In this analysis the constant parameters are* $\Phi = 0.75$, *and* $\Pi = 35$.

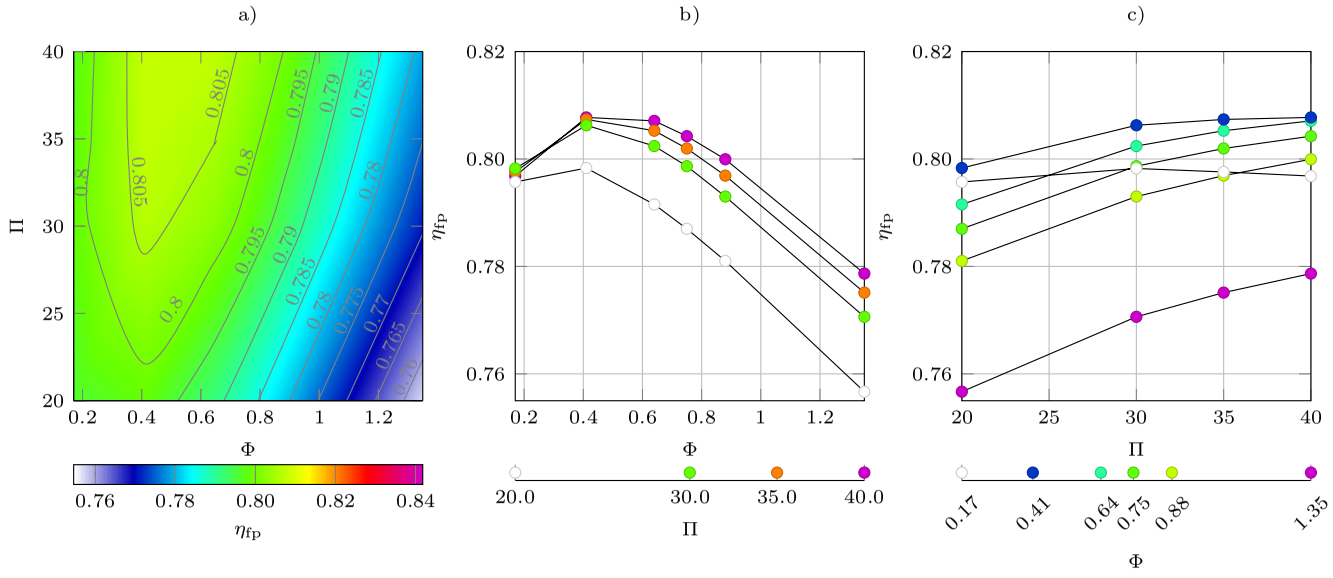

Figure 2.8: *Fuel processor efficiency as a function of the excess steam to fuel ratio and of the MHIWaR SSR side dimensionless pressure: a) contour plot, b) fuel processor efficiency as a function of the excess steam to fuel ratio for several MHIWaR SSR side dimensionless pressures, and c) fuel processor efficiency as a function of the MHIWaR SSR side dimensionless pressure for several excess steam to fuel ratios. In this analysis the constant parameters are* $\Psi = 11.6$ *and* $\tau = 7.3 \times 10^{-2}$.

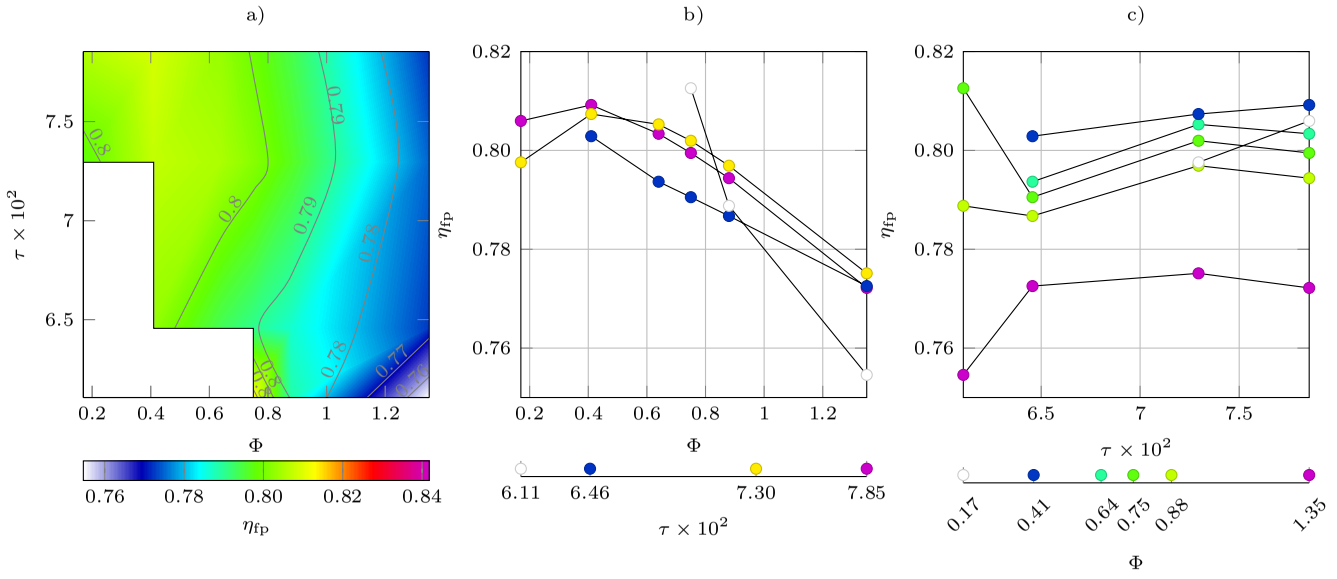

Figure 2.9: *Fuel processor efficiency as a function of the excess steam to fuel ratio and of the MHIWaR SSR side dimensionless temperature: a) contour plot, b) fuel processor efficiency as a function of the excess steam to fuel ratio for several MHIWaR SSR side dimensionless temperatures, and c) fuel processor efficiency as a function of the MHIWaR SSR side dimensionless temperature for several excess steam to fuel ratios. In this analysis the constant parameters are* $\Psi = 11.6$ *and* $\Pi = 35$.

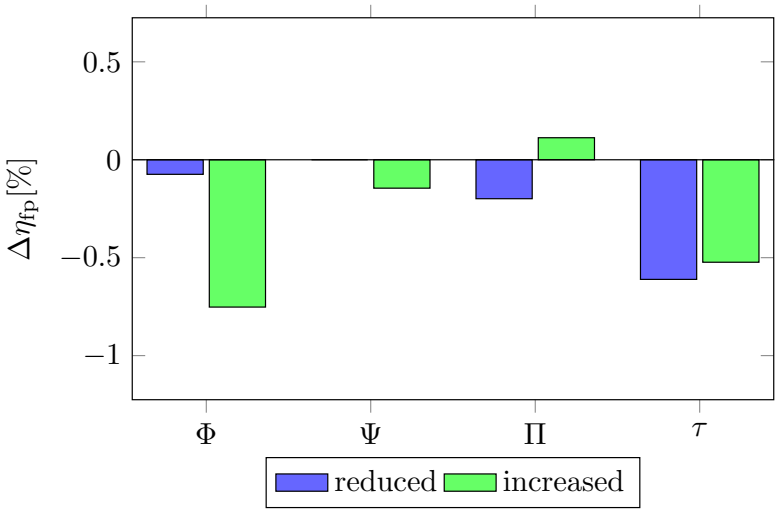

Figure 2.10: *Fuel processor efficiency variation as a function of a variation from the optimal value of the sensitivity analysis parameters. While varying each parameter the others are kept at optimal value. The range of variation is* $[-10\%; +10\%]$ *for* Φ *and* Π, $[-8\%; +10\%]$ *for* τ, *and* $[+10\%]$ *for* Ψ. *The black horizontal line represents the optimal efficiency value.*

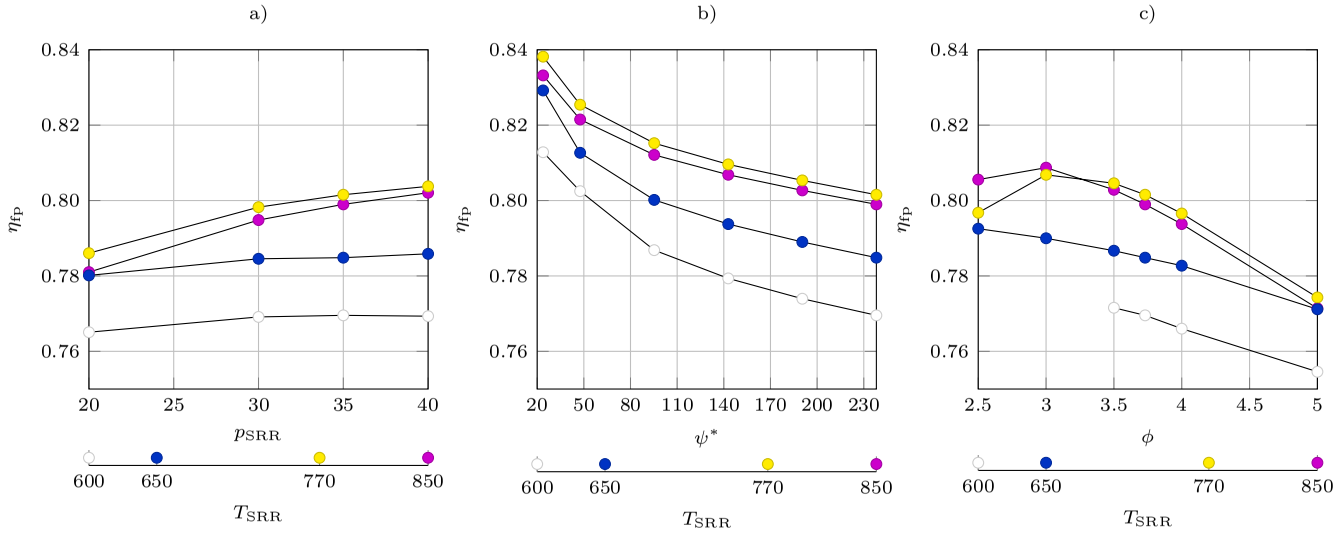

Figure 2.11: *Fuel processor efficiency as a function of: a)* p_{SRR} *for different* T_{SRR} *values with constant* $\psi^* = 50$ *and* $\phi = 3.73$*, b)* ψ^* *for different* T_{SRR} *values with constant* $p_{\mathrm{SRR}} = 35\,\mathrm{bar}$ *and* $\phi = 3.73$*, and c)* ϕ *for different* T_{SRR} *values with constant* $\psi^* = 50$ *and* $p_{\mathrm{SRR}} = 35\,\mathrm{bar}$*.* T_{SRR} *varies in the range [600, 650, 770, 850]*°C.

Chapter 3

Combined Heat, Cooling, and Power Systems Based on Half Effect Absorption Chillers and Polymer Electrolyte Membrane Fuel Cells

Fuel cell based trigeneration plants, that utilize absorption chillers to convert waste heat into cooling energy, are a promising technology to satisfy heat, power, and cooling demand in warm climates. Polymer electrolyte membrane fuel cells, that operate at low temperature ($< 100\,^{\circ}\mathrm{C}$), are one of the most technologically mature among the several types of fuel cells. Thermally activated cooling technologies are widely utilized in trigeneration plants to improve their efficiency. However, absorption chillers require relatively high grade thermal energy and their coupling with low temperature fuel cells is relatively untapped.

The automotive derivative PEMFC CHP system has already been studied in a thorough techno-economic analysis and, when used together with a mechanical chiller, provide economical benefits, with respect to business as usual scenario, for a wide range of climatic conditions and for different users (e.g. commercial, residential, or services) [80]. This is es-

pecially true if the CHP plant is managed through an optimized control strategy that maximize economical savings [80]. However, in some cases, depending on the climate, the primary energy factor, and CO_2 emission factor of the electricity grid, the environmental impact of such a power plant can be higher than in the reference scenario [80].

In this chapter, to avoid such a drawback, we maximize the thermal energy recovery throughout the whole year, by utilizing an absorption chiller. Accordingly, it could be possible to reduce the CO_2 emissions, while increasing the fuel cell utilization factor, also positively impacting the economic performance. Therefore, we perform a techno-economic analysis of a trigeneration plant based on low temperature polymer electrolyte membrane fuel cells and half-effect absorption chillers. A thermo-chemical model is developed to estimate the performance of a cogeneration plant based on low temperature fuel cells and of the half-effect absorption chiller. The behavior of such combined heat, cooling, and power plant is also analyzed within real energy management scenarios, considering different energy demands, climatic conditions, energy costs, and plant layouts. The control strategy of the power plant is optimized through a graph-based methodology previously developed and validated by the fluid machinery research group of the University of Tuscia. Total energy cost and CO_2 emissions are then compared to those of a reference scenario where electricity is acquired from the distribution grid, thermal energy is produced through a natural gas boiler, and a mechanical chiller is used for cooling.

Few works study the integration of an absorption chiller in a low temperature PEMFC CHP systems [144]. However, a thorough techno-economic analysis of such an innovative energy system is still a relatively untapped topic.

We hypothesize that the plant satisfies the energy demand of an apartment district in Europe. We selected this case among those presented in [80] because its economic performance is brilliant while the plant efficiency is less outstanding due to the low heat demand during warm seasons.

The results show that the utilization of half-effect absorption chillers boosts the environmental and economic benefits for all the considered scenarios. We also demonstrate that the utilization of the absorption chiller reduces the imbalance between the results obtained for the different scenarios (i.e. climates), although economic and environmental benefits associated to distributed generation are strongly influenced by the energy context.

The chapter is organized as follows. The considered CHCP system is presented in section 3.1. In section 3.2 we discuss the numerical modeling of the power plant. In section 3.3 the principles of the techno-economic analysis are presented. The results are presented and discussed in section 3.4. Finally, in section 3.5, we draw the conclusions of the work.

3.1 Problem statement

The aim of this chapter is to assess the environmental and economic impact of the integration of a half-effect absorption chiller in a PEMFC based CHP plant.

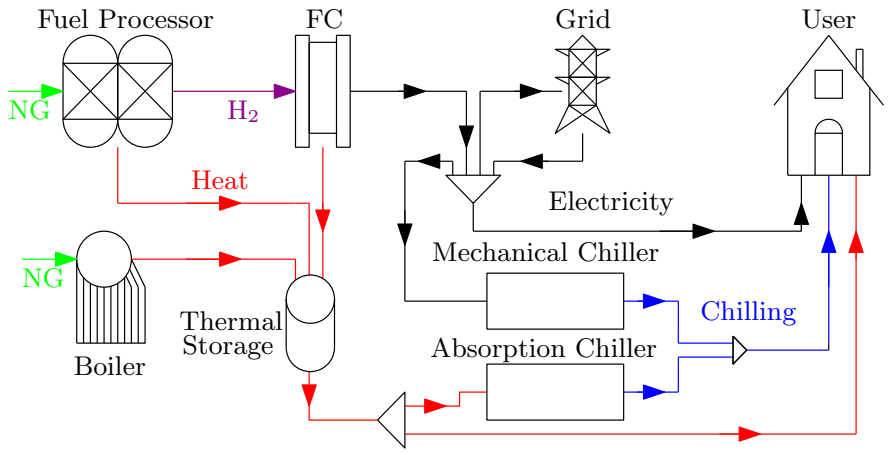

Figure 3.1: *Schematic representation of the considered CHCP plant.*

We study the low temperature PEMFC CHP system, represented in Figure 3.1, that is connected directly to the Natural Gas (NG) line through a fuel processor [104] and is the baseline scheme studied in chapter 1. A CHP system based on the same prime mover was already studied in [80, 104] for different energy demands. Therein, it was evidenced that a low heat demand during warm seasons reduces the FC utilization and the plant efficiency. Herein, we evaluate the integration within the plant of an half-effect absorption chiller [144], in order to exploit the low grade heat also in warm months.

First, we retrieve the performance of the components of the CHCP plant, as a function of the set point through thermochemical lumped parameter models (see section 3.2). Then, we study the behavior of the

resulting CHCP system in different energy management scenarios [80]. To this aim, we compare the energy consumption and costs to a reference scenario where electricity is acquired from the distribution grid, heat is produced within a NG boiler, and a mechanical chiller is used for cooling. This scenario represents the state of the art of energy supply for domestic users. We consider the energy demand of a typical apartment district in 5 different climatic conditions (Cold, Heating Based, Moderate, Chilling Based, and Hot) in the European energy context and we evaluate an optimized control strategy, determined through a graph-based approach [145–148].

3.1.1 Fuel Cell Based CHCP Plant

As already evidenced, the CHP system is the baseline power plant presented in in chapter 1. The only difference is that in this chapter, for thermal integration with the hal-effect absorption chiller we assume that the cogeneration heat is harvested through a water flow that enters the heat recovery system at 60 °C. Therefore, two kW of thermal power at 60 °C are wasted towards the environment.

The cooling system studied is a H_2O/LiBr half-effect absorption chiller [76, 77, 149, 150], whose Dühring schematic is reported in Figure 3.2.

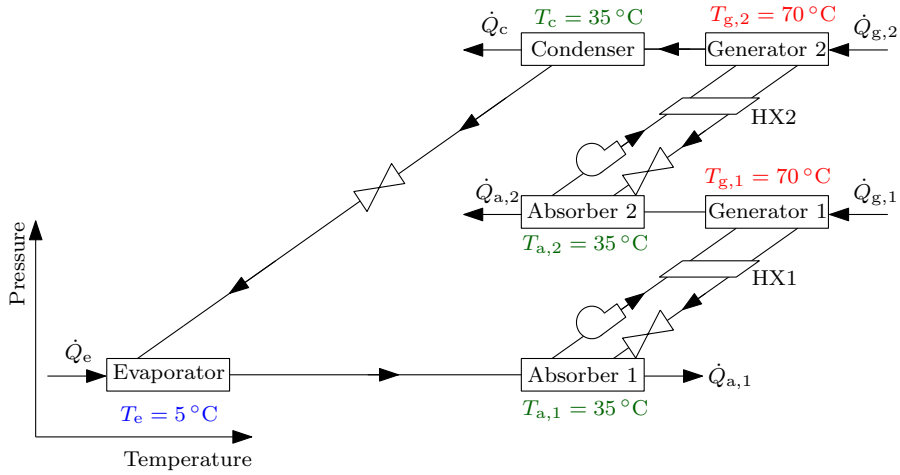

Figure 3.2: *Half-effect absorption chiller Dühring schematic.*

The half-effect absorption chiller is a three pressure level machine [149]. The low and high pressure levels are identical to traditional single effect

absorption chillers. The intermediate pressure level generator produces refrigerant water vapor that is absorbed in absorber 2. In generator 2 the H_2O/LiBr solution is heated again at high pressure to generate the refrigerant that then flows in condenser, evaporator, and absorber 1, as usual.

The three pressure levels structure is similar to that of double-effect absorption chillers. However, for half-effect machines the two step absorption-compression-generation process is conceived to exploit low grade heat, rather than high grade heat. In fact, thanks to the intermediate pressure level the generators can operate at a temperature in the range [60 °C, 80 °C] [76, 77, 149, 150]. Thermal energy in such a temperature range would not be exploitable through a traditional single effect absorption chiller.

The COP of half-effect absorption chillers is lower than the COP of single effect absorption chillers because the double absorption-compression-generation process furnishes heat twice in the generators, while there is a single useful effect in the evaporator.

The generation of refrigerant vapor at low pressure is possible thanks to the properties of the H_2O/LiBr solution. In fact, given a certain generator temperature and solution mass flow rate, the higher is the water concentration in the binary solution, the higher will be the mass flow rate of pure refrigerant generated. In other terms, it is possible to obtain the same refrigerant mass flow rate, using a lower generator temperature, with a solution richer in water. However, the maximum amount of water that can be absorbed in LiBr is limited by its solubility [151]. In addition, the refrigerant generation process is favored by decreasing the working pressure.

The water concentration within the solution in absorber 1 (see Figure 3.2) is limited by the low pressure that, in turn, is determined by the saturation pressure of the refrigerant at the temperature of the evaporator. Anyway, in generator 1 a reasonable refrigerant mass flow rate can be separated despite the low temperature ($60\,°C < T_{g,1} < 80\,°C$), thanks to the relatively low pressure. In absorber 2 the water concentration in the solution is incremented due to solubility increase with pressure. For this reason in generator 2 it is possible to obtain a good refrigerant generation, also at a relatively low generator temperature ($60\,°C < T_{g,2} < 80\,°C$).

3.2 Numerical Modeling of the CHCP Plant

We perform the steady-state characterization of the PEMFC based CHP system with the thermo-chemical model already presented in chapter 1. We consider in this chapter the overall electrical efficiency as defined in equation (1.3) in section 1.1.1 and we call it $\eta_{\mathrm{el,CHP}}$. Similarly, we evaluate the thermal efficiency as defined in equation (1.4) and we call it $\eta_{\mathrm{th,CHP}}$.

The efficiency values are functions of the plant set point, that is defined as the ratio between the effective and the nominal electrical power (see eq. (3.1)).

$$\Phi_{\mathrm{CHP}} = \dot{P}_{\mathrm{el,CHP}} / \dot{P}^{\mathrm{nom}}_{\mathrm{el,CHP}} \,, \tag{3.1}$$

where $\dot{P}^{\mathrm{nom}}_{\mathrm{el,CHP}} = 50.0\,\mathrm{kW}$ is the nominal electrical power, and $\dot{P}_{\mathrm{el,CHP}}$ is the power outputs obtained by regulating the power plant.

We model the half-effect absorption chiller within the AspenPlus®[114] environment. Despite several modeling methodologies are available for this kind of study, such as ABSIM [152, 153] and Engineering Equation Solver (EES)[150, 154–157], AspenPlus® was chosen due to its widely tested reliability and to its profitable usage in several recent works [144, 158] regarding absorption chillers. Moreover, such an approach has been validated with results provided by others simulation environments, such as EES [158].

Due to the low pressure of the water/lithium bromide solution, we compute the thermodynamic properties of working fluids through the activity coefficient method. Specifically, we use the Redlich-Kwong equation of state [159] for the vapor-phase properties together with the Non-Random Two Liquid (NRTL) model [160] for the liquid solution. Such an approach is implemented in AspenPlus® within the ELECNRTL property method. In addition, for pure water streams, the steamNBS tables implemented in AspenPlus® are used [117].

We assume that the water exiting the condenser is saturated liquid. Such a parameter can be easily controlled by varying the heat wasted towards the environment, for example through a variable speed fan. Moreover, we assume that the refrigerant just outside the evaporator is saturated vapor. The two absorbers and the condenser are considered surrounded by the same ambient temperature, that in design conditions, is considered $T_{\mathrm{env}} = 30\,^{\circ}\mathrm{C}$. To guarantee an effective heat exchange, such elements are operated at $T_{\mathrm{a},1} = T_{\mathrm{a},2} = T_{\mathrm{c}} = 35\,^{\circ}\mathrm{C}$. As a consequence, their pressure is $p^{\mathrm{high}} = 5.80\,\mathrm{kPa}$. For off-design environmental conditions

p^{high} is varied according to the temperature variation.

We assume that the cooling fluid is released to the user at $T_{\text{us}} = 10\,^{\circ}\text{C}$. Such an assumption implies that the evaporator is operated at a temperature $T_{\text{e}} = 5\,^{\circ}\text{C}$. To obtain evaporation at such a temperature, the lower level pressure is fixed to $p^{\text{low}} = 0.873\,\text{kPa}$.

We consider the intermediate pressure level at $p^{\text{int}} = 2.00\,\text{kPa}$. Such a value is commonly recognized to be the best trade-off to increase the overall performance [144, 157, 158].

Given the temperature, $T_{\text{a},1} = T_{\text{a},2} = 35\,^{\circ}\text{C}$, and pressure at both low and intermediate aborbers, it is possible to determine the minimum lithium bromide concentration necessary to absorb all the refrigerant [151]. In absorber 1 we obtain $x^{\text{low}}_{\text{LiBr}} = 56.0\,\%$ mass fraction, while at the intermediate pressure level we get $x^{\text{int}}_{\text{LiBr}} = 46.0\,\%$.

The expansions in the valves are isoenthalpic processes.

We model the generators utilizing two elements: a heat exchanger and a flash separator (see Figure 3.3).

The condenser, the evaporator, and the two absorbers are modeled as single flux heat exchanger where just the output desired conditions are specified. In fact, in the real chiller the H_2O/LiBr solution exchanges heat with external air in these elements. Then, the air flow can be regulated with an adjustable speed fan. As a consequence, the output desired conditions can be accomplished for every working condition. Pumps and valves are also modeled with built-in AspenPlus® functions.

The solution mass flow rates in the lower pressure level circuit is manipulated in order to guarantee a constant generator temperature $T_{\text{g},1} = 70\,^{\circ}\text{C}$, also at part load. The mass flow rate of the refrigerant generated in generator 2 and in generator 1 is the same to guarantee the mass balance of the low pressure circuit. Such a condition is obtained by varying the solution mass flow rate in the high pressure cycle.

The absorption chiller is sized to use, at full load, all the heat produced from the fuel cell in nominal conditions. Accordingly, a nominal cooling power of 29.5 kW is obtained.

Counter current heat exchangers are used for HX1, HX2, and for generator 1 and generator 2. Such elements are studied through the logarithmic mean temperature difference approach. An accurate modeling of the off-design performance is considered, since the thermal resistance varies as a function of the pure hydrogen mass flow produced that is the main parameter for sensitivity analyses. The product of heat exchange coefficient

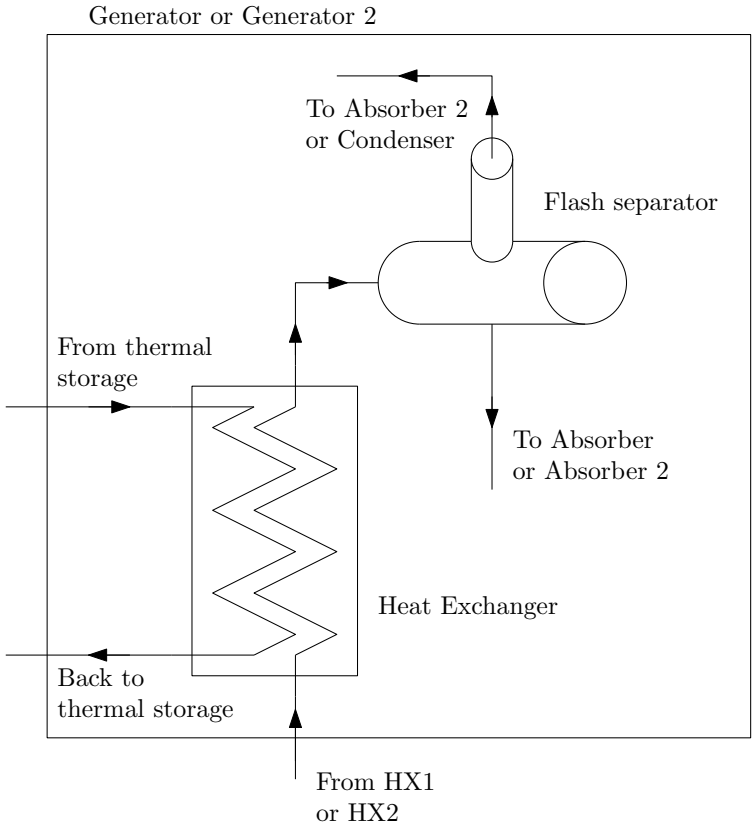

Figure 3.3: *Modeling scheme of the generators.*

U^* and area A is calculated under design conditions as [124]:

$$U^*A = \dot{Q}/\Delta \mathrm{T}_{\mathrm{ml}}, \tag{3.2}$$

where $\dot{Q}$ is the thermal power and $\Delta \mathrm{T}_{\mathrm{ml}}$ the logarithmic mean temperature difference. Both $\dot{Q}$ and $\Delta \mathrm{T}_{\mathrm{ml}}$ are known because we know the inlet conditions and mass flows, and we set output conditions, assuming a pinch point temperature difference of 5 °C.

When mass flow rates change, the thermal resistance is calculated as:

$$UA = U^*A\,(\dot{m}/\dot{m}^*)^{0.8}\,, \tag{3.3}$$

where $\dot{m}$ and $\dot{m}^*$ are the mass flow rates in off-design and design conditions, respectively. When $\dot{m}/\dot{m}^*$ is different for the hot and the cold side of the heat exchanger, the mass flow with the lower heat transfer coefficient is considered in eq. (3.3).

To calculate the performance of the half-effect absorption chiller in off-design we vary the cogenerated mass flow rate that guarantees heat to the generators. In this case, the main performance indicator is the coefficient of performance:

$$\eta_{\mathrm{co,AC}} = \frac{\dot{P}_{\mathrm{co,AC}}}{\dot{Q}_{\mathrm{g},1} + \dot{Q}_{\mathrm{g},2}}, \tag{3.4}$$

where $\dot{P}_{\mathrm{co,AC}} = \dot{Q}_{\mathrm{e}}$ is the cooling power generated in the evaporator. $\dot{Q}_{\mathrm{g},1}$ and $\dot{Q}_{\mathrm{g},2}$ are the thermal power required respectively in low and high pressure generators: generator 1 and generator 2 in Figure 3.2. We represent the results as functions of the following cooling set point:

$$\Phi_{\mathrm{AC}} = \dot{P}_{\mathrm{co,AC}} / \dot{P}^{\mathrm{nom}}_{\mathrm{co,AC}}, \tag{3.5}$$

where $\dot{P}^{\mathrm{nom}}_{\mathrm{co,AC}} = 29.5\,\mathrm{kW}$ is the nominal cooling power, and $\dot{P}_{\mathrm{co,AC}}$ the power obtained by regulating the absorption chiller.

3.3 Techno-economic analysis

3.3.1 Power Plant configurations

To evaluate the impact of thermally driven refrigeration on the CHP plant performance, we compare the three main plant configurations, summarized in Table 3.1.

	Reference	Case A	Case B
CHP Plant	✗	✓	✓
Absorption Chiller	✗	✗	✓
Mechanical Chiller	✓	✓	✓

Table 3.1: *Power plant configurations analyzed.*

Specifically, we study the reference scenario where electricity is brought from the distribution grid, heat is produced through a NG boiler and a mechanical chiller is used to satisfy the cooling load. In Case A, we consider the CHP system in study together with the mechanical chiller. Finally, Case B power plant utilizes the half-effect absorption chiller added to Case A energy system.

The mechanical chiller and the boiler are always present and sized to satisfy the peak demand of each case. The fuel cell CHP based system has a nominal power of 50 kW.

Also in Case B the mechanical chiller is able to fulfill the peak cooling demand to maximize the plant flexibility. The thermal storage is always considered and has the same power of the fuel boiler and it has a capacity equivalent to three hours of peak demand.

Figure 3.4 reports the performance of the mechanical chiller and of the fuel boiler as functions of the set point. Data are retrieved from literature [161]. The efficiency curves of the FC and of the absorption chiller will be reported in section 3.4, together with the other modeling results.

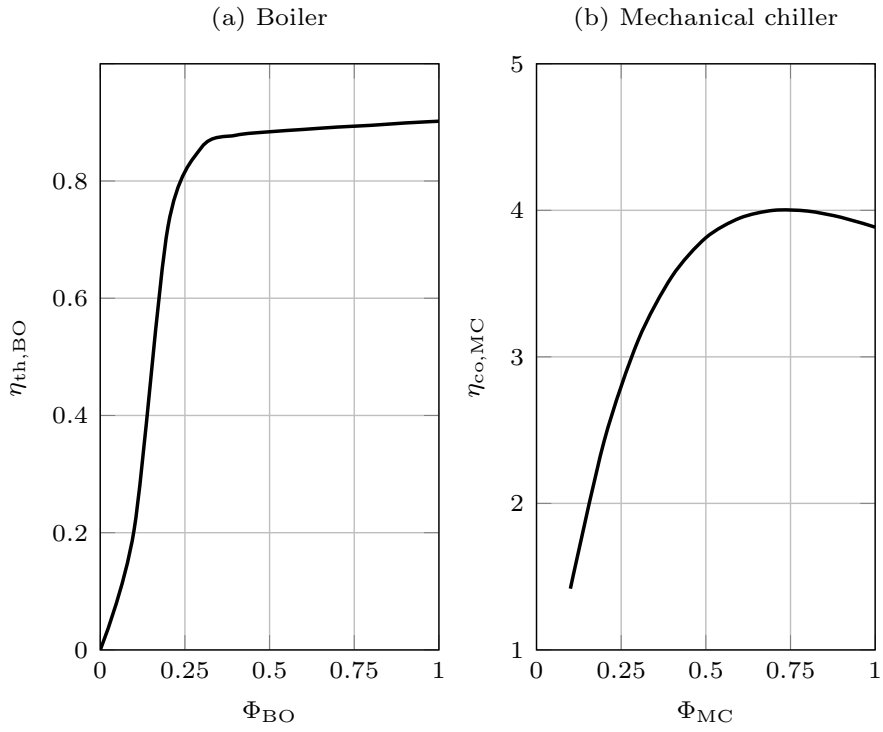

Figure 3.4: *Efficiency curve of the water boiler (a) and coefficient of performance curve of the mechanical chiller (b) as functions of the energy converter set point.*

3.3.2 Determination of the control strategy

The operating efficiency of any power plant is largely determined by its control strategy, as highlighted, for instance, in [19, 145, 147, 161–165]. Thereafter, we compare the performance of the different configurations assuming a smart management policy that minimizes the total energy cost.

The control strategy is determined through the optimization methodology introduced in [145], and further developed in [146–148]. Such a methodology minimizes a prescribed objective function on a daily basis accounting for: (i) the design performance of all the subsystems; (ii) the derating of the performance at part load; (iii) the effects of environmental conditions; (iv) energy demand and costs as functions of time; (v) maintenance, and cold start costs; (vi) constraints related to the dynamic behavior of the equipment, such as the minimum time interval between two consecutive starts or shutdowns.

All the energy converters are modeled as black-boxes, through their efficiency curves as functions of the set point and the environmental conditions. Specifically, the power output of the j-th subsystem at time t is calculated as:

$$\dot{P}_{i,j}(t) = \Phi_j(t)\dot{P}^{\text{nom}}_{i,j}\alpha_{i,j}(t)\,, \tag{3.6}$$

where $\Phi_j(t)$ is the set point, $\dot{P}^{\text{nom}}_{i,j}$ is the design power, and $\alpha_{i,j}(t)$ is the power derating coefficient, that is function of the environmental temperature, pressure, and altitude. Note that i can assume a value in the set [el; th; co], representing respectively electric, heating, and cooling power output. The corresponding required input power is:

$$\dot{U}_j(t) = \frac{\dot{P}_{i,j}(t)}{\eta_{i,j}(\Phi_j(t))\beta_{i,j}(t)} \tag{3.7}$$

where $\eta_{i,j}(\Phi_j(t))$ is the efficiency, and $\beta_{i,j}(t)$ is the efficiency derating coefficient, that is function of the environmental temperature, pressure, and altitude. Note that the problem is non-linear, since the efficiency is a function of $\Phi_j(t)$.

Economic optimization is performed through the following objective function:

$$\begin{aligned} G_{\text{Cost}} = \sum_{t=1}^{8760} & C_f(t, s(t)) + C_m(t, s(t)) + \\ & + C_s(t, s(t)) - R(t, s(t))\,, \end{aligned} \tag{3.8}$$

being t the time interval, C_f the cost of fuel, C_m the maintenance cost, C_s the cold-start cost, and R the revenue/cost yielding from the electricity exchanged with the grid. Costs are functions of the time interval and the plant state (i.e. the set point of the subsystems) $s(t)$.

Equation (3.8) is subject to constraints related to the energy flows and to the dynamic behavior of the plant subsystems. The thermal power

balance for each time interval reads:

$$\dot{P}_{\mathrm{th}}^{\mathrm{us}}(t) - \sum_{j} \dot{P}_{\mathrm{th},j}(t) + \dot{P}_{\mathrm{th,st}}(t) \geq 0 \quad \forall t\,, \tag{3.9}$$

where $\dot{P}_{\mathrm{th}}^{\mathrm{us}}(t)$ is the thermal power demand, $\sum_j \dot{P}_{\mathrm{th},j}(t)$ is the heating power produced by the energy converters within the plant, and $\dot{P}_{\mathrm{th,st}}(t)$ is the the thermal power of the heat storage. Note that, $\dot{P}_{\mathrm{th}}^{\mathrm{US}}(t)$ and $\sum_j \dot{P}_{\mathrm{th},j}(t)$ are positive, while $\dot{P}_{\mathrm{th,st}}(t)$ is positive when the system is storing energy and negative when it is releasing the heat. The cooling power balance for each time interval reads:

$$\dot{P}_{\mathrm{co}}^{\mathrm{us}}(t) - \sum_{j} \dot{P}_{\mathrm{co},j}(t) \geq 0 \quad \forall t \tag{3.10}$$

being $\dot{P}_{\mathrm{co}}^{\mathrm{US}}(t)$ and $\sum_j \dot{P}_{\mathrm{co},j}(t)$ the cooling power demand and production respectively. The following system of equations represents the constraint related to the dynamic behavior of the subsystems:

$$\begin{cases} \text{if } \tau_j(t) < \tau_j^* \text{ and } \Phi_j(t-1) > 0 \ \rightarrow \Phi_j(t) > 0 \\ \text{if } \theta_j(t) < \theta_j^* \text{ and } \Phi_j(t-1) = 0 \ \rightarrow \Phi_j(t) = 0\,, \end{cases} \tag{3.11}$$

where t is the time interval, $\Phi_j(t)$ is the set point of the j-th energy system, τ_j is the time spent since the last cold start, and τ_j^* is the minimum time interval between two consecutive cold starts. Similarly, $\theta_j(t)$ is the time spent since the last shut down and θ_j^* is the minimum time interval between two consecutive shut downs.

Equation (3.8) is discretized with respect to the plant state and in time, and the problem is represented as a weighted and oriented graph. The optimal control strategy is determined by seeking for the shortest path across the graph. The reader can refer to [145–148] for more details on the optimization methodology.

3.3.3 Economic analysis

Thanks to the control strategy optimization we determine the set point of each component of the energy system for each time-step. Then, we can calculate the cash-flow associated to the energy system, that is $C = min(G_{\mathrm{Cost}})$. As a consequence, we don not need to include the investment cost in the cost of energy, as usually done considering the Levelized Cost Of Energy (LCOE). In fact, we can compare the investment cost directly

with the cash flow of the energy system. Also, we avoid assuming the utilization factor, as usually done when considering the LCOE analysis.

As a consequence, we can evaluate the economic feasibility of Case A and Case B power plants through the pay-back period (i.e.the time in which the total savings are equal to the initial investment), calculated as:

$$\mathrm{PBP} = \frac{I_{\mathrm{add}}}{C_{\mathrm{ref}} - C}, \tag{3.12}$$

where I_{add} is the difference between the capital cost of the considered case and of the reference scenario, C_{ref} is the annual energy cost of the reference case and C is the annual cost of the analyzed case. For Case A, I_{add} accounts only for the cost of the PEMFC based CHP system, while for Case B it also considers the cost of the absorption chiller. In fact, the mechanical chiller, the water boiler and the thermal storage are present also in the reference case and do not represent an additional investment.

We consider an investment of 2000 €/kW for the automotive derivative PEMFC CHP plant, according to the European project AutoRE target [95, 96]. Moreover, for the half-effect absorption chiller we consider a unit cost of 1200 €/kW. This is a typical cost for double-effect absorption chillers. Half-effect machines are not in the commercial phase, however we assume that the cost of such devices is similar to that of double-effect absorption chillers, given the structure with three pressure levels that implies two generators, two absorbers, two pumps, and two solution heat exchangers.

3.3.4 Environmental impact evaluation

Carbon dioxide emissions are calculated through the following equation,

$$m_{\mathrm{CO_2}} = \sum_{i=1}^{N_{\mathrm{fuel}}} (m_i k_i) + E_{\mathrm{grid}} k_{\mathrm{grid}} \tag{3.13}$$

where N_{fuel} is the number of different fuels utilized in the plant, m_i is the mass of the $i-$th fuel, k_i is its CO_2 emission factor, E_{grid} is the electrical energy exchanged with the grid, and k_{grid} is the carbon dioxide intensity of the grid.

3.3.5 Energy demand

The US Department of Energy (DOE) published the "commercial reference buildings" database [166], where the hourly electricity, heat, and chilling energy demand profiles are reported for 16 different commercial reference buildings. Each structure is situated in more than 1000 locations (that represents different climatic conditions) in all the US. Data are available for an entire year.

The International Energy Agency (IEA) divided the entire world in 6 different climatic zones [80, 167]: (i) cold climate, (ii) heating based climate; (iii) combined climate; (iv) moderate climate; (v) cooling based climate; (vi) hot climate. Such a classification relies on the yearly Heating Degrees Days (HDD) and Cooling Degrees Days (CDD), as summarized in Table 3.2. Note that the reference temperature is 18°C for both CDD and HDD.

Climatic Zone	HDD [°C]	CDD [°C]	City
Cold	≥ 2000	≤ 500	Warsaw (Poland)
Heating Based	≥ 2000	$[500, 1000]$	Milan (Italy)
Moderate	≤ 2000	≤ 1000	Malaga (Spain)
Chilling Based	$[1000, 2000]$	≥ 1000	Athens (Greece)
Hot	≤ 1000	≥ 1000	Larnaca (Cyprus)

Table 3.2: *Heating and cooling degrees days and representative city for each IEA climatic zone [167].*

For clarity, we report in Table 3.2 an example of a European city for each climatic zone. Note that combined climate is not representative of any European territory, therefore we decided to neglect it.

The residential building that we consider is composed by about 10-15 apartments. Peak and average electrical, thermal, and chilling demands are represented in Figure 3.5, for each climatic zone. The electricity load is only marginally influenced by the location of the plant. On the contrary, heat and cooling demands are significantly influenced by the climatic zone. By comparing Table 3.2 and Figure 3.5, we note that for thermal and cooling demands, the difference between average and peak demand rises as the degrees day increase.

We sithetically characterize the energy demand through the cooling to

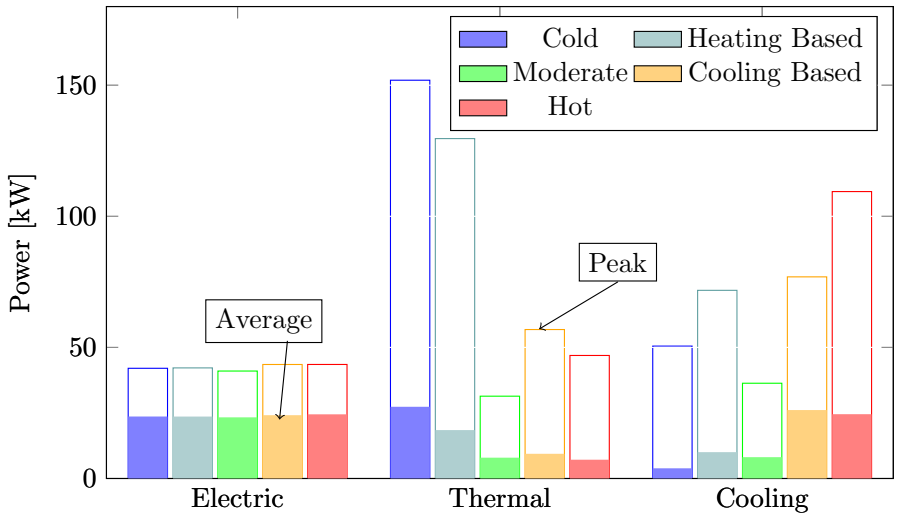

Figure 3.5: *Average and peak electricity demand for all the combinations of climatic condition and building energy demands.*

power ratio Θ, defined as:

$$\Theta = \frac{E_{\mathrm{ch}}}{E_{\mathrm{el}}}\,, \tag{3.14}$$

and the heat to power ratio Ω:

$$\Omega = \frac{E_{\mathrm{th}}}{E_{\mathrm{el}}}\,. \tag{3.15}$$

Therein E_{ch}, E_{th}, and E_{el} are the total early consumption of cooling, heating, and electrical energy.

Figure 3.6 classifies the considered case studies with respect to Θ and Ω. The red vertical line represents the ratio between the nominal thermal and electrical power of the CHP system. Since Θ is below that boundary for all the climates, following the thermal tracking plant control strategy would result in a large import of electricity, in particular for moderate, chilling based, and hot climatic zones. On the other hand, through the electrical tracking a significant amount of heat would be wasted. Thereafter, there is a large opportunity to exploit the waste heat through thermally driven refrigeration (as in Case B), to boost the CHP performance.

Similarly, the blue horizontal line in Figure 3.6 represents the ratio between the nominal cooling power of the absorption chiller and the nominal power of the CHP. We note that the absorption chiller can deliver the required cooling energy for the cold, heating based, and moderate climate.

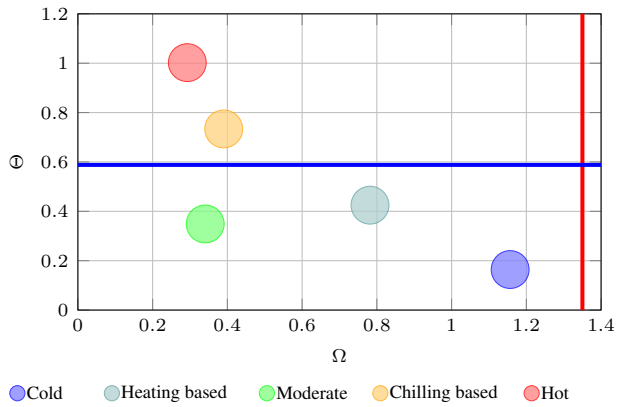

Figure 3.6: *Cooling and heat to power ratios of the energy scenarios studied. The red vertical line is the heat to power ratio of the CHP system, calculated with nominal powers. The blue horizontal line is the cooling to power ratio, calculated with nominal power of the fuel cell and of the absorption chiller.*

On the contrary, for cooling based and hot conditions an integration from the mechanical chiller is required.

Figure 3.6 also shows that Θ and Ω are strongly influenced by the climatic zone. In fact, moving from hot to cold climate Θ decreases, while Ω increases. All the cases are almost arranged along a straight line with negative slope except for the moderate climate that is characterized by very low thermal and cooling demands (see Figure 3.5).

Finally, it is worth to note that the yearly environmental temperature profile is necessary to evaluate the performance derating of the absorption chiller. Such a value is retrieved from the European commission joint research center [168] for each city reported in Table 3.2.

3.3.6 Energy prices and grid emission factors

The optimization methodology requires the prices of the energy vectors entering and exiting the power plant. Electricity is the only form of energy product of the CHCP plant that can be acquired from or sold in the external grid. However, we consider that the electricity sold to the grid is not remunerated. Such an assumption is necessary in order to perform a general study. In fact, electricity remuneration from small Distributed Generation (DG) plants, largely relies on national subsidiary mechanisms.

We underline that this is a conservative assumption that underestimates the economic profitability of the proposed power plant. Natural gas is the other possible input energy source to the plant.

Electricity and NG prices are retrieved from the Eurostat database [169], assuming an average value between the two semesters of 2016 for house-holds consumers category. All taxes and levies are included. Tables 3.3 and 3.4 report all the unit energy costs as a function of the total yearly consumption. We assume constant unit costs on a daily and yearly basis.

Electricity [c€/kWh]					
	Band DA	Band DB	Band DC	Band DD	Band DE
Poland	16.4	14.2	13.4	12.8	12.7
Italy	31.6	21.7	23.8	27.6	27.5
Spain	51.3	27.3	22.3	19.6	17.2
Greece	23.4	17.2	17.2	17.8	19.0
Cyprus	19.1	15.7	15.7	15.4	14.8
EU_{28}	33.3	22.6	20.5	19.4	18.5

Table 3.3: *electrical energy costs utilized for the different scenarios [169]. Band DA stands for yearly electrical energy consumption* $Cons.^{el.} < 10^3\,kWh$*; Band DB for* $10^3\,kWh < Cons.^{el.} < 2.5 \times 10^3\,kWh$*; Band DC for* $2.5 \times 10^3\,kWh < Cons.^{el.} < 5 \times 10^3\,kWh$*; Band DD for* $5 \times 10^3\,kWh < Cons.^{el.} < 1.5 \times 10^4\,kWh$*; Band DE for* $Cons.^{el.} > 1.5 \times 10^4\,kWh$*.*

Natural Gas [€/GJ]			
	Band D1	Band D2	Band D3
Poland	15.2	11.6	10.4
Italy	30.2	21.8	19.6
Spain	27.1	21.3	15.9
Greece	23.6	16.9	15.1
Cyprus	8.99	8.84	8.80
EU_{28}	26.8	17.5	15.6

Table 3.4: *Natural Gas prices utilized for the different scenarios [169]. Band D1 stands for yearly natural gas consumption* $Cons.^{NG} < 20\,GJ$*; Band D2 for* $20\,GJ < Cons.^{NG} < 200\,GJ$*; Band D3 for* $Cons.^{NG} > 200\,GJ$*.*

To compare the environmental performance of the several cases we consider the natural gas carbon dioxide emission factor $k_{NG} = 0.200\,kg/kWh$ [170]. Table 3.5 summarizes the carbon dioxide emission factors of the electricity available from the distribution grid for the different national scenarios. Data are retrieved from [171].

Scenario	k_{grid} [kg/kWh]
Poland	0.767
Italy	0.980
Spain	0.431
Greece	0.810
Cyprus	0.341
EU_{28}	0.447

Table 3.5: *Carbon dioxide emission factors of the electricity available from the distribution grid for the several national scenario analyzed, data are retrieved from [171].*

Note that assuming the energy consumption retrieved for US buildings [166] valid in a European energy context [169, 171] entails that the buildings occupants have similar behavior in the two geographic regions. Moreover, we implicitly consider the same technological level in home appliances and building construction. Such assumptions can be considered reasonable, given the comparable economic development level of these two regions.

3.4 Results and discussion

3.4.1 Power Plant Modeling

3.4.1.1 CHP Plant

Results obtained from the sensitivity analysis to Φ_{CHP} of the CHP plant are reported in Figure 3.7. Such results are the same already presented in section 1.3.1 with the limited thermal power recovered for the integration with the half-effect absorption chiller. Note that the minimum possible set point is $\Phi_{CHP}^{min} = 55.3\,\%$, according to limitations of the fuel processor, verified in experimental data of a real CHP plant under development within the European project AutoRe [95, 96].

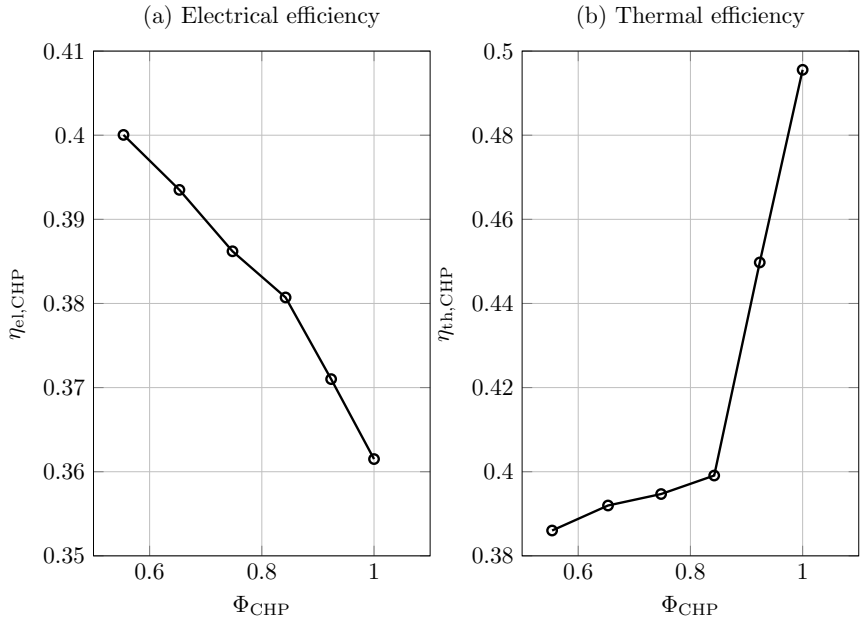

Figure 3.7: *Efficiency of the CHP power plant as functions of the power set point: (a) Overall electrical efficiency; (b) Thermal efficiency.*

We note that the overall electrical efficiency ranges between 36.1% and 40.0%, as a function of the set point, reaching its maximum at part load due to the fuel cell polarization curve [20, 21, 104].

In this model we assume that the natural gas from the distribution grid is already at 12 bar (or more), that is the operating pressure of the fuel processor. Considering the distribution pressure equal to 1 bar would reduce the electrical efficiency (due to the NG compressor work) by 1.19 %. In real conditions NG is delivered with a pressure $1\,\mathrm{bar} < p^{\mathrm{NG}} < 12\,\mathrm{bar}$, leading to an efficiency close to that here considered.

Thermal efficiency (Figure 3.7 (b)) values are in the range $38.5\,\% < \eta_{\mathrm{th,CHP}} < 50\,\%$. The efficiency increases increasing the set point, as a consequence of the reduction of $\eta_{\mathrm{el,CHP}}$. Such a phenomenon is more evident for $\Phi_{\mathrm{CHP}} > 0.800$. In this working regimen the electrical efficiency has a sharp decrease, due to ohmic and concentration losses.

The water temperature at the inlet of the CHP plant, (i.e. coming from the thermal storage) is set to 60° C, in line with the typical return temperature of domestic heating applications. Also the half-effect absorption chiller releases water at the same temperature. The resulting mass

flow rate and cogenerated water temperature are reported in Figure 3.8 as functions of Φ_{CHP}.

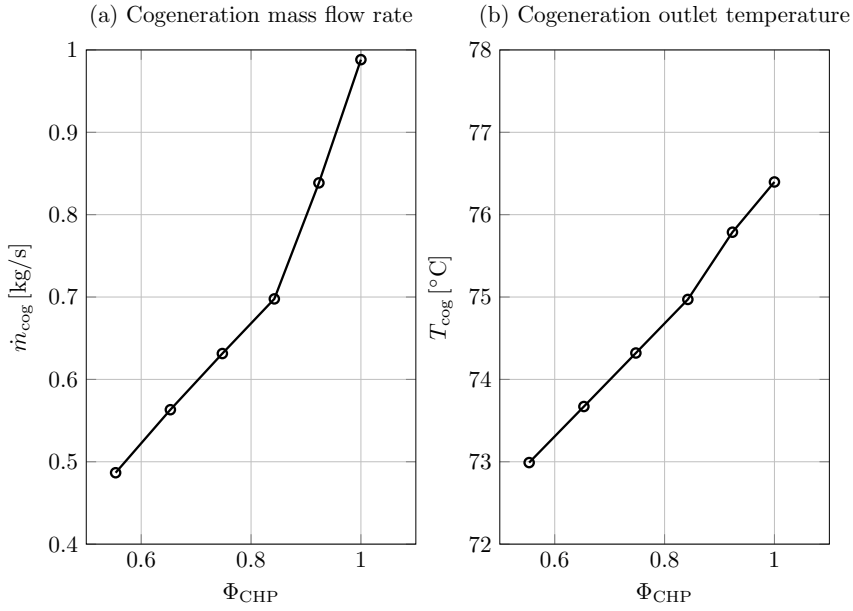

Figure 3.8: *Cogenerated outlet flow characteristics: (a) mass flow rate (b) temperature.*

The temperature values reported in Figure 3.8 are in line with domestic heating purposes. In fact, such applications require in most common appliances hot water at a temperature in the range $[45^\circ\,\text{C} - 75^\circ\,\text{C}]$. Moreover, the half-effect absorption chiller operates with a temperature of the generators equal to $70^\circ\,\text{C}$.

3.4.1.2 Absorption Chiller

Figure 3.9 shows that the COP varies in the range [0.400, 0.430] as a function of Φ_{AC}. The COP variation is moderate because the generators temperature is kept constant while varying Φ_{AC}. However, we note that the obtained nominal efficiency is in line with several results available in literature [144, 157].

Moreover, we comment that the COP value of the half effect absorption chiller it is considerably lower than the COP of a single effect absorption chiller or of a vapor compression chiller. However, we comment that only with the half-effect absorption chiller is possible to generate cooling energy

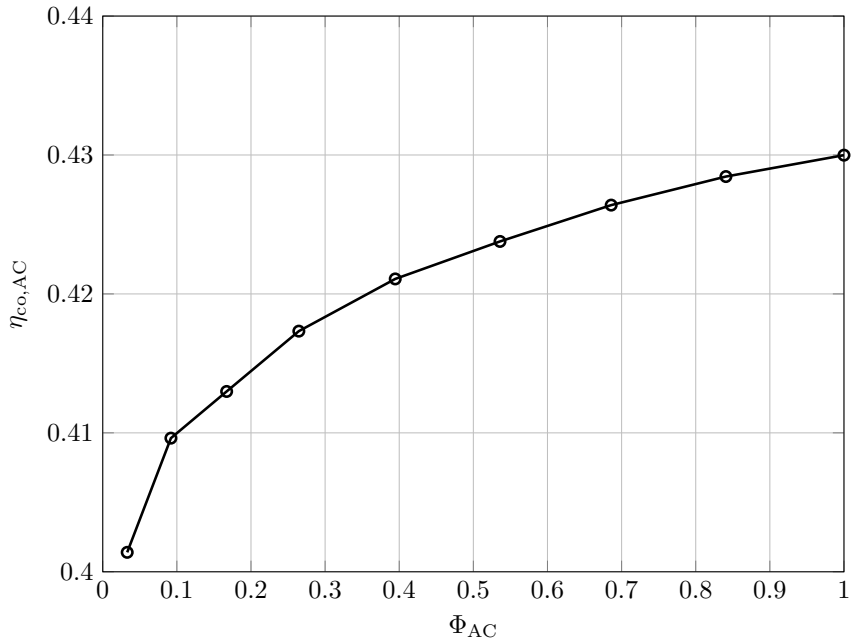

Figure 3.9: *Half-effect absorption chiller coefficient of performance as a function of the set point.*

effect from the low temperature heat of a PEMFC CHP system. As a consequence, we are able to recover an amount of heat that would otherwise be wasted in the environment. Thus, the utilization of absorption chillers reduces the cost of the rejection of heat to the environment.

Environmental conditions also significantly influence the power and COP of the absorption chiller as evidenced in Figure 3.10. In this case, the most relevant environmental variable is the temperature (T_{env}). In fact, it influences both the condenser pressure and the LiBr concentration in the the low pressure absorber (absorber 1). These two parameters affects the refrigerant separation in the generators and the cooling power and the coefficient of performance of the device.

For temperatures higher than 30 °C the maximum power is dramatically reduced. At 35 °C the maximum cooling power is halved compared to $T_{\text{env}} = 30\,°\text{C}$. For $20\,°\text{C} < T_{\text{env}} < 30\,°\text{C}$ the nominal cooling power is almost constant.

If temperature is increased from 20 °C to 35 °C, the COP is reduced by 10 %.

Note that the the absorbers and condeser temperatures are 5 °C higher

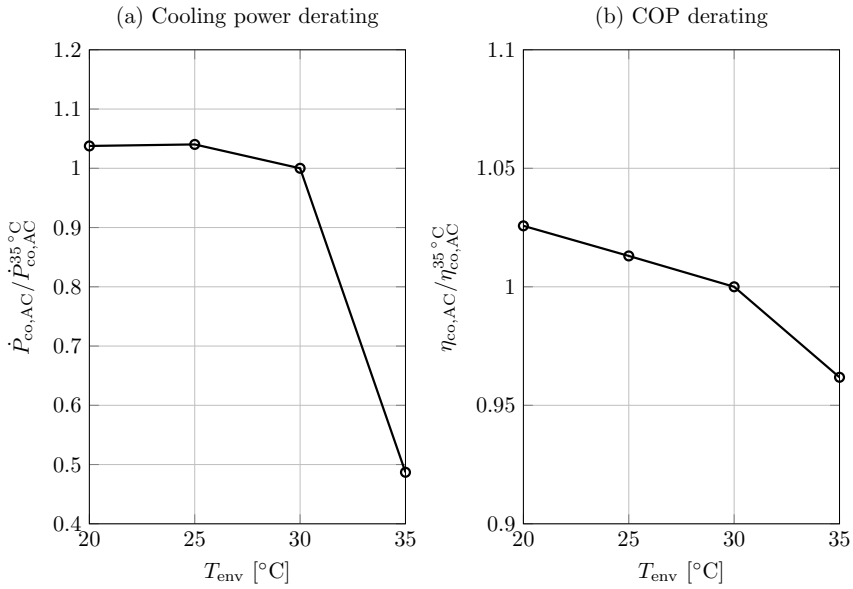

Figure 3.10: *Half-effect absorption chiller power and COP derating, as functions of environmental temperature. Nominal conditions for* $T_{env} = 35\,^\circ C$*. Absorbers and condenser temperatures are* $5\,^\circ C$ *higher than* T_{env}*.*

than T_{env} reported in Figure 3.10 (see section 3.2).

3.4.2 Economic and environmental performance in realistic scenarios

Here, we report the most representative and synthetic parameters, resulting from the CHCP plant simulation in real energy management scenarios. Specifically, we focus on the yearly total energy cost (accounting for all energy vectors), together with the annual total CO_2 emissions, and finally the Utilization Factors (UFs) of the components of the power plant. Figure 3.11 reports the results obtained considering the real energy context of each country representative of a climatic zone (see Tables 3.2, 3.3, 3.4, and 3.5). Figure 3.12 is obtained considering the average European energy context (see Tables 3.3, 3.4, and 3.5). Such a twofold analysis is necessary because, in Figure 3.11, we can analyze a real example of the adoption of a distributed generation system. On the contrary Figure 3.12 reports general results, valid for all Europe.

Both economical and environmental aspects are relevant for a dis-

tributed generation power plant. In fact, the economical convenience drives the investments towards innovative energy systems. However, our aim is to propose a CHCP system that can be effective both in economic and environmental terms.

Figure 3.11 (a) highlights the drastic cost reduction associated to the CHP plant (Case A) with respect to the reference scenario. Such advantages are further boosted when the absorption chiller is used (Case B). The economic savings are a function of the climatic zone and of the energy context, that, in turn, influence the energy loads and prices. For Case A the cost reductions, with respect to the reference case, are between 9.66 k€ and 33.9 k€ per year. On the other hand, for Case B the cost reduction varies in the range [12.8 k€, 37.2 k€] with respect to the reference scenario. As expected, Case B always reduces the energy cost compared to Case A. In particular, the hot climate yields the most relevant difference with a 8.30 % reduction of the energy cost.

Case A reduces the CO_2 emission for all the climates except for the moderate one (Figure 3.11 (b)). In the latter case, CO_2 emissions are increased by 17.6 %. In all the other climates the CO_2 emissions reductions, with respect to the reference case, are between 16.0 t and 164 t per year. Case B further reduces the carbon dioxide emissions. Specifically, CO_2 reduction ranges between -8.89 t (for moderate climate) and 171 t (for cold climate). Case B always reduces carbon emissions with respect to case A.

The utilization factor of the CHP system is always higher than 50 %, except for the moderate climatic zone. In fact, in such a climate the thermal and cooling loads are relatively low, leading to poor utilization of the CHP system. This, together with the low grid CO_2 emission factor of Spain (see Table 3.5), leads also to the negative environmental performance of the power plant in the moderate climatic zone.

Moreover, the adoption of the absorption chiller lowers the utilization factor of the FC because it reduces the electrical demand while increasing the recovery of the waste heat from the prime mover. Thereafter, the same useful effect is obtained with less fuel and power plant utilization.

Finally, we note that the CHP utilization factor rises increasing the cooling degrees days, that is passing from cold to hot climatic zones.

Figure 3.11 (d) evidences that the usage of the CHP power plant dramatically reduces the boiler utilization factor. In fact, such a component is practically useless if a distributed generation plant is utilized, for all climatic zones except for colder ones.

In Table 3.6 we present the global performance of the different power plant configurations in the case of hot climate and considering the real energy context.

	Reference	Case A	Case B
Total energy cost [k€]	49.7	27.5	23.4
CO_2 emissions [t]	274	168	134
CHP utilization factor	/	0.714	0.635
Boiler utilization factor	0.173	0.000	0.000

Table 3.6: *Global performance of the different power plant configurations in the case of hot climate and considering the real energy context.*

The results reported in Figure 3.11 combines the different climatic conditions to the national energy costs. However, the same climate might apply different country. Figure 3.12 is more general and allows studying the proposed energy systems in a European energy context. Specifically, given the same energy costs, we can dissect the influence of the climatic conditions on the general results. We observe again that Case A significantly reduces the energy cost with respect to the reference case (see Figure 3.12 (a)). Specifically, the revenues (or equivalently avoided costs) range from 13.0 k€ and 18.8 k€. Using the absorption chiller further reduces the costs by 16.1 k€ in the worst case (i.e. moderate climate), and by 22.7 k€ in best case (i.e. hot climate).

Figure 3.12 (b) highlight that, in the average European energy scenario, Case B always reduces the CO_2 emissions irrespective of the climatic condition. On the contrary, Case A increases carbon dioxide emissions for hot climates. Using the CHP plant together with the mechanical chiller we obtain CO_2 emissions reductions between -2.34 t and 30.1 t per year. The usage of the absorption chiller increases environmental benefits, with CO_2 emissions reductions in the range [14.7 t , 34.6 t].

We comment that in Case A and Case B the total energy cost is lower than the Reference case total energy cost for every climatic condition and energy context analyzed, as a consequence of the CHP system adoption. Such a result is strictly connected to the possibility to recover heat in the CHP system while producing electricity. Accordingly, the cost of natural gas necessary to satisfy the thermal energy demand is drastically reduced. Moreover, the relatively high efficiency, in particular at part load, of the

fuel cell system makes the cost of electricity produced competitive with that of the electricity bought from the grid. In fact, considering $\eta_{\mathrm{el,CHP}} = 0.36$ the cost of NG to produce electricity with the CHP varies in the range [8.8, 19.6] c€/kWh$_{\mathrm{el}}$ as function of the NG prices in Table 3.4, considering that the consumption of NG is larger than 200 GJ/year. Such costs are lower, or at least comparable with those reported in Table 3.3 for electricity from the grid.

In this work we are investigating the influence of the introduction of an absorption chiller in a CHP system. The importance of such a device is strictly related to the cooling loads. For this reason, we expect a seasonal trend in the impact on global parameters. Figure 3.13 (a) reports, the total energy cost associated to the different power plant configurations on a monthly basis for the hot climate case and assuming the energy costs and efficiencies of Cyprus. We comment that, irrespective of the energy system configuration, energy costs are higher in the hot months, due to the higher cooling demand. In addition, the power plant accounting for the absorption chiller has always the best economic performance. Similar trends are observed also for chilling based climate, considering Greek energy context.

To isolate the absorption chiller effect, we focus on the energy cost difference between the Case A and Case B (Figure 3.13 (b)). The savings, related to the thermally activated cooling machine, are minimum of in February (0.259 k€) and are maximized in August, reaching 0.486 k€. The absorption chiller reduces the energy cost also in winter months. This happens because in the hot climate a chilling load is always present, also during the cold months of the year [166].

Figure 3.14 represents the techno-economic performance of the different plant configurations by reporting the relative cost variation on the abscissa, the relative CO_2 reduction on the vertical axis and the radius of the circles is proportional to the PBP, calculated as described in section 3.3.3.

Considering the real energy context (see Figure 3.14 (a)) we obtain, for the Case A, a pay back period comprised between 3 years for heating based climate and 11 years for moderate climate. Such a variation is mainly due to the different energy costs relative to the different countries. In fact, considering the average European energy context (Figure 3.14 (b)) the PBP varies in the range [6 years, 8 years] for Case A, demonstrating that NG and electricity unit costs dominates the PBP variation with respect to

the climate. In Case B power plants PBP is almost always 1 year higher than the Case A situation. In fact, despite the higher economic savings (see Figures 3.11 and 3.12), the capital cost of the absorption chiller is dominant. We comment, however, that the cost of the absorption chillers is rapidly decreasing, as a result of the technology diffusion and mass production.

Herein, we make a conservative estimation of revenues and PBP. In fact, we do not remunerate the excess electricity and we discard incentives to distributed generation. Moreover, the high reduction of CO_2 emissions, registered in most of the analyzed cases, could generate further subsidiary mechanisms.

Focusing on the real energy context (see Figure 3.14 (a)) we obtain a cost reduction between 20.6 % and 44.7 % for Case A, and in the range [27.3 %, 53.0 %] for Case B. In the same scenario CO_2 reduction varies between -17.6 % and 56.8 % using the mechanical chiller and in the range [-8.85 %, 59.3 %] for the Case B. We comment that for every climatic zone the adoption of the absorption chiller improves both economic and environmental performance. In fact, in Figure 3.14 the spheres related to Case B are always in the north-east with respect to Case A. The negative value of CO_2 emissions reduction registered for the moderate climatic condition in the real energy context is a consequence of the low thermal energy demand of the moderate climate (see the Ω ratio in Figure 3.6) and of the low grid electricity emission factor (see Table 3.5). On the other hand, the large CO_2 emissions reduction associated to the cold climate (see Figure 3.14 (a)) is due to the high grid emission factor and high Ω ratio (see Table 3.5 and Figure 3.6). In Figure 3.14 (b) the cost reduction is between 25.6 % and 31.26 % for Case A, and in the range [27.3 %, 53.0 %] for Case B. Moreover, the carbon-dioxide emissions varies from -1.47 % to 18.2 % in Case A and from 11.6 % to 20.9 % in Case B. We note that the use of the absorption chiller allows a significant increase of the CO_2 emission reduction, especially for the minimum values. In fact, in Case B the lowest CO_2 reduction is more than 13 percentage points higher, compared to the lower environmental performing situation in Case A. Finally, within the EU_{28} scenario and with the absorption chiller, a positive CO_2 emissions reduction is achieved for all climatic zones. On the contrary, a positive cost reduction is registered for all power power plant configurations, in every climatic zone and in every energy context.

The energy context can influence economic and environmental per-

formance also within the same climatic zone. For example, for case A combining hot climate and Cyprus energy costs yields the best economic performance, with a 44.7 % cost reduction. However, in the EU_{28} scenario, the last cited case is the worst performing, accounting for the lowest cost reduction (25.6 %). Such a drastic difference is mainly related to the dramatically low natural gas price for hot climate reference country. In fact, the ratio between the mean NG price for Cyprus and for EU_{28} scenarios is $\overline{\text{Cost}}_{\text{NG}}^{\text{Cyprus}}/\overline{\text{Cost}}_{\text{NG}}^{\text{EU}_{28}} = 0.445$. Similarly, the CO_2 reduction, in the real energy context, for the Case A in hot climate is of 39.0 % while in the EU_{28} context such a variation is -1.47 %. Such a behavior is surely related to the ratio between the Cyprus and the mean EU_{28} k_{grid} that is 0.763.

Case B has an impressive performance for the hot climate and assuming the real energy context. In this case both cost and CO_2 emissions reductions are greater than 50 % (53.0 % and 51.1 %, respectively). This can be considered a promising application scenario for the coherence between economic and environmental drivers.

We conclude summarizing that, if the real energy context is evaluated, the adoption of the PEMFC based CHP power plant can be considered a viable solution, in economic and environmental terms, for all cases except the moderate climatic condition. When the CHCP system is used, CO_2 emissions and costs reductions are improved for all cases. However, the moderate climate is still a non-fertile soil of application, mostly for the negative environmental performance. In this case the absorption chiller usage is not effective because the cooling energy demand is not consistent.

Considering the average European scenario, the CHP power plant can be considered a good option only for cold and heating based climatic zones. On the other hand, the adoption of the CHCP power plant is effective for all climatic conditions.

Finally, we note that the half-effect absorption chiller with a COP of 0.4 is competitive with the mechanical chiller with a COP of 4: despite the low utilization factor the investment cost is recovered in reasonable time. We comment that the half-effect machine has a low COP, but it uses thermal energy that would be otherwise wasted in summer months. The mechanical chiller produces a cooling power 4 times higher than the input electrical power. But, the electricity has to be produced, or acquired. Moreover, the investment can be recovered relatively easily, also because the absorption chiller is not sized to cover the peak cooling demand, but its nominal power is 29.5 kW.

3.5 Summary

In this chapter we assess the environmental and economic impact of the integration of a half-effect absorption chiller in a 50 kW automotive derivative PEMFC based CHP plant. We first study the performance of the power plant components through thermo-chemical models. Specifically, we further refine a previously studied and validated model [80, 104] for the CHP plant, enhancing thermal integration for both heat of process and cogeneration. In addition, we develop a thermo-chemical model for the half-effect absorption chiller, following a validated methodology [144, 158].

These data are the main input for the second phase of the work, that is the techno-economic analysis. Therein, we assess the effective economic and environmental performance of the considered power plant in realistic scenarios.

We consider 5 different residential buildings energy demands, representative of 5 climates. We consider three different power plant configurations: (i) the reference case, that is separate production; (ii) the Case A, that is the cogeneration plant; (iii) the Case B which is the trigenerative plant. We also retrieve, from European statistics, natural gas and electricity costs, together with electrical grid CO_2 emission factors characteristic of the several countries in which the typical cities are placed. Also a mean European value of such parameters is considered.

We always operate the power plants with an optimal control strategy, based on energy cost minimization. The optimization is performed through dynamic programming.

We evaluate the economic feasibility of the distributed generation power plants through the PBP and cash flow. Specifically, we assume additional investments equals to 2000 €/kW for the automotive derivative PEMFC CHP plant and 1200 €/kW for the half-effect absorption chiller.

The results show that the adoption of the absorption chiller in the distributed generation PEMFC based power plant is a key aspect that boosts environmental and economic benefits for all the energy contexts and in every climatic condition. Considering the average European energy context, thanks to the CHCP system CO_2 emissions are reduced for all the considered climatic conditions. On the contrary for the CHP system such a behavior is not observed.

We comment that the climatic condition only marginally influence the

economic feasibility of such energy systems while the energy context dominates it. On the contrary, the climatic conditions dominates the environmental performance of DG systems.

Due to the larger investment cost, Case B are always characterized by a longer PBP (generally 1 year more). However, Case B generates higher cash flows, resulting in a larger investment value after it has been recovered.

Finally, if the real energy context is considered, the adoption of the PEMFC based CHP power plant is a viable solution, in economic and environmental terms, for all cases except the moderate climatic condition. Also using the CHCP system, the moderate climate is still unfit for this application, having negative environmental performance. Climatic conditions with high cooling over power or heating over power ratios are the most attractive cases. For example at CHCP system in hot climate yields cost and CO_2 emissions reductions both higher than 50 %.

For the average European scenario, the CHP power plant can be considered a good option only for cold and heating based climatic zones. On the contrary, Case B has a favorable performance in all the climatic conditions.

We also highlight that the adoption of the absorption chiller has a positive impact on the environmental performance of the FC based CHP plant. In fact, on average, case B further reduces the CO_2 emission by 8.33 % with respect to case A. The most relevant improvement of the environmental performance is for the hot climate and the EU_{28} context. In this case, Case A increments the CO_2 emissions, while Case B reduces the green house gases emission by 13.2 %.

Moreover, we underline that the results of this study could have a huge impact in practical applications. In fact, the residential sector can be considered a promising market for distributed energy systems. In the US, every year more than 1 Million of new residential units are built [74] and the trend is positive. Given that the CHP system in study can satisfy the energy demand of 20-30 families, a potential market of 40000 units per year can be estimated, for just the US scenario. This would result also in a drastic reduction of the technology cost [86, 93].

The analysis here performed could be further refined considering more advanced fuel processors for the CHP systems and different technologies for the low temperature thermally activated cooling machines. Moreover, the matching with the energy demand of several buildings types, such

as clinics, hotels, supermarkets, and restaurants could be investigated. Finally, we note that the cluster of tools here presented could be used to properly size a distributed energy system, performing complete business case analysis.

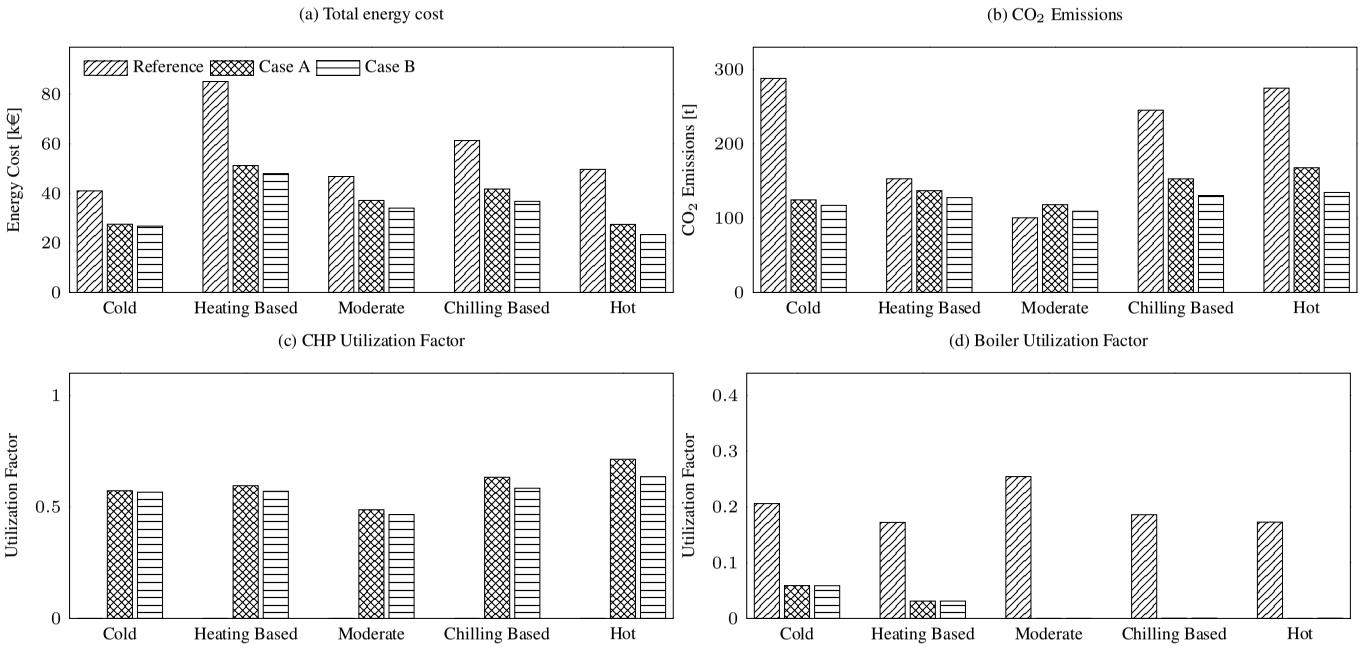

Figure 3.11: *Global performance of the different power plant configurations within the real energy context: (a) total energy cost; (b) CO_2 emissions; (c) CHP utilization factor; (d) Boiler utilization factor.*

Figure 3.12: *Global performance of the different power plant configurations within the mean European energy context: (a) total energy cost; (b) CO_2 emissions; (c) CHP utilization factor; (d) Boiler utilization factor.*

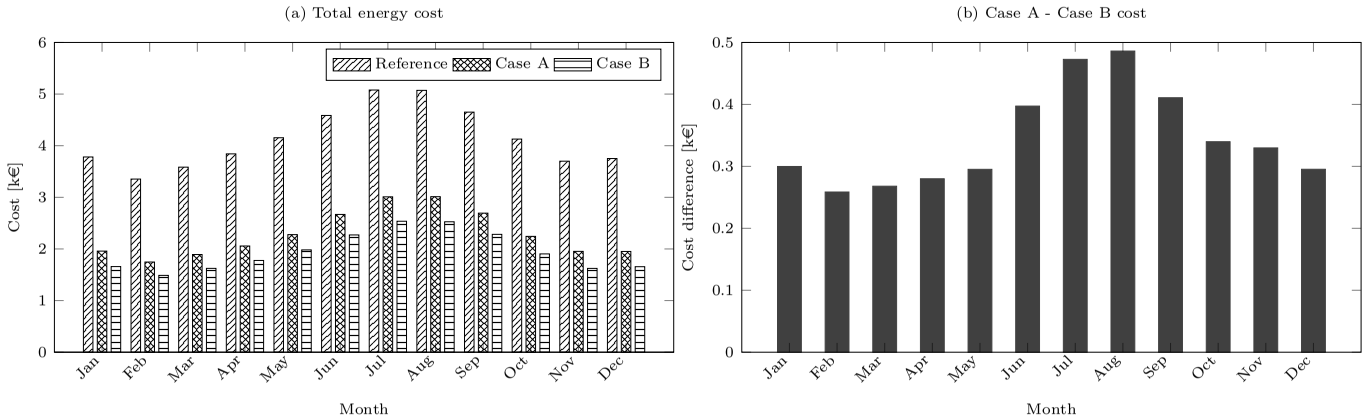

Figure 3.13: *Global performance of the of the different power plant configurations on a monthly basis for the hot climatic condition within the real energy context: (a) total energy cost; (b) total energy cost difference between the FC_ and Case B plant configurations.*

Figure 3.14: *Comparison between the different climatic zones optimization results: (a) real energy context; (b) European mean energy context. The coordinates of the center of the circles represents the cost and the CO_2 emissions reductions. The radius of the circles is proportional to the PBP. The value of the pay back period is also reported in the center of the circles.*

Chapter 4

Comparison of integrated fuel processing options for biogas-fed solid-oxide fuel cell plants

The Solid-oxide fuel cell is a highly efficient prime mover for biogas conversion, but a part of biogas needs to be reformulated externally to facilitate the electrochemical conversion, easy control of reforming conditions, and thermal management of the stack. Carbon deposition and external mineral-carrying water should be avoided to ensure the durability of the fuel processor and stack catalysts. In this chapter we study the conceptual design of the W2W plants. Using the EPFL OSMOSE platform with Aspen Plus as a process flow modeller we have run a sensitivity analysis to the fuel processing operating parameters: (i) the recirculation ratio, (ii) the temperature of the external reformer, (iii) the steam to carbon ratio, and (iv) the carbon dioxide to methane ratio. We have considered practical constraints on carbon deposition, temperature difference, and flow limits to individuate unsafe operating conditions. From the results of the sensitivity analysis, we have evaluated electrical efficiency and external water consumption of the plant. Then, we have individuated reference cases selecting the highest efficiency and the lowest external water consumption between safe operating conditions. For these reference cases we have reported the composition in all the relevant points of the plant. We have performed this analysis considering: (i) hot and cold an-

ode recirculation schemes, (ii) electrolyte- and anode-supported fuel cell, (iii) five different biogas compositions.

Section 4.1 introduces the plant schemes studied. Section 4.2 illustrates the modelling approach. Section 4.2 shows and comments the results from the sensitivity analysis. In Section 4.3 we analyze the results all together and we draw the conclusions of the work.

4.1 Integrated biogas-SOFC cogenerative system

We analyze two fuel processing plant configurations: (i) the hot recirculation scheme (Figure 4.1), and (ii) the cold recirculation scheme (Figure 4.2).

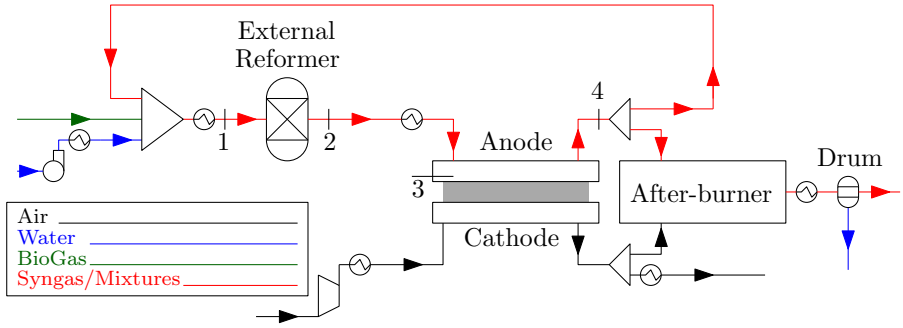

Figure 4.1: *Hot Recirculation plant scheme.*

In the hot recirculation scheme three flows mix together at the beginning of the fuel processing block: (i) purified biogas, (ii) the hot anode exhaust gases recirculated, and (iii) steam additional supply. The mixture reaches the external reformer temeperature (point 1 in Figure 4.1), and then goes in the reactor to produce syngas (point 2 in Figure 4.1). Then, the syngas reaches the anode inlet temperature and goes in the anode. In the anode both the internal reforming and the anode oxidation reactions take place. We ficticiously divide the anode in two reactors to add dimensionality to the native lumped-parameter model. Point 3 in Figure 4.1 represents the outlet of the first fictitious reactor. The anode exhaust (point 4 in Figure 4.1) divides in two parts: the first fraction recirculates to the plant inlet, the second fraction serves as fuel in the after-burner. At the same time, air is heated and enters the cathode where serves as reactant for the cathode reduction reaction. The hot air discharged from

the cathode is divided in two fractions. The first fraction goes to the afterburner and contains the oxygen necessary to burn the anode exhaust in the afterburner. The second fraction is composed of the remaining cathode air exhaust and cools down to 40 °C before flowing out of the plant. Similarly, the after-burner exhaust cools down to 40 °C, then passes in a condensate trap, and finally leave the plant.

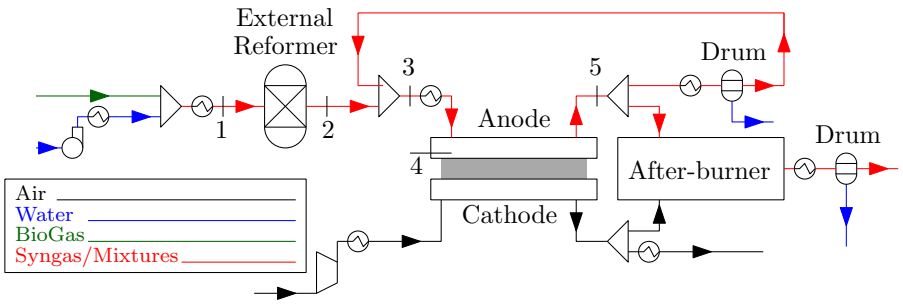

Figure 4.2: *Cold Recirculation plant scheme.*

In the cold recirculation scheme two flows mix together at the inlet of the fuel processing block: purified biogas, and additional steam supply. The mixture heated at the reformer temperature (point 1 in Figure 4.2) reacts to produce syngas (point 2 in Figure 4.2). Such syngas mixes with the anode exhaust recirculated after being cooled to 40 °C and dehumidified. The newly formed mixture (point 3 in Figure 4.2), is heated and enters the anode, where both the internal reformingand the anode oxidation reactions occur. Point 4 in Figure 4.2 has the same meaning of point 3 in Figure 4.1. The anode exhaust (point 5 in Figure 4.2) is divided in two parts: The first fraction cools down to 40 °C passes in a condensate trap, and then flows back to the mixing point after the external reformer. The second fraction is used as fuel in the after-burner. The rest of the plant is equivalent to what described for the hot recirculation scheme.

It is possible to generate hydrogen oxidizing biogas with several reactions [172]:

- partial oxidation: $CH_4 + O_2 \rightarrow CO_2 + 2H_2$; $\Delta h_{298K} = -322$ kJ/mol
- steam reforming: $CH_4 + H_2O \rightarrow 3H_2 + 2CO$; $\Delta h_{298K} = 205$ kJ/mol
- dry methane reforming: $CH_4 + CO_2 \rightarrow 2H_2 + 2CO$; $\Delta h_{298K} = 247$ kJ/mol

Moreover, the water gas shift reaction is an important complementary reaction involving carbon monoxide and water: $CO + H_2O \rightarrow H_2 + CO_2$; $\Delta h_{298K} = -41$ kJ/mol .

We focus on dry methane reforming and steam methane reforming. Dry methane reforming is a good way to exploit the carbon dioxide in the biogas and from the recirculation. Moreover, a fuel processing plant based on dry methane reforming can run without water. Coincidentally, pure water is generally not available in diffused biogas plant, and the purification unit would add energy loss and risks to the operation. However, it is not always possible to have enough carbon dioxyde to produce all the necessary hydrogen. As a consequence, we select the most efficient reforming reaction, that is steam methane refoming, to complement the dry methane reforming when needed. Even operating with complementary steam methane reforming, water self-sufficiency can be reached for some operating conditions, exploiting the water content in the recircualtion flow. Moreover, dry and steam methane reforming reactions result in less moles of CO_2 (when considering also water gas shift reaction) per each H_2 mole produced, when compared to partial oxidation. Finally, endothermic reactors are more likely to be included in the balance of plant of a SOFC system, given the high temperature thermal power available.

To determine the flow rate of the biogas and water feeds introduced from the outside of the plant we implement two different strategies of plant management. The first strategy is necessary to determine the biogas flow rate. Specifically, we define the utilization factor of the fuel as:

$$UFF = \frac{\dot{n}_{H_2}^{\text{reacted}}}{\dot{n}_{H_2,\text{eq}}^{\text{supplied}}}, \tag{4.1}$$

where $\dot{n}_{H_2,\text{eq}}^{\text{supplied}}$ is the equivalent mole flow rate of the hydrogen supplied to anode, and $\dot{n}_{H_2}^{\text{reacted}}$ is the mole flow rate of the hydrogen reacted. The equivalent mole flow rate of the hydrogen supplied to anode is $\dot{n}_{H_2,\text{eq}}^{\text{supplied}} = \dot{n}_{H_2}^{\text{supplied}} + \dot{n}_{CO}^{\text{supplied}}$, where the methane flow rate is negligible at the anode of the fuel cell (Point 3 in Figure 4.1, and point 4 Figure 4.2). We impose a value for the utilization factor. Then, we initialize a first temptative biogas flow rate and we solve the model. If the observed utilization factor of the fuel is higher than the imposed one, the biogas flow rate is increased. Vice versa, if the observed utilization factor is lower than the imposed one, the biogas flow rate is decreased. We iterate this process until convergence on the utilization factor of the fuel.

The second strategy is necessary to determine the external water intake. In detail, we consider the inlet flow before the water addition; that is biogas and anode recirculation for the hot rcirculation scheme, and only biogas for the cold recirculation scheme. We call such flow "pre-mixed". To determine the water intake we consider that the practically relevant reactions for hydrogen production are:

- dry reforming of methane $CH_4 + CO_2 \rightarrow 2H_2 + 2CO$, and
- steam reforming of methane $CH_4 + H_2O \rightarrow 3H_2 + 2CO$.

Therefore, related to the dry reforming of methane reaction we define the carbon dioxide to methane ratio as:

$$R_{CO_2/CH_4} = \frac{\dot{n}_{CO_2}}{\dot{n}_{CH_4}}, \tag{4.2}$$

where $\dot{n}_{CO_2}$ is the mole flow rate of carbon dioxide that react with $\dot{n}_{CH_4}$ mole flow rate of methane. Similarly, related to the steam reforming of methane reaction we define the steam to carbon ratio as:

$$R_{H_2O/CH_4} = \frac{\dot{n}_{H_2O}}{\dot{n}_{CH_4}}, \tag{4.3}$$

where $\dot{n}_{H_2O}$ is the mole flow rate of water consumed for $\dot{n}_{CH_4}$ of methane. Therefore, in the "pre-mixed" flow, we consider that $\dot{n}_{CH_4} = \frac{\dot{n}_{CO_2}}{R_{CO_2/CH_4}}$ mole flow rate of methane react following dry reforming. The residual mole flow rate of methane, if any, will react via steam reforming requiring $\dot{n}_{H_2O} = \frac{\dot{n}_{CH_4}}{R_{H_2O/CH_4}}$ mole flow rate of water. The difference between the required water mole flow rate, and that available in the "pre-mixed" flow, if positive, is the external water intake:

$$\dot{n}^{ext}_{H_2O} = \dot{n}_{H_2O} - \dot{n}^{rec}_{H_2O}, \tag{4.4}$$

The amount of anode exhaust recirculated towards the fuel processing part of the power plant is a key operating parameter. Therefore, we define the recirculation ratio as:

$$R_R = \frac{\dot{n}_{rec}}{\dot{n}_{off-gas}}, \tag{4.5}$$

where $\dot{n}_{rec}$ is the molar flow rate recirculated towards the fuel processing block. $\dot{n}_{off}$ is the anode exhaust molar flow rate, that is point 4 in hot recirculation scheme (Figure 4.1), and point in 5 in cold recirculation scheme (Figure 4.2).

We consider two fuel cell architectures: (i) electrolyte-supported, and (ii) anode-supported. The main operating parameters of the fuel cell stack, such as temperature, utilization factor, and current density, are necessary to build the model. Such operating parameters are different for the two architectures (Table 4.2).

Table 4.1: *Operating parameters for electrolyte-supported, and anode-supported fuel cell stacks.*

Operating parameter	Electrolyte-supported	Anode-supported
Temperature of the stack [°C]	[700-860]	[680-800]
Inlet Temperature at Anode[°C]	750	700
Maximum utilization factor of the fuel	85%	90%
Maximum utilization factor of oxygen	30%	30%
Maximum current density [A/cm^2]	0.33	0.5

4.2 Modelling and assumptions

4.2.1 Numerical model

We model the power plant described in setion 2 through a steady state thermodynamic lumped parameter approach. The modelling environment is Aspen Plus [114], consistently with other analyses available in literature[173–178].

All the reactors in the model are Aspen Plus equilibrium GIBBS elements. As a consequence, we take into account all the possible relevant reactions, such as: (i) dry methane reforming $CH_4 + CO_2 \rightarrow 2H_2 + 2CO$, (ii) steam methane reforming $CH_4 + H_2O \rightarrow 3H_2 + 2CO$, (iii) water gas shift $CO + H_2O \rightarrow H_2 + CO_2$, and its reverse $H_2 + CO_2 \rightarrow CO + H_2O$, (iv) methane cracking $CH_4 \rightarrow 2H_2$+C, (v) Boudouard reaction $2CO \rightarrow CO_2$+C, (vi) methane oxidation $CH_4 + 2O_2 \rightarrow 2H_2O + CO_2$, (vii) hydrogen oxida-

tion H_2+1/2O_2 $\rightarrow$ H_2O, (viii) carbon monoxide methanation $3H_2$+CO $\rightarrow$ CH_4+H_2O, (ix) carbon dioxide methanation $4H_2 + CO_2 \rightarrow CH_4 + 2H_2O$.

Heat exchangers performance are estimated by a mathematically formulated heat cascade calculation. In fact, the results generated in Aspen Plus (e.g., mass flowrates of material flows, temperatures and loads of heat flows) are structured as input for a mixed-integer linear programming (MILP). The MILP problem is designed to close the energy balance minimizing the hot and cold utilities [175, 179–181]. We use AMPL [182] to solve the MILP problem through the CPLEX algorithm [183].

The model for the electrolyte-supported duel cell is based on zero dimensional electrochemistry relations. Specifically, we calculate the thermodynamic potential of the stack according to the Nernst equation [21]:

$$E_{\text{thermo}} = \frac{1}{2F}\left(- \Delta\hat{g}_{\text{rxn}} - RT_{\text{SOFC}} \ln \frac{p_{H_2O}}{p_{H_2} p_{O_2}^{1/2}} \right), \tag{4.6}$$

where F=96485 C/mol is the Faraday constant. $\Delta\ \hat{g}_{\text{rxn}}$ is the diffrence of the mole specific Gibbs free energy between products and reactants of the overall hydrogen oxidation reaction $H_2 + 1/2O_2 \rightarrow H_2O$ at the actual temperature and pressure of the fuel cell. $R = 8.314 J/(molK)$ is the ideal gas constant, and T_{SOFC} is the mean operating temperature of the stack. The partial pressure of hydrogen and water at the anode, and the partial pressure of oxygen at the cathode are p_{H_2}, p_{H_2O} and p_{O_2}, respectively. To introduce dimensionality in this 0-D model, we evaluate the average partial pressure of hydrogen and water between points 2, 3, and 4 for hot recirculation scheme (Figure 4.1), and between points 3, 4, and for cold recirculation scheme (Figure 4.2). Moreover, we evaluate an average partial pressure of oxygen between cathode inlet and outlet. After the Nernst equation has been applied, we use the experimental data on Area Specific Resistance (ASR) to calculate the actual voltage produced from the stack:

$$V = E_{\text{thermo}} - ASR \cdot j, \tag{4.7}$$

where ASR is the area specific resistance extrapolated from measurements, and j is the current density. The electrical power is then calculated as:

$$\dot{W}_{\text{el}} = V \cdot j \cdot A, \tag{4.8}$$

where A is the total surface of the cells in the stack. Moreover, the thermal power is:

$$\dot{W}_{\text{th}} = - \left(\dot{W}_{\text{el}} + \Delta\hat{h}_{\text{rxn}} \dot{n}_{H_2}^{\text{reacted}} + \dot{W}_{\text{th}}^{\text{loss}} \right), \tag{4.9}$$

where $\Delta\hat{h}_{\mathrm{rxn}}$ is the difference of the mole specific enthalpy of reaction for the overall hydrogen oxidation reaction $H_2 + 1/2O_2 \rightarrow H_2O$ at the actual temperature and pressure of the fuel cell. $\dot{W}_{\mathrm{th}}^{\mathrm{loss}}$ is the thermal power lost from the stack and is equal to $\dot{W}_{\mathrm{th}}^{\mathrm{loss}} = 0.06\dot{W}_{\mathrm{el}}$, according to experimental data from anode-supported cell producer. We decide to use anode-supported thermal loss also for the elctrolyte-supported model, because the W2W prototype will be built on anode-supported architecture. Moreover, the influence of thermal losses is only marginal.

The model for the anode-supported fuel cell is based on a phenomenological approach based on experimental data. Specifically, we use experimental data to retrieve V and $\dot{n}_{\mathrm{H_2}}^{\mathrm{reacted}}$, given UFF and j. Electrical and thermal power are then evaluated with Equation 4.8, and Equation 4.9.

The most relevant performance parameter is the electrical efficiency and is evaluated as:

$$\eta_{\mathrm{el}} = \frac{\dot{W}_{\mathrm{el}}^{\mathrm{net}}}{\dot{m}_{\mathrm{CH_4}} \mathrm{LHV}_{\mathrm{CH_4}}}, \tag{4.10}$$

where $\dot{W}_{\mathrm{el}}^{\mathrm{net}}$ is the net electrical power, calculated subtracting the power required from the auxiliaries in the system to the electrical power produced from the fuel cell The power required from the auxiliaries does not consider the cleaning unit consumption. The $\dot{m}_{\mathrm{CH_4}}$ is the mass flow of methane consumed. $\mathrm{LHV}_{\mathrm{CH_4}} = 50$ MJ/kg is the lower heating value of methane.

4.2.2 Practical constraints and operating windows generation

We post-process the results obtained with Aspen Plus to verify several practical constraints: (i) thermal power equilibrium of the fuel cell, (ii) maximum allowable temperature difference in the stack; (iii) carbon deposition, and (iv) maximum and minimum flow rate at the electrodes flow channels. The cases that respect such practical constraints are safe to implement in a real system.

4.2.2.1 Thermal power equilibrium

The net thermal power of the fuel cell has to be zero. In the balance we consider the termal power produced from the fuel cell $\dot{W}_{\mathrm{th}}$, the power required to heat the air and the fuel from the inlet temperature to the stack temperature, and the thermal power required in the internal reformer.

4.2.2.2 Temperature limits

The temperature difference between different zones of the fuel cell cannot be higher than a certain limit. In fact, thermal gradients are directly related to mechanical stress of the fuel cell. Therefore, we identify a limit in the difference between the inlet temperature of the gases to the electrodes flow channels, and the mean stack operating temperature. Such a limit is 120 °C for the anode-supported fuel cell, and 210 °C for the electolyte-supported fuel cell. The robustness of the electolyte-supported structure results in the higher allowable temperature difference.

4.2.2.3 Carbon deposition

Carbon deposition depends on the chemical composition, pressure, and temperature of a gas mixture. Several experimental thermodynamic data and theorethical analysis are available for various crystallographic forms of carbon [139, 184, 185]. Moreover, Jaworski et al. [139] developed a thermodynamic equilibrium analysis of carbon deposition from C-H-O mixtures including carbon nanotubes formation. The limits on maximum allowable carbon volume fraction found in the latter study are between the most conservative. For this reason, we consider such limits in our operating windows analysis. Practically, for every case we compute the C-H-O molar fractions of the syngas all along the power plant. Then, we use the C-H-O molar fractions to find the position in the ternary plot. Finally, we verify wether the syngas composition is outside of the carbon deposition region (Figure 4.3).

In this procedure, we ignore the nitrogen content in the syngas. In fact, the nitrogen content in the syngas is only between 3% and 10% of the volume (Table 4.3 and Table 4.4). Moreover, such an assumption is conservative because considering the nitrogen would result in a lower carbon fraction, and finally less risk of carbon deposition.

4.2.2.4 Flow limits

The flow rate in the electrodes flow channels has not to be too high, to avoid unreasonable pressure drops, neither too low to avoid fuel cell reactants starvation. The the air flowing in the the cathode flow channels, and the fuel flowing in the anode flow channels has to be between 18 $\mathrm{sccm/cm^2}$ and 80 $\mathrm{sccm/cm^2}$, for both the fuel cell architectures.

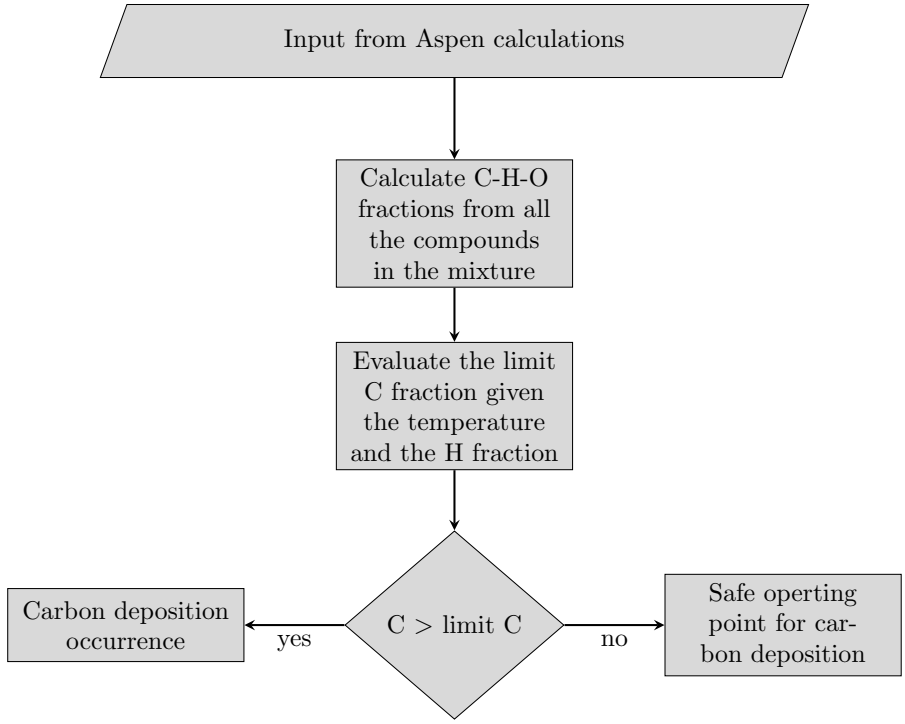

Figure 4.3: *Carbon deposition post-processing work-flow.*

4.2.3 Operating parameters and biogas compositions

We assume several operating parameters to perform the calculations. The operating parameters divides in two groups: (i) those related to the fuel cell, and (ii) those related to the fuel processing. Moreover, we assume several typical compositions for biogas.

4.2.3.1 Fuel cell operation

In this study we assume nominal operating parameters related to the fuel cell operation. Such parameters are: (i) the pressure of the system p_{SOFC}, (ii) the mean operating temperature of the stack T_{SOFC}, (iii) the utilization factor of hydrogen UFF, (iv) the current density j, (v) the utilization factor of the oxygen at the cathode UFO, and (vi) the temperature of the after-burner T_{AB}. We assume different nominal operating parameters for the two different fuel cell architectures (Table 4.2).

The temperature of the after-burner is 40 °C higher than the stack temperature. The gas inlet temperature to the anode has the values reported

Table 4.2: *Assumed nominal operating parameters related to the fuel cell operation.*

	Electrolyte-supported	Anode-supported
p_{SOFC} [bar]	1.2	1.2
T_{SOFC}[°C]	860	800
UFF	0.85%	0.85%
j [A/cm^2]	0.235	0.4
UFO	0.1	0.1
T_{AB}[°C]	900	840

in Table 4.2. The air inlet temperature to the cathode is not fixed but varies to guarantee the thermal management of the fuel cell. However, the range of variation is constrained by the maximum allowable temperature difference.

4.2.3.2 Fuel processing operation

The sensitivity analysis is focused on the operating parameters related to fuel processing. Such parameters, and the corresponding range of variation are:

- the recirculation ratio R_R, [0.1, 0.3, 0.5, 0.7, 0.9]
- the temperature of the external reformer $T_{\mathrm{REF}}^{\mathrm{ext}}$ [°C], [300, 500, 700, 800, T_{SOFC}]
- the steam to carbon ratio $R_{\mathrm{H_2O/CH_4}}$, [2, 3, 4, 5]
- the carbon dioxide to methane ratio $R_{\mathrm{CO_2/CH_4}}$, [0.5, 1, 3, 5]

The stoichiometric value of the $R_{\mathrm{CO_2/CH_4}}$ is 1, but we explore the range between 0.5 and 5 to assess the effects on carbon deposition and reaction performance [172, 186, 187]. Similarly, the stoichiometric value of the $R_{\mathrm{H_2O/CH_4}}$ is 1 when considering only the steam methane reforming, and 2 when considering also the coupled water gas shift, but we explore a range between 2 and 5 [172, 186, 187].

4.2.3.3 Biogas composition

The biomass type and digestor type determine the biogas bulk composition. According to WP1 results, we consider three different biomass types: (i) agricultural (manure) biomass, (ii) Organic Fraction of Municipal Solid Waste (OFMSW), and (iii) landfill biomass. Every biomass type results in a different biogas bulk composition (Table 4.3).

Table 4.3: *Biogas bulk composition for relevant biomass types.*

Biomass type	Acronym	CH_4 %vol.	CO_2 %vol.	N_2 %vol.	O_2 %vol.
Agricultural	Biogas 1	57	37	4.74	1.26
OFMSW	Biogas 2	58	38	3.16	0.84
Landfill	Biogas 3	53	35	9.48	2.52

Moreover, the biogas composition can vary consequently to biomass quality fluctuations, transient regimes, and cleaning techniques. Therefore, we also consider two extreme cases by spanning the maximum and minimum observed methane and carbon dioxide fractions: (i) minimum CH_4 %vol. and maximum CO_2 %vol., and (ii) maximum CH_4 %vol. and minimum CO_2 %vol. (Table 4.4).

Table 4.4: *Biogas extreme compositions.*

Biomass type	Acronym	CH_4 %vol.	CO_2 %vol.	N_2 %vol.	O_2 %vol.
Extreme 1	Biogas 4	50	45	3.95	1.05
Extreme 2	Biogas 5	70	25	3.95	1.05

In order to include the unsteady nature of biogas in the sensitivity analysis, we select and analyze biogas 1, biogas 4, and biogas 5 compositions. Biogas 1 is representative of all the three typical biomass sources in Table 3. In fact, the volume fraction of every bulk component of biogas 1 is between those of biogas 2 and 3, with a difference always lower than 5 %. Moreover, it is important to include biogas 4 and biogas 5 as limiting compositions that could affect the plant operation and performance.

4.3 Results

We present the results of the sensitivity analysis for the plants based on electrolyte-supported and anode-supported fuel cells in section 4.3.1, and section 4.3.2 respectively.

4.3.1 Electrolyte-supported fuel cell plant

Section 4.3.1.1 presents the results of the sensitivity analysis for the plant based on electrolyte-supported fuel cell separately for hot recirculation, while section 4.3.1.1 those for cold recirculation.

4.3.1.1 Hot recirculation scheme

In this section, we analyse the results of the hot recirculation scheme reporting the efficiency variation as a function of the sensitivity analysis operating parameter (recirculation ratio R_R, temperature of the external reformer $T^{\text{ext}}_{\text{REF}}$, steam to carbon ratio $R_{\text{H}_2\text{O}/\text{CH}_4}$, and carbon dioxide to methane ratio $R_{\text{CO}_2/\text{CH}_4}$) for biogas 1, 4, and 5 (Figure 4.4, 4.6, and 4.8 respectively). We also report the external water consumption as a function of the sensitivity analysis operating parameter for biogas 1, 4, and 5 (Figure 4.5, 4.7, and 4.9 respectively).

Every box in the following figures represents a case of the sensitivity analysis, resulting from a combination of the four sensitivity analysis operating parameter. White boxes represent cases that do not respect the practical constraints (see section 4.2.2). The letters in the middle of the white boxes represent the constraint not respected: TH stands for thermal power equilibrium, T stands for the temperature limit, C stands for the carbon deposition limit, and F stands for the flow limit. The colored boxes represent safe cases. The color shade represents the value of the electrical efficiency for Figures 4.4, 4.6, and 4.8, and of the external water consumption for Figures 4.5, 4.7, and 4.9. The value of the electrical efficiency or of the external water consumption is also numerically reported in the middle of each box representing safe cases.

The Figures represent the data with two x-axes and two y-axes. The outer x-axis is in red at the top of the figures and represents the carbon dioxide to methane ratio $R_{\text{CO}_2/\text{CH}_4}$. The inner x-axis is in black at the bottom of the figures and represents the recirculation ratio R_R. For every value of the $R_{\text{CO}_2/\text{CH}_4}$ axis the inner R_R spans over all the variation

dominion [0.1, 0.3, 0.5, 0.7, 0.9]. The outer y-axis is in red at the right of the figures and represents the steam to carbon ratio $R_{\mathrm{H_2O/CH_4}}$. The inner y-axis is in black at the left of the figures and represents the temperature of the external reformer $T_{\mathrm{REF}}^{\mathrm{ext}}$. For every value of the $R_{\mathrm{H_2O/CH_4}}$ axis the inner $T_{\mathrm{REF}}^{\mathrm{ext}}$ spans over all the variation dominion [300, 500, 700, 800, 860].

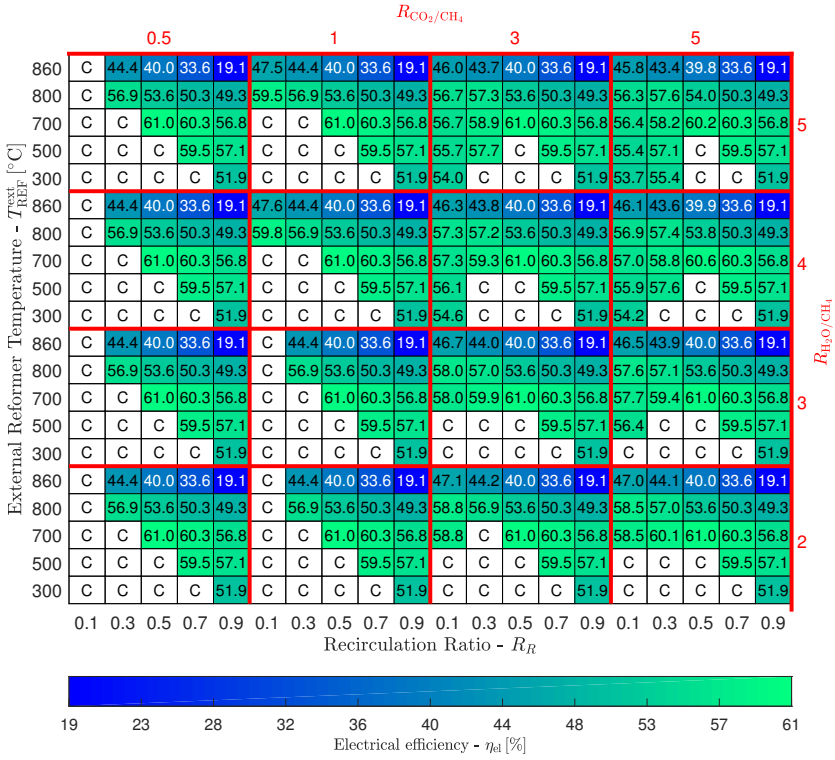

Figure 4.4: *Efficiency raster plot for hot recirculation case of the electrolyte-supported scheme with biogas 1. The figure shows feasible domain and electrical efficiency.*

Biogas 1 For biogas 1, overall 272 cases on the 400 analysed respect the practical constraints (Figure 4.4). In fact, 128 cases do not respect the constraints on carbon deposition. Unsafe operating points are concentrated towards low external reformer temperature, low recirculation ratio, low carbon dioxide to methane ratio, and low steam to carbon ratio. A lower temperature in the external reformer means that the limit carbon

faction that leads to carbon deposition is lower. Moreover, the carbon fraction in a typical recirculate flow (50 % H_2O, 40 % CO_2, 5 % H_2, and 5 % CO, Figure 4.10) is 15.5%. However, the carbon fraction in biogas 1 is 23.6 %. Therefore, operating with high recirculation ratio decreases the overall carbon fraction and the associated carbon deposition occurrence. Moreover, increasing the carbon dioxide to methane ratio implies that more carbon dioxide is needed for every mole of methane. Therefore, more water is necessary to complement dry reforming with steam reforming, according to plant management strategies (Section 4.1). The addition of water reduces the carbon deposition risk, by decreasing the carbon fraction. For the same reason, increasing the steam to carbon ratio decreases the carbon deposition risk. However, the steam to carbon ratio is a sensitive parameter only if there is external water supply, i.e. at high carbon dioxide to methane ratios. In fact, at high R_{CO_2/CH_4} and R_{H_2O/CH_4}, external water mixes with the biogas at low recirculation ratios (Figure 4.5), according to the plant management strategies (Section 4.1). Therefore, some safe cases exist also at low recirculation ratios, as a result of the carbon fraction dilution by water. For example, at $R_{CO_2/CH_4} = 5$, $R_{H_2O/CH_4} = 5$, and $T_{REF}^{ext} = 500\,°C$, the recirculation ratio of 0.3 is safe because in that case 0.9 sccm/cm^2 of external water are consumed. However, with the same condition the recirculation ratio of 0.5 is not carbon deposition safe, because the plant management strategy determines that no external water is necessary in that case, and the resulting carbon fraction is higher than the limit.

Electrical efficiency varies between 19.1% and 61.0% (Figure 4.4) and is reciprocally correlated to external reformer temperature and to recirculation ratio. For the external reformer temperatures of 300,°C and 500,°C, the highest efficiency is always reached with recirculation ratio equal to 0.7. When the temperature of the external reformer is 700,°C the highest efficiency is obtained with 0.5 recirculation ratio. For external reformer temperature of 800,°C and 860,°C, the recirculation ratio that guarantees the highest efficiency is between 0.1 and 0.3. To explain these trends, we must consider that increasing the recirculation ratio increases the recovered unused fuel. However, the recirculate flow is composed approximately of 50% H_2O, 40 % CO_2, 5 % H_2, and 5 % CO (Figure 4.10). Therefore, the recirculation flow dilutes the hydrogen fraction entering the fuel cell, especially when the external reforming ratio is high. The hydrogen fraction at the fuel cell inlet influences in turn the reversible voltage predicted

through Nernst equation (Equation (4.6)). We start by considering the case with 700,°C external reformer temperature that is in the middle of the analysed domain, and that guarantees the highest efficiency. In this case, the external reformer ratio is between 60% and 90%. Therefore, the 0.5 recirculation ratio appears as the best trade-off between the recovery of unused fuel, and the hydrogen dilution. The external reformer ratio is between 0% and 5% at 300,°C external reformer temperature, and between 30% and 50% at 500,°C. Therefore, in these cases the hydrogen dilution is less relevant than unused fuel recovery, and the 0.7 recirculation ratio appears as the best trade-off. For $T_{\mathrm{REF}}^{\mathrm{ext}}$ of 800,°C and 860,°C, the need of high temperature thermal power to heat the reactants up to the external reformer temperature becomes a relevant factor for performance, together with unused fuel recovery and hydrogen dilution. The required thermal power increases by increasing the recirculation ratio as a consequence of the increase of the mass flow rate entering the external reformer[1]. Moreover, the fuel available to the after-burner decreases by increasing the recirculation ratio. Therefore, the only source of thermal power inside the plant with a temperature high enough to sustain the thermal needs of the external reformer decreases by increasing the recirculation ratio. Considering all these facts together, we conclude that for $T_{\mathrm{REF}}^{\mathrm{ext}}$ of 800,°C and 860,°C electrical heating is necessary to fulfil the thermal needs of the external reformer. The amount of electrical heating increases by increasing R_R. Therefore, a recirculation ratio between 0.1 and 0.3 appears as the best trade-off for external reformer temperatures of 800,°C and 860,°C. Finally, we note that carbon dioxide to methane and steam to carbon ratios marginally affect the efficiency.

External water consumption varies between 0 sccm/cm^2 and 1.66 sccm/cm^2 (Figure 4.5). The hot recirculating flow carries the water produced in the anode oxidation reaction, making the plant almost always water self-sufficient. In fact, 70% of the safe cases have zero external water consumption. External water consumption decreases with increasing recirculation ratio. Water consumption increases with both the carbon dioxide to methane ratio and the steam to carbon ratio, as a consequence of the plant management strategy implemented to determine the external water

[1]In fact, the recirculate flow cannot provide methane to produce the required hydrogen. Therefore, the biogas flow rate is almost independent from the recirculation ratio. Consequently, with a higher recirculation ratio almost the same biogas flow rate sums to a higher recirculation flow rate.

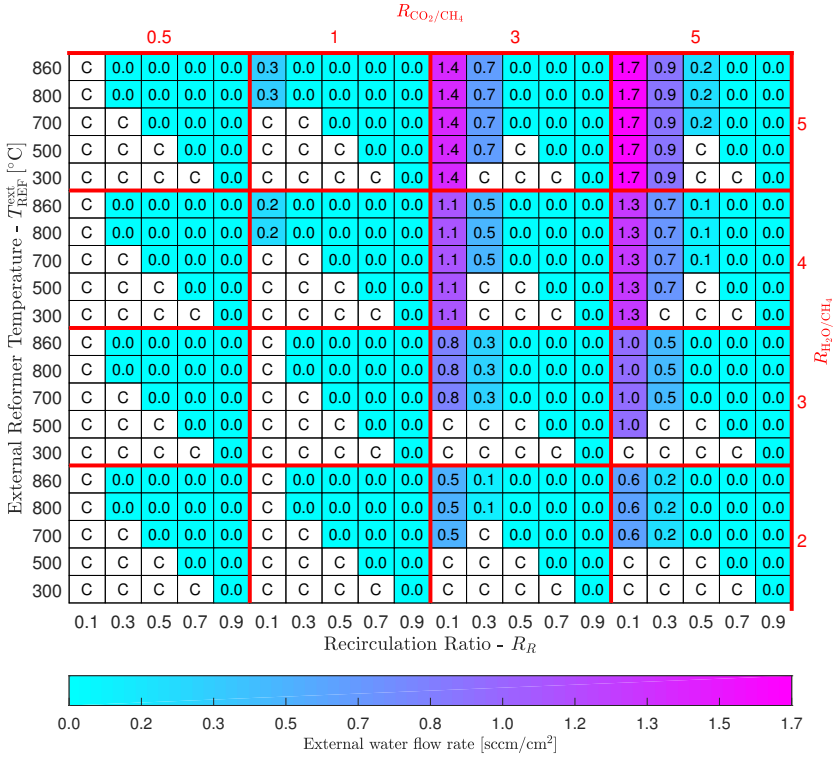

Figure 4.5: *Water consumption raster plot for hot recirculation case of the electrolyte-supported scheme with biogas 1. The figure shows the feasible domain and the water consumption.*

intake (see section4.1). External reformer temperature does not influence the water consumption.

Biogas 4 (extreme case 50% vol. CH_4**, 45**% vol. CO_2**)** Considering biogas 4, overall 263 cases on the 400 analysed respect the constraints (Figure 4.6). In fact, 137 cases do not respect the constraints on carbon deposition. The high 45% CO_2 fraction in biogas 4 results in less safe cases than those registered for operation on biogas 1. In fact, when more carbon dioxide is available as a reactant, external water supply is required in less cases and in a lower amount, according to the plant management strategies. Less, or absent external water supply means less carbon dilution and therefore increased carbon deposition risk. In fact, all the cases

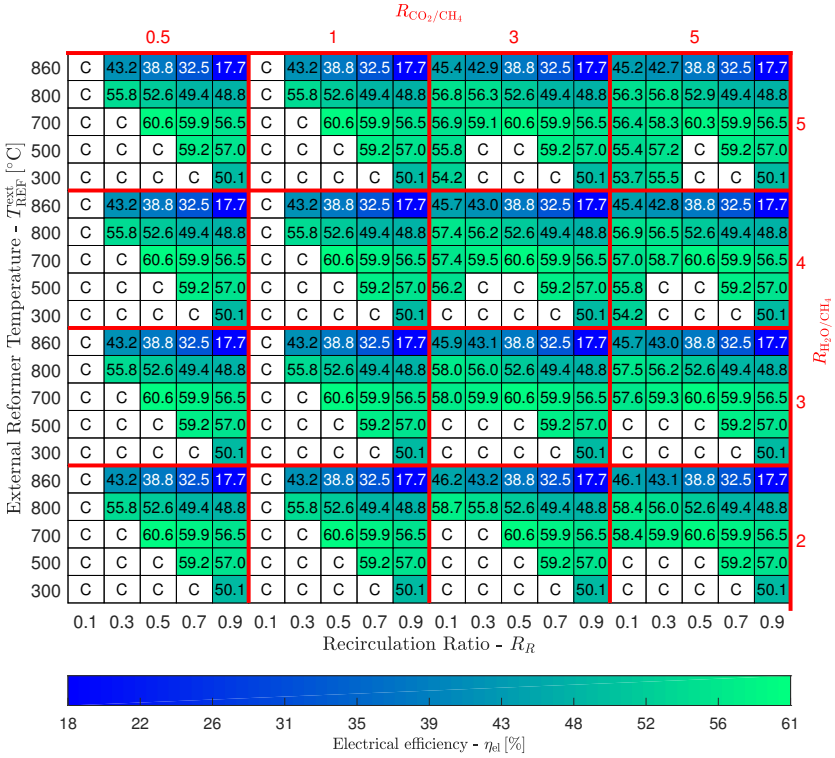

Figure 4.6: *Efficiency raster plot for hot recirculation case of the electrolyte-supported scheme with biogas 4. The figure shows feasible domain and electrical efficiency.*

carbon deposition prone for biogas 4 operation and safe for biogas 1 operation have external water consumption different from zero in biogas 1 operation.

Electrical efficiency varies between 17.7% and 60.6% Figure 4.6). The same trends concerning external reformer temperature, recirculation ratio, carbon dioxide to methane ratio, and steam to carbon ratio highlighted for biogas 1 also apply in this case. The minimum efficiency reached with biogas 4 is 8% lower than the minimum efficiency reached with biogas 1; while, the maximum efficiency reached with biogas 4 is only 1% lower than the maximum efficiency reached with biogas 1. In fact, the high 45% CO_2 fraction in the biogas makes the system running more on the less efficient dry reforming rather than on the more efficient steam reforming.

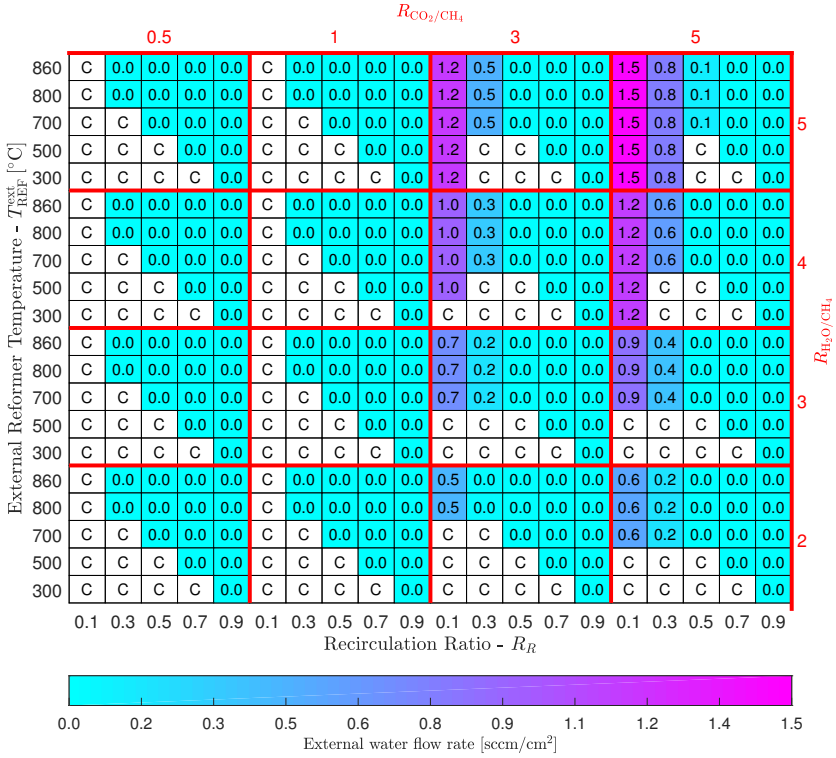

Figure 4.7: *Water consumption raster plot for hot recirculation case of the electrolyte-supported scheme with biogas 4. The figure shows the feasible domain and the water consumption.*

External water consumption varies between 0 sccm/cm^2 and 1.54 sccm/cm^2 (Figure 4.7), with the same pattern already evidence for biogas 1. The high 45% CO_2 fraction in the feeding biogas drives the fuel processing plant to run more on dry reforming, than on steam reforming. Therefore, 81 % of the safe cases are self-sufficient in water.

Biogas 5 (extreme case 70% vol. CH_4**, 25**% vol. CO_2**)** Considering biogas 5, overall 292 cases on the 400 analysed respect the constraints (Figure 4.8). In fact, 108 cases do not respect the constraints on carbon deposition. The high rate of safe cases is due to the low 25% fraction of carbon dioxide in the biogas. In fact, when less carbon dioxide is available as a reactant, external water supply is required in more cases and

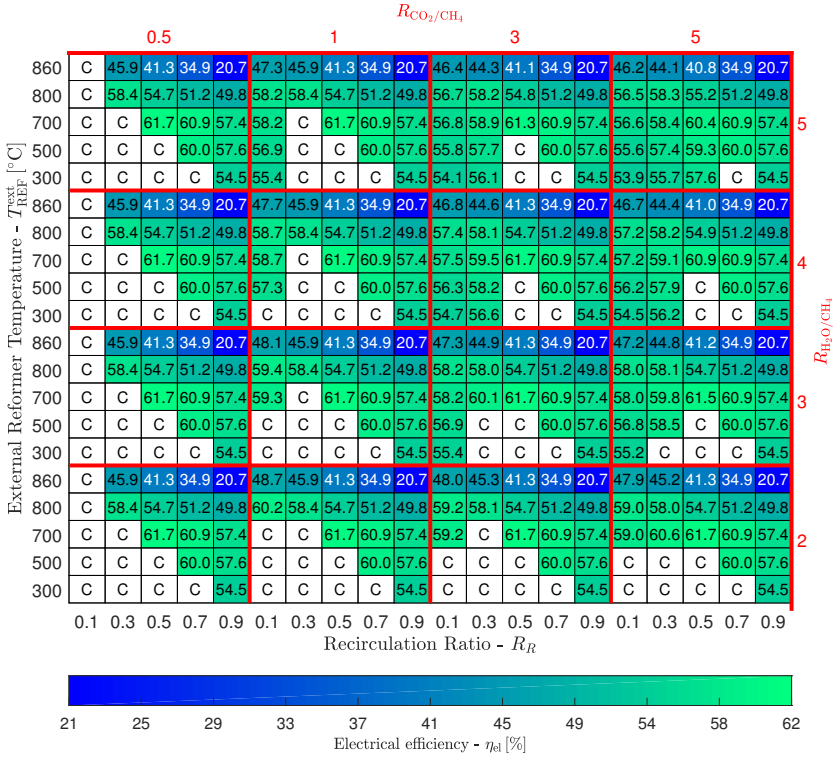

Figure 4.8: *Efficiency raster plot for hot recirculation case of the electrolyte-supported scheme with biogas 5. The figure shows feasible domain and electrical efficiency.*

in a higher amount, according to the plant management strategies. More external water supply means more carbon dilution and therefore reduced carbon deposition risk.

Electrical efficiency varies between 20.7% and 61.7% (Figure 4.8). The minimum efficiency reached with biogas 5 is 8% higher than the minimum efficiency reached with biogas 1. Similarly, the maximum efficiency reached with biogas 5 is 1% higher than the maximum efficiency reached with biogas 1. In fact, the low 25% CO_2 fraction in the biogas makes the system running more on the more efficient steam reforming rather than on the less efficient dry reforming. Moreover, operating with steam reforming each mole of methane produces 3 moles of hydrogen, while with dry reforming each mole of methane produces 2 moles of hydrogen. As

a consequence, the hydrogen is more concentrated on a syngas produced mainly from steam reforming (see also Figure 4.10), with benefits on the cell voltage , and therefore on the efficiency.

The same trends concerning external reformer temperature, recirculation ratio, carbon dioxide to methane ratio, and steam to carbon ratio highlighted for biogas 1 and 4 also apply in this case. Therefore, we can state as a general property of the hot recirculation plant that the optimal recirculation ratio decreases from 0.7 to 0.1 as the external reformer temperature increases from 300 °C to 860 °C. Moreover, carbon dioxide to methane and steam to carbon ratios do not practically affect the efficiency.

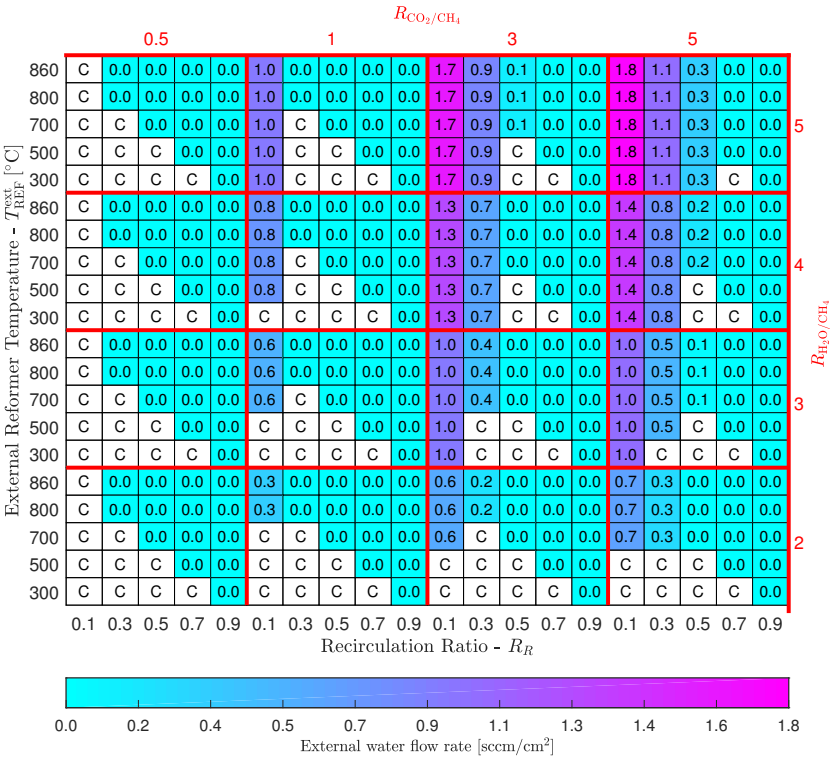

Figure 4.9: *Water consumption raster plot for hot recirculation case of the electrolyte-supported scheme with biogas 5. The figure shows the feasible domain and the water consumption.*

External water consumption varies between 0 sccm/cm^2 and 1.79 sccm/cm^2 (Figure 4.9), with the same pattern already evidenced for biogas 1 and 4.

Therefore, we can state as general evidence for the hot recirculation power plant that external water consumption: (i) decreases with increasing recirculation ratio; (ii) increases with increasing both the carbon dioxide to methane ratio and the steam to carbon ratio; and (iii) it is not influenced from the external reformer temperature. The percentage of the self-sufficient in water and safe cases is 67 %. In fact, the low 25% CO_2 fraction in the biogas makes the fuel processing plant relying more on steam reforming. Therefore, in many cases the water present in the recirculation is not enough to feed the reformer.

Comparison and discussion For all the biogas analysed, the only pratical constraint that is not always satisfied is that on the carbon deposition. In fact, the oculated choice of operating parameters makes the plant operation safe in terms of thermal gradients and flow conditions.

For each biogas composition, we select as reference the most efficient between the zero water consumption configurations (Table 4.5).

Table 4.5: *Operating parameters of the reference cases for the different biogas compositions considered for hot recirculation scheme with electrolyte-supported fuel cell.*

	Biogas 1	Biogas 4	Biogas 5
R_R	0.5	0.5	0.5
$T^{\text{ext}}_{\text{REF}}$ [°C]	700	700	700
$R_{\text{H}_2\text{O}/\text{CH}_4}$	2	2	2
$R_{\text{CO}_2/\text{CH}_4}$	0.5	0.5	0.5
η_{el} [%]	61.0	60.6	61.7
Cell voltage [V]	0.769	0.765	0.775

The optimal operating conditions are the same for all the three biogas compositions considered: i) external reforming temperature of 700 °C, ii) steam to carbon ratio 2, iii) carbon dioxide to methane ratio 0.5, and iv) recirculation ratio 0.5. The optimal $R_{\text{H}_2\text{O}/\text{CH}_4}$ and $R_{\text{CO}_2/\text{CH}_4}$ are the lowest explored in the sensitivity analysis, suggesting that the efficiency is higher when the amount of surplus reactants is minimized. However, we note that the variation of the efficiency for higher carbon dioxide to methane and steam to carbon ratios is over the third significant figure.

Moreover, we report the variation of the composition of the syngas for the three reference configurations along the CHP plant (Figure 4.10).

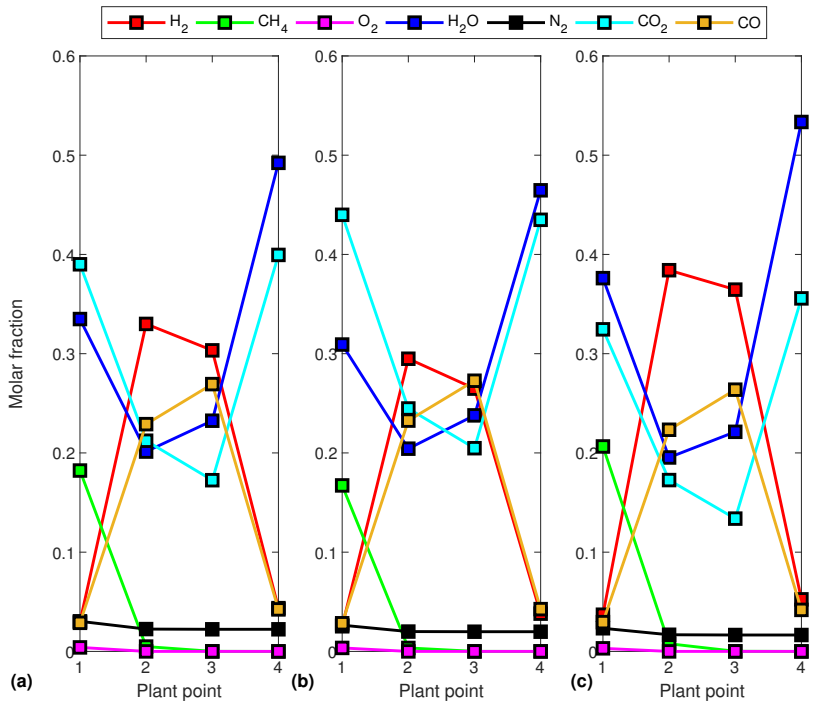

Figure 4.10: *Syngas compositions as a function of the plant points for hot recirculation scheme with electrolyte-supported fuel cell. Subplots (a), (b), and (c) represent biogas 1, 4, and 5 respectively. See the appendix for a table version of the figure.*

Molar fraction profiles for biogas 1, 4, and 5 are similar. Inside the external reformer (between points 1 and 2) the methane fraction drops because of the steam and dry methane reforming reactions, as evidenced also from the drop in water and carbon dioxide fractions. At the same time, hydrogen and carbon monoxide fractions rise, being produced from the reforming reactions. The low initial oxygen fraction goes to zero, after a certain extent of methane oxidation. In the internal reformer the most relevant reaction is the reverse water gas shift. In fact, the CO_2 and H_2 fractions decrease, while carbon monoxide and water fractions increase. Finally, in the fuel cell both the hydrogen oxidation, and the water gas shift reactions take place. In fact, both the CO and H_2 fractions decrease.

The different biogas compositions influence the absolute value of molar fractions. In fact, the H_2, CH_4, H_2O, CO_2, and CO fraction are for biogas 1 in point 1: 3%, 18%, 33%, 39%, and 3% respectively. For biogas 4 the same values are: 3%, 17%, 31%, 44%, and 3%. For biogas 5 the same values are: 4%, 21%, 38%, 32%, and 3%.

Moreover, the peak hydrogen fraction is 38% for biogas 5 operation, while it is around 33% for biogas 1 and 29% for biogas 4. In fact, the low 25% CO_2 fraction in the biogas 5 makes the system running more on steam reforming, that produces 3 moles of hydrogen per each methane mole, rather than on dry reforming, that produces 2 moles of hydrogen per each methane mole. Increasing the hydrogen fraction also increases the Nernst voltage, and therefore the efficiency.

4.3.1.2 Cold recirculation scheme

In this section, we analyse the results of the cold recirculation scheme reporting the efficiency variation as a function of the sensitivity analysis operating parameter for biogas 1, 4, and 5 (Figures 4.11, 4.13, and 4.15 respectively). We also report the external water consumption as a function of the sensitivity analysis operating parameter for biogas 1, 4, and 5 (Figures 4.12, 4.14, and 4.16 respectively).

Biogas 1 Considering biogas 1, overall 210 cases on the 400 analysed respect the practical constraints (Figure 4.11). In fact, 190 cases do not respect the constraints on carbon deposition. The unsafe operating points are concentrated towards low external reformer temperature, low carbon dioxide to methane ratio, and low steam to carbon ratio. The recirculation ratio does not strongly correlate to operating windows.

The hot recirculation plant fed with biogas 1 results in 272 safe cases. Therefore, the cold recirculation scheme is more prone to carbon deposition in the external reformer. In fact, such reactor experiences a higher carbon fraction because it is before the injection of the recirculated flow. Moreover, the pattern of unsafe cases changes by changing the recirculation scheme. In fact, the cold recirculation scheme does not have any safe case for a carbon dioxide to methane ratio of 0.5.

Electrical efficiency varies between 36.0% and 62.6% and is correlated to all the sensitivity analysis operating parameter (Figure 4.11). For external reformer temperature between 300°C and 700°C the optimal recir-

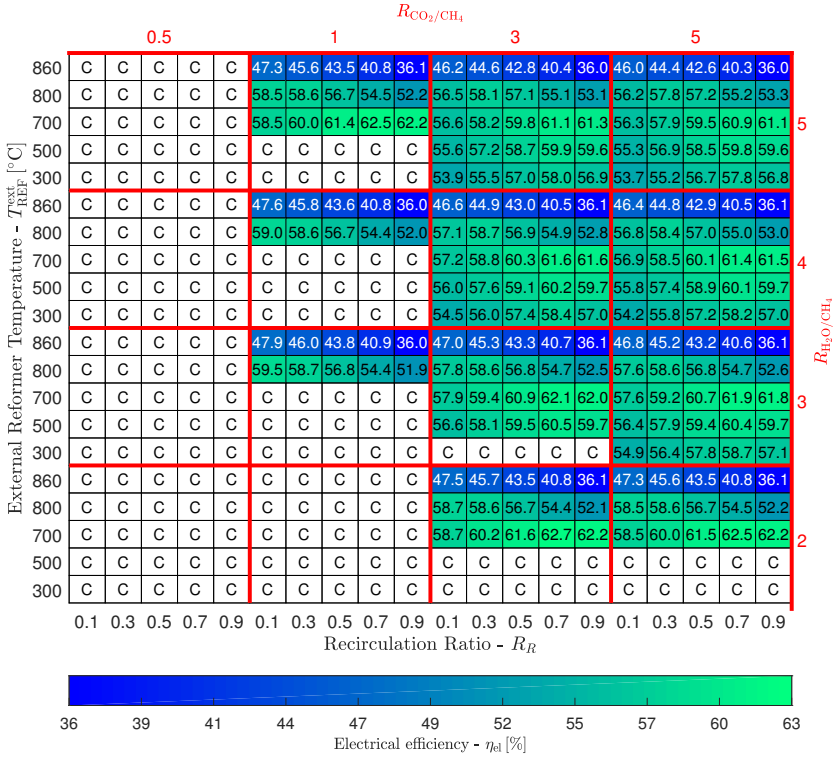

Figure 4.11: *Efficiency raster plot for cold recirculation case of the electrolyte-supported scheme with biogas 1. The figure shows feasible domain and electrical efficiency.*

culation ratio is between 0.7 and 0.9. For external reformer temperature between 800°C and 860°C the optimal recirculation ratio is between 0.1 and 0.3. These trends are similar to those evidenced for hot recirculation scheme. However, for cold recirculation scheme the hydrogen fraction in the recirculation is on average 15 %, considering the dehydration after the compositions reported in Figure 4.17. Therefore, the hydrogen dilution is less relevant, and the optimal recirculation ratio is in some cases 0.9. Moreover, for this cold recirculation scheme the efficiency is higher at low carbon dioxide to methane ratio and at low steam to carbon ratio. In this case, the steam to carbon ratio and the carbon dioxide to methane ratio are sensitive parameters. In fact, the recirculation flow adds to the syngas stream after the external reformer and cannot provide reactants to the

external reformer, according to the plant management strategies.

The maximum efficiency of the cold recirculation scheme fed with biogas 1 is 3 % higher than the maximum efficiency of the hot recirculation scheme with same feeding. Moreover, the efficiency of the safe cases for the cold recirculation scheme is higher than the efficiency of the safe cases for the hot recirculation scheme also on average. In fact, the difference between the highest and lowest efficiency is 74% for the cold recirculation scheme, while it is 219% for the hot recirculation case. The higher electrical efficiency of the cold recirculation scheme originates from the higher reliance on steam methane reforming rather than on dry methane reforming. In fact, according to the plant management strategies the only carbon dioxide available for dry reforming is that in the biogas itself, given that the recirculation flow adds to the syngas stream after the external reformer. The steam reforming reaction is more efficient than dry reforming on the hydrogen production itself. However, using steam reforming in place of dry reforming also improves the fuel cell efficiency, by increasing the cell voltage as a consequence of the higher hydrogen fraction. The hydrogen fractions in Figure 4.10 and Figure 4.17 cannot be compared, because fuel processing operating parameters of the represented reference cases are different.

External water consumption varies between 0.43 sccm/cm^2 and 2.0 sccm/cm^2 (Figure 4.12). The water self-sufficiency of the power plant is never reached. In fact, the cold and dehydrated recirculating flow carries almost no water and is added after the external reformer. External water consumption decreases with increasing recirculation ratio. Water consumption increases with both the carbon dioxide to methane ratio and the steam to carbon ratio, because of the plant external water management strategy. External reformer temperature does not influence the water consumption.

Biogas 4 (extreme case 50% vol. CH_4**, 45**% vol. CO_2**)** Considering biogas 4, overall 160 cases on the 400 analysed respect the constraints (Figure 4.13). In fact, 240 cases do not respect the constraints on carbon deposition. Therefore, 60% of the analysed cases are prone to carbon deposition, because of the high 45% CO_2 fraction in biogas 4. The number of safe cases for the cold recirculation scheme with biogas 4 is 64% lower than the equivalent for hot recirculation scheme.

Efficiency varies between 34.8% and 62.2% (Figure 4.13). The same

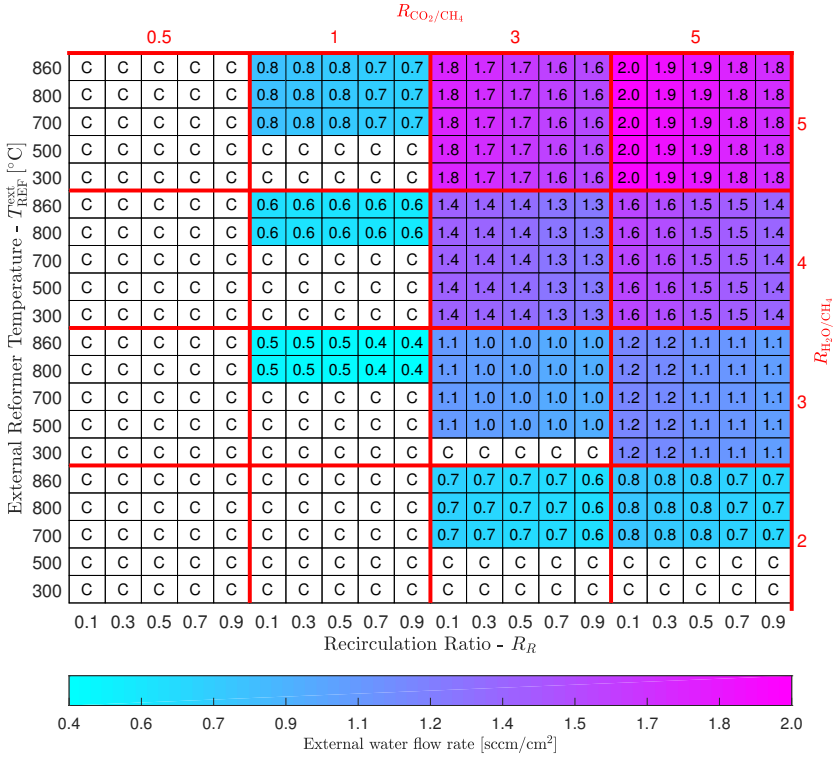

Figure 4.12: *Water consumption raster plot for cold recirculation case of the electrolyte-supported scheme with biogas 1. The figure shows the feasible domain and the water consumption.*

trends concerning external reformer temperature, recirculation ratio, carbon dioxide to methane ratio, and steam to carbon ratio highlighted for biogas 1 also apply in this case. The minimum efficiency reached with biogas 4 is 3 % lower than the minimum efficiency reached with biogas 1. Similarly, the maximum efficiency reached with biogas 4 is 1 % lower than the maximum efficiency reached with biogas 1.

External water consumption varies between 0.57 sccm/cm^2 and 1.89 sccm/cm^2 (Figure 4.14), with the same pattern already evidenced for biogas 1. The maximum water consumption reached with biogas 4 is 6 % lower than the maximum water consumption reached with biogas 1. In fact, the high 45% CO_2 fraction in the feeding biogas drives the fuel processing plant to run more on dry reforming than on steam reforming.

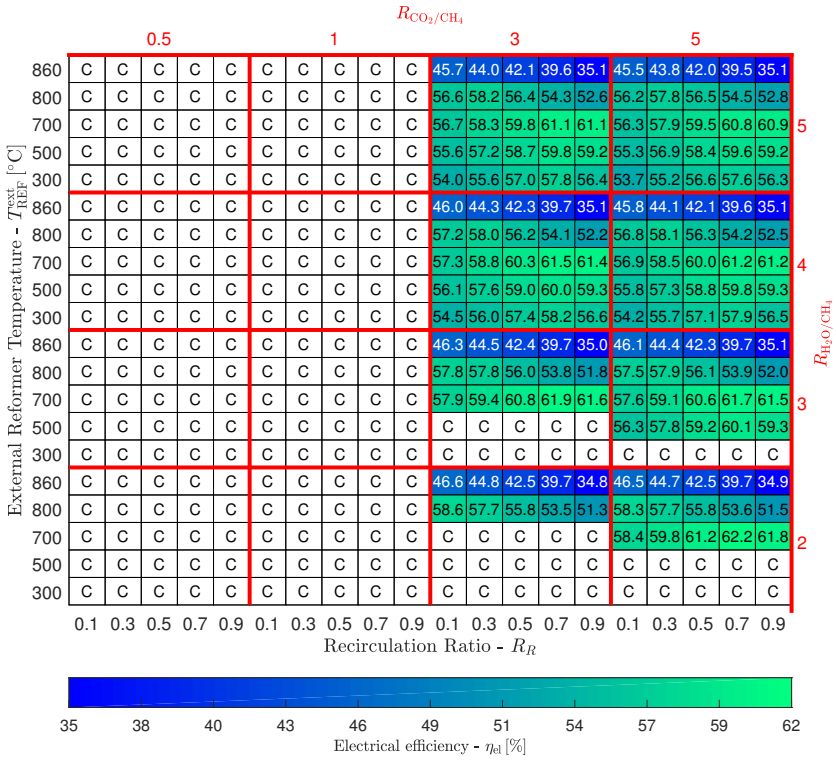

Figure 4.13: *Efficiency raster plot for cold recirculation case of the electrolyte-supported scheme with biogas 4. The figure shows feasible domain and electrical efficiency.*

Biogas 5 (extreme case 70% vol. CH_4**, 25**% vol. CO_2**)** Considering biogas 5, overall 285 cases on the 400 analysed respect the constraints (Figure 4.15). In fact, 115 cases do not respect the constraints on carbon deposition. Therefore, 29% of the analysed cases are prone to carbon deposition, because of the low 25% CO_2 fraction in biogas 5. The number of safe cases for the cold recirculation scheme with biogas 5 is 2% lower than the equivalent for hot recirculation scheme.

Electrical efficiency varies between 36.8% and 63.3% (Figure 4.15). The same trends concerning external reformer temperature, recirculation ratio, and steam to carbon ratio highlighted for biogas 1 also apply in this case. The minimum efficiency reached with biogas 5 is 2% higher than the minimum efficiency reached with biogas 1. Similarly, the maximum

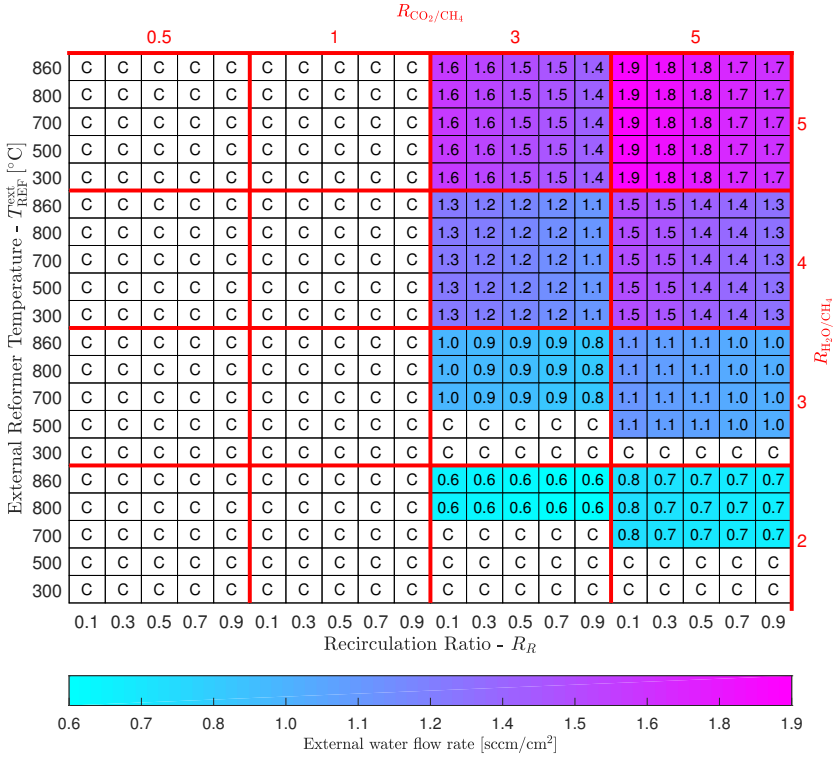

Figure 4.14: *Water consumption raster plot for cold recirculation case of the electrolyte-supported scheme with biogas 4. The figure shows the feasible domain and the water consumption.*

efficiency reached with biogas 5 is 1% higher than the maximum efficiency reached with biogas 1. These results underly the higher efficiency reachable running the system more on steam methane reforming rather than on methane dry reforming.

The maximum efficiency of the cold recirculation scheme fed by biogas 5 is 2% higher than the maximum efficiency of the corresponding hot recirculation scheme, being also higher on average.

External water consumption varies between 0.46 sccm/cm^2 and 2.13 sccm/cm^2 (Figure 4.16). The same trends concerning external reformer temperature, recirculation ratio, carbon dioxide to methane ratio, and steam to carbon ratio highlighted for biogas 1 also apply in this case. According to the low 25% CO_2 fraction in biogas 5 and to the plant man-

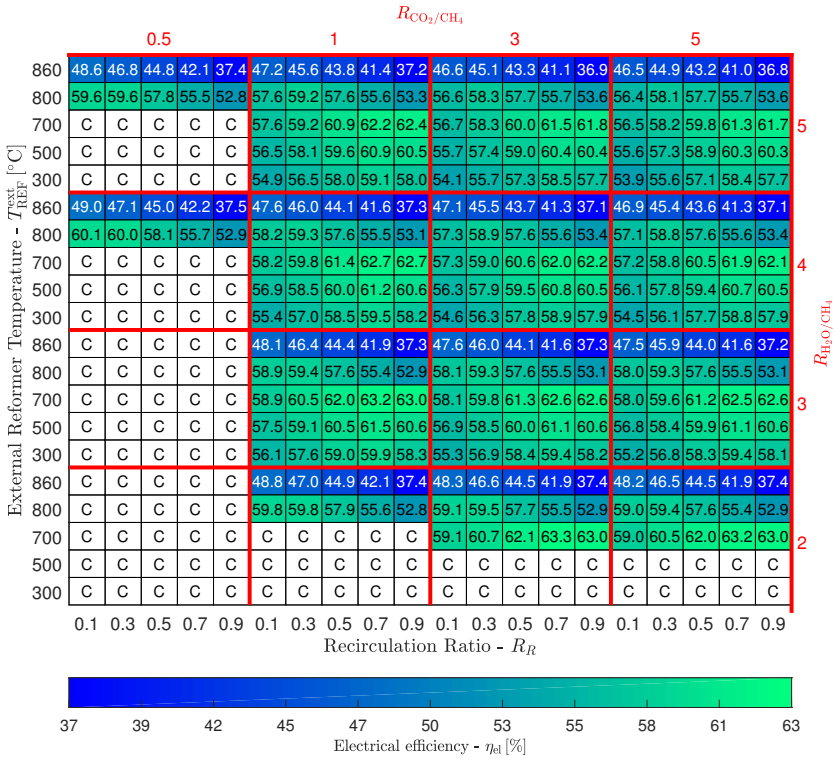

Figure 4.15: *Efficiency raster plot for cold recirculation case of the electrolyte-supported scheme with biogas 5. The figure shows feasible domain and electrical efficiency.*

agement strategies the maximum water consumption reached with biogas 5 is 6% higher than the maximum water consumption reached with biogas 1.

Comparison and discussion Also for all the cases of cold recirculation scheme the only pratical constraint that is not always satisfied is that on the carbon deposition. In this cold recirculation plant for each biogas composition we select as reference the least water consuming and the most efficient configuration (Table 4.6).

Moreover, we report the variation of the composition of the syngas for the three reference configurations along the CHP plant (Figure 4.17).

Molar fraction profiles for biogas 1, 4, and 5 are like those evidenced for

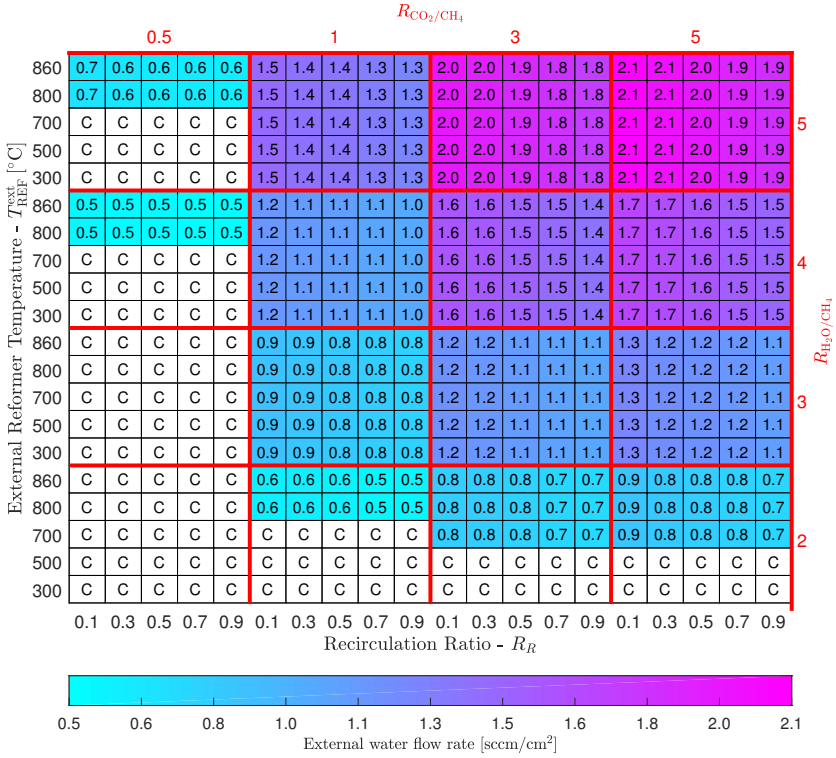

Figure 4.16: *Water consumption raster plot for cold recirculation case of the electrolyte-supported scheme with biogas 5. The figure shows the feasible domain and the water consumption.*

hot recirculation scheme commenting Figure 4.10. However, the absolute values of the concentrations are different. Moreover, between point 2 and point 3 the cold and dehumidified anode exhaust mixes with the syngas, causing a sharp decrease in H_2 and CO fractions, and a sudden increase in CO_2 fraction.

4.3.2 Anode-supported fuel cell plant

We present the results of the sensitivity analysis for the power plant based on anode-supported fuel cell separately for the hot recirculation scheme and the cold recirculation scheme, in section 4.3.2.1 and section 4.3.2.2 respectively.

Table 4.6: *Operating parameters of the reference cases for the different biogas compositions considered for cold recirculation scheme with electrolyte-supported fuel cell.*

	Biogas 1	Biogas 4	Biogas 5
R_R	0.5	0.5	0.5
$T_{\mathrm{REF}}^{\mathrm{ext}}$ [°C]	700	700	700
$R_{\mathrm{H_2O/CH_4}}$	2	2	2
$R_{\mathrm{CO_2/CH_4}}$	0.5	0.5	0.5
η_{el} [%]	61.0	60.6	61.7
Cell voltage [V]	0.769	0.765	0.775

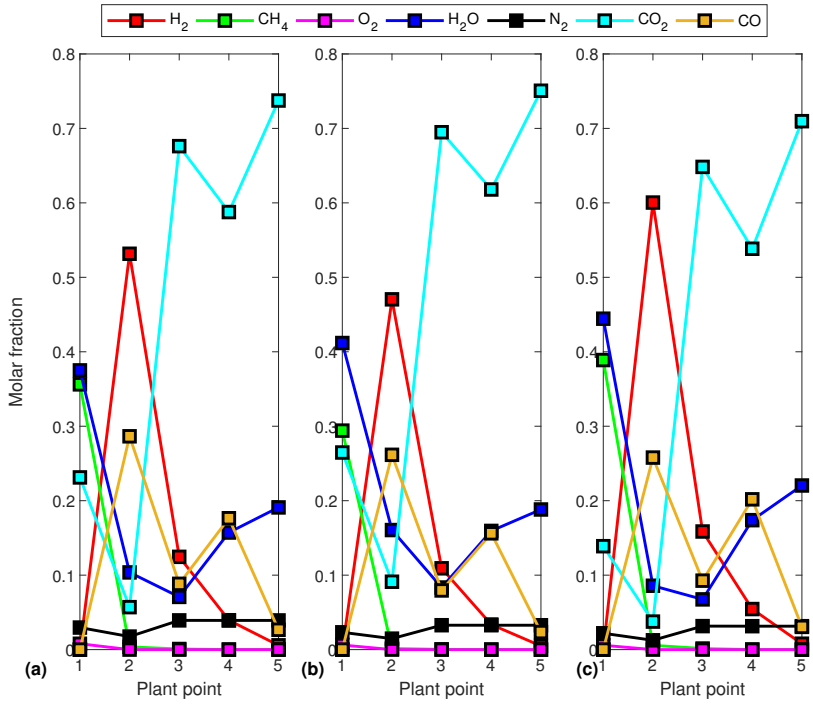

Figure 4.17: *Syngas compositions as a function of the plant points for cold recirculation scheme with electrolyte-supported fuel cell. Subplots (a), (b), and (c) represent biogas 1, 4, and 5 respectively. See the appendix for a table version of the figure.*

4.3.2.1 Hot recirculation scheme

In this section, we analyse the results of the hot recirculation scheme reporting the efficiency variation as a function of the sensitivity analysis operating parameter for biogas 1, 4, and 5 (Figures 4.18, 4.20, and 4.22 respectively). We also report the external water consumption as a function of the sensitivity analysis operating parameter for biogas 1, 4, and 5 (Figure 4.19, 4.21, and 4.23 respectively).

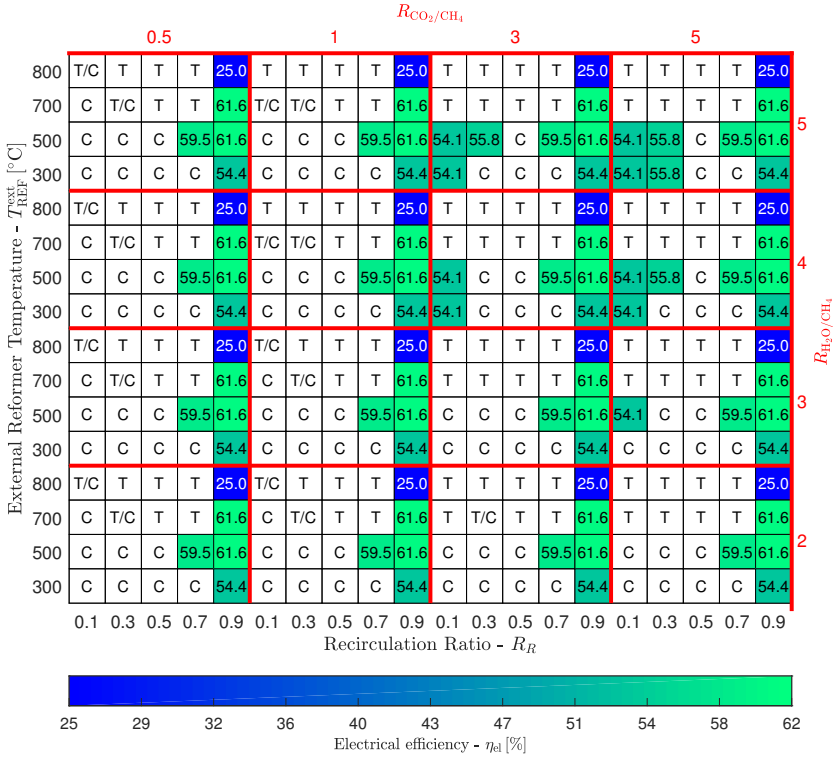

Figure 4.18: *Efficiency raster plot for hot recirculation case of the anode-supported scheme with biogas 1. The figure shows feasible domain and electrical efficiency.*

Biogas 1 Considering biogas 1, overall 93 cases on the 320 analysed respect the constraints (Figure 4.18). 122 cases do not respect the constraint on maximum allowable temperature difference. Operating at 700 °C and 800 °C $T_{\mathrm{REF}}^{\mathrm{ext}}$ with a recirculation ration between 0.1 and 0.7 always re-

sults in an unsafe case for thermal gradient, except for some cases at low R_{CO_2/CH_4}. In fact, at high T_{REF}^{ext} the endothermic reactions take place mostly in the external reformer, given its high temperature. Therefore, the internal reformer requires a low amount of thermal power. Consequently, the cathode inlet temperature must be lower to guarantee the thermal balance of the fuel cell. However, working with 0.9 recirculation ratio makes the anode flow rate higher. Consequently, more thermal power is required to bring the reactants from anode inlet temperature to stack temperature. Therefore, the inlet temperature at the cathode side is closer to the stack temperature. 122 cases do not respect the constraints on carbon deposition. The carbon deposition unsafe cases have the same pattern already evidenced analyzing hot recirculation fuel processing plant for electrolyte-supported architecture. In fact, such cases are concentrated towards low external reformer temperature, low recirculation ratio, and low carbon dioxide to methane ratio. The steam to carbon ratio does not strongly correlate to carbon deposition operating windows. Some of the cases are unsafe for both the carbon deposition and the high temperature difference. The percentage of safe cases for the hot recirculation scheme fed with biogas 1 is 30.6% for the anode-supported fuel cell and 65.0% for the electrolyte-supported fuel cell. However, considering only carbon deposition would result in a similar percentage of safe cases. Therefore, the fuel cell architecture influences the operating windows only for maximum allowable temperature difference constraint.

Electrical efficiency varies between 25.0% and 61.6% (Figure 4.18). The efficiency increases with increasing external reformer temperature in the range 300 - 700°C. The efficiency decreases further increasing the external reformer temperature to 800 °C. Given the narrow operating window it is not possible to spot a meaningful relation between efficiency and recirculation ratio. Carbon dioxide to methane and steam to carbon ratios marginally affect the efficiency.

The maximum efficiency of the hot recirculation plant with anode-supported fuel cell fed by biogas 1 is 1% higher than the same value for electrolyte-supported fuel cell. In the same way, the minimum efficiency for anode-supported is 30% higher than the minimum efficiency for electrolyte-supported. However, this difference is also accentuated from narrow operating windows of anode-supported operation, that drops off regions where the real minimum efficiency is. Anyway, the anode-supported cell is intrinsically more efficient than the electrolyte-supported cell, as

the results here shown confirm.

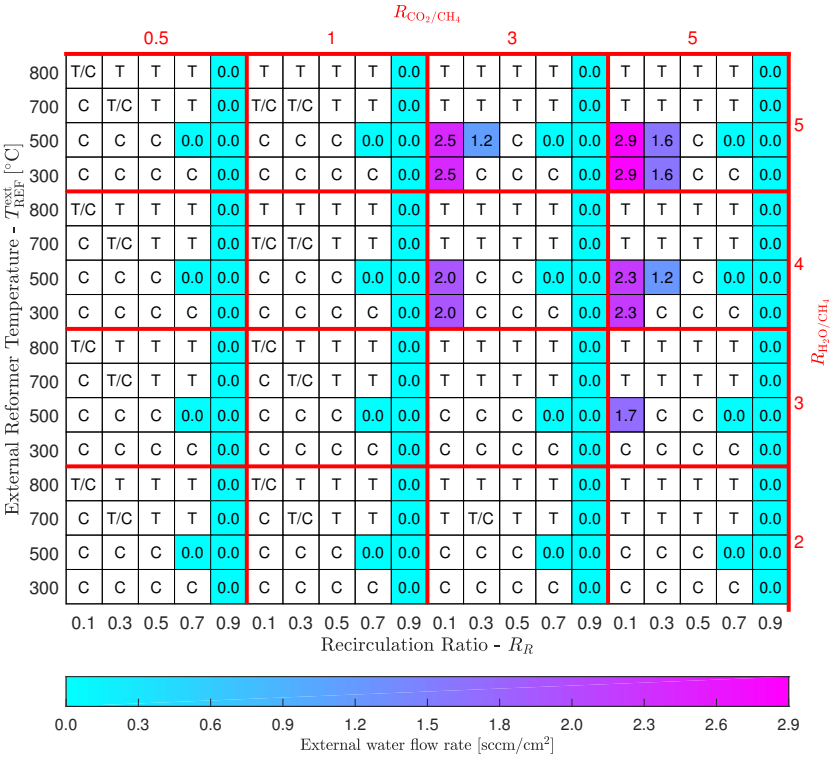

Figure 4.19: *Water consumption raster plot for hot recirculation case of the anode-supported scheme with biogas 1. The figure shows the feasible domain and the water consumption.*

External water consumption varies between 0 sccm/cm^2 and 2.92 sccm/cm^2 (Figure 4.19), with the same pattern already evidenced analysing Figure 4.5. The maximum water consumption of the hot recirculation scheme fed with biogas 1 with the anode-supported architecture is 76% higher than the same value for the electrolyte-supported architecture.

86% of the safe cases have zero external water consumption, because of the hot recirculating flow that carries the water produced in the anode oxidation reaction, and of the narrow operating windows concentrated towards high recirculation ratio. The percentage of water self-sufficient cases for the hot recirculation scheme of the anode-supported architecture fuel cell fed with biogas 1 is 23% higher than the equivalent for electrolyte-

supported architecture.

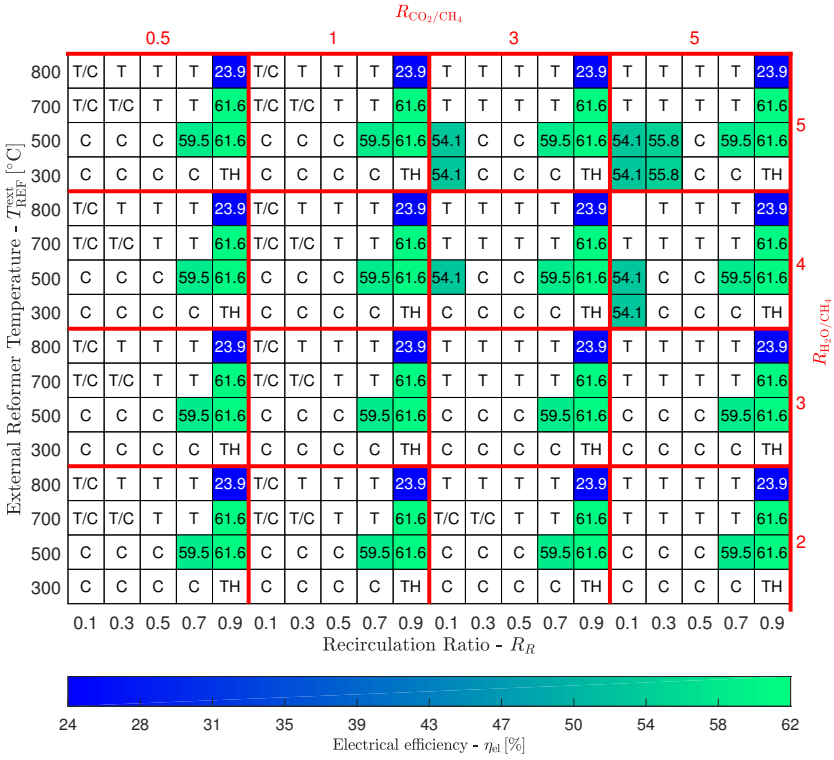

Figure 4.20: *Efficiency raster plot for hot recirculation case of the anode-supported scheme with biogas 4. The figure shows feasible domain and electrical efficiency.*

Biogas 4 (extreme case 50% vol. CH_4**, 45**% vol. CO_2**)** Considering biogas 4, overall 79 cases on the 320 analysed respect the constraints (Figure 4.20). 129 cases do not respect the constraint on maximum allowable temperature difference, with the same pattern evidenced commenting Figure 4.18. 127 cases do not respect the constraints on carbon deposition. The high 45% CO_2 fraction in biogas 4 results in less safe cases than those registered for operation on biogas 1. Moreover, 16 cases do not respect the thermal equilibrium of the fuel cell. These cases are at 300 °C $T_{\mathrm{REF}}^{\mathrm{ext}}$, where the external reforming ratio is negligible and therefore all the thermal power required from the reforming reactions has to be provided inside

the fuel cell. Moreover, the thermally unbalanced cases are at 0.9 recirculation ratio, where the flow rate is maximum, and therefore also the sensible heat to increase the reactants temperature from the stack inlet temperature to fuel cell temperature is maximum. Finally, we observe the cases that do not respect the thermal equilibrium only for biogas 4 operation. In this case, given the high 45% CO_2 fraction, dry reforming ($\Delta H_{298K} = 247$ kJ/mol) is predominant over steam reforming ($\Delta H_{298K} = 205$kJ/mol), leading to higher thermal power required for reforming.

Electrical efficiency varies between 23.9% and 61.6% (Figure 4.20), practically in the same range evidenced for biogas 1 operation. The same trends concerning external reformer temperature, recirculation ratio, carbon dioxide to methane ratio, and steam to carbon ratio highlighted for biogas 1 also apply in this case.

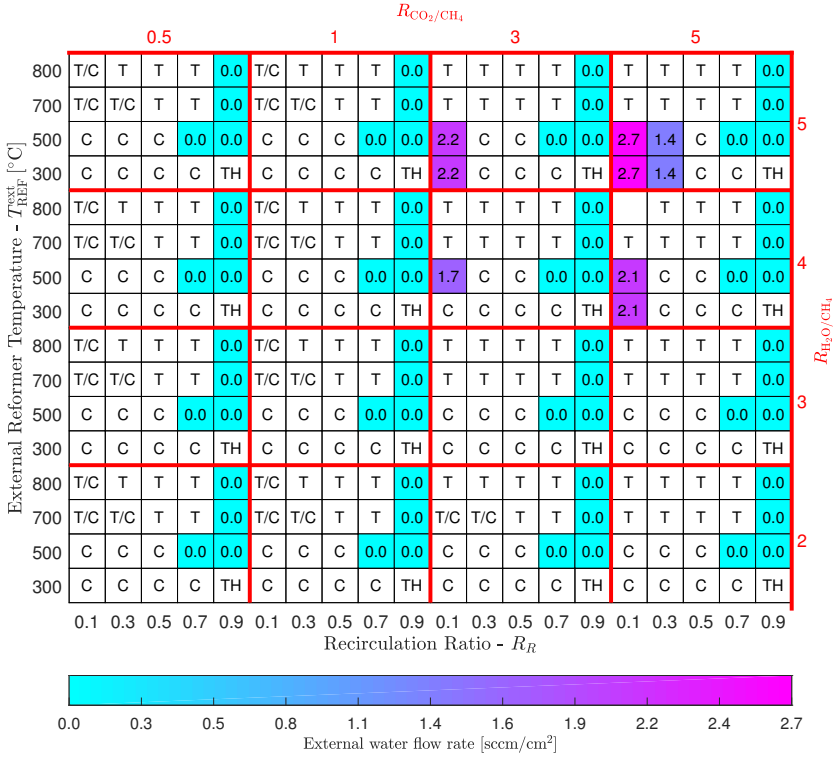

Figure 4.21: *Water consumption raster plot for hot recirculation case of the anode-supported scheme with biogas 4. The figure shows the feasible domain and the water consumption.*

External water consumption varies between 0 sccm/cm^2 and 2.72 sccm/cm^2 (Figure 4.21), with the same pattern already evidence for biogas 1. The high 45% CO_2 fraction in the feeding biogas drives the fuel processing plant to run more on dry reforming, than on steam reforming. In fact, the maximum water consumption of the hot recirculation scheme fed with biogas 4 with the anode-supported architecture is 8% lower than the same value for the biogas 1 fed plant.

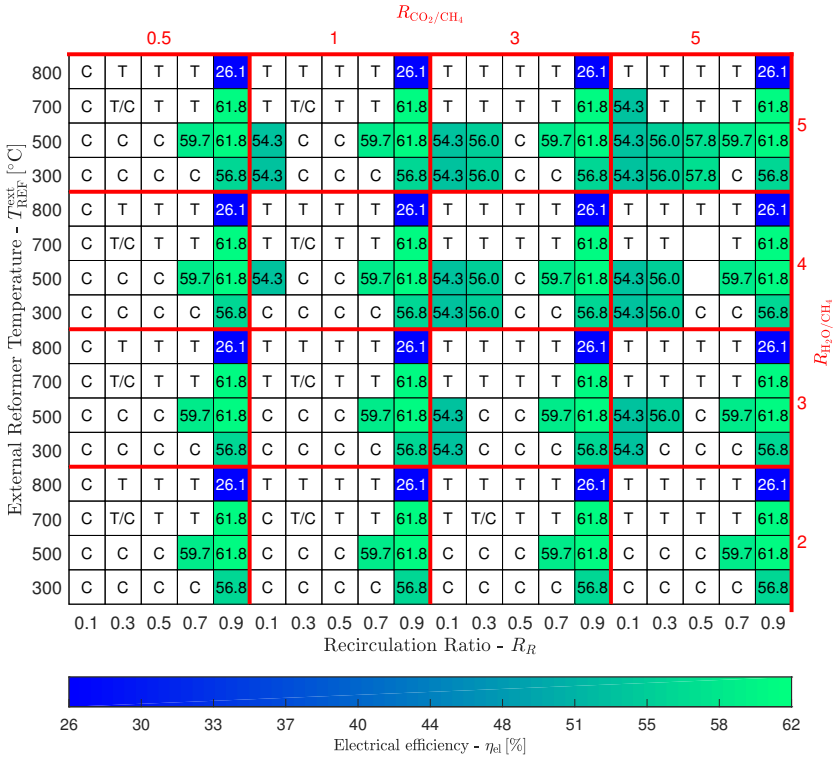

Figure 4.22: *Efficiency raster plot for hot recirculation case of the anode-supported scheme with biogas 5. The figure shows feasible domain and electrical efficiency.*

Biogas 5 (extreme case 70% vol. CH_4**, 25**% vol. CO_2**)** Considering biogas 5, overall 107 cases on the 320 analysed respect the constraints (Figure 4.22). 117 cases do not respect the constraint on maximum allowable temperature difference, with an analogous pattern to that evidenced

commenting Figure 4.18. Therefore, the biogas composition does not affect the operating window regarding the temperature difference. 103 cases do not respect the constraints on carbon deposition. Such a low value is due to the low 25% fraction of carbon dioxide in the biogas.

Efficiency varies between 26.0% and 61.8% (Figure 4.22). Operation on biogas 5 is slightly more efficient than operation on biogas 1. In fact, the percentage difference between the two maxima efficiencies and the two minima efficiencies reached with biogas 5 and with biogas 1 is 4.4% and 0.4%, respectively.

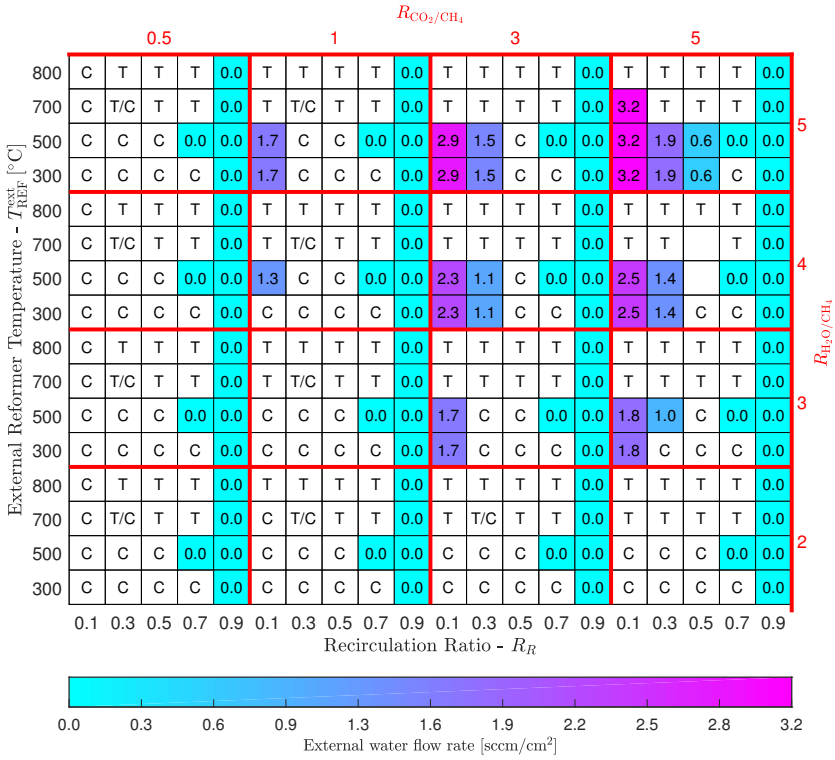

Figure 4.23: *Water consumption raster plot for hot recirculation case of the anode-supported scheme with biogas 5. The figure shows the feasible domain and the water consumption.*

External water consumption varies between 0 sccm/cm^2 and 3.15 sccm/cm^2 (Figure 4.23), with the same pattern already evidence for biogas 1. The low 25% CO_2 fraction in the biogas makes the fuel processing relying

more on steam reforming. In fact, the maximum water consumption of the hot recirculation scheme fed with biogas 5 with the anode-supported architecture is 8% higher than the same value for the biogas 1 fed plant.

Comparison and discussion For each biogas composition we select as reference the most efficient between the zero water consumption configurations (Table 4.7).

Table 4.7: *Operating parameters of the reference cases for the different biogas compositions considered for hot recirculation scheme with anode-supported fuel cell.*

	Biogas 1	Biogas 4	Biogas 5
R_R	0.9	0.9	0.9
$T_{\mathrm{REF}}^{\mathrm{ext}}$ [°C]	500	500	500
$R_{\mathrm{H_2O/CH_4}}$	2	2	2
$R_{\mathrm{CO_2/CH_4}}$	0.5	0.5	0.5
η_{el} [%]	61.6	61.6	61.8
Cell voltage [V]	0.756	0.756	0.756

Moreover, we report the variation of the composition of the syngas for the three reference configurations along the CHP plant (Figure 4.24).

Considering biogas 1, in the external reformer (between point 1 and point 2) the methane fraction drops from 2.83% to 0.43%, because of the reforming reactions. Similarly, the water fraction drops from 50% to 44%. Moreover, the carbon dioxide fraction goes from 43% to 42%. Therefore, the increase in hydrogen fraction from 0.97% to 8.89% is a consequence mainly of steam methane reforming. In the internal reforming (between point 2 and 3) the prevalent reaction is the reverse water gas shift. In fact, the CO_2 fraction decreases from 42% to 39%, and the H_2 fraction passes from 8.89% to 6.8%. At the same time, carbon monoxide fraction increases from 1.76 % to 5.48%, and water fraction passes from 44% to 47%. Finally, in the fuel cell, both the hydrogen oxidation and the water gas shift reactions take place. In fact, CO fraction decreases from 5.48% to 0.82%, while H_2 fraction decreases from 6.77% to 1.02%.

The composition profiles for biogas 4 and 5 are analogous to those described for biogas 1. However, the absolute values of the fractions are

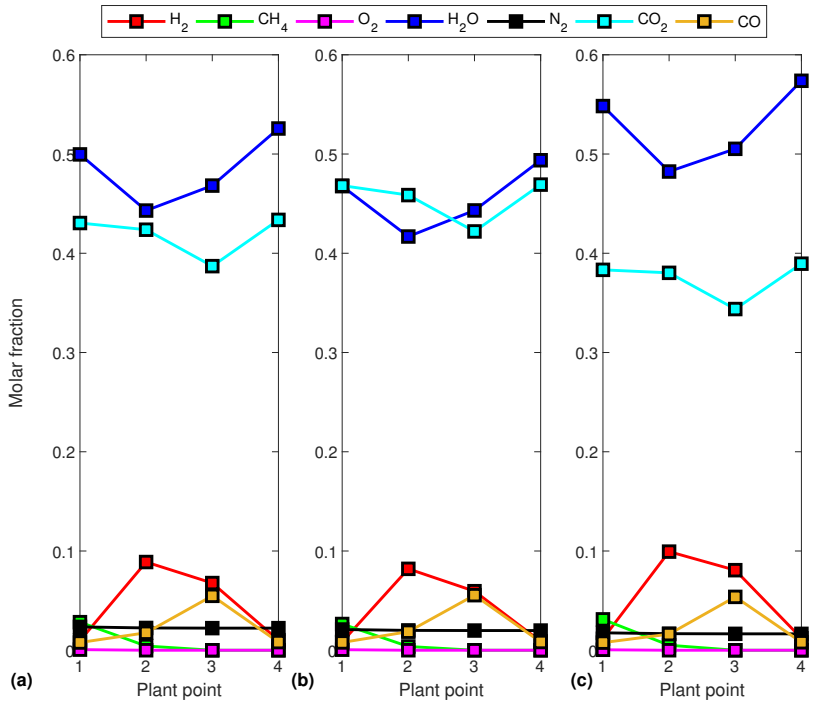

Figure 4.24: *Syngas compositions as a function of the plant points for hot recirculation scheme with anode-supported fuel cell. Subplots (a), (b), and (c) represent biogas 1, 4, and 5 respectively. See the appendix for a table version of the figure.*

different, according to the different fraction of carbon dioxide in the biogas.

The maximum hydrogen fraction for hot recirculation plant with anode-supported fuel cell is 10% and is registered with biogas 5 at the outlet of the external reformer. The same value for the electrolyte-supported architecture is 47%. We note that such a result is due to the low external reformer temperature of the reference cases for anode-supported architecture, and to the 0.9 recirculation ratio.

4.3.2.2 Cold recirculation scheme

In this section, we analyse the results of the cold recirculation scheme reporting the efficiency variation as a function of the sensitivity analysis operating parameter for biogas 1, 4, and 5 (Figures 4.25, 4.27, and 4.29 respectively). We also report the external water consumption as a func-

tion of the sensitivity analysis operating parameter for biogas 1, 4, and 5 (Figures 4.26, 4.28, and 4.30 respectively).

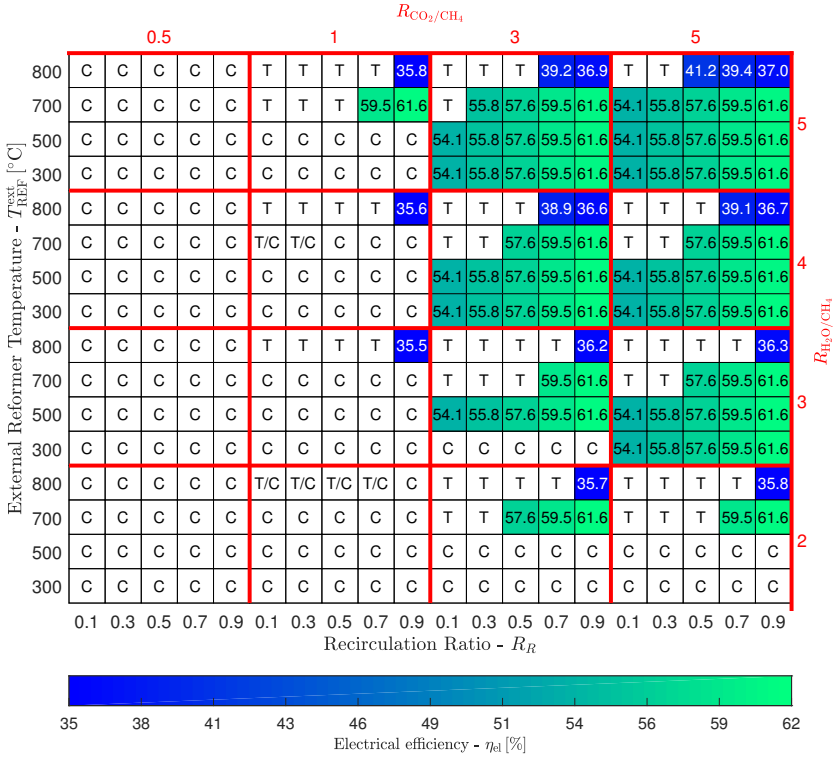

Figure 4.25: *Efficiency raster plot for cold recirculation case of the anode-supported scheme with biogas 1. The figure shows feasible domain and electrical efficiency.*

Biogas 1 Considering biogas 1, overall 98 cases on the 320 analysed respect the constraints (Figure 4.25). In fact, 63 cases do not respect the constraint on maximum allowable temperature difference. The pattern for thermal gradient unsafe cases is concentrated at high external reformer temperatures and at recirculation ratios lower than 0.9, as already evidenced commenting Figure 4.18 for hot recirculation scheme. However, for cold recirculation scheme fed with biogas 1 the number of thermal gradient unsafe cases is 94% lower than the same value for hot recirculation scheme fed with same biogas. In fact, the injection of recirculation

flow after the external reformer increases dramatically the carbon dioxide fraction at the inlet of the internal reformer (see Figure 4.31). Moreover, at 700 °C and 800 °C $T_{\mathrm{REF}}^{\mathrm{ext}}$ almost all the methane reacts in the external reformer. Consequently, the resulting gas composition favors reverse water gas shift to take place in the internal reformer. Such a reaction is endothermic and subtracts thermal power from the thermal balance of the fuel cell, lowering the temperature difference. Moreover, 165 cases do not respect the constraints on carbon deposition. The pattern for carbon deposition unsafe cases overlaps the pattern evidenced commenting Figure 4.11 for electrolyte-supported architecture results.

Efficiency varies between 35.5% and 61.6% (Figure 4.25). The steam to carbon and the carbon dioxide to methane ratios are not sensitive parameters for the electrical efficiency. For $T_{\mathrm{REF}}^{\mathrm{ext}}$ lower than 700 °C the optimal recirculation ratio is always 0.9. In fact, the phenomenological model implemented for anode-supported fuel cell is blind towards the hydrogen fraction entering the fuel cell. Therefore, the cases with higher recirculation ratio enable a higher unused fuel recovery and are optimal. This is a limitation of the phenomenological model. When $T_{\mathrm{REF}}^{\mathrm{ext}}$ is 800 °C electrical heating is necessary and the optimal recirculation ratio becomes the lowest possible.

The maximum efficiency of the cold recirculation scheme fed with biogas 1 is practically the same to the maximum efficiency of the hot recirculation scheme with same feeding. Moreover, the maximum efficiency of the cold recirculation scheme fed with biogas 1 with anode-supported fuel cell is 2% lower than the maximum efficiency achieved with the corresponding case operating with electrolyte-supported fuel cell.

External water consumption varies between 0.75 sccm/cm^2 and 3.53 sccm/cm^2 (Figure 4.26). The water self-sufficiency of the power plant is never reached, given the cold dehydrated recirculating flow. The external water consumption varies with the same pattern highlighted commenting Figure 4.12. The maximum external water consumption for the cold recirculation scheme fed with biogas 1 is 21% higher than the maximum external water consumption for the hot recirculation scheme with same feeding. Moreover, the maximum external water consumption of the cold recirculation scheme fed with biogas 1 with anode-supported fuel cell is 76% higher than the maximum external water consumption registered with the corresponding case operating on electrolyte-supported fuel cell.

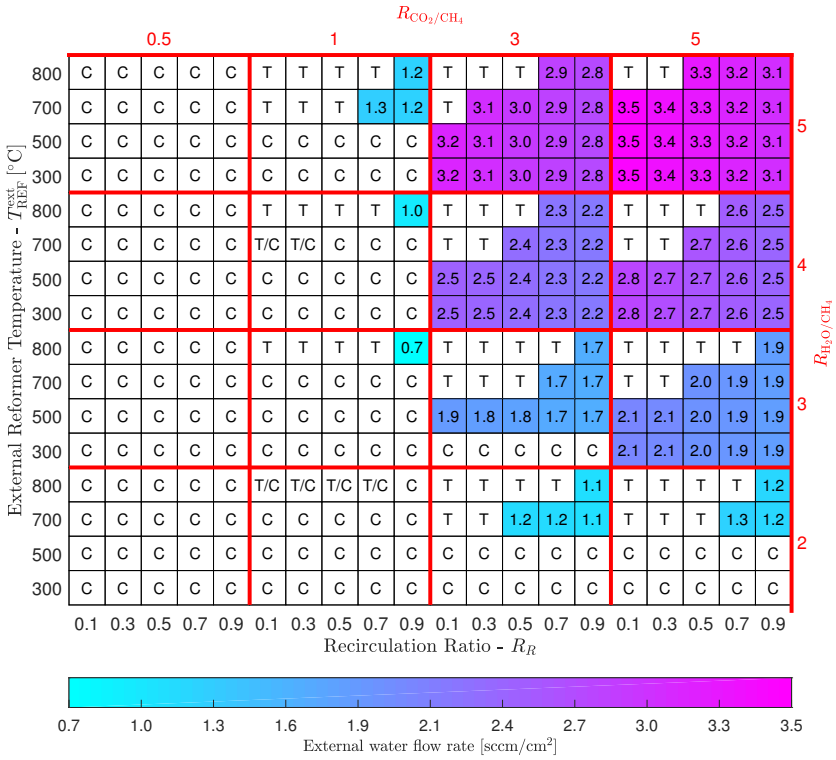

Figure 4.26: *Water consumption raster plot for cold recirculation case of the anode-supported scheme with biogas 1. The figure shows the feasible domain and the water consumption.*

Biogas 4 (extreme case 50% vol. CH_4**, 45**% vol. CO_2**)** Considering biogas 4, overall 75 cases on the 320 analysed respect the constraints (Figure 4.27). 80 cases do not respect the constraint on maximum allowable temperature difference, similarly to results obtained operating with biogas 1. 200 cases do not respect the constraints on carbon deposition. Therefore, operation with biogas 4 results in 21% more carbon deposition unsafe cases than operation with biogas 1. This is a result of the high 45% CO_2 fraction in biogas 4.

Efficiency varies between 35% and 61.6% (Figure 4.27) following the same pattern highlighted for biogas 1. The maximum efficiency reached with biogas 4 is practically the same to: (i) the maximum efficiency reached with biogas 1, and (ii) to the maximum efficiency of the cor-

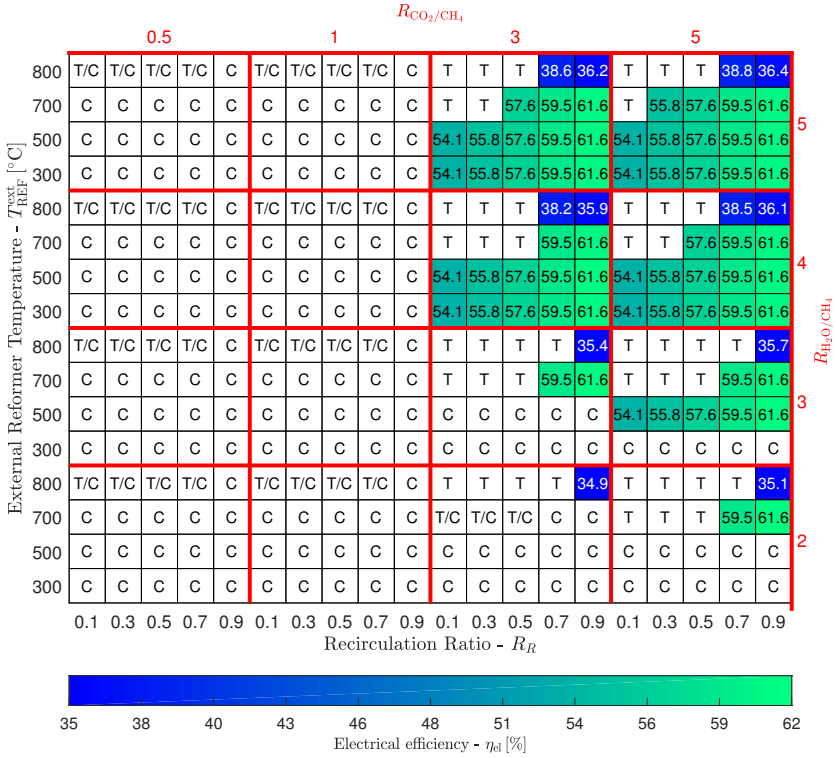

Figure 4.27: *Efficiency raster plot for cold recirculation case of the anode-supported scheme with biogas 4. The figure shows feasible domain and electrical efficiency.*

responding hot recirculation scheme. The maximum efficiency reached with the anode-supported fuel cell fed with biogas 4 is 1% lower than the maximum efficiency achieved with the corresponding case operating with electrolyte-supported fuel cell.

External water consumption varies between 1 sccm/cm^2 and 3.32 sccm/cm^2 (Figure 4.28), according to the pattern evidenced for operation on biogas 1. The maximum external water consumption operating with biogas 4 is: (i) 6% lower than the maximum external water consumption requested operating with biogas 1; (ii) 22% higher than the maximum external water consumption for the hot recirculation scheme with same feeding; and (iii) 76% lower than the maximum external water consumption registered with the same case operating with electrolyte-supported fuel cell.

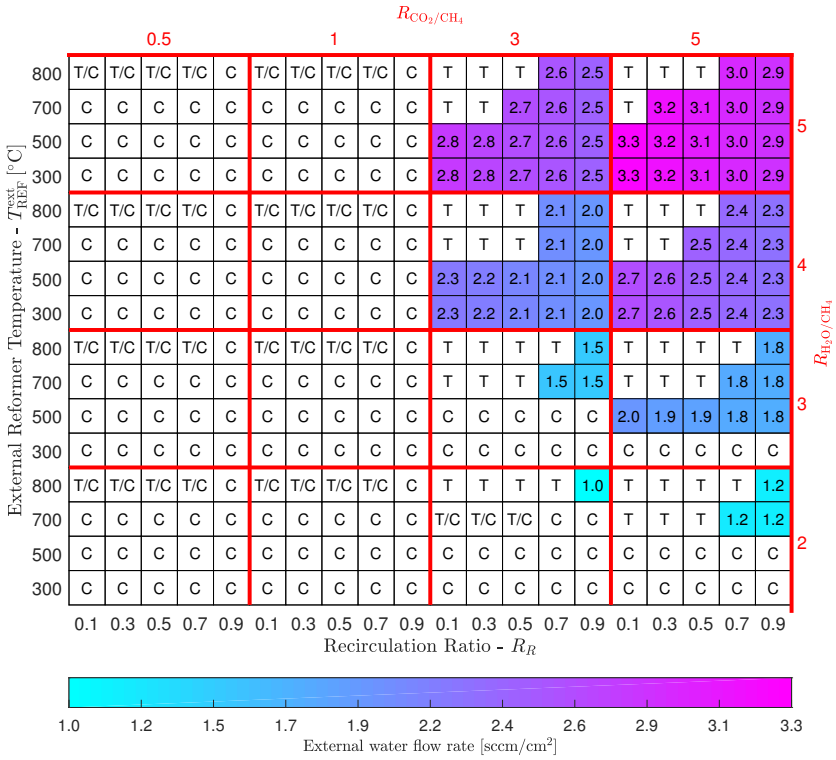

Figure 4.28: *Water consumption raster plot for cold recirculation case of the anode-supported scheme with biogas 4. The figure shows the feasible domain and the water consumption.*

Biogas 5 (extreme case 70% vol. CH_4**, 25**% vol. CO_2**)** Considering biogas 5, overall 152 cases on the 320 analysed respect the constraints (Figure 4.29). In fact, 70 cases do not respect the constraint on maximum allowable temperature difference. The number of thermal gradient unsafe cases with biogas 5 is 11% lower than the same value obtained with biogas 1. However, the pattern of unsafe cases for thermal gradient is similar to that already described for biogas 1. 105 cases do not respect the constraints on carbon deposition.

Efficiency varies between 37.1% and 62.3% (Figure 4.29) following the same pattern highlighted for biogas 1 operation. The maximum efficiency reached with biogas 5 is: (i) practically the same to the maximum efficiency reached with biogas 1; (ii) practically the same to the maximum

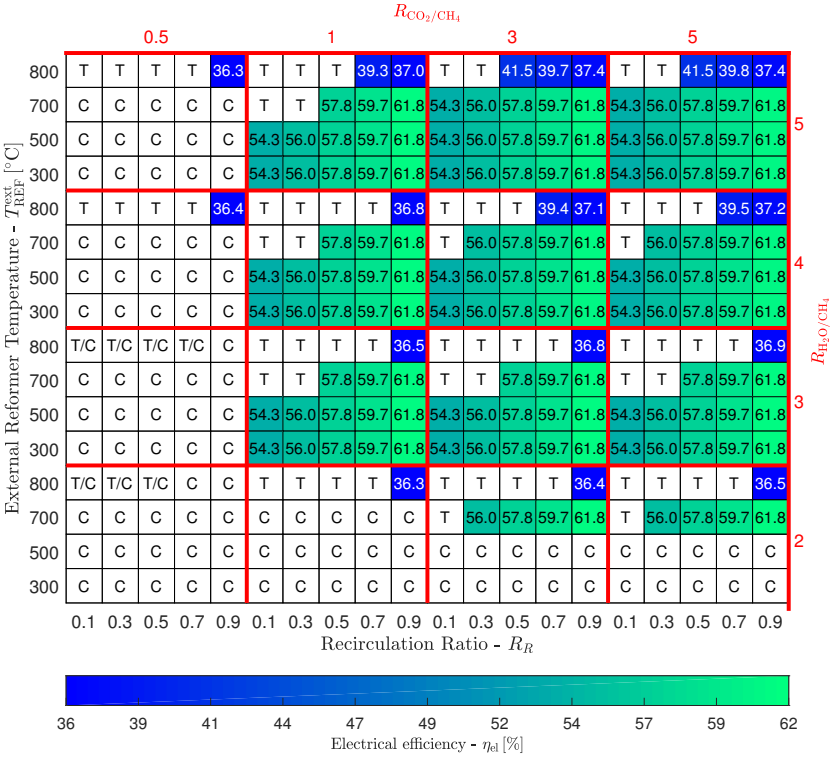

Figure 4.29: *Efficiency raster plot for cold recirculation case of the anode-supported scheme with biogas 5. The figure shows feasible domain and electrical efficiency.*

efficiency of the corresponding hot recirculation scheme; and (iii) 2% lower than the maximum efficiency achieved with the corresponding case operating with electrolyte-supported fuel cell.

External water consumption varies between 0.81 sccm/cm^2 and 3.75 sccm/cm^2 (Figure 4.30), according to the pattern evidenced for operation on biogas 1. The maximum external water consumption operating with biogas 5 is: (i) 6 % higher than the maximum external water consumption requested operating with biogas 1; (ii) 19 % higher than the maximum external water consumption for the hot recirculation scheme with same feeding; and (iii) 76 % higher than the maximum external water consumption registered with the same case operating with electrolyte-supported fuel cell.

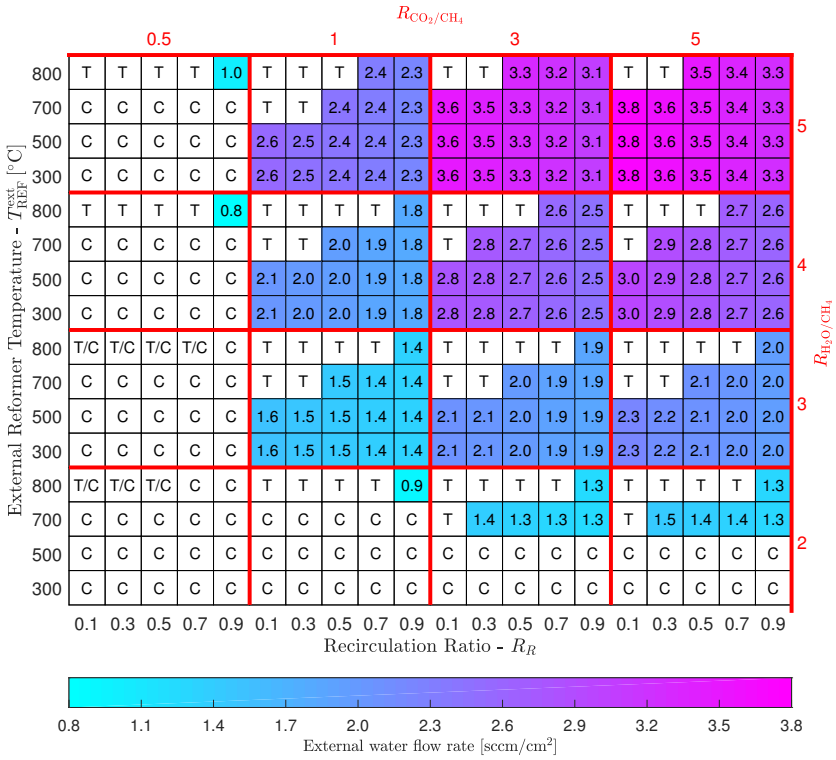

Figure 4.30: *Water consumption raster plot for cold recirculation case of the anode-supported scheme with biogas 5. The figure shows the feasible domain and the water consumption.*

Comparison and discussion In this cold recirculation plant for each biogas composition we select as reference the least water consuming and the most efficient configuration (Table 4.8).

Moreover, we report the variation of the composition of the syngas for the three reference configurations along the CHP plant (Figure 4.31).

The molar fraction profiles reported in Figure 4.31 (a), (b), and (c) are practically the same to those reported in Figure 4.17 (a), (b), and (c) respectively. In fact, the operating parameters of the sensitivity analysis reported in Table 4.8 for biogas 1, 4, and 5 are the same to those reported in Table 4.6 for biogas 1, 4, and 5 respectively. These results prove that the compositions throughout the plant are influenced mostly from the recirculation type, from the biogas type, and from the operating parameters

Table 4.8: *Operating parameters of the reference cases for the different biogas compositions considered for cold recirculation scheme with anode-supported fuel cell.*

	Biogas 1	Biogas 4	Biogas 5
R_R	0.9	0.9	0.9
$T_{\text{REF}}^{\text{ext}}$ [°C]	800	800	800
$R_{\text{H}_2\text{O}/\text{CH}_4}$	3	2	4
$R_{\text{CO}_2/\text{CH}_4}$	1	3	0.5
η_{el} [%]	35.5	35.0	36.4
Cell voltage [V]	0.756	0.756	0.756

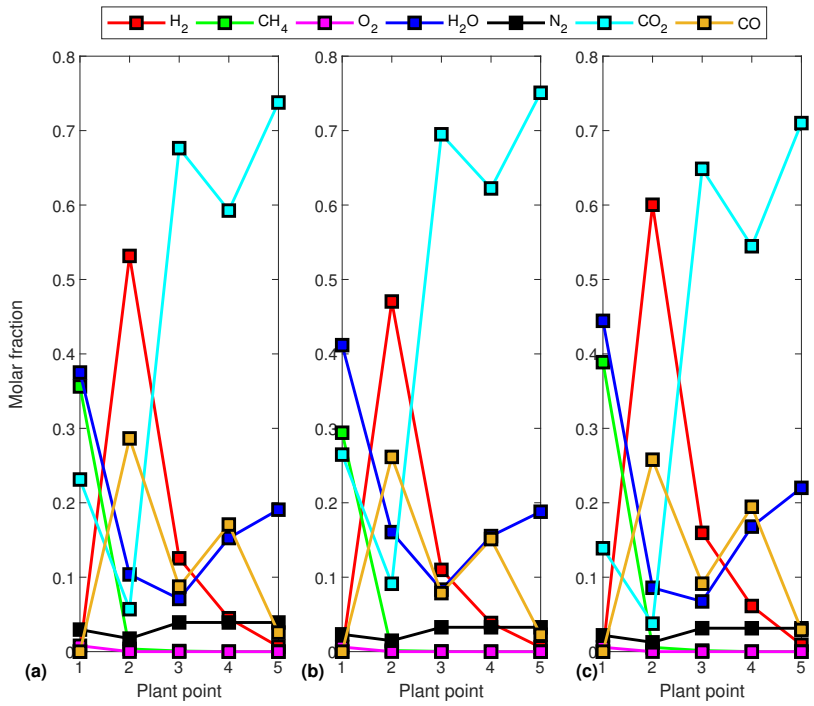

Figure 4.31: *Syngas compositions as a function of the plant points for cold recirculation scheme with anode-supported fuel cell. Subplots (a), (b), and (c) represent biogas 1, 4, and 5 respectively. See the appendix for a table version of the figure.*

of the sensitivity analysis. The fuel cell type is not a sensitive parameter for the molar fraction profiles, but only for the absolute values of the molar fractions.

4.4 Discussion

The average percentage of carbon deposition unsafe cases for biogas 1 is 42%, with a standard deviation of 8. The same values for biogas 4 are 49% and 12, while for biogas 5 are 30% and 2. Therefore, the biogas composition is a sensitive parameter for the operating windows. In fact, using a biogas with higher CO_2 fraction, increases the carbon deposition risk. The influence of the recirculation scheme on operating windows varies according to the biogas composition. In fact, using biogas 1 and 4 the hot recirculation scheme results on average in 41 more safe cases than the cold recirculation scheme. However, using biogas 5 the cold recirculation scheme results on average in 19 more safe cases than the hot recirculation scheme. The fuel cell architecture is a sensitive parameter only for the temperature difference constraint. Three of the four fuel processing operating parameters correlate in all the cases in the same way to carbon deposition risk. In fact, carbon deposition unsafe operating points concentrate: (i) at low external reformer temperature, (ii) at low carbon dioxide to methane ratio, and (iii) at low steam to carbon ratio. The recirculation ratio is a sensitive parameter for carbon deposition only for the hot recirculation scheme, in this configuration: the higher the recirculation ratio the lower the risk. However, external water supply can alter the carbon deposition sensitivity to recirculation ratio. Considering the maximum temperature difference constraint, the only sensitive fuel processing operating parameters are the external reformer temperature and the recirculation ratio. In fact, temperature difference unsafe cases concentrate at external reformer temperature in the range 700-800 °C and at low recirculation ratios.

The average maximum electrical efficiency for biogas 1 is 61.7% with a standard deviation of 0.6. The same values for biogas 4 are 61.5% and 0.6, while for biogas 5 are 62.2% and 0.7. Therefore, the biogas composition is a sensitive parameter for the electrical efficiency. In fact, using a biogas with higher CO_2 fraction increases the reliance on dry methane reforming over steam methane reforming and the efficiency is consequently lower. The influence of the recirculation scheme varies according to the fuel cell

architecture. In fact, for the electrolyte-supported fuel cell scheme the average of the maximum electrical efficiency for hot recirculation is 61.1%, while it is 62.7% for the cold recirculation scheme. However, for the anode-supported fuel cell scheme the average of the maximum electrical efficiency for hot recirculation is 61.7% and is equal to the average for the cold recirculation scheme. Therefore, the cold recirculation scheme is more efficient with electrolyte-supported fuel cell. However, such a difference is not evident for anode supported fuel cell. In fact, the phenomenological model implemented for anode-supported fuel cell is blind towards the hydrogen fraction entering the fuel cell. Therefore, the model does not consider the higher hydrogen fraction at the inlet of the fuel cell in the cold recirculation scheme, resulting from the reliance on steam reforming rather than on dry reforming. From the figures just drawn it is also evident that a direct comparison of the efficiency of electrolyte-supported and anode-supported performance is not meaningful because the different modelling approach biases the results, however the results obtained are close. Moreover, the anode-supported fuel cell in this work runs at 0.4 A/cm^2, while the electrolyte-supported fuel cell at 0.235 A/cm^2. Two of the four fuel processing operating parameters correlate in all the cases in the same way to electrical efficiency. In fact, the optimal recirculation ratio decreases as the external reformer temperature increases from 300 °C to 800 °C and above. However, a low recirculation ratio at high temperature is not always a safe case for anode-supported fuel cell. The steam to carbon ratio and the carbon dioxide to methane ratio are sensitive parameter for the electrical efficiency only for the cold recirculation scheme with electrolyte-supported. In this case the efficiency is higher at low carbon dioxide to methane ratio, and at low steam to carbon ratio.

The recirculation scheme is the most sensitive parameter for external water consumption. In fact, with the cold recirculation scheme it is never possible to reach water self-sufficiency. However, considering the hot recirculation scheme the biogas composition is also a sensitive parameter for external water consumption. In fact, the average percentage of water self-sufficient over the safe cases for biogas 1 is 78%, with a standard deviation of 8. The same values for biogas 4 are 81% and 0, while for biogas 5 are 71% and 4. Therefore, using a biogas with higher CO_2 fraction, increases the reliance on dry methane reforming over steam methane reforming, and therefore lowers the external water consumption. The fuel cell architecture is also a sensitive parameter on external water consumption. In fact,

the average percentage of water self-sufficient cases for hot recirculation scheme with the electrolyte-supported fuel cell is 73%, while it is 81% with the anode-supported fuel cell. Therefore, the anode-supported scheme is less water consuming. However, this result is partly biased from: (i) the different maximum allowable temperature difference that results in narrower operating windows for the anode-supported scheme, and (ii) from the different modelling approach. Two of the four fuel processing operating parameters correlate in all the cases in the same way to external water consumption. In fact, external water consumption increases: (i) at high steam to carbon ratio, and (ii) at low recirculation ratio. The external water consumption increases with increasing carbon dioxide to methane ratio only when dry reforming is relevantly employed, i.e. with biogas 1 and 4. The temperature of the external reformer is not a sensitive parameter for external water consumption.

4.5 Summary

In this chapter we have run a sensitivity analysis to the fuel processing operating parameters of the W2W conceptual plant in order to: (i) identify safe operating parameters, (ii) quantify the electrical efficiency, and (iii) characterize the external water consumption. In the sensitivity analysis we have considered: (i) hot and cold anode recirculation schemes, (ii) electrolyte- and anode-supported fuel cell, (iii) five different biogas compositions.

The cold recirculation scheme is never water self-sufficient. The anode-supported fuel cell results in narrower operating windows for the more severe temperature difference constraint. The biogas composition influences the operating windows, the efficiency, and the external water consumption. Specifically, with high methane content in the biogas: (i) the safe operating dominion is broader, (ii) the efficiency is higher, and (iii) the external water consumption is higher.

A possible extension of the work is to evaluate the influence on performance and on operating windows of air or carbon dioxide injection in the biogas feed, considering also partial oxidation reaction. The impact on performance and operation robustness of these options will be considered. Moreover, the carbon dioxide usage path in a broader sense will be investigated.

Chapter 5

Combined Heating and Power System through a High Temperature Polymer Electrolyte Membrane Fuel Cell and Micro Gas Turbine Hybrid System

In the previous chapters we have studied CHP systems based on low temperature (i.e. $< 100\,^{\circ}\mathrm{C}$) PEMFCs and high temperature (i.e. between $500\,^{\circ}\mathrm{C}$ and $700\,^{\circ}\mathrm{C}$) SOFCs. However, both technologies have advantages and drawbacks. In fact, the PEMFCs ensure fast load following but require high purity hydrogen. Hydrogen purification is a complex task that increases the cost and decreases the efficiency of the fuel processor. Conversely, SOFCs can even operate with biogas thanks to the fuel flexibility. However, such systems have poor dynamic performance.

HT-PEMFCs can solve both of the drawbacks of PEMFCs and SOFCS. In fact, HT-PEMFCs tolerate high impurities content in the feeding fuel (i.e. CO content up to 5%) without significantly losing efficiency [13, 35–39] thanks the higher operating temperature (i.e. between $160\,^{\circ}\mathrm{C}$ and $200\,^{\circ}\mathrm{C}$) than low temperature PEMFCs. Moreover, HT-PEMFCs have dynamical characteristics similar to PEMFCs.

Several studies explore the performance of a HT-PEMFCs CHP featuring a steam reforming-based fuel processor with simplified or absent purification [13, 39, 188]. The steam reforming is the most efficient reaction to produce hydrogen. However, when considering the whole fuel processor, also the thermal power necessary to sustain the steam reforming reaction has to be accounted. In this scenario, the exothermic Partial OXidation (POX) reaction can be potentially more efficient. Moreover, an exothermic POX reactor has better dynamic performance than an endothermic steam reforming reactor.

The POX reactor generally operates at 1000°C producing syngas with significantly higher enthalpy than the syngas to be fed to the fuel cell (i.e. at a temperature between 160 °C and 200 °C). Therefore, by increasing the operating pressure of the POX, such enthalpy difference can be partially recovered in electrical energy through a Gas Turbine (GT). Even if the yield of the mole expanding POX reaction decreases by increasing pressure, the overall CHP efficiency can increase thanks to the additional electric power from the GT. Moreover, with such scheme the fuel processor does not rely on the FC power to run the auxiliaries systems and therefore the overall system has better dynamic characteristics. Finally, the pressurized POX operation can reduce the overall system volume.

In this chapter, we study the performance of a hybrid HT-PEMFC-GT CHP system where the fuel processor implements POX reaction to produce hydrogen. Such topic is completely untapped in literature. Specifically, we evaluate the efficiency of such system as a function of the most influential operating parameters. Moreover, we compare the results to those obtained with state of the art systems.

The chapter is organyzed as follows. Section 5.1 introduces the analyzed problem. Section 5.2 describes the modeling. Section 5.3 presents and discuss the results. Finally, section 5.4 draws the conclusions of the work.

5.1 Problem statement

This chapter studies the performance of an innovative hybrid HT-PEMFC-GT CHP system whose fuel processor produces hydrogen from natural gas through the partial oxidation reaction (eq. (5.1)). Such reaction is exothermic ($\Delta h_{\mathrm{SW}} = -35.7\,\mathrm{kJ/mol}$ for methane) and generally is operated at 1000°C. Moreover, the produced carbon monoxide can react

with water to produce hydrogen according to the water gas shift reaction (see chapter 1).

$$\mathrm{C}_x\mathrm{H}_z + \frac{x}{2}\mathrm{O}_2 \rightleftharpoons x\mathrm{CO} + \frac{z}{2}\mathrm{H}_2\,. \tag{5.1}$$

Depending on the ratio between the oxygen and the natural gas flow rates also the complete oxidation can take place (eq. (5.2)). Such reaction is exothermic ($\Delta h_{\mathrm{SW}} = -890\,\mathrm{kJ/mol}$ for methane) and does not produce hydrogen.

$$\mathrm{C}_x\mathrm{H}_z + \left(\frac{z}{4} + x\right)\mathrm{O}_2 \rightarrow \frac{z}{2}\mathrm{H_2O} + x\mathrm{CO_2}\,. \tag{5.2}$$

5.1.1 Description of the fuel processors

We investigate two fuel processors concepts: concept A (Fig. 5.1) and concept B (Fig. 5.2).

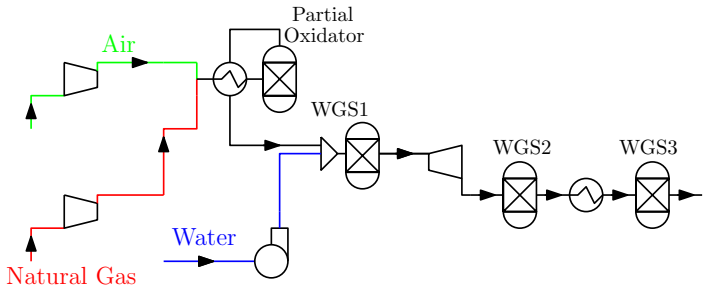

Figure 5.1: *Schematic overview of the fuel processor concept A.*

In the concept A plant, air and natural gas are compressed and then mixed. In the model we keep the two compressors separated because the natural gas could in principle come from the distribution grid at the operating or even higher pressure. The mix of air and natural gas is pre-heated before the POX reactor from the syngas. The heated reactants than enter the POX reactor to produce syngas. The cooled syngas is mixed with water that serve as reactant in the following water gas shift reactors. After the first water gas shift reactor the syngas expands in a turbine. Two other water gas shift stages follow. Between the two reactors an air cooled heat exchanger keep the syngas temperature to 150°C.

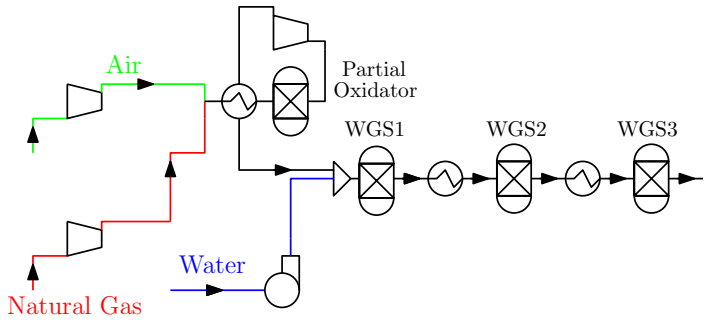

Figure 5.2: *Schematic overview of the fuel processor concept B.*

The concept B plant is similar to concept A plant, except for the fact that the turbine is placed jut after the partial oxidation reaction and before the heat exchanger that pre-heats the reactants.

Concept A fuel processor aims at maximum possible thermal integration of the reactor, in order to make the plant thermally self-sufficient in a broad operating range. Concept B fuel processor is inspired by typical regenerative gas turbine scheme and aims at increasing the turbine power by feeding higher temperature syngas.

It is already evident that the proposed fuel processor concepts are intrinsically simpler than the fuel processors needed for PEMFCs, such as those studied in chapters 1 and 2.

We compare the results of the proposed fuel processor schemes with a state of the art fuel processor implementing steam reforming, water gas shift, and catalytic combustion (Fig. 5.3). Such system is the purification-free version of the fuel processor presented in section 1.3.1. Such comparison serves to prove the advantages of the partial oxidation-based CHP with respect to state of the art steam reforming-based systems.

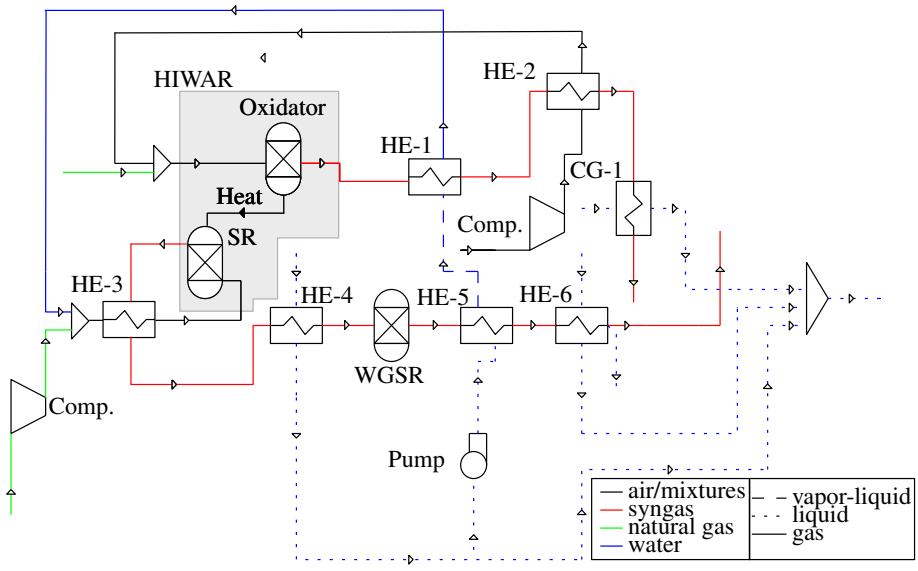

Figure 5.3: *Schematic overview of the baseline fuel processor.*

Moreover, we compare the results of the proposed fuel processor schemes with a non pressurized fuel processor based on partial oxidation (Fig. 5.4). Such comparison serves to prove the advantages of the hybrid CHP with respect to a fuel cell only CHP.

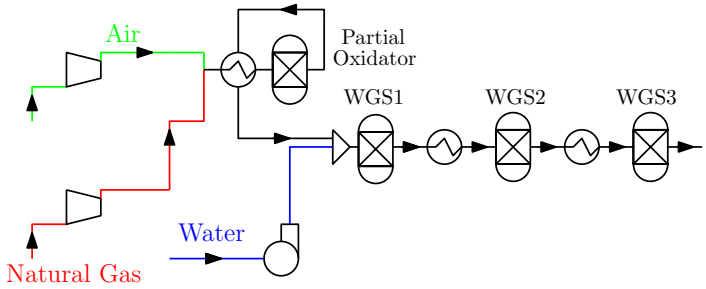

Figure 5.4: *Schematic overview of the non pressurized fuel processor based on partial oxidation.*

5.2 Methodology

We study the performance of the partial oxidation based fuel processors introduced in section 5.1.1 through steady state models implementing a lumped parameter approach in Aspen Plus® [114]. The main compo-

nents of the analyzed fuel processors are: (i) partial oxidation reactor, (ii) water gas shift reactors, (iii) heat exchangers, and (iv) Auxiliaries. The partial oxidation and the water gas shift reactors are modeled as equilibrium reactors (called RGibbs in the modeling environment).In fact, Aspen Plus® calculates the equilibrium composition of the resulting flows minimizing the Gibbs free energy [114]. We consider the WGS and POX reactors adiabatic, therefore the thermal power produced increases the syngas temperature. The heat exchanger before the POX reactor is sized such that the reactants temperature entering the POX makes the syngas exiting the reactor at 1000 °C. Given that we do not perform off-design analysis we vary the heat exchanger size for every analyzed case, and we do not consider the variation of the heat transfer coefficient as a function of the flow rate. The heat exchanger between the water gas shift stages is an air cooled heat exchanger that keep the syngas temperature at 150 °C. The thermal power extracted in the latter could even be used for cogeneration in a detailed design of the system. The compressors have polytropic efficiency equal to 0.85 and mechanical efficiency equal to 0.9. The turbine, where present, has polytropic efficiency equal to 0.825 and mechanical efficiency equal to 0.9. Such values are conservative in order to be appropriate even for small scale systems.

In the modeling environment we use the Peng Robinson equation [114] of state to compute the thermodynamic properties of working fluids. In addition, for pure water streams, the steamNBS tables are used [117].

The methodology for the baseline fuel processor (Fig. 5.3) is similar and is reported in detail in chapter 1.

The fuel processor efficiency follows the definition given in chapter 1 and reads:

$$\eta_{\mathrm{fp}} = \frac{\dot{m}_{\mathrm{H_2}} \mathrm{LHV}_{\mathrm{H_2}}}{\dot{m}_{\mathrm{NG}} \mathrm{LHV}_{\mathrm{NG}}}, \tag{5.3}$$

where $\dot{m}_{\mathrm{H_2}}$ is the mass flow rate of the produced H_2 and $\mathrm{LHV}_{\mathrm{H_2}} = 120\,\mathrm{MJ/kg}$ is its lower heating value, $\dot{m}_{\mathrm{NG}}$ is the natural gas flow rate entering in the fuel processor, and $\mathrm{LHV}_{\mathrm{fuel}} = 46.7\,\mathrm{MJ/kg}$ is the lower heating value of the natural gas. In this chapter, we consider a NG based on UK composition that represent an average of all european compositions (Table 5.1) [136].

The power plant efficiency reads:

$$\eta_{\mathrm{pp}} = \frac{\dot{m}_{\mathrm{H_2}} \mathrm{LHV}_{\mathrm{H_2}} \eta_{\mathrm{FC}} + W_{\mathrm{t}} - W_{\mathrm{c}}}{\dot{m}_{\mathrm{NG}} \mathrm{LHV}_{\mathrm{NG}}}, \tag{5.4}$$

Table 5.1: *United Kingdom natural gas molar fraction composition [136].*

Component	Molar fraction [%]
CH_4	92.078
C_2H_6	3.405
C_3H_8	0.761
Normal butane (C_4H_{10})	0.177
Isobutane (C_4H_{10})	0.14
Normal pentane (C_5H_{12})	0.048
Isopentane (C_5H_{12})	0.061
Hexane and heavier ($C_6H_{14}+$)	0.09
CO_2	0.865
N_2	2.375

where η_{FC} is the estimated efficiency of a fuel cell downstream the fuel processor, W_{t} is the power of the turbine (where present), and W_{c} is the power of the compressors and pumps. The aim of this chapter is to characterize the fuel processor performance. Therefore, we assume that the produced syngas goes in a HT-PEMFC with $\eta_{\mathrm{FC}} = 0.5$ (based on LHV) and unitary hydrogen utilization factor. Such assumption on η_{FC} is consistent with literature on HT-PEMFCs [13, 39, 188] and with the results found in previous chapters. In fact, the efficiency of the automotive derivative fuel cell presented in chapter 1 varies between 45 % and 55 %. Moreover, the FCH-JU targets [189] consider $42\,\% < \eta_{\mathrm{FC}} < 62\,\%$ in 2024 for mid-sized installations. Finally, we note that the efficiency of HT-PEMFCs is not higly affected by fuel diluition [35]. Therefore, it is correct to perform initial evaluations considering a constant efficiency even if the syngas composition is not constant.

The power ratio is another relevant parameter to evaluate:

$$P = \frac{W_{\mathrm{t}} - W_{\mathrm{c}}}{\dot{m}_{\mathrm{H_2}} \mathrm{LHV}_{\mathrm{H_2}} \eta_{\mathrm{FC}}}. \tag{5.5}$$

Such power ratio is an important indicator to gain insights in the design of the CHP system.

5.2.1 Sensitivity Analysis

Three operating parameters are considered for the sensitivity analysis: (i) the air flow rate ratio, (ii) the water flow rate ratio, and (iii) the pressure

ratio. Such parametes influence η_{fp}, η_{pp}, and P by influencing the POX and WGS reactions yield, the thermal balance of the CHP system, and the power extracted from the turbine.

The air flow rate ratio reads:

$$\psi = \frac{\dot{n}_{\mathrm{air}}}{\dot{n}_{\mathrm{air,STO}}}, \tag{5.6}$$

where $\dot{n}_{\mathrm{air}}$ is the air molar flow rate, and $\dot{n}_{\mathrm{air,STO}}$ is the stoichiometric air molar flow rate considering the partial oxidation reaction. We explore the range $1 < \psi < 1.5$ expecting that the optimal value is higher than the stoichiometric $\psi = 1$ ratio.

The water flow rate ratio reads:

$$\phi = \frac{\dot{n}_{\mathrm{H_2O}}}{\dot{n}_{\mathrm{H_2O,STO}}}, \tag{5.7}$$

where $\dot{n}_{\mathrm{H_2O}}$ is the water molar flow rate, and $\dot{n}_{\mathrm{H_2O,STO}}$ is the stoichiometric water molar flow rate considering the water gas shift reaction with the carbon monoxide theoretically produced from the partial oxidation of the natural gas. We explore the range $0.5 < \phi < 1.4$ expecting that the optimal value is close to the stoichiometric $\phi = 1$ ratio. While varying ψ we fix ϕ to the optimal value and vice versa.

The pressure ratio reads:

$$\beta = \frac{p_{\mathrm{h}}}{p_{\mathrm{l}}}, \tag{5.8}$$

where p_{h} and p_{l} are the pressure values respectively at the outlet and at the inlet of the air compressor. We explore the range $3 < \beta < 9$ being the most common for TG systems with net electric power lower than 1 MW [190].

5.3 Results and discussion

The baseline power plant (Fig. 5.3) achieves $\eta_{\mathrm{fp}} = 0.804$ and $\eta_{\mathrm{pp}} = 0.396$ in optimal operating conditions. The fuel processor efficiency is 7 % higher than that observed in chapter 1 because the produced hydrogen is not lost for the purification.

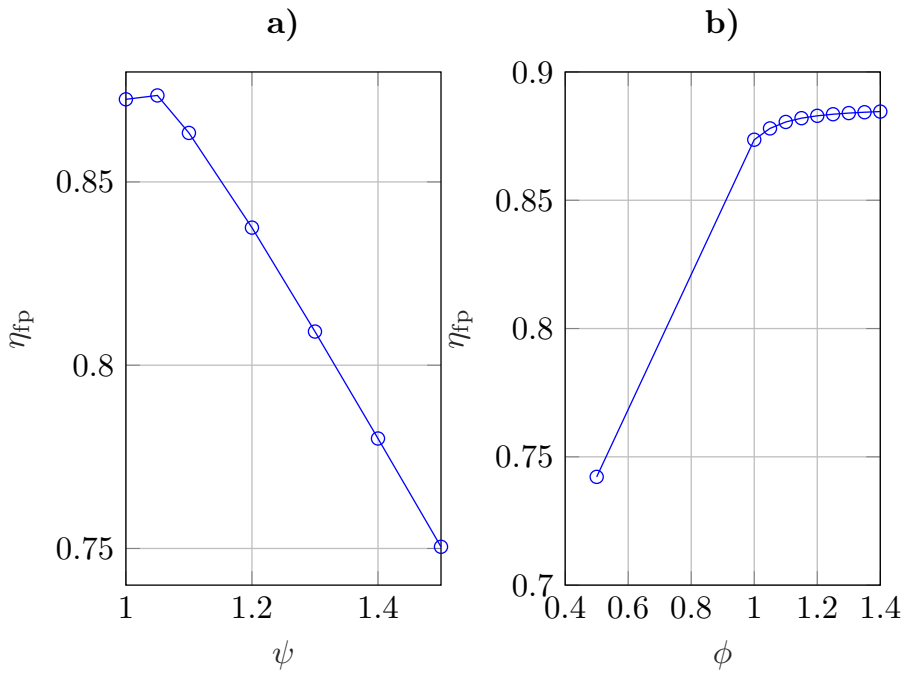

Figure 5.5: *Fuel processor efficiency of the non pressurized fuel processor based on partial oxidation as a function of: a) ψ while keeping $\phi = 1$, and b) ϕ while keeping $\psi = 1.05$.*

The fuel processor efficiency of the non pressurized scheme based on partial oxidation varies between 74.2 % and 88.5 % as a function of ψ and ϕ (Figure 5.5). The amount of excess air is a beneficial effect until $\psi = 1.05$ (Figure 5.5 a), further increasing such value makes the fuel processor to run on complete oxidation, reducing the amount of H_2 produced given the same NG input. The water gas shift is a crucial aspect for the POX based fuel processor (Figure 5.5 b). In fact, when feeding the system with sub-stoichiometric $\phi = 0.5$, η_{fp} is lower than 0.75 and reasonably the high CO content in the syngas can have negative effects on the fuel cell as well. Moreover, we observe that increasing the water intake always increases the efficiency because it increases the CO that is converted to H_2. However, such a trend is limited by the CO content in the syngas. In fact, η_{fp} increases with a decreasing marginal gain by increasing ϕ. Moreover, we expect that high water excess results in a decrease of the fuel cell efficiency due to the dilution of H_2 in the syngas.

The POX based fuel processor is thermally self-sufficient and all the

reacted hydrocarbons take part in the hydrogen production. Therefore, this fuel processor achieves the maximum $\eta_{\text{fp}} = 0.885$, that is 10% higher than the peak efficiency of the baseline fuel processor based on steam reforming.

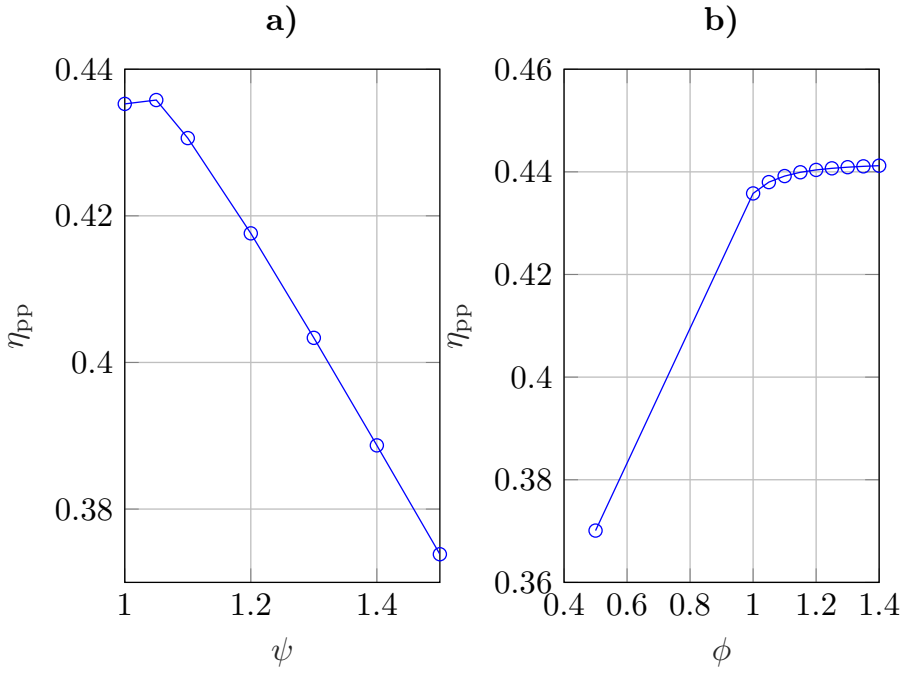

Figure 5.6: *Power plant efficiency of the non pressurized fuel processor based on partial oxidation as a function of: a) ψ while keeping $\phi = 1$, and b) ϕ while keeping $\psi = 1.05$.*

The power plant efficiency of the non pressurized fuel processor based on partial oxidation varies between 37 % and 44.1 % as a function of ψ and ϕ (Figure 5.6). η_{pp} has similar trends to η_{fp} because we consider the constant $\eta_{\text{FC}} = 0.5$ and the analyzed scheme dose not feature the gas turbine (whose power would depend on the flow rate and therefore on ψ and ϕ). The peak $\eta_{\text{pp}} = 0.441$ value is 11.4% higher than the peak power plant efficiency of the baseline plant.

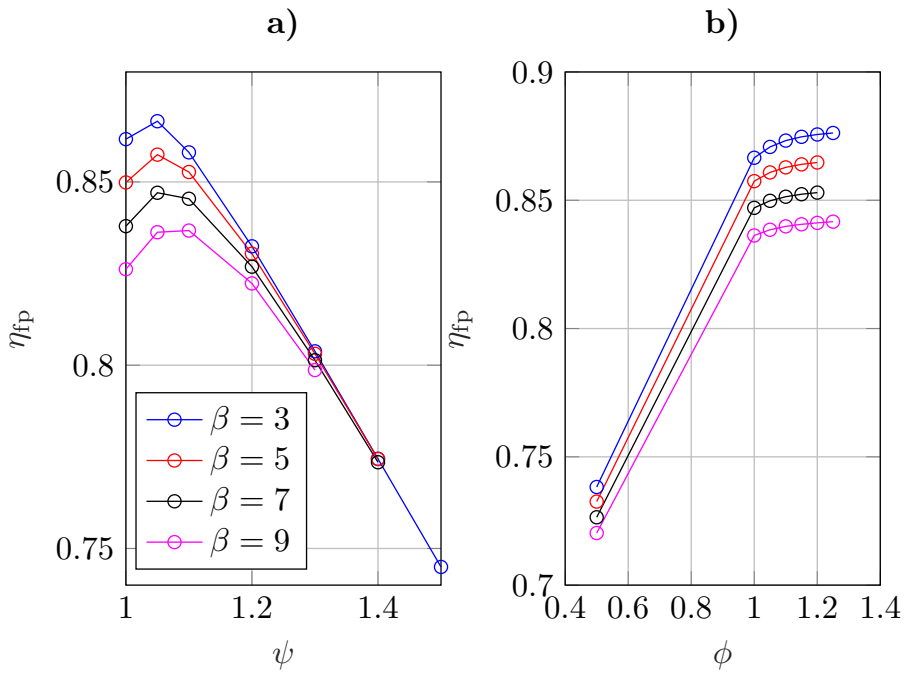

Figure 5.7: *Fuel processor efficiency of the concept A fuel processor as a function of: a) ψ while keeping $\phi = 1$, and b) ϕ while keeping $\psi = 1.05$.*

The fuel processor efficiency of the concept A fuel processor varies between 72 % and 87.6 % as a function of ψ, ϕ, and β (Figure 5.7). η_{fp} has the same correlation with ψ and ϕ observed commenting Figure 5.5. Moreover, increasing β decreases the fuel processor efficiency as a consequence of the shift in equilibrium compositions of the reactions. Specifically, increasing the pressure favors the complete combustion that is a mole preserving reaction and disfavors the partial oxidation that is a mole increasing reaction. The maximum $\eta_{\mathrm{fp}} = 87.6\,\%$ is observed at $\beta = 3$ and is 1% lower than the maximum value observed for the non pressurized fuel processor based on partial oxidation.

The pressure ratio also affects the operability of the fuel processor (Figure 5.7 a). In fact, by increasing ψ the switch from partial to complete oxidation appears sooner at high β, given the shift in equilibrium compositions of the reactions. Moreover, increasing β increases the compressor discharge temperature. The combination of these effects makes in some cases the reactor outlet temperature higher than 1000 °C even if the pre-heating heat exchanger is bypassed. We discard such exothermic

cases, in fact in Figure 5.7 a) the maximum ψ is 1.5 for $\beta = 3$, it is 1.4 for $5 \leq \beta \leq 7$, and it is 1.3 for $\beta = 9$.

The expansion in the turbine lowers the WGS inlet temperature limiting to $\phi = 1.25$ the maximum water flow rate ratio (Figure 5.7 b). In fact, by further increasing ϕ the low turbine discharge temperature makes the first stage WGS discharge temperature lower than the 150 °C resulting in the WGS line to be endothermic. Such an issue could be solved thermally integrating the FC and the fuel processor. However, the added plant cost and complexity would not justify the marginal η_{fp} gain. Also, at high ϕ the fuel cell could operate with lower efficiency given the H_2 dilution.

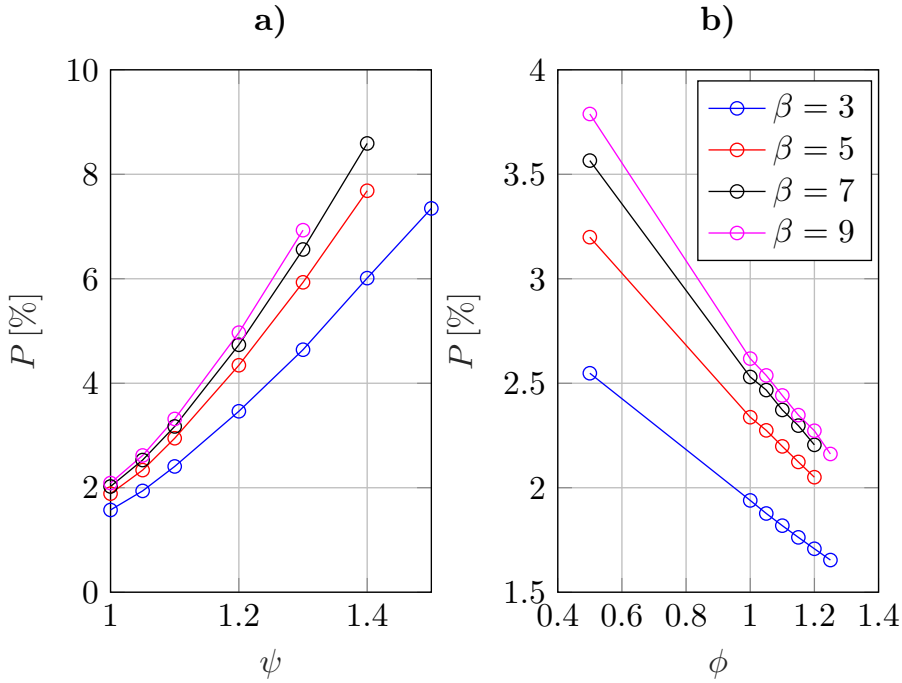

Figure 5.8: *Power ratio of the concept A fuel processor as a function of: a) ψ while keeping $\phi = 1$, and b) ϕ while keeping $\psi = 1.05$.*

The power ratio varies between 1.57 % and 8.59 % as a function of ψ, ϕ, and β (Figure 5.8). The power ratio monotonically increases by increasing ψ (Figure 5.8 a). In fact, by increasing ψ the fuel processor efficiency decreases, and therefore the HT-PEMFC power decreases. At the same time, the turbine power increases because both the flow rate and the inlet temperature increase with ψ. The inlet turbine temperature

increases by increasing ψ because the syngas furnishes less thermal power to the reactants given that the thermal power produced in the reactor increases. Moreover, the inlet turbine temperature increases because the higher syngas flow rate entails higher temperature of the mix of syngas and cold water, considering constant ϕ. P monotonically increases by increasing β (Figure 5.8) because the reactor is more prone to complete oxidation and therefore the turbine inlet temperature increases. Also, we can observe a compound effect of ψ and β on P (Figure 5.8 a). In fact, the power ratio increases of 195 % and of 232 % by increasing ψ from 1 to 1.3 for $\beta = 3$ and $\beta = 9$ respectively. Such compound effect originates because both ψ and β increase the gas turbine inlet temperature. The power ratio monotonically decreases by increasing ϕ (Figure 5.8 b). In fact, by increasing ϕ the fuel processor efficiency increases, and therefore the HT-PEMFC power increases. At the same time, increasing ϕ increases the flow rate in the turbine and also decreases the turbine inlet temperature due to the mix of hot syngas with cold water. The temperature decrease effect prevails the flow rate increase effect, globally lowering the turbine power.

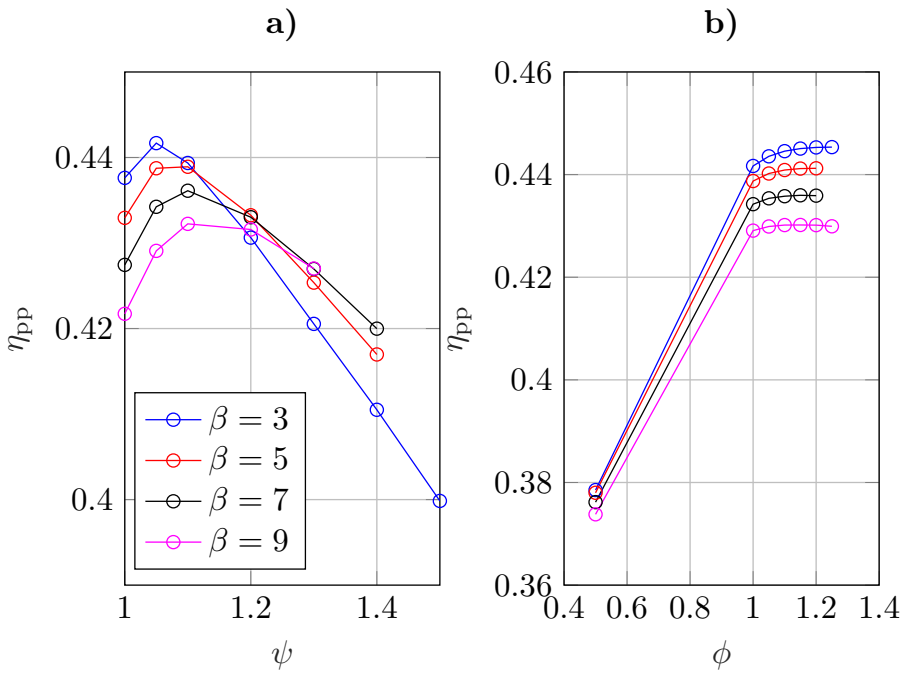

Figure 5.9: *Power plant efficiency of the concept A fuel processor as a function of: a) ψ while keeping $\phi = 1$, and b) ϕ while keeping $\psi = 1.05$.*

The power plant efficiency of the concept A fuel processor varies between 37.4 % and 44.5 % as a function of ψ, ϕ, and β (Figure 5.9). The power extracted from the turbine enables the concept A power plant to be more efficient than the non pressurized scheme, compensating the drop in the fuel processor efficiency. In fact, the maximum η_{pp} is 1% higher than the maximum value observed for the non pressurized fuel processor. The optimal operating conditions for η_{pp} are $\psi = 1.05$, $\phi = 1.25$, and $\beta = 3$.

Similar trends to those observed commenting Figure 5.7 correlate η_{pp} to ψ and ϕ. However, increasing β the optimal ψ increases from 1.05 to 1.1 (Figure 5.9 a)). In fact, the turbine power increases by increasing ψ because the flow rate and the turbine inlet temperature increase. Moreover, increasing β the power ratio increases (see Figure 5.8) meaning that the turbine power has higher impact on the overall CHP performance. For the same reasons, increasing ψ the optimal β increases. In fact, at $\psi = 1$ the optimal pressure ratio is $\beta = 3$, while at $\psi = 1.3$ the optimal β is 9.

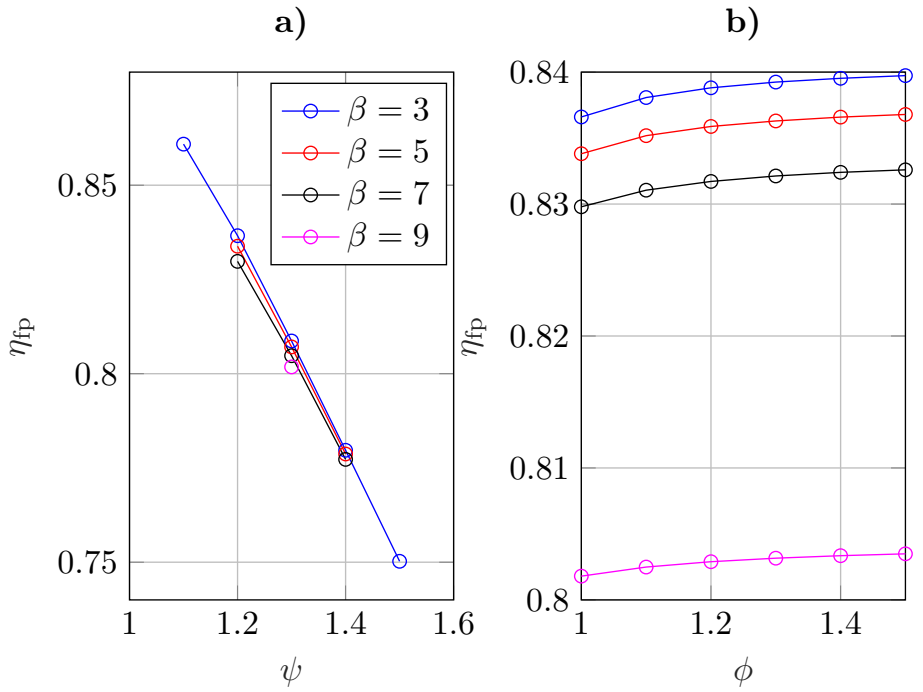

Figure 5.10: *Fuel processor efficiency of the concept B fuel processor as a function of: a) ψ while keeping $\phi = 1$, and b) ϕ while keeping $\psi = 1.2$ for $\beta \leq 7$, and $\psi = 1.3$ for $\beta = 9$.*

The fuel processor efficiency of the concept B scheme varies between 75 % and 86.1 % as a function of ψ, ϕ, and β (Figure 5.10). As already observed in Figure 5.7, also for concept B scheme η_{fp} monotonically decreases as ψ and β increase. Moreover, η_{fp} increases with a decreasing marginal gain by increasing ϕ. The feasible domain for the concept B scheme is narrower than the feasible domain for the concept A scheme. In fact, the syngas pre-heats the reactants after expanding the turbine and therefore at lower temperature than in concept A plant. As a consequence, the fuel processor is thermally self-sufficient only with a certain amount of complete oxidation i.e. for $\psi > 1.1$ at $\beta = 3$. Moreover, the discharge turbine temperature decreases as β increases. As a consequence, the minimum ψ is 1.2 for $5 \leq \beta \leq 7$ and 1.3 for $\beta = 9$. For the same reasons already observed for concept A fuel processor, the fuel processor turns in exothermic regime for $\psi > 1.3$ at $\beta = 9$ and for $\psi > 1.4$ at $5 \leq \beta \leq 7$.

The maximum η_{fp} is 2.8% lower than the maximum value observed for the non pressurized fuel processor based on partial oxidation. However,

the peak η_{fp} for concept B scheme is lower that for concept A scheme only for the narrower feasible domain. In fact, at the same ψ, β, and ϕ the two concepts achieve the same efficiency.

In this case, the global η_{fp} optimum is at $\phi = 1$ and $\psi = 1.1$ for $\beta = 3$. However, in the results reported in Figure 5.10 b) we fix for $\beta < 9$ $\psi = 1.2$, and for $\beta = 9$ $\psi = 1.3$ because it is the only feasible value at such pressure ratio. In this way, we do not explore the efficiency of the $\beta = 3$ case at $\psi = 1.1$ and high ϕ but we can compare most of the results with the same ψ. Also, for concept B scheme we do not investigate $\phi = 0.5$ having already concluded in the previous analysis that such operating point is far from optimal conditions.

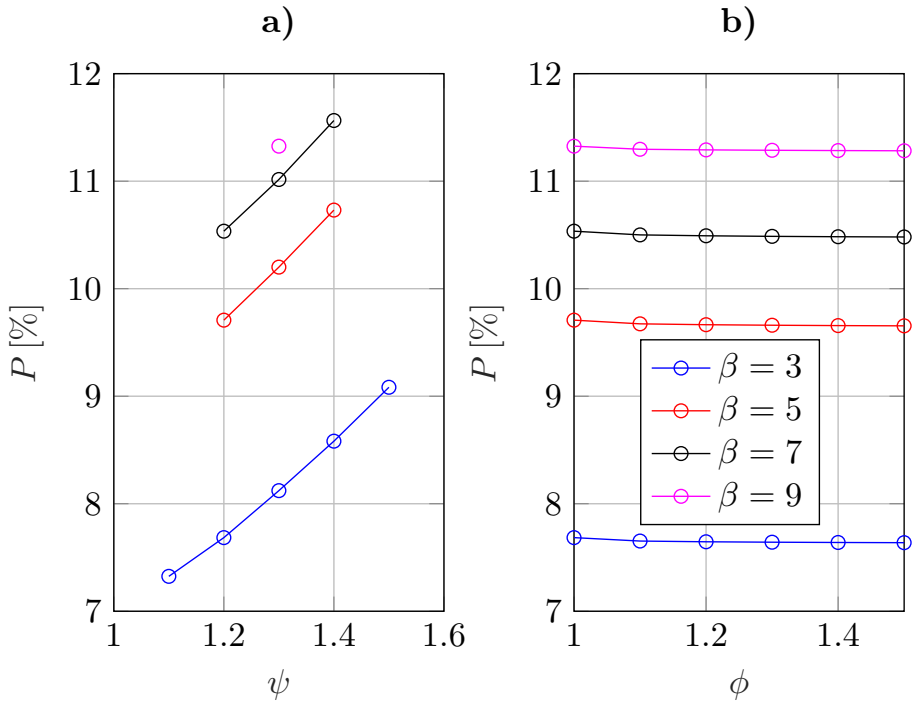

Figure 5.11: *Power ratio of the concept B fuel processor as a function of: a) ψ while keeping $\phi = 1$, and b) ϕ while keeping $\psi = 1.2$ for $\beta \leq 7$, and $\psi = 1.3$ for $\beta = 9$.*

The power ratio varies between 7.3 % and 11.6 % as a function of ψ, ϕ, and β (Figure 5.11). The peak P of concept B plant is 35 % higher than the peak P of concept A plant thanks to the fixed inlet turbine temperature to 1000 °C. The power ratio monotonically increases with ψ

(Figure 5.11 a) as a consequence of the decrease of the HT-PEMFC power and of the increase of the turbine power due to the increased flow rate. P is insensitive to ϕ (Figure 5.11 b) because water injection occurs after the turbine.

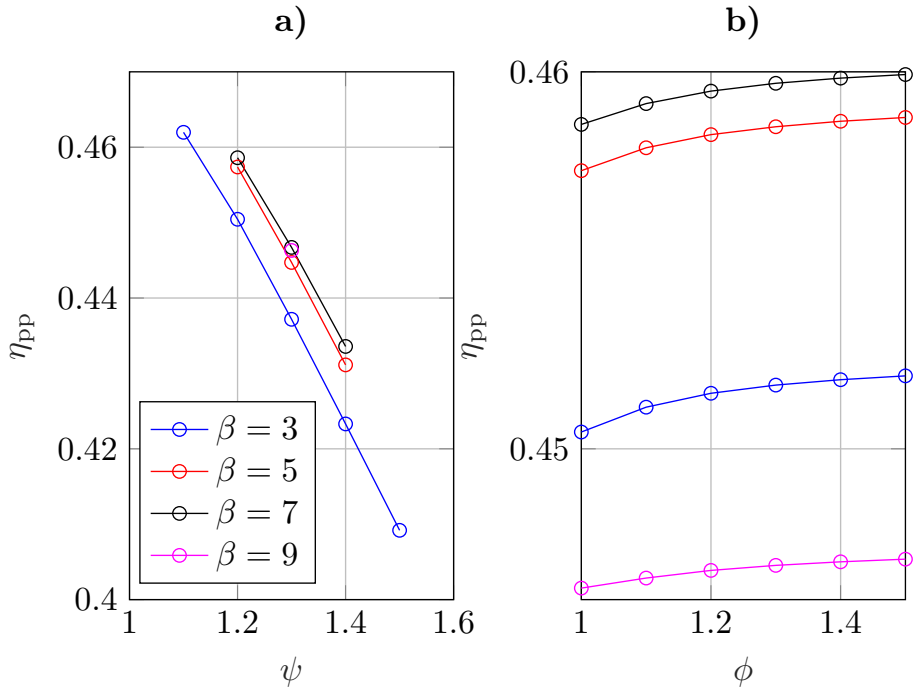

Figure 5.12: *Power plant efficiency of the concept B fuel processor as a function of: a) ψ while keeping $\phi = 1$, and b) ϕ while keeping $\psi = 1.2$ for $\beta \leq 7$, and $\psi = 1.3$ for $\beta = 9$.*

The power plant efficiency of the concept B fuel processor varies between 41 % and 46.2 % as a function of ψ, ϕ, and β (Figure 5.12). The optimal operating parameters are $\psi = 1.1$, $\phi = 1$, and $\beta = 3$. The overall peak efficiency could be few decimal points higher analyzing high ϕ values at $\psi = 1.1$ and $\beta = 3$. η_{pp} varies with ψ and ϕ following the same trends observed in Figure 5.10. Moreover, at fixed ψ and ϕ, η_{pp} monotonically increases with β (Figure 5.12 a), given the increase in the turbine power.

The power extracted from the turbine enables the concept B power plant to be more efficient than the concept A and also of the non pressurized schemes. In fact, the maximum η_{pp} is 4.5% higher than the maximum value observed for the non pressurized fuel processor and 3.7% higher than

the maximum value observed for the concept A scheme.

5.3.1 Discussion

The POX fuel processor appears to be the most efficient choice considering η_{pp} for HT-PEMFCs. Such fuel cells have a temperature high enough to tolerate impurities in the feed. However, the operating temperature is not high enough to produce thermal power that can sustain the reforming reactor. For PEMFCs the steam reforming is still the best choice because it gives relatively clean syngas that is easier to purify. For SOFCs the steam reforming can be competitive as well because high temperature thermal power can be recovered from the fuel cell to sustain the reaction without decreasing the fuel processor efficiency.

The power ratio for the optimal operating conditions for concept A scheme is 2 %. The smallest turbine on the market is the 3 kW MTT Enertwin [190]. Using such turbine would result in a 150 kW fuel cell. Considering the more usual micro turbine, the 30 kW Capstone C30 [190] (the smallest of such manufacturer) would result in a 1.5 MW fuel cell. Fuel cells units of such power are above the potential of the nowadays industry [9].

Considering concept B scheme in the optimal operating conditions the power ratio is 7.5 % and makes the application of state of the art micro turbines and fuel cells possible. Moreover, the fuel processor can run on higher pressure ratios resulting in a power ratio around 10.5 % only with a marginal efficiency drop. However, also with concept B scheme, micro turbines are the best choice to match the fuel cell industry production capabilities. Micro turbines are the best choice also because they run with limited pressure ratio that matches the optimal $\beta = 3$ found from the sensitivity analysis. Such micro turbines with low pressure ratio are generally regenerative. In this sense, the concept B scheme appears the best choice also because is intrinsically similar to a regenerative turbine scheme and can be developed starting from state of the art commercial systems.

The high $\eta_{pp} = 46.2\,\%$ for the concept B scheme is a relevant result. Such high efficiency can be reached with CHP systems based on PEMFCs only with membrane-integrated fuel reformer and with very low set point (see Chapter 1). Moreover, such high efficiency of the HT-PEMFCs-based system is achieved with a very simple fuel processor that presumably has

a lower cost than the membrane-integrated steam reforming-based fuel processor needed for PEMFCs.

5.4 Summary

In this chapter we present the concept of an innovative hybrid HT-PEMFC-GT CHP system. Specifically, we retrieve the performance of such system using a steady state and lumped parameters model. In the chapter we prove the advantages of the proposed system with respect to a HT-PEMFC CHP featuring a state of the art fuel processor based on steam reforming. Also, we evaluate the advantages of the turbine integration by comparing the performance of the innovative hybrid HT-PEMFC-GT CHP system with a system without gas turbine in the fuel processor. Finally, by comparing two different fuel processors concepts we find the optimal configuration to integrate the gas turbine in the fuel processor.

Results show that the fuel processor efficiency of the non-pressurized POX based system can be as high as 88.5 %. Such value is 10% higher than the peak efficiency of the baseline fuel processor based on steam reforming. Also, the fuel processor efficiency of the concept A and concept B hybrid systems is respectively 1% and 2.8% lower than the maximum value observed for the non pressurized fuel processor based on partial oxidation. However, the concept A and concept B hybrid systems register respectively power plant efficiency 1% and 4.5% higher than the non pressurized fuel processor based on partial oxidation. Therefore, the most performing scheme is the concept B plant that with $\eta_{\mathrm{pp}} = 46.2\,\%$ has comparable performance to CHP systems based on PEMFCs with membrane-integrated fuel processor. Also, we note that the turbine-integrated POX-based fuel processor is intrinsically simpler and presumably cheaper than the membrane-integrated steam reforming-based fuel processor needed for PEMFCs. Moreover, the POX-based fuel processor has better dynamic performance being based on exothermic reactions and not requiring external power to run the auxiliaries. The ratio between the turbine and fuel cell power is lower than 15 %, meaning that state of the art fuel cell systems with power lower than 1 MW can be coupled only with micro gas turbines. Also, the optimal $\beta = 3$ and the concept B scheme that is similar to traditional regenerative gas turbine schemes confirm that the most appropriate choice is the micro gas turbines.

The nitrogen dilution of the POX based schemes could affect the fuel cell performance. To thoroughly evaluate this aspect we are developing a 1-D HT-PEMFC model to integrate with the fuel processor model. With such refinement we also will be able to precisely quantify the thermal power produced from the CHP.

Also, the proposed system can effectively integrate with renewable energy sources. In fact, the POX based fuel processor can be fed with the oxygen produced from the electrolyzer producing high purity syngas. In this way, it is possible to exploit and potentially store the O_2 produced from the electrolyzers that is generally dispersed in the atmosphere.

Conclusions

This thesis studies through steady state modeling and optimization algorithms the performance and the economic and environmental advantages of innovative energy systems based on three different fuel cell technologies: (i) polymer electrolyte membrane fuel cells, (ii) high temperature polymer electrolyte membrane fuel cells, and (iii) solid oxide fuel cells.

Chapter 1 studies the performance of combined heating and power systems based on automotive derivative fuel cell whose fuel processors integrate selective membranes. The results show that the usage of selective membranes can significantly boost the power plant efficiency. Specifically, the fuel processor nominal efficiency increases from 75.1 %, for a state of the art configuration using PSA purification, to 83.8 %, for a fuel processing plant with selective membranes integrated in the steam reformer. As a consequence, the overall electrical efficiency rises from 35.0 % to 38.4 % at maximum power output. The positive effect of membrane integration lies in the shift of the reforming reaction towards products and in the better thermal integration of the fuel processor. Moreover, it appears that selective membranes used as separator or integrated in the water gas shift reactor can ensure limited performance boost. In addition, the necessary membrane surface, that largely determine the power plant cost, decreases if the separator is integrated in the reactors. The integration of Pd-based selective membranes leads also to an important fuel processing plant simplification, in particular when the reforming membrane reactor configuration is considered.

Chapter 2 studies the design of a membrane-integrated natural gas reforming system throuh a systematic sensitivity analysis. Specifically, such analysis considers as variables: (i) the excess steam to fuel ratio Φ, (ii) the excess air to fuel ratio Ψ, (iii) the dimensionless reformer pressure Π, and (iv) the dimensionless reformer temperature τ. The results show that the operating parameters have a relevant impact on the fuel processor

efficiency, that varies between 75 % and 84 %. Also, the operating parameters do not mutually interact if the retentante is not rich in fuel content. In fact, the retentate composition has a significant impact on the results. Moreover, the fuel processor efficiency is mostly sensitive to a variation of Φ and τ near the global optimum. Also, the operating temperature has a relevant impact on the operation of the system. In fact, decreasing τ for more than 8 % from the optimal value results in oxygen starvation in the catalytic oxydation reactor. Finally, the analysis shows that only dense ceramic membranes can withstand the optimal operation of the fuel processor. Moreover, such membranes appear to be compatible for the integration in a SRR reactor without drastically changing its design.

Chapter 3 studies the integration of low temperature thermally driven cooling technologies in an automotive derivative combined heating and power system. The results show that the integration of a half-effect absorption chiller in an automotive derivative PEMFC based power plant is technically feasible and guarantees environmental and economic benefits for a broad spectrum of energy contexts and climatic conditions. Specifically, in an average European energy context, thanks to the CHCP system CO_2 emissions are reduced for all the considered climatic conditions. On the contrary for the CHP only system such a behavior is not observed. Moreover, the climatic condition only marginally influence the economic feasibility of the CHCP systems while the energy context dominates it. On the contrary, the climatic conditions dominates the environmental performance of distributed generation systems.

Chapter 4 compares integrated fuel processing options for biogas-fed solid oxide fuel cell combined heating and power systems. Results show that the cold recirculation scheme always requires external water supply, implying durability issues. Also, the anode-supported fuel cell results in narrower operating windows for the more severe temperature difference constraint. Moreover, the biogas composition influences the operating windows, the efficiency, and the external water consumption. Specifically, with high methane content in the biogas: (i) the safe operating dominion is broader, (ii) the efficiency is higher, and (iii) the external water consumption is higher.

Chapter 4 studies an innovative hybrid high temperature polymer electrolyte membrane fuel cell - gas turbine combined heating and power system whose fuel processor produces hydrogen from natural gas through the partial oxidation reaction. Results show that the fuel processor efficiency

of the non-pressurized POX based system can be as high as 88.5 %. Such value is 10% higher than the peak efficiency of the baseline fuel processor based on steam reforming. Therefore, the POX based system is the best alternative for HT-PEMFCs based CHP systems, given the fuel flexibility. The regenerative turbine configuration of the POX based system reaches in optimal operating conditions a power plant electrical efficiency of 46.2 %. Such value is 4.5% higher than that observed for the non pressurized fuel processor based on partial oxidation, meaning that the turbine in the fuel processor has a relevant impact. Moreover, the hybrid HT-PEMFC-GT CHP system achieves an electrical efficiency value comparable to that of a CHP systems based on PEMFCs with membrane-integrated fuel processor while being intrinsically simpler, presumably cheaper, and having better dynamic performance. Finally, the ratio between the turbine and fuel cell power is lower than 15 %, meaning that state of the art fuel cell systems can only be coupled with micro gas turbines.

List of Figures

List of Tables

Bibliography

[1] Climate.gov, Climate Change: Atmospheric Carbon Dioxide.
URL https://www.climate.gov/news-features/understanding-climate/climate-change-atmospheric-carbon-dioxide#:~:text=The%20global%20average%20atmospheric%20carbon,least%20the%20past%20800%2C000%20years

[2] J.-R. Petit, J. Jouzel, D. Raynaud, N. I. Barkov, J.-M. Barnola, I. Basile, M. Bender, J. Chappellaz, M. Davis, G. Delaygue, et al., Climate and atmospheric history of the past 420,000 years from the vostok ice core, antarctica, Nature 399 (6735) (1999) 429–436.

[3] O. Edenhofer, Climate change 2014: mitigation of climate change, Vol. 3, Cambridge University Press, 2015.

[4] S. Solomon, G.-K. Plattner, R. Knutti, P. Friedlingstein, Irreversible climate change due to carbon dioxide emissions, Proceedings of the national academy of sciences 106 (6) (2009) 1704–1709.

[5] E. SNET, ETIP SNET VISION 2050.
URL https://www.etip-snet.eu/etip-snet-vision-2050/

[6] P. Colbertaldo, G. Guandalini, S. Campanari, Modelling the integrated power and transport energy system: The role of power-to-gas and hydrogen in long-term scenarios for italy, Energy 154 (2018) 592–601.

[7] D. Hart, F. Lehner, R. Rose, J. Lewis, M. Klippenstein, The Fuel Cell Industry Review 2017, Tech. rep., E4tech (2017).
URL http://www.fuelcellindustryreview.com/archive/TheFuelCellIndustryReview2017.pdf

[8] D. Hart, F. Lehner, S. Jones, J. Lewis, M. Klippenstein, The Fuel Cell Industry Review 2018, Tech. rep., E4tech (2018).
URL http://www.fuelcellindustryreview.com/archive/TheFuelCellIndustryReview2018.pdf

[9] D. Hart, F. Lehner, S. Jones, J. Lewis, The Fuel Cell Industry Review 2019, Tech. rep., E4tech (2019).
URL http://www.fuelcellindustryreview.com/

[10] R. Peters, R. Deja, M. Engelbracht, M. Frank, L. Blum, D. Stolten, et al., Efficiency analysis of a hydrogen-fueled solid oxide fuel cell system with anode off-gas recirculation, Journal of Power Sources 328 (2016) 105–113.

[11] Y. Haseli, Maximum conversion efficiency of hydrogen fuel cells, international journal of hydrogen energy 43 (18) (2018) 9015–9021.

[12] F. Cappa, A. L. Facci, S. Ubertini, Proton exchange membrane fuel cell for cooperating households: A convenient combined heat and power solution for residential applications, Energy 90 (2015) 1229–1238.

[13] E. Jannelli, M. Minutillo, A. Perna, Analyzing microcogeneration systems based on LT-PEMFC and HT-PEMFC by energy balances, Applied Energy 108 (2013) 82–91.

[14] S. Pellegrino, A. Lanzini, P. Leone, Techno-economic and policy requirements for the market-entry of the fuel cell micro-CHP system in the residential sector, Applied Energy 143 (2015) 370–382.

[15] A. Adam, E. S. Fraga, D. J. Brett, Options for residential building services design using fuel cell based micro-CHP and the potential for heat integration, Applied Energy 138 (2015) 685–694.

[16] F. Calise, R. D. Figaj, N. Massarotti, A. Mauro, L. Vanoli, Polygeneration system based on PEMFC, CPVT and electrolyzer: Dynamic simulation and energetic and economic analysis, Applied Energy 192 (2017) 530–542.

[17] E. Jannelli, M. Minutillo, R. Cozzolino, G. Falcucci, Thermodynamic performance assessment of a small size CCHP (combined cooling heating and power) system with numerical models, Energy 65 (2014) 240–249.

[18] N. Sammes, R. Boersma, Small-scale fuel cells for residential applications, Journal of Power sources 86 (1-2) (2000) 98–110.

[19] H. Onovwiona, V. I. Ugursal, Residential cogeneration systems: review of the current technology, Renewable and Sustainable Energy Reviews 10 (5) (2006) 389–431.

[20] F. Barbir, PEM fuel cells, in: Fuel Cell Technology, Springer, 2006, pp. 27–51.

[21] R. O'hayre, S.-W. Cha, F. B. Prinz, W. Colella, Fuel Cell Fundamentals, John Wiley & Sons, 2016.

[22] EG&G technical services, Fuel Cell Handbook, seventh edition, Inc., Albuquerque, NM, DOE/NETL-2004/1206 (2004).

[23] F. Baratto, U. M. Diwekar, D. Manca, Impacts assessment and tradeoffs of fuel cell based auxiliary power units: part II. Environmental and health impacts, LCA, and multi-objective optimization, Journal of power sources 139 (1-2) (2005) 214–222.

[24] S. C. Singhal, Advances in solid oxide fuel cell technology, Solid State Ionics 135 (1-4) (2000) 305–313.

[25] T. Ackermann, G. Andersson, L. Söder, Distributed generation: a definition, Electric power systems research 57 (3) (2001) 195–204.

[26] J. Sadhukhan, Distributed and micro-generation from biogas and agricultural application of sewage sludge: Comparative environmental performance analysis using life cycle approaches, Applied Energy 122 (2014) 196–206.

[27] The fuel cell industry review 2013, Tech. rep., Fuel Cell Today (2013).
URL http://www.fuelcelltoday.com/media/1889744/fct_review_2013.pdf

[28] R. Cozzolino, L. Tribioli, G. Bella, Power management of a hybrid renewable system for artificial islands: A case study, Energy 106 (2016) 774–789.

[29] Y. Zhang, A. Lundblad, P. E. Campana, J. Yan, Comparative study of battery storage and hydrogen storage to increase photovoltaic

self-sufficiency in a residential building of sweden, Energy Procedia 103 (2016) 268–273.

[30] International Energy Agency, Medium-Term Renewable Energy Market Report, OECD/IEA., http://www.iea.org/textbase/npsum/mtrenew2013sum.pdf (2013).

[31] G. W. Crabtree, M. S. Dresselhaus, M. V. Buchanan, The hydrogen economy, Physics today 57 (12) (2004) 39–44.

[32] Y. Zhang, P. E. Campana, A. Lundblad, J. Yan, Comparative study of hydrogen storage and battery storage in grid connected photovoltaic system: Storage sizing and rule-based operation, Applied energy 201 (2017) 397–411.

[33] C. Zhang, J. B. Greenblatt, M. Wei, J. Eichman, S. Saxena, M. Muratori, O. J. Guerra, Flexible grid-based electrolysis hydrogen production for fuel cell vehicles reduces costs and greenhouse gas emissions, Applied Energy 278 (2020) 115651.

[34] D. Carter, Fuel Cell Residential Micro-CHP Developments in Japan, Tech. rep., Fuel Cell Today (2012).
URL http://www.fuelcelltoday.com/media/1597029/\29-02-12_ene-farm.pdf

[35] M. G. Waller, M. R. Walluk, T. A. Trabold, Performance of high temperature pem fuel cell materials. part 1: Effects of temperature, pressure and anode dilution, international journal of hydrogen energy 41 (4) (2016) 2944–2954.

[36] Y. Devrim, A. Albostan, H. Devrim, Experimental investigation of co tolerance in high temperature pem fuel cells, International Journal of Hydrogen Energy 43 (40) (2018) 18672–18681.

[37] V. K. Krastev, G. Falcucci, E. Jannelli, M. Minutillo, R. Cozzolino, 3d cfd modeling and experimental characterization of ht pem fuel cells at different anode gas compositions, International Journal of Hydrogen Energy 39 (36) (2014) 21663–21672.

[38] A. H. Mamaghani, B. Najafi, A. Casalegno, F. Rinaldi, Predictive modelling and adaptive long-term performance optimization of an

ht-pem fuel cell based micro combined heat and power (chp) plant, Applied Energy 192 (2017) 519–529.

[39] N. Zuliani, R. Taccani, Microcogeneration system based on htpem fuel cell fueled with natural gas: Performance analysis, Applied energy 97 (2012) 802–808.

[40] L. Wang, Y. Zhang, M. Pérez-Fortes, P. Aubin, T.-E. Lin, Y. Yang, F. Maréchal, et al., Reversible solid-oxide cell stack based power-to-x-to-power systems: Comparison of thermodynamic performance, Applied Energy 275 (2020) 115330.

[41] D. Simbeck, E. Chang, Hydrogen supply: cost estimate for hydrogen pathways–scoping analysis, National Renewable Energy Laboratory 71.

[42] I. Dincer, C. Acar, Review and evaluation of hydrogen production methods for better sustainability, International journal of hydrogen energy 40 (34) (2015) 11094–11111.

[43] R. S. El-Emam, H. Özcan, Comprehensive review on the techno-economics of sustainable large-scale clean hydrogen production, Journal of Cleaner Production 220 (2019) 593–609.

[44] E. Barbuzza, G. Buceti, A. Pozio, M. Santarelli, S. Tosti, Gasification of wood biomass with renewable hydrogen for the production of synthetic natural gas, Fuel 242 (2019) 520–531.

[45] J. D. Holladay, J. Hu, D. L. King, Y. Wang, An overview of hydrogen production technologies, Catalysis today 139 (4) (2009) 244–260.

[46] E. Drioli, G. Barbieri, A. Brunetti, Membrane Engineering for the Treatment of Gases Volume 2: Gas-separation Issues Combined with Membrane Reactors: Edition 2, Royal Society of Chemistry, 2017.

[47] J. A. Turner, Sustainable hydrogen production, Science 305 (5686) (2004) 972–974.

[48] A. Iulianelli, S. Liguori, Y. Huang, A. Basile, Model biogas steam reforming in a thin pd-supported membrane reactor to generate clean hydrogen for fuel cells, Journal of Power Sources 273 (2015) 25–32.

[49] F. C. S. Committee, et al., Information Report on the Development of a Hydrogen Quality Guideline for Fuel Cell Vehicles, SAE, J2719, International Organization for Standardization 2 (2008) 14687–2.

[50] G. Bernardo, T. Araújo, T. da Silva Lopes, J. Sousa, A. Mendes, Recent advances in membrane technologies for hydrogen purification, International Journal of Hydrogen Energy 45 (12) (2020) 7313–7338.

[51] N. Al-Mufachi, N. Rees, R. Steinberger-Wilkens, Hydrogen selective membranes: A review of palladium-based dense metal membranes, Renewable and Sustainable Energy Reviews 47 (2015) 540–551.

[52] S. Sircar, T. Golden, Purification of hydrogen by pressure swing adsorption, Separation Science and Technology 35 (5) (2000) 667–687.

[53] F. V. Lopes, C. A. Grande, A. E. Rodrigues, Activated carbon for hydrogen purification by pressure swing adsorption: Multicomponent breakthrough curves and psa performance, Chemical Engineering Science 66 (3) (2011) 303–317.

[54] A. Malek, S. Farooq, Hydrogen purification from refinery fuel gas by pressure swing adsorption, AIChE Journal 44 (9) (1998) 1985–1992.

[55] S.-I. Yang, D.-Y. Choi, S.-C. Jang, S.-H. Kim, D.-K. Choi, Hydrogen separation by multi-bed pressure swing adsorption of synthesis gas, Adsorption 14 (4-5) (2008) 583–590.

[56] T. Bacquart, K. Arrhenius, S. Persijn, A. Rojo, F. Auprêtre, B. Gozlan, N. Moore, A. Morris, A. Fischer, A. Murugan, et al., Hydrogen fuel quality from two main production processes: Steam methane reforming and proton exchange membrane water electrolysis, Journal of Power Sources 444 (2019) 227170.

[57] M. Asgari, H. Anisi, H. Mohammadi, S. Sadighi, Designing a commercial scale pressure swing adsorber for hydrogen purification, Pet. Coal 56 (5) (2014) 552–561.

[58] H. Li, Z. Liao, J. Sun, B. Jiang, J. Wang, Y. Yang, Modelling and simulation of two-bed psa process for separating h2 from methane steam reforming, Chinese Journal of Chemical Engineering 27 (8) (2019) 1870–1878.

[59] A. Abdeljaoued, F. Relvas, A. Mendes, M. H. Chahbani, Simulation and experimental results of a psa process for production of hydrogen used in fuel cells, Journal of environmental chemical engineering 6 (1) (2018) 338–355.

[60] S. Reddy, S. Vyas, Recovery of carbon dioxide and hydrogen from psa tail gas, Energy Procedia 1 (1) (2009) 149–154.

[61] S. Peramanu, B. Cox, B. Pruden, Economics of hydrogen recovery processes for the purification of hydroprocessor purge and off-gases, International Journal of Hydrogen Energy 24 (5) (1999) 405–424.

[62] X. Hu, Y. Huang, S. Shu, Y. Fan, N. Xu, Toward effective membranes for hydrogen separation: Multichannel composite palladium membranes, Journal of power sources 181 (1) (2008) 135–139.

[63] Z. W. Dunbar, D. Chu, Thin palladium membranes supported on microstructured nickel for purification of reformate gases, Journal of Power Sources 217 (2012) 47–53.

[64] L. Roses, G. Manzolini, S. Campanari, E. De Wit, M. Walter, Techno-economic assessment of membrane reactor technologies for pure hydrogen production for fuel cell vehicle fleets, Energy & Fuels 27 (8) (2013) 4423–4431.

[65] L. F. Cabeza, D. Urge-Vorsatz, M. A. McNeil, C. Barreneche, S. Serrano, Investigating greenhouse challenge from growing trends of electricity consumption through home appliances in buildings, Renewable and Sustainable Energy Reviews 36 (2014) 188–193.

[66] D. Ürge-Vorsatz, L. F. Cabeza, S. Serrano, C. Barreneche, K. Petrichenko, Heating and cooling energy trends and drivers in buildings, Renewable and Sustainable Energy Reviews 41 (2015) 85–98.

[67] S. Serrano, D. Ürge-Vorsatz, C. Barreneche, A. Palacios, L. F. Cabeza, Heating and cooling energy trends and drivers in Europe, Energy 119 (2017) 425–434.

[68] International Energy Agency , Combined heat and power Evaluating the benefits of greater global investment (2008).

[69] G. Chicco, P. Mancarella, Distributed multi-generation: a comprehensive view, Renewable and Sustainable Energy Reviews 13 (3) (2009) 535–551.

[70] International Energy Agency , Distributed Generation in Liberalised Electricity Markets (2002).

[71] K. Y. Lau, M. Yousof, S. Arshad, M. Anwari, A. Yatim, Performance analysis of hybrid photovoltaic/diesel energy system under Malaysian conditions, Energy 35 (8) (2010) 3245–3255.

[72] A. Franco, P. Salza, Strategies for optimal penetration of intermittent renewables in complex energy systems based on techno-operational objectives, Renewable Energy 36 (2) (2011) 743–753.

[73] M. Naqvi, E. Dahlquist, J. Yan, Complementing existing CHP plants using biomass for production of hydrogen and burning the residual gas in a CHP boiler, Biofuels 8 (6) (2017) 675–683.

[74] The U.S. Census Bureau and the U.S. Department of Housing and Urban Development, Monthly new residential construcitons (February 2018).
URL https://www.census.gov/construction/nrc/pdf/newresconst.pdf

[75] A. L. Facci, V. Cigolotti, E. Jannelli, S. Ubertini, Technical and economic assessment of a sofc-based energy system for combined cooling, heating and power, Applied Energy.

[76] J. Deng, R. Wang, G. Han, A review of thermally activated cooling technologies for combined cooling, heating and power systems, Progress in Energy and Combustion Science 37 (2) (2011) 172–203.

[77] P. Srikhirin, S. Aphornratana, S. Chungpaibulpatana, A review of absorption refrigeration technologies, Renewable and sustainable energy reviews 5 (4) (2001) 343–372.

[78] H. Demir, M. Mobedi, S. Ülkü, A review on adsorption heat pump: Problems and solutions, Renewable and Sustainable Energy Reviews 12 (9) (2008) 2381–2403.

[79] K. Daou, R. Wang, Z. Xia, Desiccant cooling air conditioning: a review, Renewable and Sustainable Energy Reviews 10 (2) (2006) 55–77.

[80] A. L. Facci, S. Ubertini, Analysis of a fuel cell combined heat and power plant under realistic smart management scenarios, Applied Energy 216 (2018) 60–72.

[81] Ballard, ClearGen specification sheet.
URL http://pdf.directindustry.com/pdf/ballard/\cleargen-multi-mw-systems/22779-383697.html

[82] Ballard, Economics of Fuel Cell Solutions for Backup Power.
URL http://ballard.com/files/PDF/Backup_Power/\BUP_EmrgncyEcon_EGen_091712-01.pdf

[83] Micro-CHP, PEM fuel cells.
URL http://www.microchap.info/pem_fuel_cells.htm

[84] Doosan, PuroCell Model 400.
URL http://www.doosanfuelcell.com/attach_files/link/\PureCell%20Model%20400%20Datasheet.pdf

[85] Elcore 2400 Max - das Komplettpaket.
URL http://www.elcore.com/elcore-energiesysteme/\elcore-2400-max/

[86] I. Staffell, R. Green, The cost of domestic fuel cell micro-chp systems, International Journal of hydrogen energy 38 (2) (2013) 1088–1102.

[87] Inhouse engineering, Fuel cell μCHP system inhouse5000+.
URL https://www.inhouse-engineering.com/en/fuel-cell\-systems/products/fuel-cell-chp-system-\inhouse5000plus/

[88] Tropical Green technologies, 5 kW Hydrogeno Fuel Cell Generator.
URL http://www.tropical.gr/fuel-cell-power-\generators/5kw-fc-power-generator.html$\sharp$5kw_2

[89] Fuel cell boiler Vitovalor 300-P.
URL http://www.viessmann.co.uk/en/residential\-buildings/combined-heat-and-power-generation/

\micro-chp-unit-based-on-a-fuel-cell/vitovalor-\300p.html

[90] Fuel cells and hydrogen joint undertaking (FCH JU) multi-annual work plan 2014-2020.
URL http://www.fch.europa.eu/sites/default/files/\FCH2%20JU%20-%20Multi%20Annual%20Work%20Plan%20\-%20MAWP%20%28ID%20623483%29.pdf

[91] F. Cappa, A. L. Facci, S. Ubertini, Proton exchange membrane fuel cell for cooperating households: A convenient combined heat and power solution for residential applications, Energy 90 (2015) 1229–1238.

[92] J. Spendelow, J. Marcinkoski, D. Papageorgopoulos, Micro CHP fuel cell system targets (2012).
URL https://www.hydrogen.energy.gov/pdfs/\11016_micro_chp_target.pdf

[93] B. D. James, A. B. Spisak, W. G. Colella, Manufacturing cost analysis of stationary fuel cell systems, Tech. rep., Strategic Analysis (2012).

[94] M. R. Weimar, L. A. Chick, G. D. W, G. A. Whyatt, Cost study for manufacturing of solid oxide fuel cell power systems, Tech. Rep. PNNL-22732, U.S. Department of Energy (2012).

[95] AutoRe (2016).
URL https://www.autore-eu.com/

[96] European Commission, CORDIS the Community Research and Development Information Service. (2016).
URL https://cordis.europa.eu/project/rcn/197929_en.html

[97] Waste 2 Watts Project (2019).
URL https://waste2watts-project.net/

[98] A. Perna, S. Cicconardi, R. Cozzolino, Performance evaluation of a fuel processing system based on membrane reactors technology integrated with a PEMFC stack, International Journal of Hydrogen Energy 36 (16) (2011) 9906–9915.

[99] G. Di Marcoberardino, F. Sosio, G. Manzolini, S. Campanari, Fixed bed membrane reactor for hydrogen production from steam methane reforming: Experimental and modeling approach, International Journal of Hydrogen Energy 40 (24) (2015) 7559–7567.

[100] G. Di Marcoberardino, L. Roses, G. Manzolini, Technical assessment of a micro-cogeneration system based on polymer electrolyte membrane fuel cell and fluidized bed autothermal reformer, Applied Energy 162 (2016) 231–244.

[101] G. Di Marcoberardino, F. Gallucci, G. Manzolini, M. van Sint Annaland, Definition of validated membrane reactor model for 5 kW power output CHP system for different natural gas compositions, International Journal of Hydrogen Energy 41 (42) (2016) 19141–19153.

[102] T. A. Peters, R. Bredesen, H. J. Venvik, Pd-based Membranes in Hydrogen Production: Long-term Stability and Contaminant Effects, in: Membrane Engineering for the Treatment of Gases, 2017, pp. 177–211.

[103] A. Heinzel, B. Vogel, P. Hübner, Reforming of natural gas - hydrogen generation for small scale stationary fuel cell systems, Journal of Power Sources 105 (2) (2002) 202–207.

[104] A. L. Facci, G. Loreti, S. Ubertini, F. Barbir, T. Chalkidis, R.-P. Eßling, T. Peters, E. Skoufa, R. Bove, Numerical assessment of an automotive derivative chp fuel cell system, Energy Procedia 105 (2017) 1564 – 1569.

[105] N. W. Ockwig, T. M. Nenoff, Membranes for hydrogen separation, Chemical reviews 107 (10) (2007) 4078–4110.

[106] K. Atsonios, K. Panopoulos, A. Doukelis, A. Koumanakos, E. Kakaras, T. Peters, Y. van Delft, Introduction to palladium membrane technology, Palladium Membrane Technology for Hydrogen Production, Carbon Capture and Other Applications: Principles, Energy Production and Other Applications. Elsevier (2014) 1–21.

[107] T. Peters, P. M. Rørvik, T. Sunde, M. Stange, F. Roness, T. Reinertsen, J. Ræder, Y. Larring, R. Bredesen, Palladium (pd) membranes

as key enabling technology for pre-combustion co2 capture and hydrogen production, Energy Procedia 114 (2017) 37–45.

[108] H_2 site, Membrane reactors for H_2 generation.
URL https://www.h2site.eu/en/

[109] L. Ansaloni, E. Louradour, F. Radmanesh, H. van Veen, M. Pilz, C. Simon, N. E. Benes, T. A. Peters, Upscaling polyposs-imide membranes for high temperature h2 upgrading, Journal of Membrane Science (2020) 118875.

[110] H. Kurokawa, H. Yakabe, I. Yasuda, T. Peters, R. Bredesen, Inhibition effect of co on hydrogen permeability of pd–ag membrane applied in a microchannel module configuration, International journal of hydrogen energy 39 (30) (2014) 17201–17209.

[111] T. Peters, P. Carvalho, J. van Wees, J. Overbeek, E. Sagvolden, F. van Berkel, O. Løvvik, R. Bredesen, Leakage evolution and atomic-scale changes in pd-based membranes induced by long-term hydrogen permeation, Journal of membrane science 563 (2018) 398–404.

[112] H. Malerød-Fjeld, D. Clark, I. Yuste-Tirados, R. Zanón, D. Catalán-Martinez, D. Beeaff, S. H. Morejudo, P. K. Vestre, T. Norby, R. Haugsrud, et al., Thermo-electrochemical production of compressed hydrogen from methane with near-zero energy loss, Nature Energy 2 (12) (2017) 923–931.

[113] J. M. Polfus, B. Yildiz, H. L. Tuller, R. Bredesen, Adsorption of co2 and facile carbonate formation on bazro3 surfaces, The Journal of Physical Chemistry C 122 (1) (2018) 307–314.

[114] Aspen Technology, Inc. Aspen Technology Limited, Cambridge, Massachusetts, United States, Aspen Plus user guide (2003).

[115] S. Campanari, G. Valenti, E. Macchi, G. Lozza, N. Ravidà, Development of a micro-cogeneration laboratory and testing of a natural gas CHP unit based on PEM fuel cells, Applied Thermal Engineering 71 (2) (2014) 714–720.

[116] R. Cozzolino, S. Cicconardi, E. Galloni, M. Minutillo, A. Perna, Theoretical and experimental investigations on thermal management of

a PEMFC stack, International Journal of Hydrogen Energy 36 (13) (2011) 8030–8037.

[117] ASHRAE, ASHRAE handbook fundamentals. Atlanta: American Society of Heating, Refrigerating and Air-Conditioning Engineers, Inc (1989).

[118] A. Sieverts, Absorption of gases by metals, Zeitschrift für Metallkunde 21 (1929) 37–46.

[119] Ø. Hatlevik, S. K. Gade, M. K. Keeling, P. M. Thoen, A. Davidson, J. D. Way, Palladium and palladium alloy membranes for hydrogen separation and production: history, fabrication strategies, and current performance, Separation and Purification Technology 73 (1) (2010) 59–64.

[120] DOE Hydrogen and Fuel Cell Program (Last Accessed 2018).
URL https://www.hydrogen.energy.gov/

[121] A. Piga, X. E. Verykios, An advanced reactor configuration for the partial oxidation of methane to synthesis gas, Catalysis today 60 (1-2) (2000) 63–71.

[122] European Patent 94600005.6/13.07.94. U.S.A. Patent No. 6, 605 376 (Aug. 12 .2003).

[123] H. S. Fogler, Elements of Chemical Reaction Engineering (Prentice Hall International Series in the Physical and Chemical Engineering Sciences)(Hardcover), 2005.

[124] F. Kreith, R. M. Manglik, M. S. Bohn, Principles of heat transfer, Cengage Learning, 2012.

[125] I. Dybkjaer, Tubular reforming and autothermal reforming of natural gas - an overview of available processes, Fuel Processing Technology 42 (2) (1995) 85 – 107, trends in Natural Gas Utilisation.
URL http://www.sciencedirect.com/science/article/pii/037838209400099F

[126] M.-B. Hägg, R. Quinn, Polymeric facilitated transport membranes for hydrogen purification, MRS bulletin 31 (10) (2006) 750–755.

[127] G. Di Marcoberardino, J. Knijff, M. Binotti, F. Gallucci, G. Manzolini, Techno-economic assessment in a fluidized bed membrane reactor for small-scale h2 production: effect of membrane support thickness, Membranes 9 (9) (2019) 116.

[128] G. Di Marcoberardino, S. Foresti, M. Binotti, G. Manzolini, Potentiality of a biogas membrane reformer for decentralized hydrogen production, Chemical Engineering and Processing-Process Intensification 129 (2018) 131–141.

[129] F. Gallucci, L. Paturzo, A. Basile, A simulation study of the steam reforming of methane in a dense tubular membrane reactor, International Journal of Hydrogen Energy 29 (6) (2004) 611–617.

[130] C.-H. Kim, J.-Y. Han, S. Kim, B. Lee, H. Lim, K.-Y. Lee, S.-K. Ryi, Hydrogen production by steam methane reforming in a membrane reactor equipped with a Pd composite membrane deposited on a porous stainless steel, International Journal of Hydrogen Energy.

[131] C.-H. Kim, J.-Y. Han, H. Lim, K.-Y. Lee, S.-K. Ryi, Methane steam reforming using a membrane reactor equipped with a Pd-based composite membrane for effective hydrogen production, International Journal of Hydrogen Energy.

[132] A. Fedotov, D. Antonov, V. Uvarov, M. Tsodikov, Original hybrid membrane-catalytic reactor for the Co-Production of syngas and ultrapure hydrogen in the processes of dry and steam reforming of methane, ethanol and DME, International Journal of Hydrogen Energy 43 (14) (2018) 7046–7054.

[133] H. Yakabe, H. Kurokawa, Y. Shirasaki, I. Yasuda, Operation of a palladium membrane reformer system for hydrogen production: the case of tokyo gas, Palladium Membrane Technology for Hydrogen Production, Carbon Capture and Other Applications: Principles, Energy Production and Other Applications (2014) 303.

[134] Helbio, Helbio S.A. - Hydrogen & Energy Systems.
URL https://helbio.com/

[135] M. Pen, J. Gomez, J. G. Fierro, et al., New catalytic routes for syngas and hydrogen production, Applied Catalysis A: General 144 (1-2) (1996) 7–57.

[136] G. Di Marcoberardino, G. Manzolini, Investigation of a 5 kw micro-chp pem fuel cell based system integrated with membrane reactor under diverse eu natural gas quality, International Journal of Hydrogen Energy 42 (19) (2017) 13988–14002.

[137] P. Silvestroni, Fondamenti di chimica, Veschi, 1996.

[138] P. J. Linstrom, W. G. Mallard, The nist chemistry webbook: A chemical data resource on the internet, Journal of Chemical & Engineering Data 46 (5) (2001) 1059–1063.

[139] Z. Jaworski, B. Zakrzewska, P. Pianko-Oprych, On thermodynamic equilibrium of carbon deposition from gaseous cho mixtures: updating for nanotubes, Reviews in Chemical Engineering 33 (3) (2017) 217–235.

[140] A. L. Facci, D. Sánchez, E. Jannelli, S. Ubertini, Trigenerative micro compressed air energy storage: Concept and thermodynamic assessment, Applied Energy 158 (2015) 243–254.

[141] M. Zeppieri, P. Villa, N. Verdone, M. Scarsella, P. De Filippis, Kinetic of methane steam reforming reaction over nickel-and rhodium-based catalysts, Applied Catalysis A: General 387 (1-2) (2010) 147–154.

[142] D. Pashchenko, Effect of the geometric dimensionality of computational domain on the results of cfd-modeling of steam methane reforming, International Journal of Hydrogen Energy 43 (18) (2018) 8662–8673.

[143] D. Hoang, S. Chan, O. Ding, Kinetic and modelling study of methane steam reforming over sulfide nickel catalyst on a gamma alumina support, Chemical Engineering Journal 112 (1-3) (2005) 1–11.

[144] R. Cozzolino, Thermodynamic performance assessment of a novel micro-cchp system based on a low temperature pemfc power unit and a half-effect li/br absorption chiller, Energies 11 (2).
URL http://www.mdpi.com/1996-1073/11/2/315

[145] A. L. Facci, L. Andreassi, S. Ubertini, Optimization of chcp (combined heat power and cooling) systems operation strategy using dynamic programming, Energy 66 (2014) 387–400.

[146] A. L. Facci, L. Andreassi, S. Ubertini, E. Sciubba, Analysis of the influence of thermal energy storage on the optimal management of a trigeneration plant, Energy Procedia 45 (2014) 1295–1304.

[147] A. L. Facci, L. Andreassi, F. Martini, S. Ubertini, Comparing energy and cost optimization in distributed energy systems management, Journal of Energy Resources Technology 136 (3) (2014) 032001.

[148] A. L. Facci, S. Ubertini, Meta-heuristic optimization for a high-detail smart management of complex energy systems.

[149] K. E. Herold, R. Radermacher, S. A. Klein, Absorption chillers and heat pumps, CRC press, 2016.

[150] B. H. Gebreslassie, M. Medrano, D. Boer, Exergy analysis of multi-effect water–libr absorption systems: from half to triple effect, Renewable Energy 35 (8) (2010) 1773–1782.

[151] ASHRAE, Product directory ashrae handbook, System 1974.

[152] Z. Yang, X. Tang, M. Qu, O. Abdelaziz, K. R. Gluesenkamp, Development of updated absorption simulation software (absim), Tech. rep., Oak Ridge National Laboratory (ORNL); Building Technologies Research and Integration Center (BTRIC) (2014).

[153] G. Grossman, A. Zaltash, Absim - modular simulation of advanced absorption systems, International Journal of Refrigeration 24 (6) (2001) 531–543.

[154] S. A. Klein, F. Alvarado, EES: Engineering equation solver for the Microsoft Windows operating system, F-Chart software, 1992.

[155] H. Yin, An absorption chiller in a micro bchp application: model based design and performance analysis, Ph.D. thesis, Citeseer (2006).

[156] M. H. Beitelmal, C. D. Patel, Model - based approach for optimizing a data center centralized cooling system, Hewlett-Packard (HP) Lab Technical Report.

[157] R. Maryami, A. Dehghan, An exergy based comparative study between libr/water absorption refrigeration systems from half effect to triple effect, Applied Thermal Engineering 124 (2017) 103–123.

[158] C. Somers, A. Mortazavi, Y. Hwang, R. Radermacher, P. Rodgers, S. Al-Hashimi, Modeling water/lithium bromide absorption chillers in aspen plus, Applied Energy 88 (11) (2011) 4197–4205.

[159] O. Redlich, J. N. Kwong, On the thermodynamics of solutions. v. an equation of state. fugacities of gaseous solutions., Chemical reviews 44 (1) (1949) 233–244.

[160] H. Renon, J. M. Prausnitz, Local compositions in thermodynamic excess functions for liquid mixtures, AIChE journal 14 (1) (1968) 135–144.

[161] E. Fabrizio, M. Filippi, J. Virgone, An hourly modelling framework for the assessment of energy sources exploitation and energy converters selection and sizing in buildings, Energy and Buildings 41 (10) (2009) 1037–1050.

[162] A. Hawkes, M. Leach, Cost-effective operating strategy for residential micro-combined heat and power, Energy 32 (5) (2007) 711–723.

[163] L. Andreassi, M. Ciminelli, M. Feola, S. Ubertini, Innovative method for energy management: Modelling and optimal operation of energy systems, Energy and Buildings 41 (4) (2009) 436–444.

[164] D. Chiappini, A. L. Facci, L. Tribioli, S. Ubertini, SOFC management in distributed energy systems, Journal of Fuel Cell Science and Technology 8 (3).

[165] L. Tribioli, R. Cozzolino, L. Evangelisti, G. Bella, Energy management of an off-grid hybrid power plant with multiple energy storage systems, Energies 9 (8) (2016) 661.

[166] Office of Energy Efficiency and Renewable Energy, Commercial reference buildings, http://energy.gov/eere/buildings/commercial-reference-buildings (November 2016).

[167] M. J. Laustsen, Energy efficiency requirements in building codes, energy efficiency policies for new buildings (2008).

[168] Joint Research Center, Photovoltaic geographical information system (pvgis), http://re.jrc.ec.europa.eu/pvgis/ (March 2018).

[169] Eurostat, Eurostat, your key to european statistics (2016).
URL http://ec.europa.eu/eurostat/web/energy/data/\database

[170] D. Sari, A. Bayram, Quantification of emissions from domestic heating in residential areas of izmir, turkey and assessment of the impact on local/regional air-quality, Science of the Total Environment 488 (2014) 429–436.

[171] A. Moro, L. Lonza, Electricity carbon intensity in european member states: Impacts on ghg emissions of electric vehicles, Transportation Research Part D: Transport and Environment.

[172] J.-M. Lavoie, Review on dry reforming of methane, a potentially more environmentally-friendly approach to the increasing natural gas exploitation, Frontiers in chemistry 2 (2014) 81.

[173] M. Hauck, S. Herrmann, H. Spliethoff, Simulation of a reversible sofc with aspen plus, International Journal of Hydrogen Energy 42 (15) (2017) 10329–10340.

[174] G. Jeanmonod, L. Wang, S. Diethelm, F. Maréchal, et al., Trade-off designs of power-to-methane systems via solid-oxide electrolyzer and the application to biogas upgrading, Applied energy 247 (2019) 572–581.

[175] L. Wang, M. Pérez-Fortes, H. Madi, S. Diethelm, F. Maréchal, et al., Optimal design of solid-oxide electrolyzer based power-to-methane systems: A comprehensive comparison between steam electrolysis and co-electrolysis, Applied Energy 211 (2018) 1060–1079.

[176] L. Wang, M. Rao, S. Diethelm, T.-E. Lin, H. Zhang, A. Hagen, F. Maréchal, et al., Power-to-methane via co-electrolysis of h2o and co2: The effects of pressurized operation and internal methanation, Applied Energy 250 (2019) 1432–1445.

[177] L. Wang, Z. Yang, S. Sharma, A. Mian, T.-E. Lin, G. Tsatsaronis, F. Maréchal, Y. Yang, A review of evaluation, optimization and synthesis of energy systems: methodology and application to thermal power plants, Energies 12 (1) (2019) 73.

[178] H. Zhang, L. Wang, F. Maréchal, U. Desideri, et al., Techno-economic optimization of co2-to-methanol with solid-oxide electrolyzer, Energies 12 (19) (2019) 3742.

[179] F. Marechal, B. Kalitventzeff, Targeting the integration of multi-period utility systems for site scale process integration, Applied thermal engineering 23 (14) (2003) 1763–1784.

[180] M. Gassner, Process design methodology for thermochemical production of fuels from biomass, Tech. rep., EPFL (2010).

[181] A. Mian, Optimal design methods applied to solar-assisted hydrothermal gasification plants, Tech. rep., EPFL (2016).

[182] R. Fourer, D. M. Gay, B. W. Kernighan, Ampl. a modeling language for mathematical programming.

[183] I. I. Cplex, V12. 1: User's manual for cplex, International Business Machines Corporation 46 (53) (2009) 157.

[184] K. Sasaki, Y. Teraoka, Equilibria in fuel cell gases, ECS Proceedings Volumes 2003 (1) (2003) 1225.

[185] K. Sasaki, Y. Teraoka, Equilibria in fuel cell gases: Ii. the cho ternary diagrams, Journal of The Electrochemical Society 150 (7) (2003) A885.

[186] Y. Li, Y. Wang, X. Zhang, Z. Mi, Thermodynamic analysis of autothermal steam and co2 reforming of methane, International Journal of Hydrogen Energy 33 (10) (2008) 2507–2514.

[187] M. K. Nikoo, N. Amin, Thermodynamic analysis of carbon dioxide reforming of methane in view of solid carbon formation, Fuel Processing Technology 92 (3) (2011) 678–691.

[188] A. R. Korsgaard, M. P. Nielsen, S. K. Kær, Part one: A novel model of htpem-based micro-combined heat and power fuel cell system, International Journal of Hydrogen Energy 33 (7) (2008) 1909–1920.

[189] Fuel Cells and Hydrogen Joint Undretaking, STATE-OF-THE-ART AND FUTURE TARGETS (KPIS).
URL https://www.fch.europa.eu/soa-and-targets

[190] G. Lozza, Turbine a gas e cicli combinati, Società Editrice Esculapio, 2020.

Ringraziamenti

Mi sento in primo luogo di dover ringraziare i miei familiari che, con il loro supporto materiale ed umano, mi hanno dato la possibilità di raggiungere questo importante traguardo.

Vorrei poi ringraziare Andrea ed il prof. Ubertini per la loro preziosa guida ed il sostegno profusi in tutti questi anni. Senza il loro esempio ed i loro insegnamenti non credo sarei mai riuscito a completare nemmeno una minima parte del lavoro che ho svolto nel corso di dottorato. Vorrei inoltre ringraziare i miei tutor all'EPFL Jan Van Herle, Stefan Diethelm e Ligang Wang.

Un ringraziamento speciali infine a tutti gli amici e colleghi dell'Unitus e dell'EPFL per aver reso memorabile il percorso condiviso.